

## Letter of Intent: The Precision IceCube Next Generation Upgrade (PINGU)

**The IceCube Gen2 Collaboration**<sup>1</sup>: M. G. Aartsen<sup>b</sup>, M. Ackermann<sup>bg</sup>, J. Adams<sup>p</sup>, J. A. Aguilar<sup>l</sup>, M. Ahlers<sup>t</sup>, M. Ahrens<sup>ax</sup>, I. Al Samarai<sup>y</sup>, D. Altmann<sup>x</sup>, K. Andeen<sup>aj</sup>, T. Anderson<sup>bd</sup>, I. Anseau<sup>l</sup>, G. Anton<sup>x</sup>, C. Argüelles<sup>n</sup>, T. C. Arlen<sup>bd</sup>, J. Auffenberg<sup>a</sup>, S. Axani<sup>n</sup>, H. Bagherpour<sup>p</sup>, X. Bai<sup>au</sup>, A. Balagopal V.<sup>ab</sup>, J. P. Barron<sup>w</sup>, I. Bartos<sup>aq</sup>, S. W. Barwick<sup>aa</sup>, V. Baum<sup>ah</sup>, R. Bay<sup>h</sup>, J. J. Beatty<sup>r,s</sup>, J. Becker Tjus<sup>k</sup>, K.-H. Becker<sup>bf</sup>, S. BenZvi<sup>aw</sup>, D. Berley<sup>q</sup>, E. Bernardini<sup>bg</sup>, D. Z. Besson<sup>ac</sup>, G. Binder<sup>i,h</sup>, D. Bindig<sup>bf</sup>, E. Blaufuss<sup>q</sup>, S. Blot<sup>bg</sup>, C. Boehm<sup>ax</sup>, M. Bohmer<sup>al</sup>, M. Börner<sup>u</sup>, F. Bos<sup>k</sup>, D. Bose<sup>az</sup>, S. Böser<sup>ah</sup>, O. Botner<sup>be</sup>, E. Bourbeau<sup>t</sup>, J. Bourbeau<sup>ag</sup>, F. Bradascio<sup>bg</sup>, J. Braun<sup>ag</sup>, L. Brayeur<sup>m</sup>, M. Brenzke<sup>a</sup>, H.-P. Bretz<sup>bg</sup>, S. Bron<sup>y</sup>, J. Brostean-Kaiser<sup>bg</sup>, A. Burgman<sup>be</sup>, T. Carver<sup>y</sup>, J. Casey<sup>ag</sup>, M. Casier<sup>m</sup>, E. Cheung<sup>q</sup>, D. Chirkin<sup>ag</sup>, A. Christov<sup>y</sup>, K. Clark<sup>ad</sup>, L. Classen<sup>an</sup>, S. Coenders<sup>al</sup>, G. H. Collin<sup>n</sup>, J. M. Conrad<sup>n</sup>, D. F. Cowen<sup>bd,bc</sup>, R. Cross<sup>aw</sup>, M. Day<sup>ag</sup>, J. P. A. M. de André<sup>v</sup>, C. De Clercq<sup>m</sup>, J. J. DeLaunay<sup>bd</sup>, H. Dembinski<sup>ao</sup>, S. De Ridder<sup>z</sup>, P. Desiati<sup>ag</sup>, K. D. de Vries<sup>m</sup>, G. de Wasseige<sup>m</sup>, M. de With<sup>j</sup>, T. DeYoung<sup>v</sup>, J. C. Díaz-Vélez<sup>ag</sup>, V. di Lorenzo<sup>ah</sup>, H. Dujmovic<sup>az</sup>, J. P. Dumm<sup>ax</sup>, M. Dunkman<sup>bd</sup>, M. A. DuVernois<sup>ag</sup>, E. Dvorak<sup>au</sup>, B. Eberhardt<sup>ah</sup>, T. Ehrhardt<sup>ah</sup>, B. Eichmann<sup>k</sup>, P. Eller<sup>bd</sup>, R. Engel<sup>ab</sup>, J. J. Evans<sup>ai</sup>, P. A. Evenson<sup>ao</sup>, S. Fahey<sup>ag</sup>, A. R. Fazely<sup>g</sup>, J. Felde<sup>q</sup>, K. Filimonov<sup>h</sup>, C. Finley<sup>ax</sup>, S. Flis<sup>ax</sup>, A. Franckowiak<sup>bg</sup>, E. Friedman<sup>q</sup>, T. Fuchs<sup>u</sup>, T. K. Gaisser<sup>ao</sup>, J. Gallagher<sup>af</sup>, A. Gartner<sup>al</sup>, L. Gerhardt<sup>i</sup>, R. Gernhaeuser<sup>al</sup>, K. Ghorbani<sup>ag</sup>, W. Giang<sup>w</sup>, T. Glauch<sup>a</sup>, T. Glüsenskamp<sup>x</sup>, A. Goldschmidt<sup>i</sup>, J. G. Gonzalez<sup>ao</sup>, D. Grant<sup>w</sup>, Z. Griffith<sup>ag</sup>, C. Haack<sup>a</sup>, A. Hallgren<sup>be</sup>, F. Halzen<sup>ag</sup>, K. Hanson<sup>ag</sup>, J. Haugen<sup>ag</sup>, A. Haungs<sup>ab</sup>, D. Hebecker<sup>j</sup>, D. Heereman<sup>l</sup>, K. Helbing<sup>bf</sup>, R. Hellauer<sup>q</sup>, F. Henningsen<sup>al</sup>, S. Hickford<sup>bf</sup>, J. Hignight<sup>v</sup>, G. C. Hill<sup>b</sup>, K. D. Hoffman<sup>q</sup>, B. Hoffmann<sup>ab</sup>, R. Hoffmann<sup>bf</sup>, B. Hokanson-Fasig<sup>ag</sup>, K. Holzappel<sup>al</sup>, K. Hoshina<sup>ag,ba</sup>, F. Huang<sup>bd</sup>, M. Huber<sup>al</sup>, T. Huber<sup>ab</sup>, T. Huege<sup>ab</sup>, K. Hultqvist<sup>ax</sup>, M. Hünnefeld<sup>u</sup>, S. In<sup>az</sup>, A. Ishihara<sup>o</sup>, E. Jacobi<sup>bg</sup>, G. S. Japaridze<sup>e</sup>, M. Jeong<sup>az</sup>, K. Jero<sup>ag</sup>, B. J. P. Jones<sup>d</sup>, P. Kalaczynski<sup>a</sup>, O. Kalekin<sup>x</sup>, W. Kang<sup>az</sup>, D. Kang<sup>ab</sup>, A. Kappes<sup>an</sup>, T. Karg<sup>bg</sup>, A. Karle<sup>ag</sup>, T. Katori<sup>ae</sup>, U. Katz<sup>x</sup>, M. Kauer<sup>ag</sup>, A. Keivani<sup>bd</sup>, J. L. Kelley<sup>ag</sup>, A. Kheirandish<sup>ag</sup>, J. Kim<sup>az</sup>, M. Kim<sup>o</sup>, T. Kintscher<sup>bg</sup>, J. Kiryluk<sup>ay</sup>, T. Kittler<sup>x</sup>, S. R. Klein<sup>i,h</sup>, G. Kohnen<sup>ak</sup>, R. Koirala<sup>ao</sup>, H. Kolanoski<sup>j</sup>, L. Köpke<sup>ah</sup>, C. Kopper<sup>w</sup>, S. Kopper<sup>bb</sup>, J. P. Koschinsky<sup>a</sup>, D. J. Koskinen<sup>t</sup>, M. Kowalski<sup>bj,bg</sup>, C. B. Krauss<sup>w</sup>, K. Krings<sup>al</sup>, M. Kroll<sup>k</sup>, G. Krückl<sup>ah</sup>, J. Kunnen<sup>m</sup>, S. Kunwar<sup>bg</sup>,

---

<sup>1</sup>Please send correspondence to analysis@icecube.wisc.edu

N. Kurahashi<sup>at</sup>, T. Kuwabara<sup>o</sup>, A. Kyriacou<sup>b</sup>, M. Labare<sup>z</sup>, J. L. Lanfranchi<sup>bd</sup>,  
 M. J. Larson<sup>t</sup>, F. Lauber<sup>bf</sup>, D. Lennarz<sup>v</sup>, M. Lesiak-Bzdak<sup>av</sup>, A. Leszczynska<sup>ab</sup>,  
 M. Leuermann<sup>a</sup>, Q. R. Liu<sup>ag</sup>, J. LoSecco<sup>ar</sup>, L. Lu<sup>o</sup>, J. Lünemann<sup>m</sup>, W. Luszczyk<sup>ag</sup>,  
 J. Madsen<sup>av</sup>, G. Maggi<sup>m</sup>, K. B. M. Mahn<sup>v</sup>, S. Mancina<sup>ag</sup>, S. Mandalia<sup>ae</sup>, S. Marka<sup>aq</sup>,  
 Z. Marka<sup>aq</sup>, R. Maruyama<sup>ap</sup>, K. Mase<sup>o</sup>, R. Maunu<sup>q</sup>, F. McNally<sup>ag</sup>, K. Meagher<sup>l</sup>,  
 M. Medici<sup>t</sup>, M. Meier<sup>u</sup>, T. Menne<sup>u</sup>, G. Merino<sup>ag</sup>, T. Meures<sup>l</sup>, S. Miarecki<sup>i,h</sup>, J. Micallef<sup>v</sup>,  
 G. Momenté<sup>ah</sup>, T. Montaruli<sup>v</sup>, R. W. Moore<sup>w</sup>, M. Moulai<sup>n</sup>, R. Nahnauer<sup>bg</sup>,  
 P. Nakarmi<sup>bb</sup>, U. Naumann<sup>bf</sup>, G. Neer<sup>v</sup>, H. Niederhausen<sup>ay</sup>, S. C. Nowicki<sup>w</sup>,  
 D. R. Nygren<sup>i</sup>, A. Obertacke Pollmann<sup>bf</sup>, M. Oehler<sup>ab</sup>, A. Olivas<sup>q</sup>, A. O’Murchadha<sup>l</sup>,  
 A. Palazzo<sup>am</sup>, T. Palczewski<sup>i,h</sup>, H. Pandya<sup>ao</sup>, D. V. Pankova<sup>bd</sup>, L. Papp<sup>al</sup>, P. Peiffer<sup>ah</sup>,  
 J. A. Pepper<sup>bb</sup>, C. Pérez de los Heros<sup>be</sup>, T. C. Petersen<sup>t</sup>, D. Pieloth<sup>u</sup>, E. Pinat<sup>l</sup>,  
 J. L. Pinfold<sup>w</sup>, M. Plum<sup>aj</sup>, P. B. Price<sup>h</sup>, G. T. Przybylski<sup>i</sup>, C. Raab<sup>l</sup>, L. Rädcl<sup>a</sup>,  
 M. Rameez<sup>t</sup>, K. Rawlins<sup>c</sup>, I. C. Rea<sup>al</sup>, R. Reimann<sup>a</sup>, B. Relethford<sup>at</sup>, M. Relich<sup>o</sup>,  
 M. Renschler<sup>ab</sup>, E. Resconi<sup>al</sup>, W. Rhode<sup>u</sup>, M. Richman<sup>at</sup>, M. Riegel<sup>ab</sup>, S. Robertson<sup>b</sup>,  
 M. Rongen<sup>a</sup>, C. Rott<sup>az</sup>, T. Ruhe<sup>u</sup>, D. Ryckbosch<sup>z</sup>, D. Rysewyk<sup>v</sup>, T. Sälzer<sup>a</sup>,  
 S. E. Sanchez Herrera<sup>w</sup>, A. Sandrock<sup>u</sup>, J. Sandroos<sup>ah</sup>, P. Sandstrom<sup>ag</sup>, M. Santander<sup>bb</sup>,  
 S. Sarkar<sup>t,as</sup>, S. Sarkar<sup>w</sup>, K. Satalecka<sup>bg</sup>, H. Schieler<sup>ab</sup>, P. Schlunder<sup>u</sup>, T. Schmidt<sup>q</sup>,  
 A. Schneider<sup>ag</sup>, S. Schoenen<sup>a</sup>, S. Schöneberg<sup>k</sup>, F. G. Schröder<sup>ab</sup>, L. Schumacher<sup>a</sup>,  
 D. Seckel<sup>ao</sup>, S. Seunarine<sup>av</sup>, M. H. Shaevitz<sup>aq</sup>, J. Soedingrekso<sup>u</sup>, D. Soldin<sup>bf</sup>,  
 S. Söldner-Rembold<sup>ai</sup>, M. Song<sup>q</sup>, G. M. Spiczak<sup>av</sup>, C. Spiering<sup>bg</sup>, J. Stachurska<sup>bg</sup>,  
 M. Stamatikos<sup>r</sup>, T. Stanev<sup>ao</sup>, A. Stasik<sup>bg</sup>, J. Stettner<sup>a</sup>, A. Steuer<sup>ah</sup>, T. Stezelberger<sup>i</sup>,  
 R. G. Stokstad<sup>i</sup>, A. Stöbl<sup>o</sup>, N. L. Strotjohann<sup>bg</sup>, T. Stuttard<sup>t</sup>, G. W. Sullivan<sup>q</sup>,  
 M. Sutherland<sup>r</sup>, I. Taboada<sup>f</sup>, A. Taketa<sup>ba</sup>, H. K. M. Tanaka<sup>ba</sup>, J. Tatar<sup>i,h</sup>, F. Tenholt<sup>k</sup>,  
 S. Ter-Antonyan<sup>g</sup>, A. Terliuk<sup>bg</sup>, G. Tešić<sup>bd</sup>, S. Tilav<sup>ao</sup>, P. A. Toale<sup>bb</sup>, M. N. Tobin<sup>ag</sup>,  
 S. Toscano<sup>m</sup>, D. Tosi<sup>ag</sup>, M. Tselengidou<sup>x</sup>, C. F. Tung<sup>f</sup>, A. Turcati<sup>al</sup>, C. F. Turley<sup>bd</sup>,  
 B. Ty<sup>ag</sup>, E. Unger<sup>be</sup>, M. Usner<sup>bg</sup>, J. Vandenbroucke<sup>ag</sup>, W. Van Driessche<sup>z</sup>,  
 N. van Eijndhoven<sup>m</sup>, S. Vanheule<sup>z</sup>, J. van Santen<sup>bg</sup>, D. Veberic<sup>ab</sup>, M. Vehring<sup>a</sup>,  
 E. Vogel<sup>a</sup>, M. Vraeghe<sup>z</sup>, C. Walck<sup>ax</sup>, A. Wallace<sup>b</sup>, M. Wallraff<sup>a</sup>, F. D. Wandler<sup>w</sup>,  
 N. Wandkowsky<sup>ag</sup>, A. Waza<sup>a</sup>, C. Weaver<sup>w</sup>, A. Weindl<sup>ab</sup>, M. J. Weiss<sup>bd</sup>, C. Wendt<sup>ag</sup>,  
 J. Werthebach<sup>u</sup>, S. Westerhoff<sup>ag</sup>, B. J. Whelan<sup>b</sup>, K. Wiebe<sup>ah</sup>, C. H. Wiebusch<sup>a</sup>,  
 L. Wille<sup>ag</sup>, D. R. Williams<sup>bb</sup>, L. Wills<sup>at</sup>, M. Wolf<sup>ag</sup>, J. Wood<sup>ag</sup>, T. R. Wood<sup>w</sup>,  
 E. Woolsey<sup>w</sup>, K. Woschnagg<sup>h</sup>, S. Wren<sup>ai</sup>, D. L. Xu<sup>ag</sup>, X. W. Xu<sup>g</sup>, Y. Xu<sup>ay</sup>, J. P. Yanez<sup>w</sup>,  
 G. Yodh<sup>aa</sup>, S. Yoshida<sup>o</sup>, T. Yuan<sup>ag</sup>, M. Zoll<sup>ax</sup>

<sup>a</sup>*III. Physikalisches Institut, RWTH Aachen University, D-52056 Aachen, Germany*

<sup>b</sup>*Department of Physics, University of Adelaide, Adelaide, 5005, Australia*

<sup>c</sup>*Dept. of Physics and Astronomy, University of Alaska Anchorage, 3211 Providence Dr., Anchorage, AK 99508, USA*

<sup>d</sup>*Dept. of Physics, University of Texas at Arlington, 502 Yates St., Science Hall Rm 108, Box 19059, Arlington, TX 76019, USA*

<sup>e</sup>*CTSPS, Clark-Atlanta University, Atlanta, GA 30314, USA*

<sup>f</sup>*School of Physics and Center for Relativistic Astrophysics, Georgia Institute of Technology, Atlanta, GA 30332, USA*

<sup>g</sup>*Dept. of Physics, Southern University, Baton Rouge, LA 70813, USA*

<sup>h</sup>*Dept. of Physics, University of California, Berkeley, CA 94720, USA*

<sup>i</sup>*Lawrence Berkeley National Laboratory, Berkeley, CA 94720, USA*

<sup>j</sup>*Institut für Physik, Humboldt-Universität zu Berlin, D-12489 Berlin, Germany*

<sup>k</sup>*Fakultät für Physik & Astronomie, Ruhr-Universität Bochum, D-44780 Bochum, Germany*

<sup>l</sup>*Université Libre de Bruxelles, Science Faculty CP230, B-1050 Brussels, Belgium*

<sup>m</sup>*Vrije Universiteit Brussel (VUB), Dienst ELEM, B-1050 Brussels, Belgium*

<sup>n</sup>*Dept. of Physics, Massachusetts Institute of Technology, Cambridge, MA 02139, USA*

<sup>o</sup>*Dept. of Physics and Institute for Global Prominent Research, Chiba University, Chiba 263-8522, Japan*

<sup>p</sup>*Dept. of Physics and Astronomy, University of Canterbury, Private Bag 4800, Christchurch, New Zealand*

<sup>q</sup>*Dept. of Physics, University of Maryland, College Park, MD 20742, USA*

<sup>r</sup>*Dept. of Physics and Center for Cosmology and Astro-Particle Physics, Ohio State University, Columbus, OH 43210, USA*

<sup>s</sup>*Dept. of Astronomy, Ohio State University, Columbus, OH 43210, USA*

<sup>t</sup>*Niels Bohr Institute, University of Copenhagen, DK-2100 Copenhagen, Denmark*

<sup>u</sup>*Dept. of Physics, TU Dortmund University, D-44221 Dortmund, Germany*

<sup>v</sup>*Dept. of Physics and Astronomy, Michigan State University, East Lansing, MI 48824, USA*

- <sup>w</sup>*Dept. of Physics, University of Alberta, Edmonton, Alberta, Canada T6G 2E1*
- <sup>x</sup>*Erlangen Centre for Astroparticle Physics, Friedrich-Alexander-Universität Erlangen-Nürnberg, D-91058 Erlangen, Germany*
- <sup>y</sup>*Département de physique nucléaire et corpusculaire, Université de Genève, CH-1211 Genève, Switzerland*
- <sup>z</sup>*Dept. of Physics and Astronomy, University of Gent, B-9000 Gent, Belgium*
- <sup>aa</sup>*Dept. of Physics and Astronomy, University of California, Irvine, CA 92697, USA*
- <sup>ab</sup>*Institut für Kernphysik, Karlsruhe Institute of Technology, D-76021 Karlsruhe, Germany*
- <sup>ac</sup>*Dept. of Physics and Astronomy, University of Kansas, Lawrence, KS 66045, USA*
- <sup>ad</sup>*SNOLAB, 1039 Regional Road 24, Creighton Mine 9, Lively, ON, Canada P3Y 1N2*
- <sup>ae</sup>*School of Physics and Astronomy, Queen Mary University of London, London E1 4NS, United Kingdom*
- <sup>af</sup>*Dept. of Astronomy, University of Wisconsin, Madison, WI 53706, USA*
- <sup>ag</sup>*Dept. of Physics and Wisconsin IceCube Particle Astrophysics Center, University of Wisconsin, Madison, WI 53706, USA*
- <sup>ah</sup>*Institute of Physics, University of Mainz, Staudinger Weg 7, D-55099 Mainz, Germany*
- <sup>ai</sup>*School of Physics and Astronomy, The University of Manchester, Oxford Road, Manchester, M13 9PL, United Kingdom*
- <sup>aj</sup>*Department of Physics, Marquette University, Milwaukee, WI, 53201, USA*
- <sup>ak</sup>*Université de Mons, 7000 Mons, Belgium*
- <sup>al</sup>*Physik-department, Technische Universität München, D-85748 Garching, Germany*
- <sup>am</sup>*Max-Planck-Institut für Physik (Werner Heisenberg Institut), Föhringer Ring 6, D-80805 München, Germany*
- <sup>an</sup>*Institut für Kernphysik, Westfälische Wilhelms-Universität Münster, D-48149 Münster, Germany*
- <sup>ao</sup>*Bartol Research Institute and Dept. of Physics and Astronomy, University of Delaware, Newark, DE 19716, USA*

*<sup>ap</sup>Dept. of Physics, Yale University, New Haven, CT 06520, USA*

*<sup>aq</sup>Columbia Astrophysics and Nevis Laboratories, Columbia University, New York, NY 10027, USA*

*<sup>ar</sup>Dept. of Physics, University of Notre Dame du Lac, 225 Nieuwland Science Hall, Notre Dame, IN 46556-5670, USA*

*<sup>as</sup>Dept. of Physics, University of Oxford, 1 Keble Road, Oxford OX1 3NP, UK*

*<sup>at</sup>Dept. of Physics, Drexel University, 3141 Chestnut Street, Philadelphia, PA 19104, USA*

*<sup>au</sup>Physics Department, South Dakota School of Mines and Technology, Rapid City, SD 57701, USA*

*<sup>av</sup>Dept. of Physics, University of Wisconsin, River Falls, WI 54022, USA*

*<sup>aw</sup>Dept. of Physics and Astronomy, University of Rochester, Rochester, NY 14627, USA*

*<sup>ax</sup>Oskar Klein Centre and Dept. of Physics, Stockholm University, SE-10691 Stockholm, Sweden*

*<sup>ay</sup>Dept. of Physics and Astronomy, Stony Brook University, Stony Brook, NY 11794-3800, USA*

*<sup>az</sup>Dept. of Physics, Sungkyunkwan University, Suwon 440-746, Korea*

*<sup>ba</sup>Earthquake Research Institute, University of Tokyo, Bunkyo, Tokyo 113-0032, Japan*

*<sup>bb</sup>Dept. of Physics and Astronomy, University of Alabama, Tuscaloosa, AL 35487, USA*

*<sup>bc</sup>Dept. of Astronomy and Astrophysics, Pennsylvania State University, University Park, PA 16802, USA*

*<sup>bd</sup>Dept. of Physics, Pennsylvania State University, University Park, PA 16802, USA*

*<sup>be</sup>Dept. of Physics and Astronomy, Uppsala University, Box 516, S-75120 Uppsala, Sweden*

*<sup>bf</sup>Dept. of Physics, University of Wuppertal, D-42119 Wuppertal, Germany*

*<sup>bg</sup>DESY, D-15738 Zeuthen, Germany*

---

## Abstract

The Precision IceCube Next Generation Upgrade (PINGU) is a proposed low-energy in-fill

array of the IceCube Neutrino Observatory. Leveraging technology proven with IceCube, PINGU will feature the world’s largest effective volume for neutrinos at an energy threshold of a few GeV, improving the sensitivity to several aspects of neutrino oscillation physics at modest cost. With its unprecedented statistical sample of low-energy atmospheric neutrinos, PINGU will have highly competitive sensitivity to  $\nu_\mu$  disappearance, the  $\theta_{23}$  octant, and maximal mixing, will make the world’s best  $\nu_\tau$  appearance measurement, allowing a unique probe of the unitarity of the PMNS mixing matrix, and will be able to distinguish the neutrino mass ordering at  $3\sigma$  significance with less than 4 years of data. PINGU can also extend the indirect search for solar WIMP dark matter complementary to the on-going and planned direct dark matter experiments. At the lower end of the energy range, PINGU may use neutrino tomography to directly probe the composition of the Earth’s core. With its increased module density, PINGU will improve IceCube’s sensitivity to galactic supernova neutrino bursts and enable it to extract the neutrino energy spectral shape.

*Keywords:*

neutrinos, neutrino oscillations, neutrino ordering, neutrino hierarchy, cosmic rays, dark matter, supernovae

---

## Contents

<b>1</b>	<b>Introduction</b>	<b>11</b>
<b>2</b>	<b>Detector Design and Predicted Performance</b>	<b>16</b>
2.1	Introduction . . . . .	16
2.2	Detector Geometries . . . . .	16
2.3	Detector Hardware and Simulation . . . . .	19
2.4	Event Reconstruction . . . . .	22
2.5	Event Selection . . . . .	26
2.6	Particle ID . . . . .	28

<b>3</b>	<b>Atmospheric Neutrino Oscillations</b>	<b>31</b>
3.1	Introduction . . . . .	31
3.1.1	Sample Generation and Event Selection . . . . .	34
3.1.2	Overview of Analyses . . . . .	35
3.2	Muon Neutrino Disappearance . . . . .	36
3.2.1	Event Selection and Reconstruction . . . . .	37
3.2.2	Analysis Method . . . . .	37
3.2.3	Results . . . . .	38
3.3	Sensitivity to the Octant of $\theta_{23}$ and Maximal Mixing . . . . .	41
3.4	Neutrino Mass Ordering . . . . .	45
3.4.1	Systematics . . . . .	45
3.4.2	Results . . . . .	49
3.4.3	Impact of the Charge-Parity Phase $\delta_{\text{CP}}$ . . . . .	50
3.4.4	Conclusions . . . . .	52
3.5	Tau Neutrino Appearance . . . . .	54
3.5.1	Event Selection and Reconstruction . . . . .	55
3.5.2	Analysis method . . . . .	57
3.5.3	Systematic uncertainties . . . . .	60
3.5.4	Results . . . . .	61
3.5.5	Comparison to other measurements . . . . .	63
3.5.6	Conclusion . . . . .	64

<b>4</b>	<b>Other Neutrino–Based Analyses</b>	<b>65</b>
4.1	Neutrino Tomography . . . . .	65
4.1.1	Motivation . . . . .	65
4.1.2	Introduction and Earth Composition Models . . . . .	65
4.1.3	Methodology . . . . .	66
4.1.4	Analysis Method . . . . .	67
4.1.5	Conclusions . . . . .	71
4.2	Supernova Neutrinos . . . . .	73
4.2.1	IceCube Sensitivity to Supernova Neutrino Bursts . . . . .	73
4.2.2	Monte Carlo Simulation . . . . .	74
4.2.3	Determination of the average neutrino energy . . . . .	75
4.2.4	Providing a measure of the spectral shape . . . . .	76
4.2.5	Conclusions and outlook . . . . .	77
4.3	Dark Matter . . . . .	79
4.3.1	Motivation . . . . .	79
4.3.2	Limit Calculation . . . . .	80
4.3.3	Experience from DeepCore . . . . .	80
4.3.4	Solar WIMPs . . . . .	80
4.3.5	Galactic Center WIMPs . . . . .	82
4.3.6	Outlook and conclusions . . . . .	84

<b>5</b>	<b>Instrumentation</b>	<b>85</b>
5.1	Introduction . . . . .	85
5.2	Sensor Configuration . . . . .	85
5.3	Optical Sensor Design . . . . .	85
5.4	New Photon Detection Technologies . . . . .	90
5.4.1	Multi-PMT Optical Modules (mDOMs) . . . . .	94
5.4.2	Dual optical sensors in an Ellipsoid Glass (D-Egg) . . . . .	96
5.4.3	Wavelength-Shifting Optical Modules (WOMs) . . . . .	100
5.5	Cable . . . . .	102
5.6	Drilling and Deployment . . . . .	104
<b>6</b>	<b>The Data Acquisition System</b>	<b>111</b>
6.1	Firmware and Software . . . . .	111
6.2	Integration of PINGU Channels into IceCube Surface DAQ . . . . .	111
6.2.1	Communications System and Readout Electronics . . . . .	112
6.2.2	Triggers . . . . .	114
6.3	Event Builder . . . . .	114
<b>7</b>	<b>Calibration</b>	<b>115</b>
7.1	Overview . . . . .	115
7.2	Impact of Detector Systematics in PINGU . . . . .	115
7.3	Detector Calibration . . . . .	116

7.3.1	Geometry . . . . .	116
7.3.2	Timing . . . . .	118
7.3.3	Module Gain and Sensitivity . . . . .	118
7.3.4	Ice Properties . . . . .	119
7.4	Calibration Devices . . . . .	120
7.4.1	LED Flashers . . . . .	120
7.4.2	POCAM . . . . .	122
7.4.3	Cameras . . . . .	126
7.4.4	Muon Tagging Optical Module (mTOM) . . . . .	128
<b>8</b>	<b>Monte Carlo Simulation Software</b>	<b>130</b>
8.1	Neutrino Event Generator . . . . .	130
8.2	Atmospheric Muon Event Generators . . . . .	131
8.3	Particle Propagation . . . . .	132
8.4	Light Propagation . . . . .	132
8.5	Detector Response . . . . .	132
<b>9</b>	<b>Schedule and Cost</b>	<b>134</b>
<b>10</b>	<b>Antarctic South Pole Facility and Logistics</b>	<b>137</b>
<b>11</b>	<b>Acknowledgements</b>	<b>138</b>
	<b>Appendix</b>	<b>141</b>

## 1. Introduction

Over the past decade, the South Pole has emerged as a site for world-class astronomy, particle astrophysics and neutrino physics. The Amundsen-Scott South Pole Station offers very special characteristics — the deep, clear ice below the surface and the dry air and clear sky above. The glacial ice at the South Pole is 2.8 km thick and extremely clear [1], making possible neutrino telescopes of unprecedented scale and sensitivity. The South Pole ice at depths below 2100 m is not only exceptionally clear but also extremely pure. The age of the ice at a depth of 2500 m is about 100 000 years, and radioactive contaminants in the deep ice are in the range of  $0.1\text{--}1 \times 10^{-12}$  g(Uranium or Thorium)/g and  $0.1\text{--}1 \times 10^{-9}$  g(Potassium)/g [2]. The cold environment greatly reduces thermionic electron noise in the photomultipliers. Thus, the South Pole provides a uniquely hospitable environment to host large-scale detectors. IceCube [3], the world’s largest neutrino detector, has been in operation with 5160 optical sensors distributed on 86 strings (cables) since 2011, transforming one gigaton of clear ice into a kilometer-scale Cherenkov detector.

Two smaller subarrays that were deployed along with IceCube – IceTop and DeepCore – are key elements of the facility. DeepCore [3] is the low-energy extension of IceCube, located in the lower region of the detector’s center, which provides substantially increased sensitivity to neutrinos with energies of approximately 10–100 GeV. The IceTop surface detector consists of 162 detector tanks, deployed approximately in coincidence with IceCube strings, for measurements of air showers above  $\tilde{100}$  TeV and, therefore, may also act as a veto against muons from these same events for the buried array. IceCube was constructed with funding from the Major Research Equipment and Facilities Construction (MREFC) program of the National Science Foundation (NSF) <sup>2</sup> and a roughly 10% contribution from non-US sources. The NSF’s Amundsen-Scott station provides excellent infrastructure for support of IceCube’s scientific activities, including the IceCube Laboratory building (see Fig. 1) that houses power, communications, and data acquisition systems.

By using IceCube sensors to veto incoming muons, background rates due to undetected muons in the deep detector can be reduced to levels comparable to deep mines. Figure 2 shows an estimate of the muon rate after applying a downward-going muon veto based on a simple majority trigger.

---

<sup>2</sup>which supports the acquisition and construction of major research facilities and equipment that extend the boundaries of science, engineering, and technology



Figure 1: The IceCube Laboratory building houses power, communications and data acquisition systems for IceCube and other experiments at the South Pole (photo by S. Lidström/NSF).

The discovery of high energy neutrinos of astrophysical origin by IceCube [5], as well as competitive measurements of neutrino oscillations [6, 7] and uniquely sensitive searches for dark matter with DeepCore [8], have led the IceCube Collaboration to begin investigating possible extensions of IceCube with improved performance at both high and low energies. The technological solutions to drill and deploy instruments in the deep ice are proven, the risks are small, and the costs are well understood.

At high energies ( $>1$  TeV), an expanded array in the deep ice and an improved surface array for identifying air showers that produce atmospheric neutrinos are under consideration [9]. At low energies (around 10 GeV), the Precision IceCube Next Generation Upgrade (PINGU) is proposed as an in-fill array for IceCube. PINGU is designed to study neutrino oscillations using atmospheric neutrinos that undergo Mikheyev-Smirnov-Wolfenstein (MSW) [10, 11] and parametric [12, 13] oscillations as they pass through the Earth.

Using these neutrinos, PINGU will have enhanced sensitivity to several important aspects of neutrino oscillation physics. It will be capable of determining the neutrino mass ordering (NMO), making high precision measurements of atmospheric muon neutrino disappearance and tau neutrino appearance, studying whether or not the mixing angle  $\theta_{23}$  is maximal, and PINGU will also explore a lower mass range for Weakly Interacting Massive Particles in searches for annihilation to neutrinos in the terrestrial and solar cores, the galactic center, dwarf spheroidals and other candidate astrophysical bodies. The detector will have enhanced sensitivity to very low energy neutrinos from supernovae, and also has

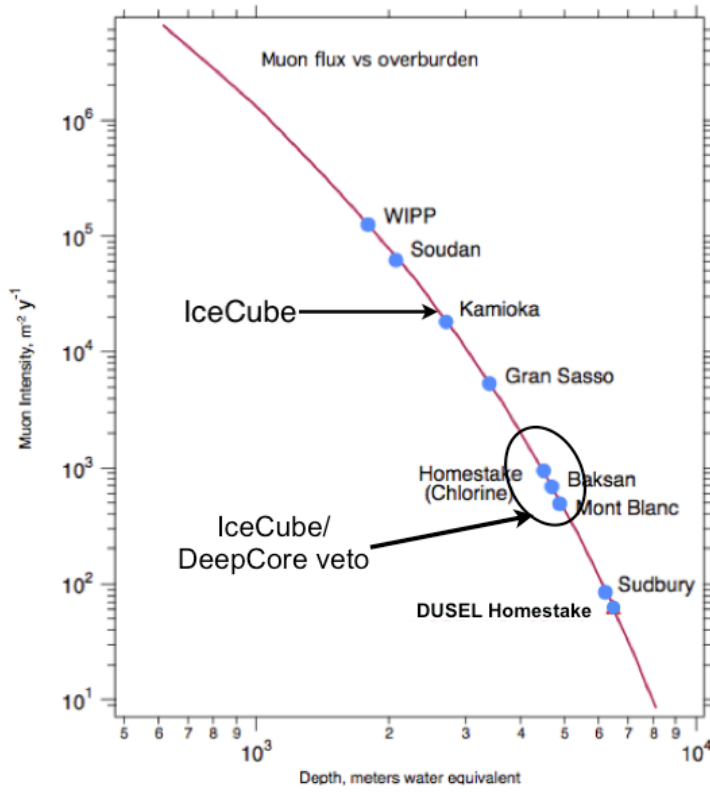


Figure 2: Estimated muon rate in the deep ice after applying a veto based on a simple majority trigger (see, *e.g.*, [4]).

the potential to perform the first neutrino-based tomographic probe of the Earth.

Together, the proposed detector enhancements at low and high energies are denoted “IceCube-Gen2.” As a stepping stone to a full-scale IceCube-Gen2 detector, a proposal to build IceCube-Gen2 Phase 1 (“Phase 1”), comprised of roughly one-quarter the strings envisioned for the full PINGU array, has been submitted to the NSF and cognizant funding agencies at collaborating institutions worldwide. The goals of Phase 1 are to perform the world’s most stringent tests of the unitarity of the PMNS neutrino mixing matrix in the tau sector, and to improve the sensitivity of IceCube at both high and low energies through better calibration of the optical properties of the ice and the *in situ* response of IceCube photodetectors. Better calibrations will improve reconstruction of neutrino directions and energies in both archived and future data, extending IceCube’s sensitivity to sources of high energy astrophysical neutrinos as well as increasing the precision of neutrino oscillation measurements.

Our simulations of PINGU, informed by experience with data from IceCube, and in particular DeepCore, indicate that our reconstruction algorithms will provide sufficient angular and energy resolutions to achieve the project goals. Known systematic uncertainties are found to be sufficiently small to enable a measurement of neutrino oscillation parameters with a few months to a few years of data. These estimates are based on a conservative analysis in which the detector geometry has yet to be fully optimized and a number of possible improvements: such as the use of event elasticity to provide some  $\nu$ - $\bar{\nu}$  separation, down-going atmospheric neutrinos to provide an oscillation-free control sample, possible improvements in event reconstructions, and better control and understanding of various systematic errors, not yet included, increasing our confidence in this estimate.

PINGU will be composed of sensors of similar nature and size as the IceCube DOMs, and installed in only two deployment seasons using the same techniques and equipment. The expertise developed in designing, deploying, and operating IceCube means that the PINGU detector could be deployed quickly and with well-understood and minimal risk. Designed as an extension of IceCube, close integration of PINGU with IceCube’s online and offline systems will be straightforward, enabling us to use the surrounding IceCube DOMs to provide a nearly hermetic active veto against downward-going cosmic ray muons, the chief background of all PINGU physics channels. In addition, the cost of both developing software systems and operating PINGU will be incremental and thus considerably lower than normally expected for a project of this scale.

This Letter of Intent (LoI), an update of our original LoI [14], presents the detailed physics

cases for the muon neutrino disappearance, maximal mixing, tau neutrino appearance, neutrino mass ordering, Earth tomography, supernova neutrino burst and WIMP dark matter indirect detection measurements. We describe the baseline design of the PINGU detector and requirements for the hot water drill and calibration devices, highlighting salient points of departure from what was used in IceCube [15, 16, 17]. In [Appendix D](#), we describe “Gen2 Phase 1,” the proposed first step for PINGU and the future IceCube Gen2 array, highlighting the important physics measurements attainable at both low and high neutrino energies with its reduced string count. Finally, we provide an estimate of the schedule and cost for the design, construction, deployment and operation of PINGU.

## 2. Detector Design and Predicted Performance

### 2.1. Introduction

The design of the PINGU detector closely follows that of the DeepCore low-energy extension for IceCube. The current design consists of a further in-fill of the central DeepCore volume using hardware following the design principles of the standard DeepCore Digital Optical Modules (DOMs). The additional modules will lower the neutrino detection threshold in energy and significantly improve the sensitivity below 20 GeV.

### 2.2. Detector Geometries

An artist’s rendering of the existing IceCube and DeepCore vertical strings, with each string holding 60 DOMs, is shown in Fig. 3. The PINGU strings will be deployed around the center of the existing DeepCore strings, with both sub-arrays surrounded by the IceCube array. This location maximizes the sensitive volume for the PINGU detector while preserving the use of the IceCube strings as a veto for incoming atmospheric muons.

Several geometries for PINGU have been studied, where the evaluation metric between geometries was set by the sensitivity to the neutrino mass ordering. This particular metric was chosen since the experimental signal has a small but measureable impact on the oscillation probabilities. Further, the geometry-dependent quantities (the energy threshold, the angle and energy reconstruction resolution, and the particle identification efficiency) affecting the determination of the mass ordering are also common features affecting the majority of the other analyses.

The first version of this LoI [14] used a “40 × 60” baseline geometry composed of 40 strings with 60 DOMs per string, all situated within the DeepCore fiducial volume. Following a subsequent period of optimization, the number of DOMs per string was increased to 96 and the inter-string spacing was increased slightly. This 40 × 96 geometry provided improved access to the lower-energy neutrino signal and therefore to the physics topics discussed in this document. Subsequent simulations using a similar photocathode area with fewer strings (achieved by having more DOMs per string) showed comparable physics reach at reduced overall cost by virtue of one fewer drilling season and many fewer holes, translating to lower on-ice personnel costs, less required fuel, and other savings.

The studied geometries differ in the number of strings, their positions, and (as detailed above) the number of DOMs per string. A summary of the geometries studied in the

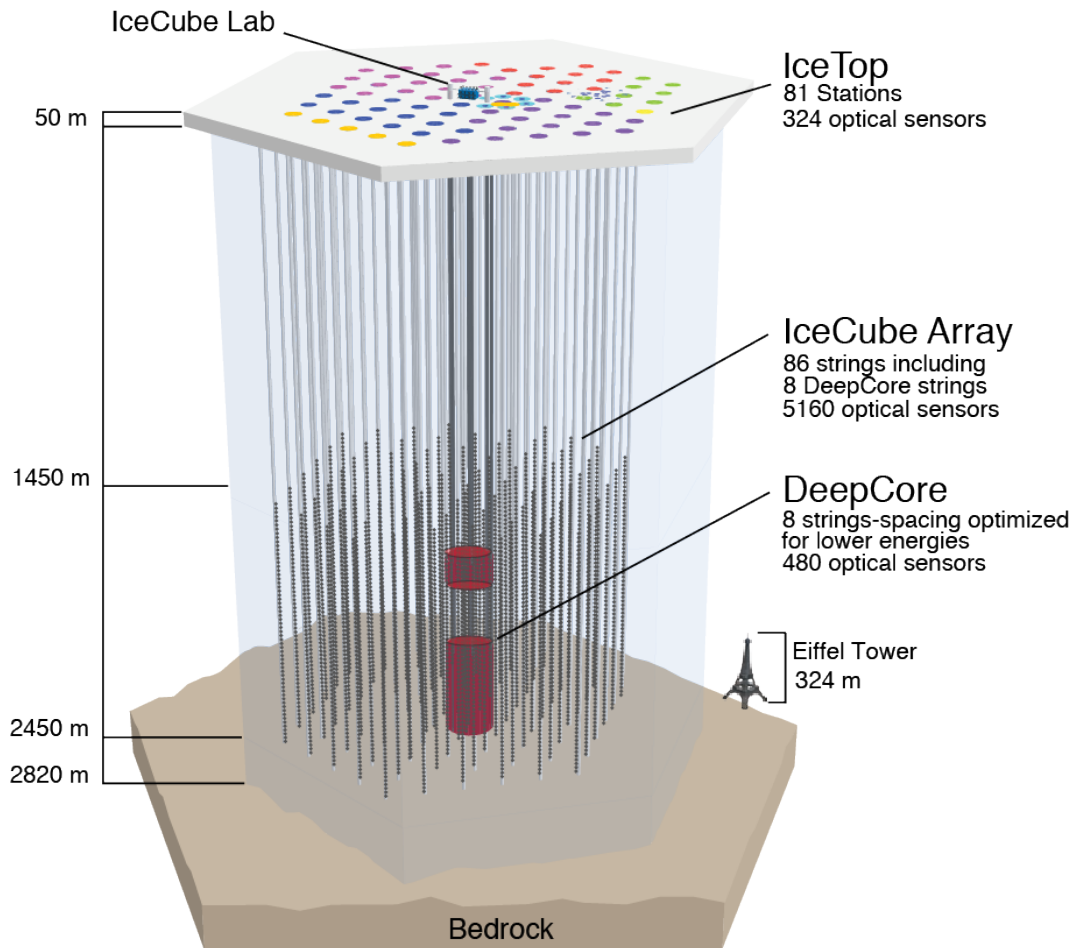


Figure 3: Artist’s rendering of the IceCube and DeepCore detectors. The PINGU detector strings would in-fill the existing DeepCore array at similar depths, with substantially closer vertical spacing between modules. PINGU modules would occupy only the lower region of DeepCore indicated in the figure.

greatest detail is shown in Table 1. The configuration used in the previous version of this LoI is shown first for comparison. For reference, the  $40 \times 96$  geometry has undergone the most study, and was the focus of PINGU presentations until March 2016.

The new baseline PINGU geometry features 26 strings and 192 DeepCore-style modules per string. This geometry delivers comparable physics sensitivities at significantly reduced cost relative to the previous  $40 \times 96$  geometry. The anticipated installation schedule calls for eight strings to be installed in the first deployment season and 18 in the following

season. This schedule fits well with the knowledge gained during the installation of IceCube and DeepCore, when up to 20 strings were installed per season. With each string populated with 192 modules, the photocathode in the ice is increased (30% compared to the  $40 \times 96$  geometry) and offsets the reduced number of strings. To model the physics impact of a challenging drilling scenario, we have also studied a scaled-down version of the new baseline geometry with only 20 strings deployed in two seasons. This  $20 \times 192$  geometry matches the total photocathode area of the previous  $40 \times 96$  geometry, but has a slightly larger inter-string spacing.

Configuration	Number of Strings	Average Inter-string Spacing	Number of DOMs/String	Inter-DOM Spacing
$40 \times 60$ (initial baseline)	40	20 m	60	5 m
$40 \times 96$	40	22 m	96	3 m
$26 \times 192$ (new baseline)	26	24 m	192	1.5 m
$20 \times 192$	20	30 m	192	1.5 m

Table 1: Summary of the parameters for the studied PINGU detector geometries. Shown are the initial LOI [14] baseline  $40 \times 60$  geometry, its enhanced  $40 \times 96$  version with greater deployed photocathode, the new baseline  $26 \times 192$  geometry, and its scaled-back  $20 \times 192$  version used to study the impact of a challenging drilling scenario.

More recently we have explored the physics potential of a geometry with 6–7 PINGU baseline strings, deployed as “Gen2 Phase 1” (more simply, “Phase 1”) in one season. The Phase 1 configuration is effectively what the first year of PINGU deployment would provide. Phase 1 is described in more detail in [Appendix D](#).

A more detailed view of the IceCube, DeepCore, and future PINGU strings for the new baseline geometry is shown in Fig. 4. The top figure shows the complete IceCube detector, with an average 125 m spacing between strings (shown in black circles) and a footprint comprising roughly one square kilometer. The 8 DeepCore strings, with average string spacings of approximately 70 m, are located in the center of the IceCube geometry and shown in blue squares. These are co-situated with the 26 PINGU strings (shown in red circles) having an average string spacing of 24 m. The vertical module distribution is also shown in the bottom left of Fig. 4, showing the decrease in module spacing from IceCube (17 m) to DeepCore (7 m) to PINGU (1.5 m). This plot also shows the position of the “dust layer,” a region of ice with a much higher concentration of particulate matter than the surrounding areas. The DeepCore DOM positions show the location of the “plug” of 10 DOMs above this layer while the remaining 50 DOMs are located below. The veto

plug provides additional information about events which enter the dust layer since in that region their photons are largely lost due to the increased absorption. The PINGU modules would be positioned below the dust layer, and inset slightly with respect to the DeepCore DOMs to facilitate the veto of the cosmic ray muon background.

The final, zoomed-in portion of Fig. 4 shows a more detailed overhead view of the center of the IceCube detector. The figure shows all strings that are used in the PINGU trigger, including the 15 strings comprising DeepCore. The dashed line indicates the approximate fiducial region of PINGU, a radius of 85 m around the center of the detector and a length of 290 m, for a total fiducial mass of roughly 6 Mton.

One of the metrics used to determine the efficiency of the detector to incoming neutrinos is the “effective mass” of the geometry. This value is calculated using Monte Carlo simulation at analysis level and is defined as

$$M_{\text{eff}} = M_{\text{gen}} \times \frac{N_{\text{reco}}^{\nu}}{N_{\text{gen}}^{\nu}}, \quad (1)$$

where  $M_{\text{gen}}$  is the mass of ice in which the simulated neutrinos interact,  $N_{\text{reco}}^{\nu}$  is the number of simulated neutrinos passing all analysis selection criteria, and  $N_{\text{gen}}^{\nu}$  is the total number of neutrinos generated. The final selection criteria used for this calculation are described in the following parts of this Section, with the results of this calculation shown as a function of the true neutrino energy for CC  $\nu_{\mu}$  interactions in Fig. 5(a) and for CC  $\nu_e$  interactions in Fig. 5(b).

### 2.3. Detector Hardware and Simulation

Anticipated improvements to the modules, described in Sec. 5.4, are designed to provide more useful single photoelectron (SPE) information compared to that collected by DeepCore DOMs. However, we have conservatively built upon the existing IceCube and DeepCore Monte Carlo software to produce the PINGU simulated data (see Sec. 8 for full details). To simulate low-energy events, the GENIE neutrino generator [18] is used to model the neutrino interactions. Following the interaction, GEANT4 [19] is used to track the produced particles as they travel through the ice (including full simulation of all secondaries produced at the interaction vertex). The Cherenkov photons produced by these particles are tracked individually using CLSim, a GPU-based software similar to that described in [20] which properly treats the position-dependent photon scattering and absorption in IceCube (see Sec. 8.4 for more details). For more information on the simulation please see Sec. 8.

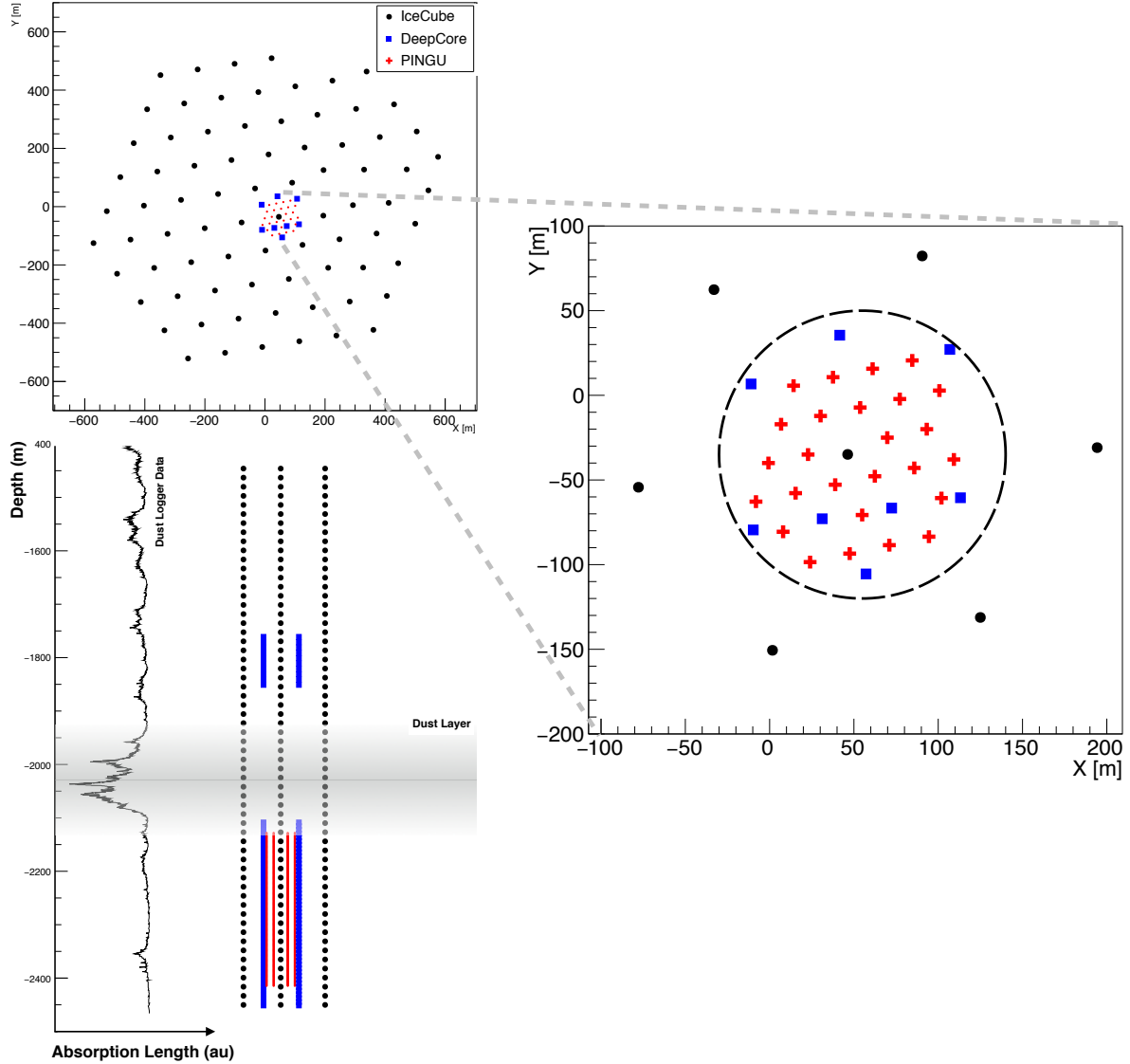
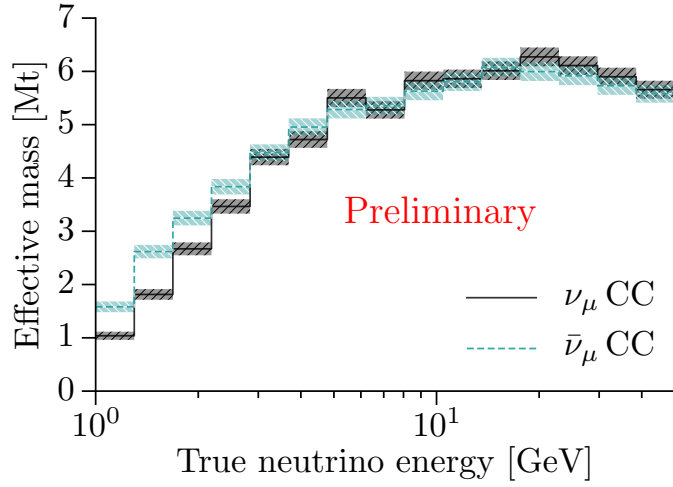
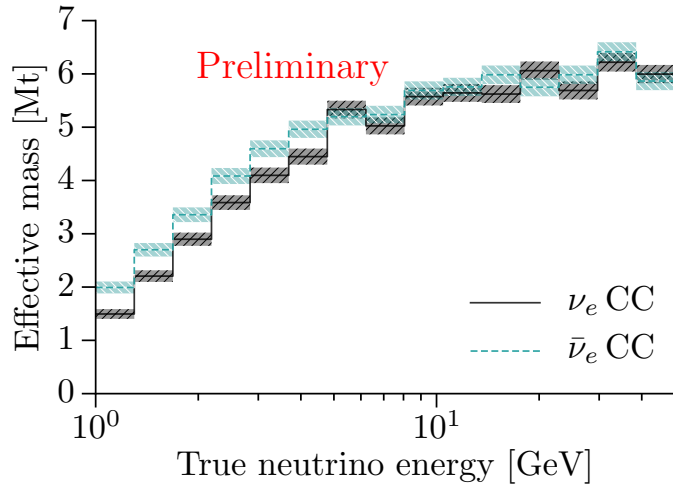


Figure 4: The left figure shows the overhead and side views of the new baseline PINGU geometry. It also shows the surrounding IceCube and DeepCore strings, and vertical spacings for DeepCore and PINGU modules. In the side view only some of the strings are shown for clarity. The leftmost graph along the side of the figure delineates the dust concentration in the ice and shows that PINGU occupies the clearest ice. Contained in the right figure is a zoom-in of the new baseline PINGU geometry, showing only the strings used in the PINGU triggering algorithm as well as the fiducial radius of PINGU (dashed line).



(a)  $M_{\text{eff}}(\nu_{\mu} \text{ CC})$



(b)  $M_{\text{eff}}(\nu_{\text{all}} \text{ NC})$

Figure 5: Effective mass for (a) CC  $\nu_{\mu}$  and (b) CC  $\nu_e$  interactions in the new baseline PINGU geometry as a function of neutrino energy. Only events passing the final event selection criteria described in this Section are included in the histograms, causing a slight turnover in the effective mass from CC  $\nu_{\mu}$  events producing a muon that is not fully contained in the PINGU fiducial volume.

In addition to the particle and photon tracking, the simulation software also generates the non-physics-related signals, *i.e.*, instrumental noise. The model for these noise hits has changed since the first version of this Letter of Intent in that improvements have been made to the method by which the noise is simulated [21]. The current noise generation method matches the data measured using the IceCube detector better than the previous version, largely due to the addition of intra-DOM correlated noise. The resulting increase in noise hits has affected the performance of the event reconstruction which will be discussed in detail next.

#### 2.4. Event Reconstruction

The most advanced PINGU reconstruction employs likelihood methods at the single photon level for energy and direction estimation, as well as neutrino flavor identification, building on the algorithms used for IceCube [22]. Since the scattering length of Cherenkov photons in the deep Antarctic ice is approximately 20–30% of the absorption length, we are in an intermediate regime between free-streaming photons and diffusive propagation and therefore rely on numerical descriptions of light propagation through the ice. The expected detector responses are computed and tabulated for a variety of event topologies in the detector, in addition to different depths and angular orientations. These tables are then fit with splines to reduce numerical instabilities from the binning and ensure a smooth parametrization [23]. To reconstruct an event, all DOM readouts are subdivided in time, and a Poisson likelihood is calculated for the contents of each time bin for all DOMs in PINGU, DeepCore, and IceCube, comparing a reconstruction hypothesis to the data. The interaction hypothesis is adjusted, and the process is repeated until the hypothesis with the maximum likelihood is found.

PINGU is designed to observe neutrinos with energies as low as a few GeV. At this energy-scale, most or all of the secondary particles and Cherenkov photons created in a detected neutrino interaction will be contained within the detector volume. This is a significant change from the most frequent events observed in the IceCube detector – high-energy through-going muons from cosmic ray air showers. Furthermore, at neutrino energies below roughly 100 GeV, the hadronic shower at the interaction vertex can contribute a significant fraction of all the Cherenkov photons detected in the event and must be considered in the event reconstruction. However, stochastic processes such as bremsstrahlung are much more rare than at high energies, and muon tracks produced by the CC  $\nu_\mu$  events most relevant for PINGU analyses are in the minimum-ionizing regime.

This change in the anticipated signal necessitated a new reconstruction strategy appropri-

ate for the low energy events relevant for the study of neutrino oscillations. A simultaneous global likelihood fit is performed using all eight event parameters: the interaction vertex position and time, the zenith and azimuthal angles, the energy of the cascade at the vertex, and the length of the daughter muon (primarily for CC  $\nu_\mu$  events). For CC  $\nu_\mu$  events, the angles are those of the emerging muon, while for all other events, the angles are those of the cascade at the interaction vertex. In principle, since the muon and the hadronic shower at the CC  $\nu_\mu$  interaction vertex are not perfectly aligned, their relative directions could be treated as independent parameters in the fit, but this is not done in these analyses. It is possible to extract the measured event inelasticity from the fit and use that information to improve the sensitivity to the neutrino oscillation parameters [24], but for the analyses covered in this letter we do not yet take advantage of this. Use of the event inelasticity and complete interaction kinematics will be explored in future refinements of the analyses presented here.

In order to successfully fit all eight parameters described above, we use the nested sampling algorithm MultiNest [25]. This reconstruction was applied to fully simulated PINGU events, independent of interaction type, for the geometries shown in Table 1. In order to remove events close to the boundaries of the sampling space and ensure good reconstruction quality, the reconstructed vertex of each event was required to be contained within the PINGU fiducial volume.

Since the previous version of this Letter of Intent [14], we have updated the expected detector response spline table with newer parameterizations of the ice model surrounding the detector and with the better simulation of noise described above. Both of these changes affected the accuracy of the reconstruction with respect to energy. To permit a direct comparison of the effect of the change of geometry, we have shown results from both the previous and current baselines in Figs. 6 and 7. An important note is that the cylindrical radius used for containment has changed from the previous baseline (where it was 75 m) to the new baseline (where it is 85 m), meaning that more events are available for analysis with the latter.

It should also be noted that in several of our analyses described in Sec. 3 the information in Figs. 6 and 7 is not used directly. Instead, the distributions—created using the full PINGU simulation and reconstruction—are parameterized as functions of energy. This parametrization was done using a variable-bandwidth kernel density estimate (VBW KDE), based on [26, 27, 28], of the distributions of the reconstruction errors for several energy bins. Example energy and cosine-zenith error distributions and the computed VBW KDE resolutions are shown in Fig. 8.

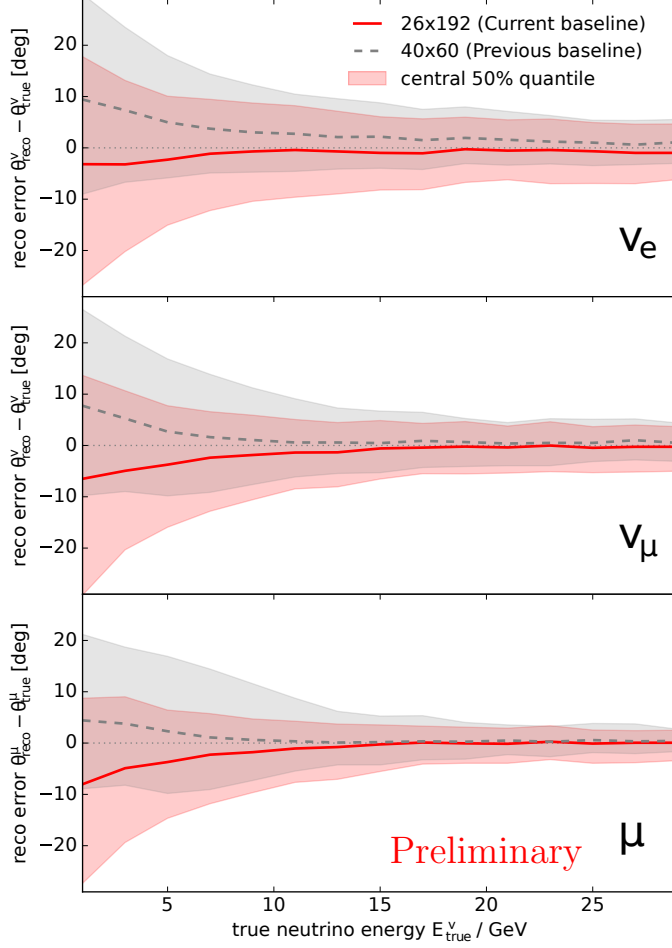


Figure 6: Zenith angle accuracy for events used in our atmospheric-neutrino-based analyses. The lines show the median of the distribution and the shaded bands indicate the central 50% of events. The top and center plots show the resolution of the reconstructed zenith angle with respect to the incoming neutrino for  $\nu_e$  and  $\nu_\mu$  events, respectively. The bottom plot shows the zenith angle resolution with respect to the outgoing muon for  $\nu_\mu$  CC events. Values are shown for the current baseline ( $26 \times 192$ ) and the previous baseline ( $40 \times 60$ ) in all cases.

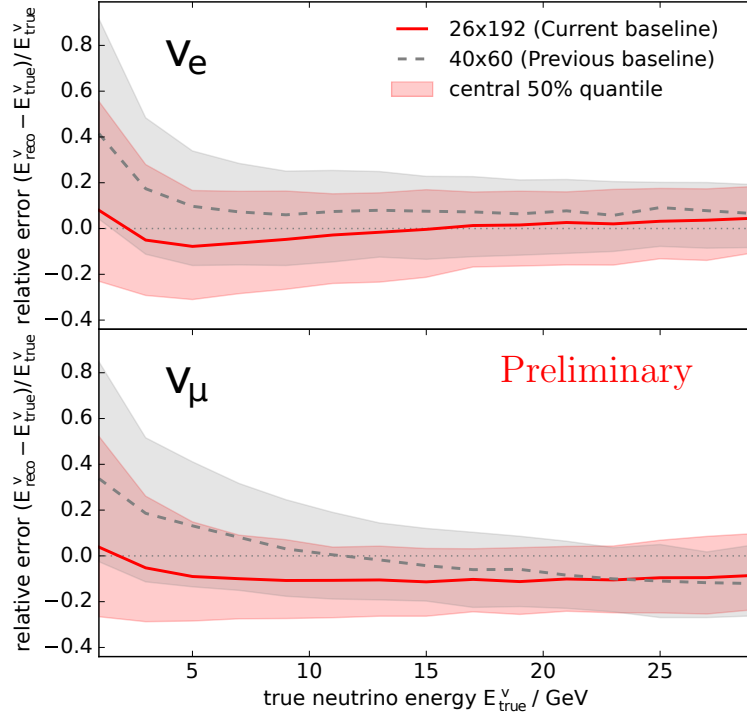


Figure 7: The relative reconstructed energy resolution for events used in our atmospheric-neutrino-based analyses. The lines show the median of the distribution and the shaded bands indicate the central 50% of events. The top plot shows the resolution of the reconstructed energy for  $\nu_e$  events while the bottom is for  $\nu_\mu$ , both relative to the energy of the incoming neutrino. Values are shown for the current baseline ( $26 \times 192$ ) and the previous baseline ( $40 \times 60$ ) in all cases.

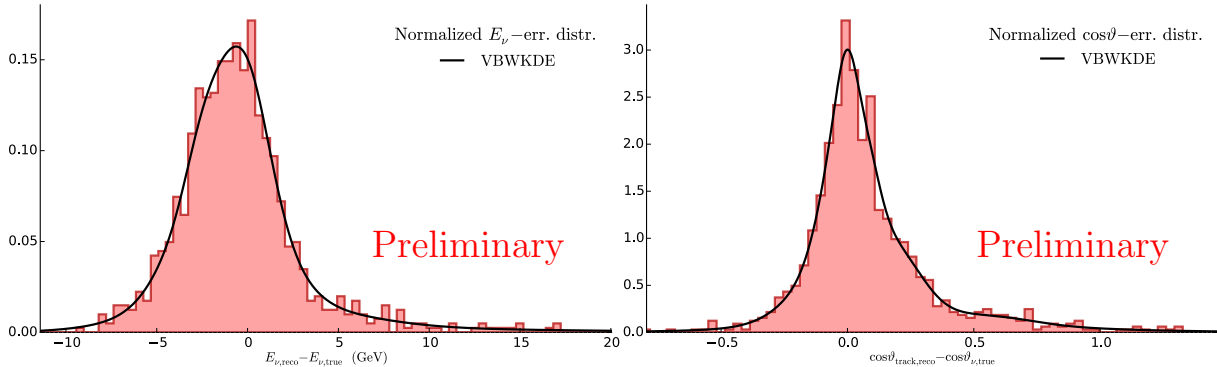


Figure 8: Resolutions for energy (left) and cosine-zenith (right) for CC  $\nu_\mu$  and  $\bar{\nu}_\mu$  events simulated with neutrino energies from 9.46–10.59 GeV. Plotted are histograms of the individual events’ reconstruction errors overlaid by lines showing the variable-bandwidth kernel density estimates of the underlying distributions.

The reconstruction algorithm described above successfully reconstructs about 90% of atmospheric neutrino events that satisfy a loose trigger criterion (three modules hit in spatial and temporal coincidence) and whose true vertex is contained within the PINGU fiducial volume; these events produce enough photoelectrons to fully constrain the fit. We do not attempt to recover the remaining 10% of events although that could be done by re-running the fit with a different random selection of starting points.

### 2.5. Event Selection

Downward-going atmospheric muons dominate the event rate in the detector, outnumbering atmospheric neutrinos by a factor of roughly  $10^6:1$  at the initial trigger level. Criteria must be put in place to reject this background at high efficiency. The published analysis of showering events induced by atmospheric neutrinos [29] in the IceCube/DeepCore detector attained an atmospheric muon rejection factor of over  $10^7$  by vetoing events with “early” light (detected before the light in the fiducial volume) in the surrounding IceCube modules. Furthermore, the improved reconstruction performance for low energy events described in Sec. 2.4 also provides the ability to reject any remaining downward-going events based on the reconstructed direction (at the cost of rejecting downward-going neutrinos). We therefore anticipate minimal contamination from this particular source of background in PINGU, especially when restricting the analysis to up-going events only.

In order to select events we reconstruct well, we require events to consist of at least 8 optical modules that have detected light. We also require the reconstructed interaction

vertices of the events (described in Section 2.4) to be within the more densely instrumented PINGU fiducial volume, which is defined as a cylinder with radius 85 m and height 320 m that runs vertically between depths of 2450 m and 2130 m from the surface as shown in Figure 4. We do not require full containment of muon tracks produced in  $\nu_\mu$  charged current interactions; depending on incident angle, muon tracks will be contained in the IceCube volume up to energies of  $E_\mu \sim \mathcal{O}(100 \text{ GeV})$ .

Downward-going atmospheric muons dominate the event rate in the detector, outnumbering atmospheric neutrinos by a factor of roughly  $10^6$  at the initial trigger level. Event selection criteria must be put in place to reject this background at high efficiency. Current measurements of muon neutrino disappearance in the IceCube/DeepCore detector [30] attain an atmospheric muon rejection factor of more than  $10^8$  by vetoing events with ‘early’ light in the surrounding IceCube modules (i.e. light detected before the light in the DeepCore fiducial volume), highly elongated events without a visible shower characteristic of a neutrino-nucleon interactions, and events with hits too widely spread in time, which are associated with muons traversing the full detector. The current PINGU analysis applies similar criteria to account for the impact of these selection criteria on the neutrino signals.

In current IceCube/DeepCore measurements, sideband data are used to model the residual atmospheric muon contamination, and neutrinos from the full sky (downward-going as well as upward-going) are used to help constrain systematic uncertainties. However, it is not currently possible to simulate enough atmospheric muons to make a full estimation of the impact of atmospheric muons in the PINGU analyses, nor to use data to make such an estimate. We have therefore decided to remove all downgoing events in the analyses presented here. Once PINGU data is available we are confident the current methods used to estimate such background contamination from data in IceCube/DeepCore will continue working and will allow us to perform full-sky analyses in PINGU, which will aid in controlling flux systematics as discussed in Appendix C.

With the cuts described above and the requirement of events to be reconstructed as upgoing, we do not anticipate contamination from atmospheric muons in PINGU, given that the similar techniques used in IceCube/DeepCore analyses have already led to very small contaminations from this source in the upgoing region. We will therefore neglect such atmospheric muon contamination in the physics studies presented here. A summary of the expected events rates after the full event selection is given in Table 2.

Interaction type	Events per year
$\nu_\tau + \bar{\nu}_\tau$ CC	2,800
$\nu_\mu + \bar{\nu}_\mu$ CC	32,600
$\nu_e + \bar{\nu}_e$ CC	25,400
$\nu + \bar{\nu}$ NC	7,400

Table 2: Annual event rates expected in the PINGU detector after the full event selection and including the effects of neutrino oscillation (assuming the normal mass ordering).

## 2.6. Particle ID

Neutrino events at the energies relevant for PINGU analyses fall into two channels: track-like events with an associated muon from CC  $\nu_\mu$  interactions and cascade-like events coming from CC  $\nu_{e,\tau}$  as well as all neutral current (NC) interactions. The ability to separate track-like and cascade-like events benefits many PINGU analyses as we expect different flavors of neutrinos to carry different pertinent information. In the context of the neutrino oscillation measurements described in detail in Sec. 3,  $\nu_\mu$  (classified mostly as track-like) and  $\nu_e$  (classified mostly as cascade-like) undergo effects that are induced at different energies and different baselines, and the differences in those signatures affect the oscillation measurements.

The central goal of classifying the event as track-like or cascade-like is the identification of the presence (or absence) of a muon track. Figure 9 shows an example of a track-like and a cascade-like event in PINGU. To classify events as track-like or cascade-like we have trained a “multilayer perceptron” (MLP) neural network (NN) using the TMVA toolkit [31] with variables based on the output of the event reconstruction described in Sec. 2.4. These include variables such as the reconstructed muon length, the fraction of the energy reconstructed in the muon to total energy reconstructed, and the difference in the log-likelihood between the best fit and the fit forcing the assumption that there was no track present. Another class of variables that provides information related to the classification of events is the timing of the hits. Since muons travel at roughly the speed of light  $c$  (while emitting Cherenkov radiation), but the Cherenkov photons emitted during hadronic and electromagnetic cascades travel at  $c/n$  (where  $n$  is the refractive index of the ice), the light emitted in events with muons will be detected earlier than for those with only cascades. Figure 10 shows the output of the algorithm described above, and Fig. 11 shows the separation achieved between track-like and cascade-like events used in the oscillation analysis based on the use of the MLP neural network with a score of 0.55. This creates a relatively pure CC  $\nu_\mu$  track-like sample, while mixing all neutrino flavors

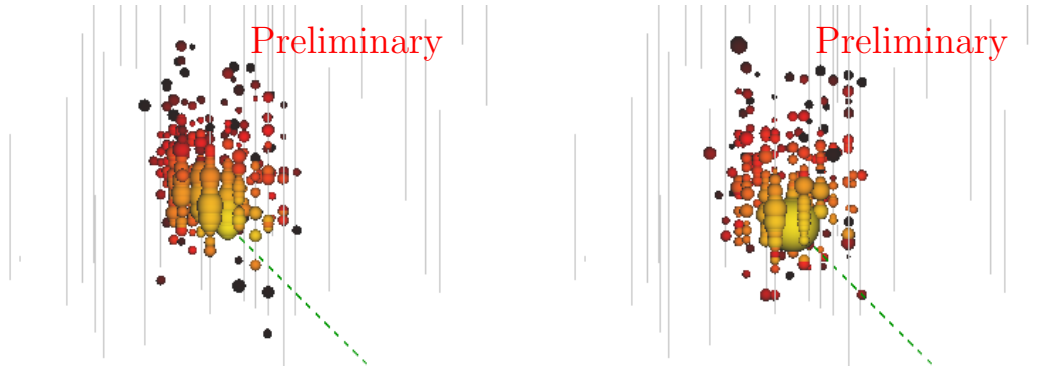


Figure 9: Event displays of a CC  $\nu_\mu$  (left) and a CC  $\nu_e$  (right) event. The spheres indicate the DOMs which recorded photons where the total amount of charge is indicated by the size of the sphere. The color indicates the time when the DOM observed the first photon, while the dashed line shows the true neutrino direction. In both panels are shown 12 GeV CC  $\nu$  producing a 10 GeV lepton ( $\mu$  or  $e$ ) crossing the detector leaving several groupings of hits on consecutive strings in a short time interval. In both cases the interaction vertex and direction is identical to make the comparison between events easier. We can distinguish the CC  $\nu_\mu$  and CC  $\nu_e$  events by comparing if the charge is extended in the diagonal (which happens in CC  $\nu_\mu$  events) or more concentrated around the vertex (which indicates no  $\mu$  is present in the event).

in the cascade channel.

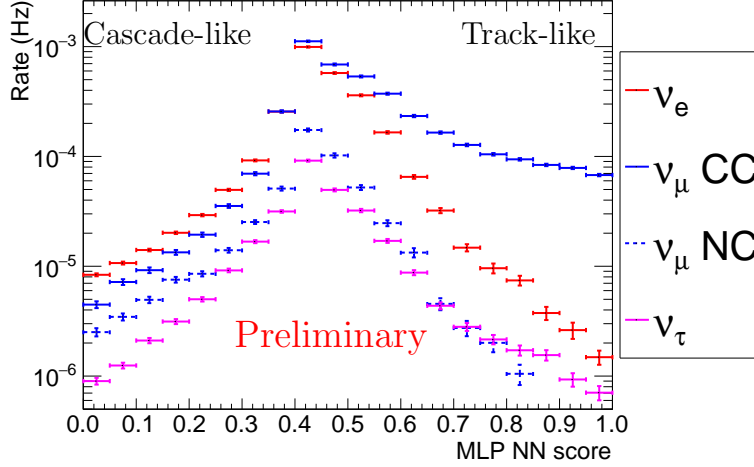


Figure 10: Output of the MLP neural network classifier for the new baseline geometry. Coefficients close to 1 represent more track-like events, while values closer to 0 correspond to events being more cascade-like. The large number of events around 0.4 typically will contain mainly lower energy events which are harder to classify. The TMVA MLP method with the BFGS algorithm was used for training and Bayesian regulators, with 600 training cycles,  $N+5$  hidden layers, “tanh” as the function type for neuron activation, and an overtraining test performed every 5 epochs [31].

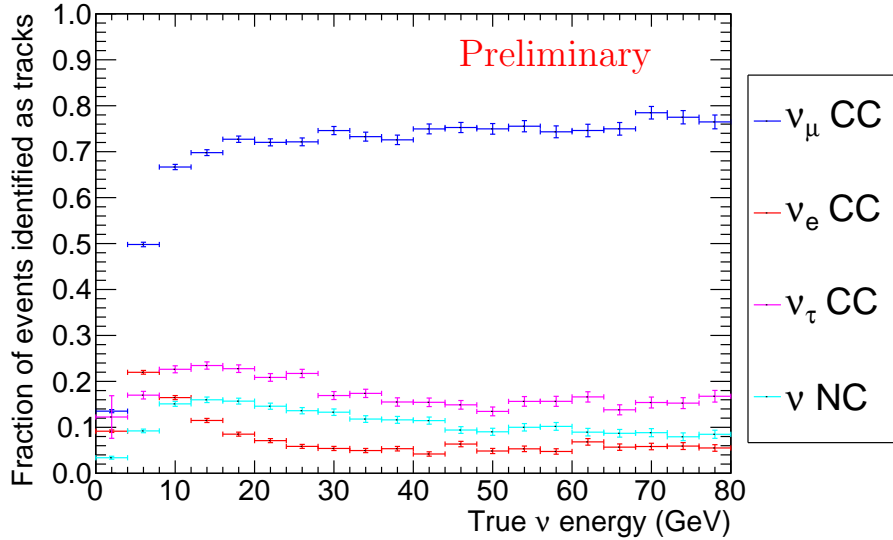


Figure 11: The fraction of events identified as track-like in the new baseline geometry as a function of true neutrino energy for each neutrino flavor and interaction type (CC or NC) using the TMVA [31] MLP method described in Fig. 10 and a score of 0.55.

### 3. Atmospheric Neutrino Oscillations

#### 3.1. Introduction

The atmosphere of the Earth is one of a number of sources that can be used to provide a large sample of neutrinos [32, 33]. A constant flux of cosmic rays (primarily protons but with a component of light nuclei) interacts in the upper atmosphere, producing a shower of hadrons. The majority of these are charged pions, which decay quickly into a muon and a muon-type antineutrino (or an antimuon and muon-type neutrino). The muon can then decay into an electron, a muon neutrino and an electron-type antineutrino, with a similar chain for the antimuon decays. As shown in Fig. 12, these fluxes are described to first order as a power law spanning many orders of magnitude in energy from roughly 10 GeV to beyond the TeV scale.

The propagation of neutrinos through vacuum (in their mass eigenstates and natural units) can be described by plane wave solutions of the form [32]

$$| \nu_j(t) \rangle = e^{-i(E_j t - \vec{p}_j \cdot \vec{x})} | \nu_j(0) \rangle, \quad (2)$$

in which  $j \in \{1, 2, 3\}$ ,  $t$  is the propagation time,  $E_j$  and  $\vec{p}_j$  are the energy and momentum of the neutrinos and  $\vec{x}$  is the position relative to the starting position. All neutrinos observed have energies of at least 1 GeV,  $|\vec{p}_i| \gg m_i$ , and therefore the ultrarelativistic version of the momentum can be used, and  $t$  can be approximated by the distance travelled  $L$ . These modifications to Eq. 2 produce the following equation:

$$| \nu_j(L) \rangle = e^{-im_j^2 L/2E} | \nu_j(0) \rangle. \quad (3)$$

Using Eq. 3, the probability of a neutrino of flavor  $\alpha$  being observed as flavor  $\beta$  after propagation can be expressed as

$$\begin{aligned} P_{\alpha \rightarrow \beta} &= | \langle \nu_\beta | \nu_\alpha(t) \rangle |^2 \\ &= \left| \sum_i U_{\alpha i}^* U_{\beta i} e^{-im_i^2 L/2E} \right|^2 \\ &= \sum_{j,k} U_{\alpha j}^* U_{\beta j} U_{\alpha k} U_{\beta k}^* e^{-i\Delta m_{jk}^2 L/2E}, \end{aligned} \quad (4)$$

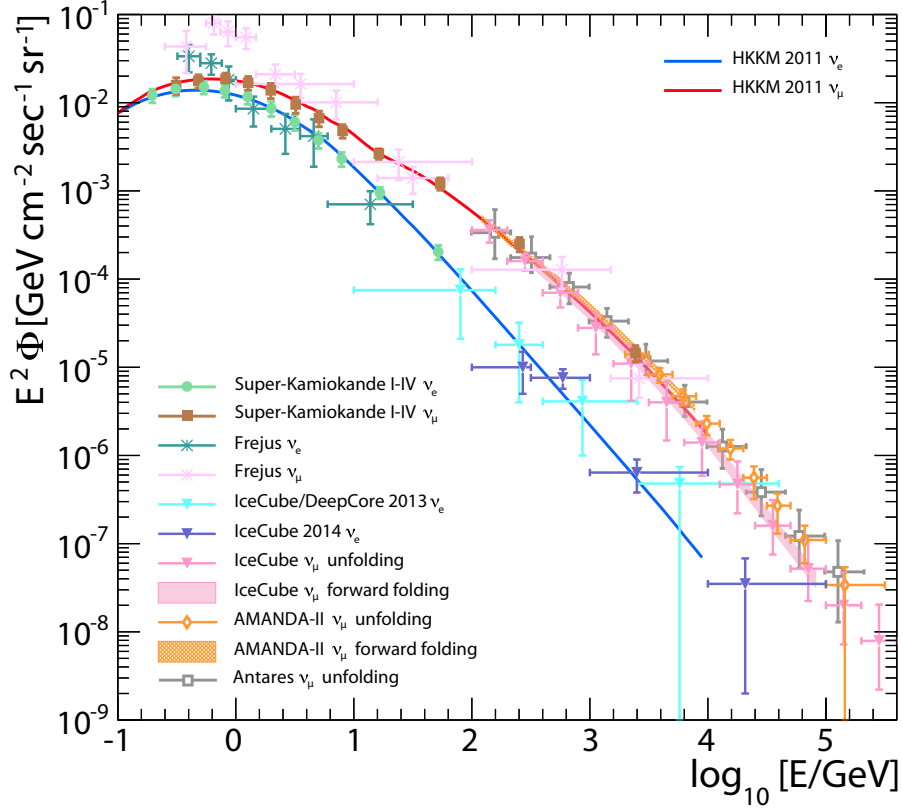


Figure 12: Energy spectra of the atmospheric  $\nu_e$  and  $\nu_\mu$  fluxes measured by Super-Kamiokande [34], Frejus [35], AMANDA-II [36, 37], Antares [38] and IceCube [29, 39, 40, 41]. The solid lines show the prediction from the HKKM'11 model [42] including the effects of oscillations. Figure adapted from [34].

where  $U_{\alpha j}$  are the elements of the PMNS matrix, as shown in Eq. 5, and  $\Delta m_{jk}^2 = m_j^2 - m_k^2$  are the mass squared differences. If we assume there are only three families of neutrinos it follows that the  $U_{\text{PMNS}}$  written in Eq. 6 is a unitary matrix and can be parametrized using three mixing angles ( $\theta_{13}$ ,  $\theta_{23}$  and  $\theta_{12}$ ) and a Charge-Parity (CP)-violating phase  $\delta$ :

$$\begin{pmatrix} \nu_e \\ \nu_\mu \\ \nu_\tau \end{pmatrix} = U_{\text{PMNS}} \begin{pmatrix} \nu_1 \\ \nu_2 \\ \nu_3 \end{pmatrix} \quad (5)$$

$$= \begin{pmatrix} U_{e1} & U_{e2} & U_{e3} \\ U_{\mu1} & U_{\mu2} & U_{\mu3} \\ U_{\tau1} & U_{\tau2} & U_{\tau3} \end{pmatrix} \begin{pmatrix} \nu_1 \\ \nu_2 \\ \nu_3 \end{pmatrix}. \quad (6)$$

The mixing angles and mass-squared differences that describe oscillations in the neutrino sector have been measured with good precision through the efforts of a variety of experiments worldwide [32]. IceCube, with its DeepCore extension, has demonstrated [8] the ability to measure the “atmospheric” mixing parameters  $\theta_{23}$  and  $\Delta m_{32}^2$  and, as analysis techniques are refined and systematic uncertainties are better understood, is on track to produce results that are competitive with those of world-leading experiments. The remaining unknowns in the leptonic sector include the nature of the neutrino (Dirac or Majorana), the extent to which CP symmetry may be violated in the sector, determination of the presence of a potential sterile neutrino, and the ordering of the mass eigenstates.

In addition to vacuum oscillations there are two distinct physical effects that play a role in the neutrino flavor propagation through the Earth. The first is the MSW effect [10, 11] that enhances the oscillation probability for  $\nu_\mu \rightarrow \nu_e$  or  $\bar{\nu}_\mu \rightarrow \bar{\nu}_e$  (depending on the neutrino mass ordering), which is strongly dependent on the matter density for all path lengths through the Earth. The second effect arises from the density transition at the Earth’s mantle-core interface (see Fig. 13) where neutrinos passing through this interface can undergo “parametric enhancement”, which is also called “neutrino oscillation length resonance”, of their oscillation probability [12, 13], further enhancing neutrino or anti-neutrino oscillation probabilities depending on the ordering as in the MSW effect.

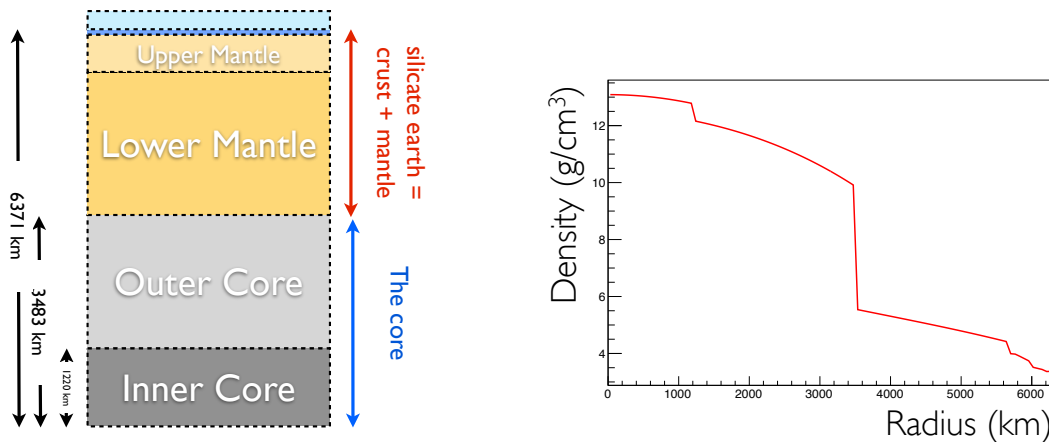


Figure 13: The Preliminary Reference Earth Model (PREM) [43] model’s structure of the Earth and density as a function of radius  $r$  from the center, showing the large change in density at  $r \simeq 3500$  km. The PREM is used to map the Earth’s interior mass density and to account for matter effects in neutrino oscillations.

The effects of these additional modifications to the oscillation probabilities can be seen

in the “oscillograms” that represent the probability of oscillation of the neutrino across a range of travel distances and energies. Examples of these oscillograms are shown in Fig. 14, which displays the probability that a neutrino created as a muon-type is detected as a muon-type ( $P_{\nu_\mu \rightarrow \nu_\mu}$ ). Since these plots show the oscillation probability for neutrinos, the resonance conditions are met in the normal ordering case. For anti-neutrinos, the conditions are met for the inverted ordering.

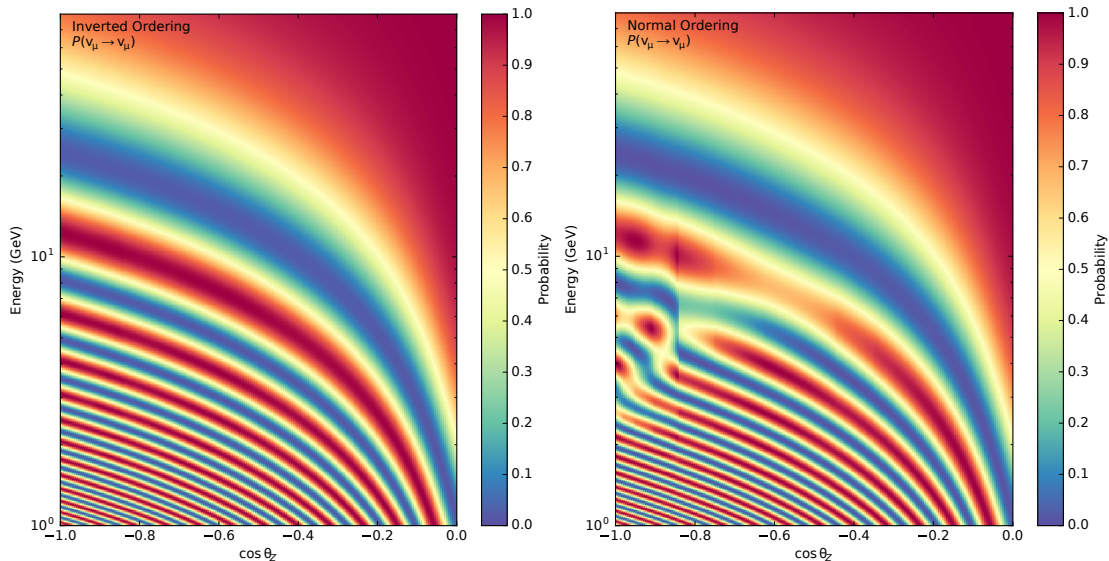


Figure 14: Muon neutrino survival probability after traveling through the Earth, as a function of the true neutrino energy and cosine of the true zenith angle, shown for the inverted ordering (left) and normal ordering (right). A path directly through the center of the Earth corresponds to  $\cos \theta = -1$ . The survival probabilities for antineutrinos in a given ordering are essentially the same as those for neutrinos under the opposite ordering.

### 3.1.1. Sample Generation and Event Selection

In order to investigate the sensitivity of PINGU to the various neutrino oscillation parameters, a large sample of simulated neutrino events is required. This sample is generated with the Monte Carlo software previously used for IceCube and DeepCore, using the GENIE and GEANT4 packages as described in Sec. 2.3. The entire sample of these events is then reconstructed as described in Sec. 2.4 and Particle Identification (PID) is applied to it as described in Sec. 2.6.

Although we conservatively reject downward-going atmospheric neutrinos using the recon-

structed event direction, in the future the subset of these events that start in the PINGU fiducial volume could be retained and used as an un-oscillated dataset for normalization purposes, with the benefit of further understanding and constraining various systematics.

### *3.1.2. Overview of Analyses*

While we have employed several different high-level analysis techniques, many of the analyses described below use a common framework and all use the same general methodology. A detailed discussion of the statistical approach is provided in [Appendix A](#). In the following sections we will highlight where a particular analysis deviates from this common approach.

The analysis methods developed begin by binning the data based on the reconstructed energy, zenith angle and particle identification. The current analysis uses 20 linearly spaced bins in the cosine of the zenith angle for  $-1 < \cos\theta_\nu < 0$  and 39 logarithmically spaced bins in energy for  $1 < E_\nu < 80$  GeV, and also 2 bins for particle identification referred to as track-like and cascade-like. The content of these bins is derived from the previously-described simulations, and primarily depends on the neutrino flux, the oscillation probabilities, the cross-sections, and the effects of the detector. These values also depend on nuisance parameters that can be adjusted to account for systematic effects (cf. [Table 3](#)).

In the following sections, we present analyses that use atmospheric neutrinos in the energy range of 1–80 GeV with fluxes as predicted by [\[44\]](#). The neutrinos are tracked through the Earth using a full three-flavor formalism [\[45\]](#) including matter effects based on the standard “PREM” model of the Earth [\[43\]](#). Our predicted measurement of the neutrino oscillation probabilities is given in [Sec. 3.2](#), followed by our sensitivities to maximal mixing in [Sec. 3.3](#) and the neutrino mass ordering in [Sec. 3.4](#), and finally our predicted measurement of tau neutrino appearance and PMNS unitarity in [Sec. 3.5](#). Unless otherwise noted, all results presented below were fully simulated and reconstructed with the new baseline PINGU geometry ( $26 \times 192$ ).

The first analysis method, referred to as the “LLR” (log-likelihood ratio) method, is primarily used for the neutrino mass ordering analysis (see [Sec. 3.4](#)), in which two possibilities for the ordering need to be compared (as opposed to the study of a continuous parameter space). This method begins with a “template” histogram generated using chosen values of the parameters being studied. A pseudo-experiment is then created by making a copy of the template histogram and applying Poisson fluctuations to the contents of each bin.

Then, for both the orderings being studied, systematic uncertainties are varied in order to find those parameter values that yield the template that maximizes the likelihood of observing the pseudo-experiment under each hypothesis. This process is repeated for many pseudo-experiments, building up a distribution of the log-likelihood ratio with respect to the parameters studied. A more detailed description of this method is presented in [Appendix A.2](#). A variation of this method is also used in [Secs. 3.5](#) and [4.1](#).

In the second, “ $\overline{\Delta\chi^2}$ ” method, we make the Asimov assumption, i.e. that the mean sensitivity of the experiment is well represented by the significance obtained from the mean experimental outcomes, removing the need for individual pseudo-experiments. This translates to a reduction of  $\mathcal{O}(10^4)$  in processing time for the neutrino mass ordering analysis.<sup>3</sup> The significance for the NMO determination follows from the two  $\Delta\chi^2$  values separating the mean experimental outcomes under the different hypotheses, using a Gaussian approximation for the distribution of  $\Delta\chi^2$ , as detailed in [Appendix A.3](#). In other analyses using this method, described in [Secs. 3.2](#) and [3.3](#), Wilks theorem [46] is used to convert the  $\Delta\chi^2$  to significance.

Note that for the analyses in the following two sections, [3.2](#) and [3.3](#), we have included a nuisance parameter that explicitly accounts for a systematic error in the overall efficiency of the individual optical modules, assumed to be known with 10% uncertainty. Wherever this parameter is present, the uncertainty on the energy scale is reduced from 10% to 0.5%.

### *3.2. Muon Neutrino Disappearance*

The recent atmospheric neutrino oscillation results from IceCube/DeepCore [8] have demonstrated the physics potential of a neutrino detector in the ice at the South Pole. The combination of the large flux of neutrinos incident on the detector, along with their range of path lengths and energies, provides a highly suitable dataset for analysis of the neutrino oscillation parameters. This dataset will be increased with the PINGU detector and the reconstructions upgraded, significantly improving the final result. The method and projected results will be discussed here.

The determination of the atmospheric neutrino parameters relies on the disappearance of muon-type neutrinos; following their travel through the Earth, the flux of these neutrinos

---

<sup>3</sup>The overline in “ $\overline{\Delta\chi^2}$ ” indicates that no statistical fluctuations are applied, cf. [Appendix A.3](#).

will be reduced. The probability of muon neutrino survival during propagation through the Earth is shown in Eq. 7 in the limit that  $|\Delta m_{32}^2| \gg |\Delta m_{21}^2|$  and ignoring matter effects:

$$P(\nu_\mu \rightarrow \nu_\mu) \simeq 1 - 4 \cos^2(\theta_{13}) \sin^2(\theta_{23}) [1 - \cos^2(\theta_{13}) \times \sin^2(\theta_{23})] \sin^2(1.27 \Delta m_{32}^2 L / E_\nu). \quad (7)$$

In Eq. 7 the atmospheric mixing angle and square of the mass difference ( $\theta_{23}$  and  $\Delta m_{32}^2$ ) can be determined using the range of distances ( $L[\text{km}]$ ) and energies ( $E_\nu[\text{GeV}]$ ) available in the data set. The remaining mixing angle ( $\theta_{13}$ ) is treated as a nuisance parameter with central value and uncertainty given by best-fit values (from [47]).

There have been many improvements to the analysis following the work presented in [8]: The inclusion of additional photodetectors in the PINGU geometry lowers the energy threshold for neutrino detection (see Sec. 2.4); the use of more sophisticated reconstruction algorithms retains a much larger fraction of the events, resulting in a much larger data set at all energies; the use of flavor identification (see Sec. 2.4) and cascade-like events lends added statistical power to the analysis and sharpens the features to which it is sensitive. These increases combine to significantly improve the sensitivity of PINGU to the neutrino oscillation parameters.

### 3.2.1. Event Selection and Reconstruction

The sample used for this study contains neutrinos of all flavors, and uses the previously described PID algorithm to separate track-like and cascade-like events. The majority of the analyses in the previous version of this document [14] used only the track-like events in the final analysis, but newer analysis methods have shown that the inclusion of the cascade-like events can serve to constrain the non-atmospheric mixing parameters, producing an improvement in the results.

### 3.2.2. Analysis Method

In order to determine the oscillation parameter constraints obtained for a given NMO and corresponding fiducial model, we make use of the Asimov approach described in Appendix A.3. Given the Asimov dataset for the true ordering, we perform a fine scan in the  $(\sin^2(\theta_{23}), \Delta m_{31}^2)$  plane, and evaluate  $\overline{\Delta\chi^2}$ , defined in analogy with Eq. A.9, but minimized only over the parameters within the true ordering and over the remaining systematic parameters, including  $\theta_{13}$  which is allowed to vary around the global fit to the data

in [47]. The solar neutrino oscillation parameters  $\theta_{12}$  and  $\Delta m_{12}^2$  are fixed to their global best values from the same fit since PINGU is insensitive to them. Similarly,  $\delta_{\text{CP}}$  is fixed to zero. We then report the Confidence Level (C.L.) at which any pair of  $(\sin^2(\theta_{23}), \Delta m_{31}^2)$  values can be excluded by assuming a  $\chi^2$  distribution with 2 d.o.f..

An example of the process is presented in Fig. 15 in which the  $\overline{\Delta\chi^2}$  space is shown for the oscillation parameters with the assumption of maximal mixing within the normal ordering. The three contours shown here correspond to the 68%, 90% and 99% C.L. regions.

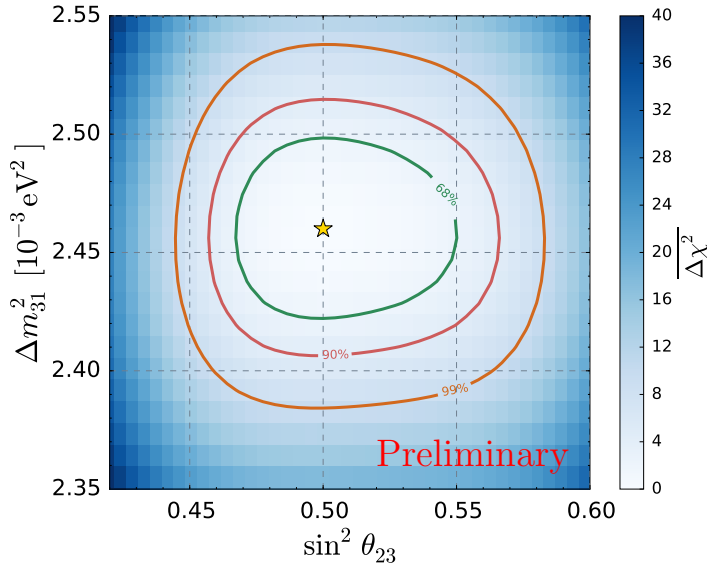


Figure 15:  $\overline{\Delta\chi^2}$  profile and various confidence regions for the atmospheric oscillation parameters  $\Delta m_{31}^2, \sin^2(\theta_{23})$  for maximal mixing and normal ordering, assuming a four-year exposure time.

### 3.2.3. Results

The analysis described above has been performed for a detector livetime of four years. Since the precision with which  $\theta_{23}$  can be measured depends strongly on its true value, we report the confidence regions for three different values of  $\sin^2(\theta_{23})$ : maximal mixing and two values taken from recent global best fits. In addition to performing scans using the Asimov method, we have generated around 5 000 pseudo-experiments for each true value of  $\sin^2(\theta_{23})$  and fit each experiment by optimizing all nine free parameters simultaneously in order to verify the coverages of the different contours obtained under the  $\chi^2$  approx-

imation. The outcomes of the pseudo-experiments, projected into the  $(\sin^2(\theta_{23}), \Delta m_{31}^2)$  plane, are superimposed on the scan results in Fig. 16. Identification of the experimental trials that are contained within a certain contour allows for a comparison between the expected and actual coverages, based on the Asimov assumption and obtained from pseudo-experiments, respectively. In testing the Asimov assumptions with many generated experiments, we find that the contours are conservative all the way up to a C.L. of around 99%. For an expected coverage of 90%, we find true coverages that are on the order of 3% larger. This is more thoroughly discussed in Appendix A.

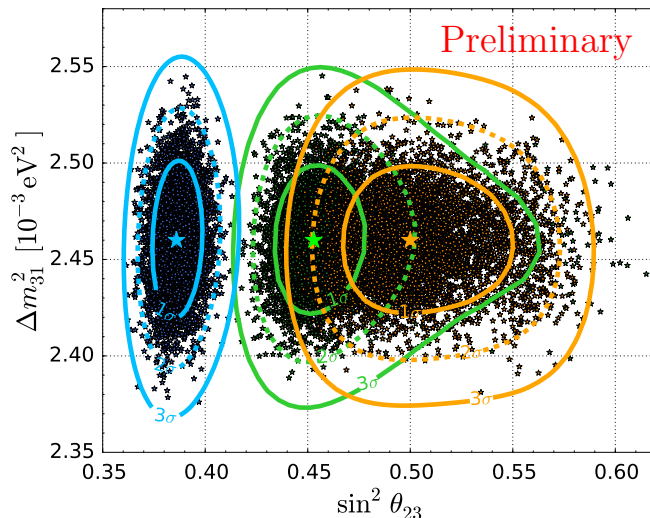
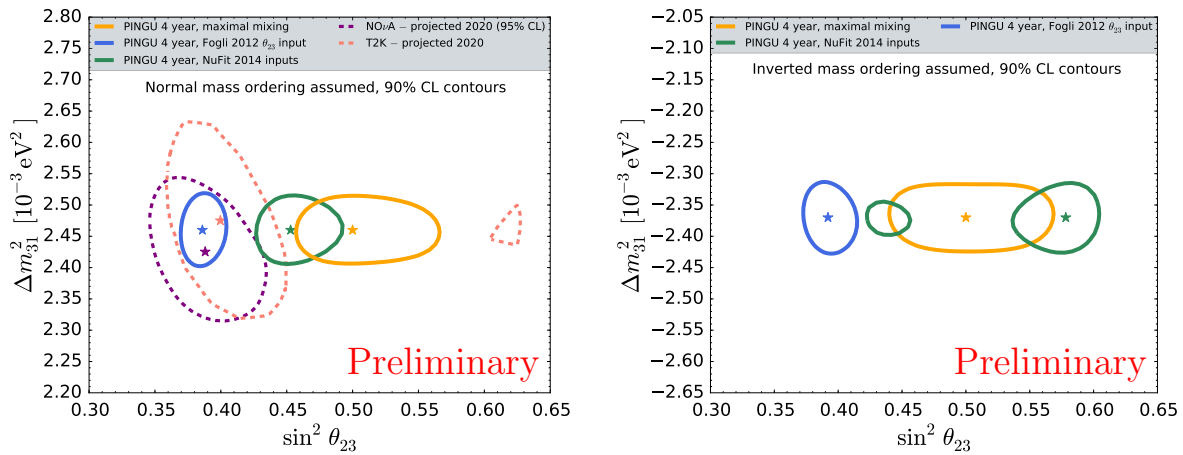


Figure 16: Normal ordering confidence regions under a  $\chi^2$  approximation for the atmospheric oscillation parameters obtained from injecting the respective Asimov dataset, superimposed on the best fit points from around 5000 pseudo-experiments, using three different true values for  $\sin^2(\theta_{23})$ . The blue points and lines represent the Fogli 2012 input [48] for  $\theta_{23}$ , the green points and lines represent the NuFit 2014 inputs [47], and the orange lines and points represent the maximal mixing case.

In Fig. 17 we display the 90% confidence regions for the atmospheric oscillation parameters for the different injected values of  $\sin^2(\theta_{23})$ , assuming correctly identified normal mass ordering in the left panel and inverted in the right. The precision of the  $\sin^2(\theta_{23})$  measurement improves as the true value moves away from maximal ( $\sin^2(\theta_{23}) = 0.5$ ), while the measurement of  $\Delta m_{31}^2$  remains unaffected. In the inverted ordering case, a first octant solution is still allowed at the 90% C.L. if the true value of  $\sin^2(\theta_{23})$  is at its current global best fit. Projected constraints in the normal ordering case from the running NOvA and T2K experiments are also included in the left panel for comparison.



(a) Normal neutrino mass ordering assumed.

(b) Inverted neutrino mass ordering assumed.

Figure 17: The atmospheric neutrino oscillation contours are shown under assumptions of both the normal and inverted orderings. Both orderings show the effect of the use of different inputs for  $\theta_{23}$ ; maximal mixing, Fogli 2012 [48] and NuFit 2014 [47]. The normal ordering assumption includes projected contours from NOvA [49] and T2K [50].

### 3.3. Sensitivity to the Octant of $\theta_{23}$ and Maximal Mixing

One of the open questions in neutrino physics is that of the near-maximal value of  $\theta_{23}$ . In this section we examine the prospects for excluding maximal mixing if  $\theta_{23}$  differs from maximal (*i.e.*,  $\theta_{23} \neq 45^\circ$ ) and, if so, of determining its octant, *i.e.*, whether  $\theta_{23} < 45^\circ$  or  $\theta_{23} > 45^\circ$ . The analysis follows the NMO sensitivity studies; see Table 3 (Sec. 3.4.1), for a list of the oscillation, flux, cross-section and detector-related systematics that are taken into account. In order to determine the confidence level at which a certain hypothesis (in this case a value of  $\theta_{23}$ ) can be rejected, we make use of the Asimov dataset, and convert the resulting  $\overline{\Delta\chi^2}$  from any given fit to an experimental outcome into a statistical significance by assuming a  $\chi^2$  distribution with one degree of freedom.

Figure 18 shows the projected sensitivity of PINGU to the octant of  $\theta_{23}$  for an assumed exposure time of four years as a function of the true value of  $\sin^2(\theta_{23}^{\text{true}})$  (where  $\sin^2(\theta_{23}^{\text{true}}) = 0.5$  corresponds to maximal mixing). The solid line labeled “NO” assumes that the true neutrino mass ordering is normal, while that labelled “IO” refers to data generated assuming the inverted ordering. Due to the existence of the ordering-octant degeneracy (see Appendix A.3 and especially the right panel of Fig. A.72), we show two additional lines which are obtained by minimizing over not only the regular set of continuous nuisance parameters, but also over the ordering itself. All  $\overline{\Delta\chi^2}$  values result from restricting  $\theta_{23}$  to the wrong octant in the fitting procedure. Note that for some values of  $\sin^2(\theta_{23}^{\text{true}})$  and combinations of true and tested mass ordering, there might be a second minimum in the wrong octant apart from  $\sin^2(\theta_{23}^{\text{test}}) = 0.5$ , which we have ensured will be captured correctly in the case in which it provides a better fit to the data.

If the ordering is inverted, and whether it is correctly identified or not, four years of data taking with PINGU will allow the octant to be determined at more than  $3\sigma$  C.L. if  $\sin^2\theta_{23} < 0.38$  or  $\sin^2\theta_{23} > 0.62$ . If the ordering is normal and correctly identified,  $\overline{\Delta\chi^2}$  increases much faster as  $\theta_{23}$  deviates from maximal mixing, and a  $3\sigma$  octant determination becomes possible for  $\sin^2\theta_{23} < 0.44$  or  $\sin^2\theta_{23} > 0.58$ .

If the ordering is inverted, we find that testing for a wrong octant solution within the NO has no effect on the octant sensitivity for  $\sin^2\theta_{23} < 0.62$ , and only very slightly reduces it above. The latter region is where the ordering-octant degeneracy is largest. A much more significant reduction in  $\overline{\Delta\chi^2}$  occurs for the true NO case if the test ordering is optimized, but only for  $\sin^2\theta_{23} < 0.45$ . The second octant can then only be excluded at the  $3\sigma$  level for  $\sin^2\theta_{23} < 0.38$ .

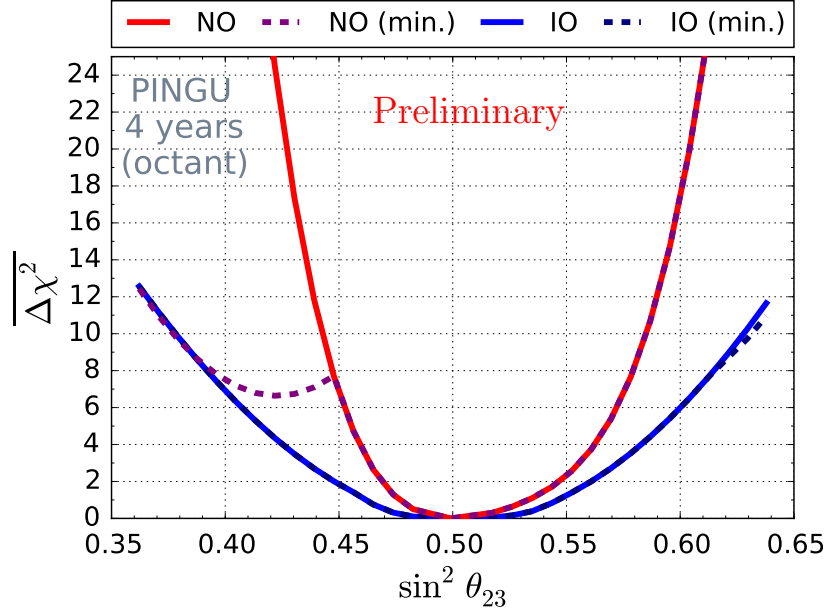


Figure 18: PINGU sensitivity to the octant of  $\theta_{23}$  assuming four years of exposure time, as a function of  $\sin^2 \theta_{23}$  and depending on the true neutrino mass ordering. For the solid curves, the test ordering is kept fixed at the truth, while for the dashed curves we treat it as a free parameter in the fit.

In addition to fixing the exposure time as in Fig. 18, we have investigated how many years of exposure time it would require in order for PINGU to make a 90% C.L. measurement of the octant, again depending on the true NMO and  $\sin^2(\theta_{23}^{\text{true}})$ . This effectively probes the scaling of  $\overline{\Delta\chi^2}$  with time. In Fig. 19 the results of this study are presented; minimization over the ordering is included in both curves. The very flat behavior of the value of  $\overline{\Delta\chi^2}$  at roughly 0 when  $\theta_{23}$  is close to maximal observed in Fig. 18 finds its counterpart here in the very steep rise in exposure time as maximal mixing is approached from both sides. The “shoulder” in the NO case for  $\sin^2 \theta_{23} < 0.45$  and the barely visible bump at  $\sin^2 \theta_{23} > 0.62$  for IO again correspond to the regions where misidentification of the NMO degrades the octant sensitivity and leads to an increase in the exposure time required to determine it. PINGU is projected to make a 90% C.L. determination of the octant of  $\theta_{23}$  within less than a year if the NO is true and either  $\sin^2 \theta_{23} < 0.38$  or  $\sin^2 \theta_{23} > 0.59$ , or if the IO is true and either  $\sin^2 \theta_{23} < 0.39$  or  $\sin^2 \theta_{23} > 0.63$ . A five-year measurement at the 90% C.L. is in reach for NO and  $\sin^2 \theta_{23} < 0.47$  or  $\sin^2 \theta_{23} > 0.55$ , or for IO and  $\sin^2 \theta_{23} < 0.44$  or  $\sin^2 \theta_{23} > 0.56$ .

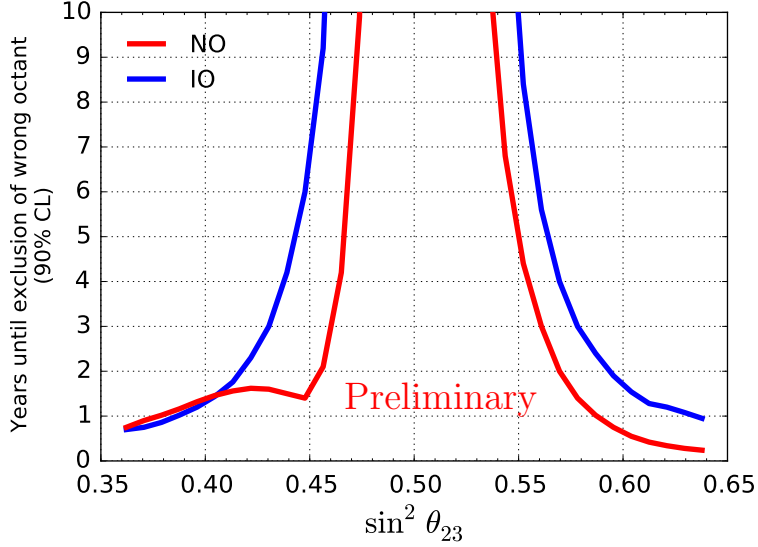


Figure 19: Exposure time in years required for PINGU to exclude the wrong octant of  $\theta_{23}$  at 90% C.L., as a function of  $\sin^2 \theta_{23}$  and the true neutrino mass ordering.  $\Delta\chi^2$  is also minimized over the test ordering.

If we instead examine the time it takes until a non-maximal  $\theta_{23}$  is established at 90% C.L. assuming it is non-maximal (Fig. 20), the overall trend is quite similar. Since the best wrong-octant fit of  $\theta_{23}$  is never a worse match to the data than maximal mixing, the exposure time that is required to exclude a maximal  $\theta_{23}$  at a given C.L. provides a lower bound on the time to exclude the wrong octant at the same C.L. Uncertainty of the NMO only has minor impact on the measurement for NO and  $\sin^2 \theta_{23} < 0.45$ , where assuming maximal mixing in the wrong IO yields better fits than it does in the true NO. Minimization over the test ordering does not impact the sensitivity to maximal mixing at all if the IO is true.

A non-maximal  $\theta_{23}$  can be established at 90% C.L. with a one-year exposure time if the ordering is normal and  $\sin^2 \theta_{23} < 0.44$  or  $\sin^2 \theta_{23} > 0.59$ , or if the ordering is inverted and  $\sin^2 \theta_{23} < 0.43$  or  $\sin^2 \theta_{23} > 0.58$ . Non-maximal mixing can be determined in less than five years in the NO case for  $\sin^2 \theta_{23} < 0.47$  or  $\sin^2 \theta_{23} > 0.55$ , and in the IO case for  $\sin^2 \theta_{23} < 0.45$  or  $\sin^2 \theta_{23} > 0.56$ .

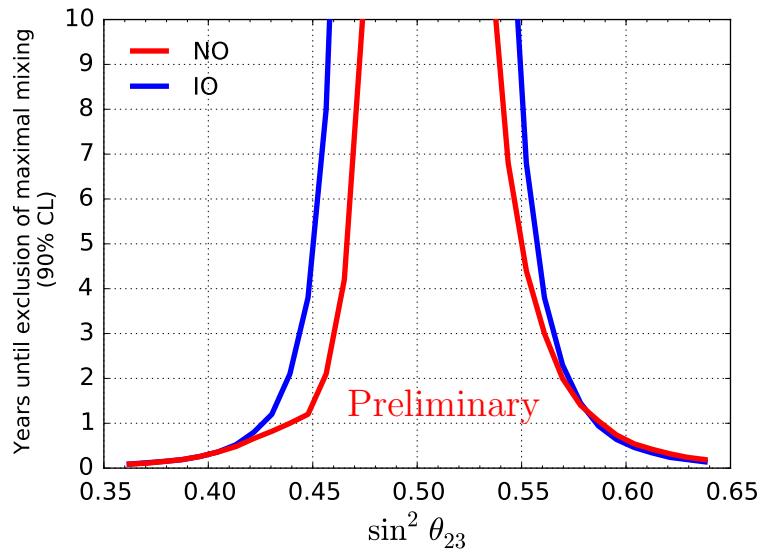


Figure 20: Exposure time in years required for PINGU to exclude maximal mixing at 90% C.L., as a function of  $\sin^2 \theta_{23}$  and the true neutrino mass ordering.  $\overline{\Delta\chi^2}$  is also minimized over the test ordering.

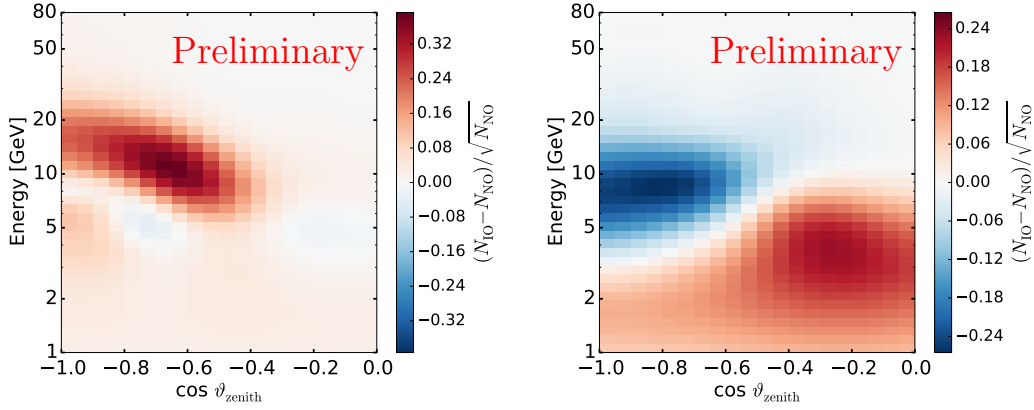
### 3.4. Neutrino Mass Ordering

Data from solar neutrino measurements [51] have shown that  $m(\nu_2) > m(\nu_1)$ , but the position of  $\nu_3$  in the ordering of these masses is, as yet, unknown. The sensitivity of the PINGU detector to neutrinos with energies in the range of roughly 5–15 GeV allows this ordering to be determined. Figure 21 shows three distinguishability plots similar to those described in Ref. [52]. To illustrate the individual contributions to the ordering signal, three neutrino flavors are shown separately under the assumption of perfect particle identification (PID). These plots identify regions in which the number of events expected for the NO is greater than that expected for the IO (blue regions) and vice-versa (red regions). While this metric is helpful for highlighting the regions of interest in the energy-angle space from which useful information may be extracted, it provides only an approximation of the PINGU sensitivity to the NMO without systematics. More detailed simulations and analysis methods are required to determine the actual PINGU sensitivity, as discussed below.

Compared to the first version of this document [14], we have incorporated several improvements into our NMO analysis. In addition to changing the geometry of the detector (see Sec. 2), we have also included a detailed simulation of the intrinsic noise. We use a detector livetime of four years which matches the study of atmospheric  $\nu_\mu$  disappearance (Sec. 3.2). Continuing to employ a full event reconstruction and particle identification to discriminate track-like and cascade-like events, we have studied the impact of numerous additional systematic uncertainties. These have been partly implemented in the log-likelihood ratio (LLR) analysis, as will be described. We have also changed the choice of the wrong ordering hypothesis to be the one that most resembles the true ordering Asimov template, *i.e.*, that which maximizes the confusion between orderings (see Sec. Appendix A.2 for more details).

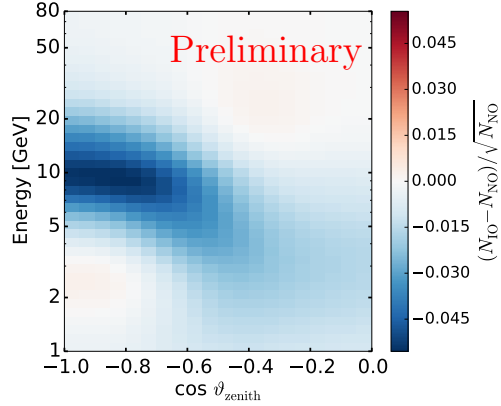
#### 3.4.1. Systematics

Numerous sources of systematic errors have been identified and their impact on the PINGU sensitivity to the determination of the NMO has been quantified. For convenience, we have categorized these uncertainties into three subsets: neutrino oscillation parameters, neutrino flux and cross section, and detector modeling. In what follows we describe and quantify each of these subsets of systematics, and indicate possible ways to better constrain them to reduce their impact on the final significance. It should be noted that the calibration systems installed with the PINGU detector (see Sec. 7) will reduce the magnitude of the detector-related systematics.



(a)  $\nu_\mu$  CC events.

(b)  $\nu_e$  CC events.



(c)  $\nu_\tau$  CC events.

Figure 21: Distinguishability metric as defined in [52] for one year of simulated PINGU data, with parametrized reconstruction resolutions as described in Sec. 3.1.2. The square-root of a quadratic sum over the bins in each plot gives an estimate of the number of  $\sigma$  separating the two orderings. For illustrative purposes we have assumed perfect flavor ID. The top left figure (a) shows track-like events from CC  $\nu_\mu$  interactions. The top right figure (b) shows CC  $\nu_e$  events and the bottom figure (c) shows CC  $\nu_\tau$ .

	LLR	$\overline{\Delta\chi^2}$	
Oscillation	*	*	$\Delta m_{31}^2 = 2.46 \times 10^{-3} \text{ eV}^2, -2.37 \times 10^{-3} \text{ eV}^2$ [47]
	*	*	$\theta_{23} = 42.3^\circ, 49.5^\circ$ [47]
	*	*	$\theta_{13} = 8.5^\circ \pm 0.2^\circ$ [47]
		†	$\delta_{\text{CP}} = 0^\circ$
Flux & Cross Section	*	*	Event rate = nominal
	*	*	$\nu_e/\nu_\mu$ flux ratio = nominal $\pm 3\%$ [53]
	*	*	$\nu/\bar{\nu}$ flux ratio = nominal $\pm 10\%$ [53]
	*	*	Atmospheric spectral index = nominal $\pm 0.05$ [53]
		†	Air-shower interactions [53]
		†	Neutrino cross-section (see Sec. <a href="#">Appendix B</a> )
Detector	*	*	Energy scale = $1.0 \pm 10\%$ († $\pm 0.5\%$ )
		†	Individual module efficiency = nominal $\pm 10\%$ Ice properties

Table 3: List of uncertainties studied in the NMO analysis, with nominal values and Gaussian priors (where applicable) shown. Asterisks indicate those systematics that were implemented as nuisance parameters in the analysis procedures. Daggers indicate systematics used only in specific studies and not fully incorporated into the main analysis.

The specific systematic uncertainties we have studied are listed in Table 3. Those implemented as nuisance parameters in the analysis procedures (see Sec. 3.1.2) are indicated with an asterisk, with central values and priors indicated for most parameters in the table. The uncertainties related to the atmospheric flux and cross-sections were investigated only using the  $\overline{\Delta\chi^2}$  approach and are not included in the results of the LLR analysis due to the computational time required to study them. The oscillation parameters to which PINGU is most sensitive are  $\theta_{23}$  and  $\Delta m_{31}^2$ . We present significances with these included as nuisance parameters in the ordering analysis, both with (LLR analysis only) and without priors. The other oscillation parameters allowed to vary in the analysis are  $\theta_{13}$  and  $\delta_{\text{CP}}$ , but they have smaller impact on the overall sensitivity (the implementation of  $\delta_{\text{CP}}$  as a systematic is discussed in Sec. 3.4.3). The remaining oscillation parameters ( $\Delta m_{12}^2$ ,  $\theta_{12}$ ) were also considered but they have negligible impact and are held fixed. The injected true values of these parameters are taken from the global best fit analysis [47], and the  $1\sigma$  error is used as a prior on  $\theta_{13}$ . The analysis exhibits a strong degeneracy between the octant of  $\theta_{23}$  and the ordering in most of the allowed parameter space of  $\theta_{23}$ , as discussed in Sec. [Appendix A](#) (and, *e.g.*, in [54]), and this is accounted for in the analysis procedure.

The flux uncertainties are also treated as nuisance parameters. For the atmospheric neutrino flux ratios and spectral index we use central values and  $1\sigma$  uncertainties from [53] as the nominal values and priors, respectively. The overall atmospheric flux normalization is allowed to vary without a prior in order to account not only for the atmospheric flux normalization, but also any uncertainties in the overall detector rate normalization. The systematic impact of numerous parameters describing neutrino interaction cross-sections were studied using the GENIE [18] neutrino event generator, full details of which are available in Secs. 8 and Appendix B.

Detector-related systematics introduce uncertainties in the visible event energy as determined by our reconstruction algorithms. These uncertainties could arise from miscalibrated module detection efficiencies or imperfections in our modeling of the optical properties of the ice in which PINGU will be deployed. A complete study of these effects requires a significant amount of simulated data. Instead of implementing these uncertainties as nuisance parameters, we evaluated the NMO significance for a small number of independent datasets, each of which featured a variation of either the overall module efficiency or the ice property model. As a proxy for other possible uncertainties, we allow the reconstructed visible energy to vary globally as a nuisance parameter, with a conservative prior of 10% guided by estimations from IceCube calibrations with *in situ* light sources (see Sec. 7 for more details). None of these uncertainties had a strong impact on the NMO significance.

In the energy range of relevance to the NMO measurement, neutrino interactions with matter are dominated by deep inelastic scattering (DIS). Since DIS uncertainties are relatively modest, the overall impact of these uncertainties was found to be small. The impact of the neutrino cross section systematics on the NMO determination have also been studied using the  $\overline{\Delta\chi^2}$  analysis method but with the addition of six more systematic parameters listed in Table 4. The impact of these systematics on the NMO measurement is found to be very small. More details on these systematics and how they were implemented can be found in Sec. Appendix B.

To quantitatively assess the impact of each of these groupings of systematics, each was varied independently of the other groups. Table 5 indicates the “impact” of these different groups of systematics by comparing the 4-year PINGU sensitivity with each set of systematics to the theoretical limit where statistical uncertainties dominate (all the systematics are known to arbitrary precision). Clearly, the oscillation parameter uncertainties are the dominant contributors to the decrease in significance compared to the “no systematics” case. The other two groups shown have only a moderate effect when

Name	nominal value	uncertainty (%)
$M_A^{CCQE}$	0.99	-15, +25
$M_A^{RES}$	1.120	$\pm 20$
$A_{HT}^{BY}$	0.538	$\pm 25$
$B_{HT}^{BY}$	0.305	$\pm 25$
$C_{V1u}^{BY}$	0.291	$\pm 30$
$C_{V2u}^{BY}$	0.189	$\pm 30$

Table 4: List of parameters and their associated uncertainties based on GENIE. Nominal values of the parameters are taken from Appendix B of the GENIE User Manual. See Sec. 8 for more details.

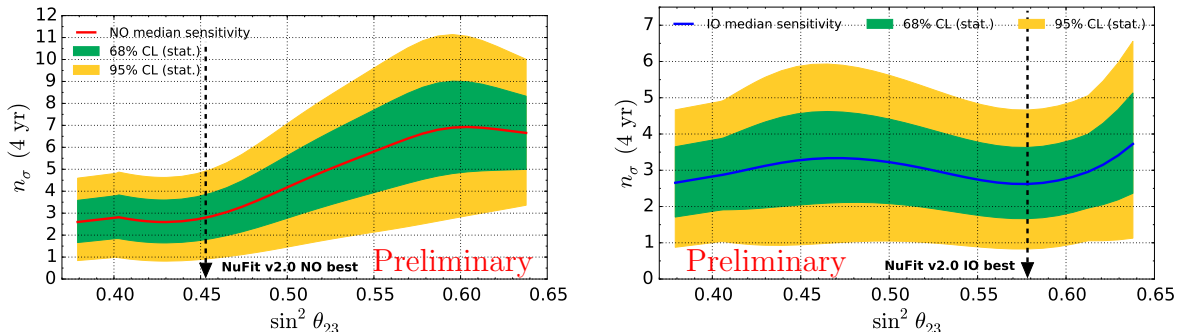
Systematic	LLR		$\overline{\Delta\chi^2}$	
	4 yr $n_\sigma$ (NO)	4 yr $n_\sigma$ (IO)	4 yr $n_\sigma$ (NO)	4 yr $\sigma$ (IO)
None	5.5	5.5	5.5	5.5
Flux only	5.2	5.0	5.1	5.1
Detector only	4.3	4.4	4.5	4.5
Oscillation only	3.4, 3.5	2.9, 3.1	3.4	3.0
All	2.9, 3.3	2.6, 2.9	2.8	2.6

Table 5: Summary of the systematic errors and their impacts on the estimated four-year significance of the mass ordering measurement, for both the LLR and  $\overline{\Delta\chi^2}$  analysis methods and for the cases in which the normal and inverted orderings are true. Where two significances are given, the first value is for the case where NuFit 2.0 [47] priors are not used in the fit and the second is for where they are used (see Sec. Appendix A for details).

included by themselves.

### 3.4.2. Results

Several numerical studies have been performed to quantify the ability of PINGU to determine the NMO with all systematics considered. Using global best fit values [47] for the oscillation parameters, PINGU will determine the ordering with a significance of  $3\sigma$  in roughly 4 years. This significance depends quite strongly on the actual value of  $\theta_{23}$ , which is not well known (see, *e.g.*, [55] and [56]). The expectation of 4 years to reach  $3\sigma$  significance is conservative in the sense that PINGU’s sensitivity to the NMO would be



(a) Normal neutrino mass ordering assumed.

(b) Inverted neutrino mass ordering assumed.

Figure 22: Expected significance with which the neutrino mass ordering will be determined using four years of data, as a function of the true value of  $\sin^2(\theta_{23})$ . Solid red (NO) and blue (IO) lines show median significances, while the green and yellow bands indicate the range of significances obtained in 68% and 95% of hypothetical experiments. The significance for determining the ordering when the true ordering is inverted is relatively insensitive to  $\theta_{23}$ , while for the normal ordering large values of  $\theta_{23}$  are advantageous. The range shown corresponds roughly to the current  $3\sigma$  allowed region of  $\theta_{23}$ ; the global best-fit values from the NuFit group [47] for both orderings are indicated by black arrows.

greater in almost any region of the allowed parameter space of  $\theta_{23}$  other than the assumed global best fit, as shown in Figs. 22 and 23.

In addition, the NMO sensitivity of PINGU as a function of time has been calculated assuming the same global best fit oscillation parameters, with and without world-average priors from [47] on  $\theta_{23}$  and  $\Delta m_{31}^2$ . The technical description of how the priors were applied, as well as the plot of NMO sensitivity vs. time, are presented in Sec. Appendix A. Finally, it is worth noting that the time required to achieve a significant result is shortened by roughly 6 months if the partially deployed PINGU detector data, as well as roughly 10 years of DeepCore data available by then, are included in the analysis.

### 3.4.3. Impact of the Charge-Parity Phase $\delta_{\text{CP}}$

Using the  $\overline{\Delta\chi^2}$  method we have investigated the effect of taking into account  $\delta_{\text{CP}}$  as a nuisance parameter in our NMO analysis. This was included following all other systematics considered since  $\delta_{\text{CP}}$  represents a highly nonlinear parameter. Making sure that it is correctly treated by the minimizer would therefore require a very large computational effort. Instead, for a given true ordering hypothesis, we opted to vary the injected  $\delta_{\text{CP}}$  in steps of  $45^\circ$  between  $0^\circ$  and  $360^\circ$  and finely scan  $\delta_{\text{CP}}$  in the opposite-ordering fit, simul-

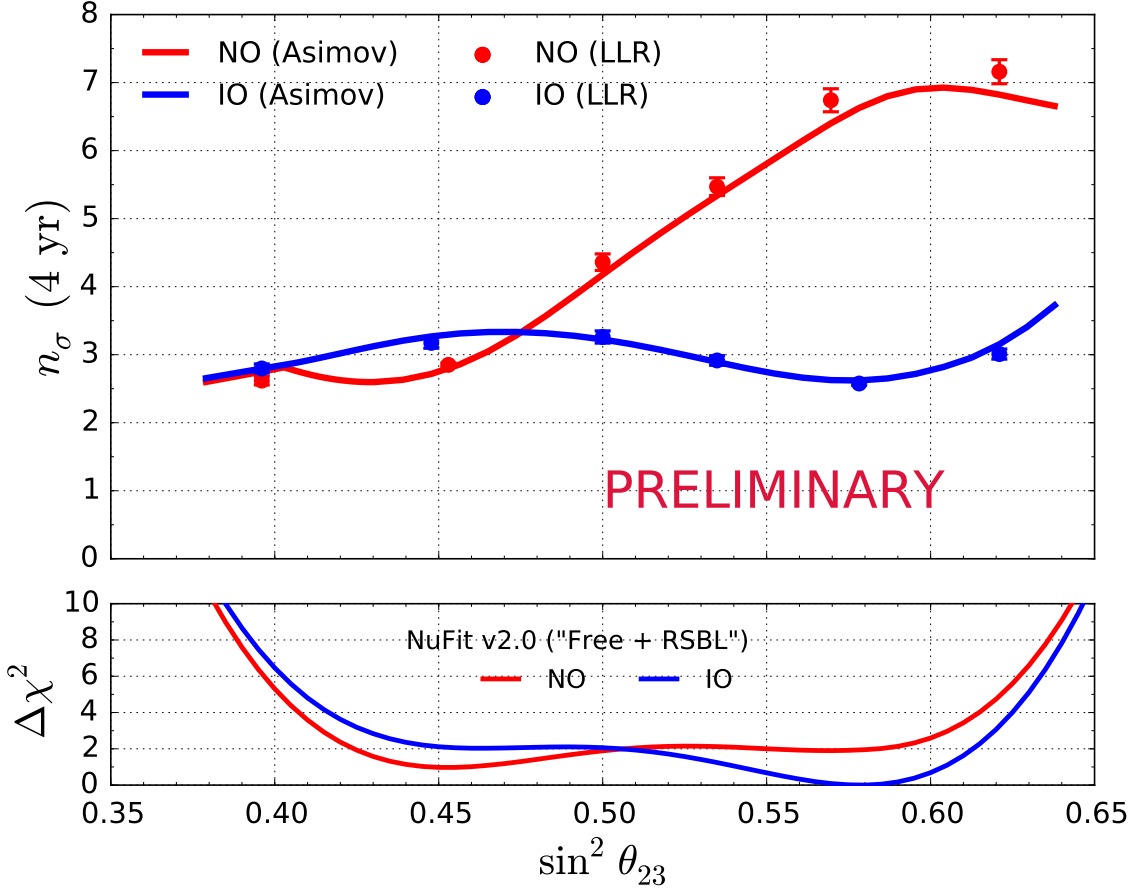


Figure 23: *Upper panel:* Projected four-year significance of the neutrino mass-ordering determination as a function of  $\sin^2(\theta_{23})$  for the cases where the true mass ordering is normal (red) and inverted (blue). The significance for determining the ordering when the true ordering is inverted is relatively insensitive to  $\theta_{23}$ , while for the normal ordering large values of  $\theta_{23}$  are advantageous. The NuFIT 2.0  $\sin^2(\theta_{23})$  values used here (0.451 for NO and 0.576 for IO) produce almost the lowest significance possible in each ordering, and thus correspond to nearly the most conservative values in the entire range. *Lower panel:* Constraints on  $\sin^2(\theta_{23})$  from NuFIT 2.0 [47] under the assumption of both normal and inverted ordering.

taneously minimizing over our default set of eight systematics at each step. As before, we have taken care to find the correct solution for  $\theta_{23}$ , by searching for a minimum in both octants for each fixed value of the hypothesized  $\delta_{\text{CP}}$ . Figure 24 shows the resulting reduction of the projected NMO sensitivity as a function of  $\sin^2 \theta_{23}$  for four years of exposure time, compared to the reference projection from Fig. 23. Note that we show the

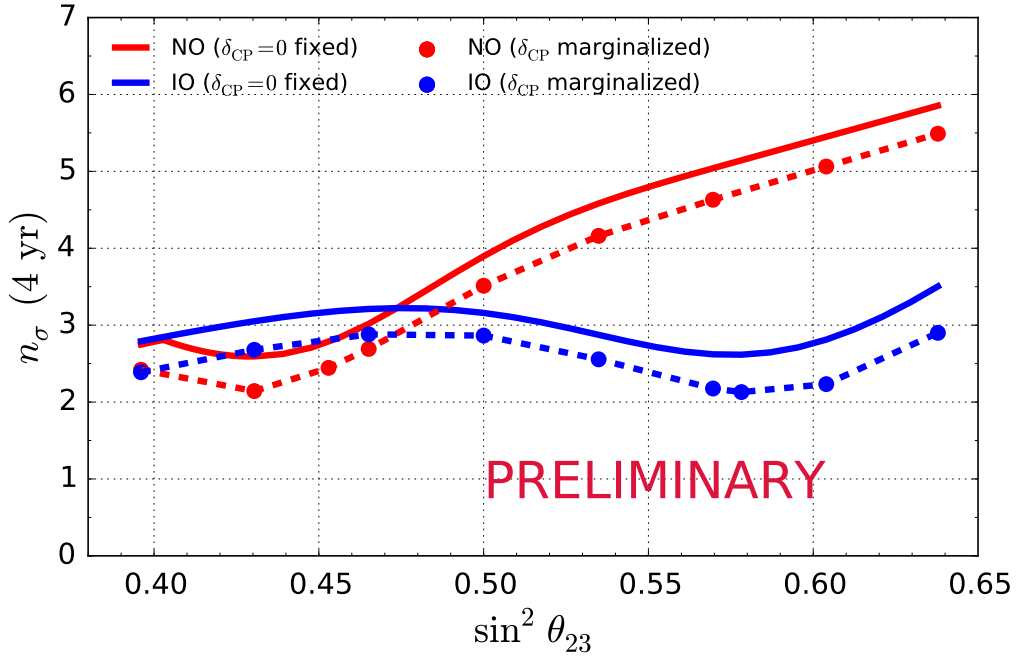


Figure 24: Projected reduction of the four-year significance of the NMO determination as a function of  $\sin^2 \theta_{23}$  when  $\delta_{\text{CP}}$  is included as a nuisance parameter, compared to our nominal case where  $\delta_{\text{CP}} = 0$  and  $\delta_{\text{CP}}$  is not minimized over, cf. Fig. 23. Note that the dashed lines are only present in order to guide the eye. See text for details.

maximum impact on the sensitivity here, i.e.  $\delta_{\text{CP}}$  is allowed to take any value. Also, the absolute significances in this figure deviate from those in the previous figures since here we make the approximation that the absolute values of the means of the two test statistic distributions (one for each NMO hypothesis) are the same; see Appendix A.3 for details. We find that  $\delta_{\text{CP}}$  has a non-negligible influence on the significance of the NMO measurement, leading to a decrease of about  $\sim 10\% - 20\%$ . It does not obscure the NMO signal, however, independent of whether the ordering is inverted or normal, and independent of the octant of  $\theta_{23}$ .

#### 3.4.4. Conclusions

We have performed a detailed study of the expected sensitivity of PINGU to the neutrino mass ordering. The sensitivity estimates are based on detailed Monte Carlo simulations

of the detector and full event reconstructions, and the statistical methods used were validated against a full likelihood analysis for a more limited range of systematics. Our estimates are also in agreement with external studies [57, 58, 59, 60].

We find that most detector-related systematics investigated so far, with the exception of the energy calibration scale, play a smaller role than physics-related systematics. The latter arise from uncertainties in measured oscillation parameters, some of which PINGU itself will be able to measure. We also find that including non- $\nu_\mu$ -CC events in the final sample with simple particle ID greatly improves the significance of the measurement.

Using the  $\overline{\Delta\chi^2}$  technique with parameterizations based on fully simulated and fully reconstructed events of all flavors, incorporating a wide array of detector- and physics-related systematics, and using an initial form of particle ID, we estimate that PINGU will be able to determine the neutrino mass ordering to  $\sim 3\sigma$  with 4 years of data. However, this significance may very well be higher if the true value of  $\theta_{23}$  differs from the current world average.

There are a number of future improvements that will further enhance the NMO significance. The most prominent involve refinements in reconstruction, flavor identification, and the use of the reconstructed inelasticity of the neutrino event, which is a weak  $\nu/\bar{\nu}$  discriminator. More sophisticated particle ID will enable us to better exploit the distinct patterns of  $\nu_\mu$  events relative to those of  $\nu_e$  and  $\nu_\tau$ . The use of the inelasticity would help us distinguish neutrinos from antineutrinos on a statistical basis and could provide a 20–50% increase in significance [24]. In addition, further detector geometry optimization, improved event selection efficiency and more accurate event reconstruction will also improve the significance.

### 3.5. Tau Neutrino Appearance

Following the IceCube-DeepCore detector’s success in measuring  $\nu_\mu$  disappearance [8], a  $\nu_\tau$  appearance analysis was started and is still underway at the time of this writing. Tau neutrinos are not present in the conventional atmospheric neutrino flux but can appear in significant quantities due to  $\nu_\mu \rightarrow \nu_\tau$  oscillations. Generally speaking, the appearance measurement faces two challenges: the  $\nu_\tau$  must have a minimum energy of 3.5 GeV to undergo a charged-current (CC) interaction, and the expected signal rate from this interaction is low compared to the signal from other neutrino interactions. In the PINGU detector, the increased photocathode density will mainly improve the separation of the tau-type interactions from the muon-type. Better energy and zenith angle resolutions will also enable improved measurements of the regions that are richest in the oscillated  $\nu_\tau$  flux.

In the “three neutrino framework” discussed previously, the two clear channels to measure  $|U_{\tau 3}|$  directly are  $\nu_\tau \rightarrow \nu_\tau$  and  $\nu_\mu \rightarrow \nu_\tau$ . The  $\nu_\tau \rightarrow \nu_\tau$  channel probes  $|U_{\tau 3}|$  directly, but requires an experimentally challenging (and hitherto unrealized) high statistics  $\nu_\tau$  beam and long baseline setup. A more feasible experimental channel is  $\nu_\mu \rightarrow \nu_\tau$ , which probes a combination of  $U_{\mu 3}$  and  $U_{\tau 3}$ , where any degeneracy between  $|U_{\mu 3}|$  and  $|U_{\tau 3}|$  can be broken by either external constraints on  $|U_{\mu 3}|$  or by simultaneously measuring  $\nu_\mu \rightarrow \nu_\mu$  and  $\nu_\mu \rightarrow \nu_\tau$ .

Going beyond the three-neutrino-family framework, *i.e.*, assuming  $U_{\text{PMNS}}$  is not unitary, means that the summation in Eq. 4 cannot be simplified as discussed above. In that case, a long-baseline  $\nu_\mu \rightarrow \nu_\tau$  measurement probes a combination of  $U_{\tau i}$  and  $U_{\mu i}$  elements, which can then be compared to combinations of  $U_{e i}$  and  $U_{\mu i}$  obtained from  $\nu_\mu \rightarrow \nu_e$  and  $\nu_\mu \rightarrow \nu_\mu$  measurements at similar  $L/E$  values. For simplicity, in the following discussion where comparisons to cases outside the three-neutrino-family framework are made, the Standard Model expectation to measure  $|U_{\tau 3}|^2 \approx 1/2$  is used as equivalent to  $P(\nu_\mu \rightarrow \nu_e) + P(\nu_\mu \rightarrow \nu_\mu) + P(\nu_\mu \rightarrow \nu_\tau) = 1$ .

A measured value of  $|U_{\tau 3}|^2 \approx \frac{1}{2}$  would:

- Strengthen the three-active-neutrino interpretation, and
- Confirm unitarity of the third mass eigenstate.

A measured value of  $|U_{\tau 3}|^2 \not\approx \frac{1}{2}$  would:

- Provide a distinct signature of new physics,
- Further motivate explorations of possible Non-Standard Interactions (NSI) [61, 62, 63], and
- Offer an additional experimental anomaly including a possible sterile neutrino(s) explanation via  $|U_{e3}|^2 + |U_{\mu3}|^2 + |U_{\tau3}|^2 + |U_{\text{sterile}3}|^2 = 1$ .

### 3.5.1. Event Selection and Reconstruction

The analysis for measuring  $\nu_\tau$  appearance in PINGU follows the prescription described in Sec. 3.1.1 for the study of atmospheric neutrino parameters with a notable difference related to the particle identification.

The Particle IDentification (PID) used for this analysis utilizes the same training that is applied for all analyses, described in Sec. 2.6. The division of the sample into track-like and cascade-like events is accomplished by requiring the output score of the PID calculation to be more cascade-like (MVA score  $< 0.424$ ), the efficiency of which is shown in Fig. 25.

The goal of applying a stricter PID criterion is to reject the mis-identified low-energy  $\nu_\mu$  CC events that would reduce the ability to distinguish  $\nu_\tau$  events. Some events that are not in the “purer cascade” category are selected in a “purer track” sample that is used as a control sample. Table 6 shows expected rates for signal and background in each sample. Even though there is still a larger fraction of  $\nu_e$  and  $\nu_\mu$ , primarily made up of charged-current interactions in the sample, we can further improve the measurement given that  $\nu_e$  and  $\nu_\mu$  will pile up around the horizon ( $\cos \theta_{\text{zenith}} = 0$ ), while  $\nu_\tau$  from  $\nu_\mu \rightarrow \nu_\tau$  oscillations will mostly be found close to the up-going region, as shown in Fig. 26. Note that in this analysis we consider explicitly the “sterile neutrino” scenario where oscillation to sterile neutrinos will impact both the charged-current and neutral-current (NC) interactions, as sterile neutrinos by definition do not interact with the  $Z^0$  boson. In the case of NSI we could imagine a different effective change to charged-current and neutral-current events, however this is currently not considered in this analysis.

To better evaluate the potential of the measurement we construct a distinguishability metric shown in Fig. 27, similar to the one described in Sec. 3 (and in [52]), that shows where the expected  $\nu_\tau$  can be best distinguished. In that figure, the color scale indicates the significance of a given bin in the final analysis (in the absence of systematic effects)

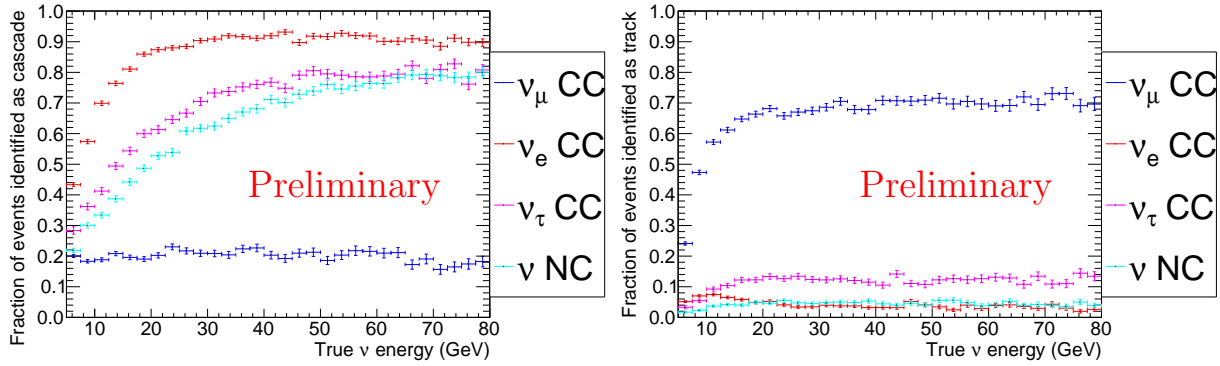


Figure 25: Particle identification efficiency of the samples used for the  $\nu_\tau$  appearance analysis. On the left is shown the efficiency to identify the event as a cascade in the “purer cascade PID” region. The efficiency to identify the event as a track in the “purer track PID” control sample is shown on the right.

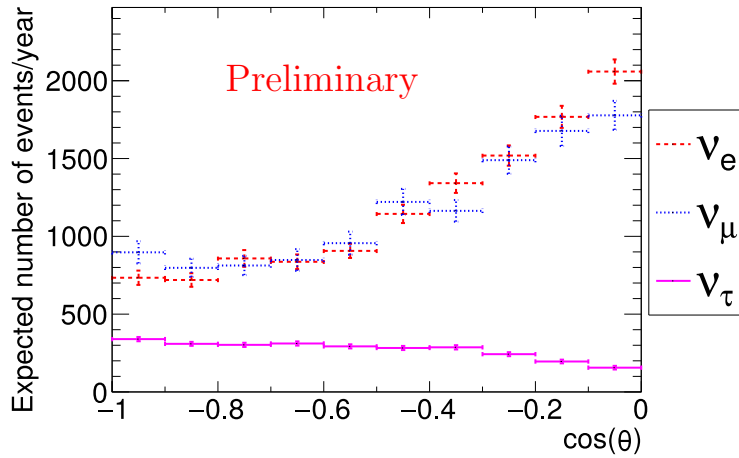


Figure 26: The expected number of neutrino events per year per flavor as a function of the reconstructed  $\nu$  incidence angle after regular NMO event selection and the “purer” cascade PID cut.

	Exp. number of events/year/ $10^3$	
	Purer cascade PID	Purer track PID
Background: $\nu_e + \nu_\mu$	23.7	12.0
CC	20.7	11.7
NC	3.0	0.3
Signal: $\nu_\tau$	2.7	0.4
CC	1.7	0.3
NC	1.0	0.1

Table 6: Rates for signal and background on the cascade and track samples used for this analysis. Breakdown in CC and NC events for the signal and background samples are also shown.

when trying to distinguish the case without  $\nu_\tau$  appearance. It is important to note that the peak of the  $\nu_\tau$  appearance signal is at a lower energy than the first oscillation maximum (around 25 GeV for neutrinos traversing the Earth). This difference is due to the undetected outgoing neutrinos produced either at the  $\tau$  decay for  $\nu_\tau$  CC interactions or at the vertex of the NC interaction. These secondary neutrinos carry away part of the interacting  $\nu_\tau$  energy, resulting in event reconstruction at lower energy.

Another way to visualize the potential to measure the  $\nu_\tau$  component is to look at the expected distribution of events as a function of the ratio of neutrino pathlength and energy (L/E), on which the neutrino oscillations depend directly as shown in Eq. 4. This is illustrated in Fig. 28, where the expected number of events for different scenarios is shown. A clear difference is observed between the usual three-flavor oscillations and the scenarios where oscillation-induced  $\nu_\tau$  do not appear. In the figure, the case where only  $\nu_\tau$  CC events disappear is also shown for reference.

### 3.5.2. Analysis method

The analysis method measures the  $\nu_\tau$  normalization, defined as the ratio of the number of measured tau neutrinos to the number expected in the standard three-neutrino paradigm. The methodology is similar to that described in Appendix A.2, but the pseudo-data set generation is handled differently. The main difference here is that the pseudo-data generation is marginalized over the systematics.

To exemplify the procedure described above we consider the first trial run for the  $\nu_\tau$  normalization at the nominal value for one month of livetime. First the expected distri-

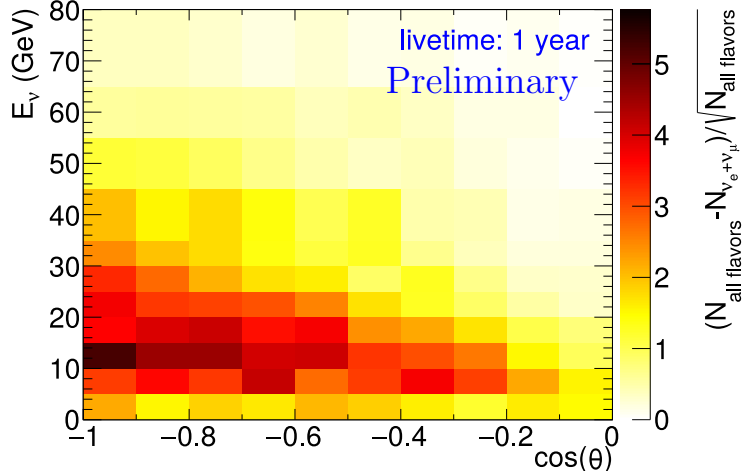


Figure 27: The distinguishability metric, as defined in [52], for one year of simulated PINGU data. The quadratic sum of the absolute values in each bin gives an estimate of the number of  $\sigma$  separating the no- $\nu_\tau$  appearance hypothesis from the standard oscillation picture with  $\nu_\tau$  appearance, without accounting for any systematic uncertainties.

bution of events for a realization of the systematic errors was calculated from the PINGU simulation; for this example:  $\Delta m_{31}^2 = 2.52 \times 10^{-3} \text{ eV}^2$  [ $+1.01\sigma$ ],  $\sin^2 \theta_{23} = 0.491$  [ $-0.16\sigma$ ], overall normalization of 1.11 [ $+0.72\sigma$ ],  $\nu_e/\nu_\mu$  flux normalization of 0.96 [ $-2.00\sigma$ ],  $\bar{\nu}/\nu$  normalization of 0.94 [ $-0.40\sigma$ ], spectral index of 0.05 above nominal [ $+1.00\sigma$ ], and energy scale reduced by 2.5% [ $-0.25\sigma$ ]. This expectation is then scaled to the equivalent number of events after 1 month of data, and a Poisson fluctuation is applied to each bin in the  $(\cos \theta_\nu, E_\nu)$  histogram to create the pseudo-data template. The pseudo-data is then used to estimate which  $\nu_\tau$  normalization is better represented by the given histogram while marginalizing over all systematic parameters; for this example:  $\nu_\tau$  normalization of 0.89,  $\Delta m_{31}^2 = 2.54 \times 10^{-3} \text{ eV}^2$  [ $+1.20\sigma$ ],  $\sin^2 \theta_{23} = 0.520$  [ $+0.35\sigma$ ], overall normalization of 1.13 [ $+0.85\sigma$ ],  $\nu_e/\nu_\mu$  flux normalization of 1.01 [ $+0.27\sigma$ ],  $\bar{\nu}/\nu$  normalization of 0.97 [ $-0.17\sigma$ ], spectral index of 0.038 above nominal [ $+0.75\sigma$ ], and energy scale reduced by 4.8% [ $-0.48\sigma$ ].

The procedure detailed above was run with 30 000 generated pseudo-data trials for several different  $\nu_\tau$  normalizations (ranging between 0 and 1). By comparing the spread of the reconstructed  $\nu_\tau$  normalizations among those cases we obtain the sensitivity to distinguish between different true  $\nu_\tau$  normalizations, as shown in Fig. 29.

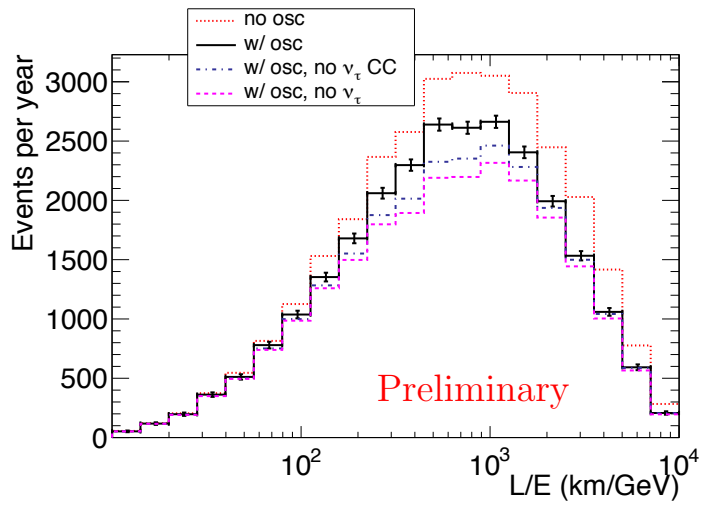


Figure 28: Expected number of neutrino events per year as a function of reconstructed  $L/E$  after regular event selection and for the “purer” cascade PID cut. Four different scenarios are shown: no neutrino oscillations occur (red dotted line), regular three-flavor neutrino oscillations (black line) shown with statistical error bars, neutrino oscillations with  $\nu_\mu \rightarrow \nu_s$  (magenta dashed line) and neutrino oscillations with the assumption that the  $\nu_\tau$  CC vanish while the  $\nu$  NC interactions do not vanish (blue dot-dashed line).

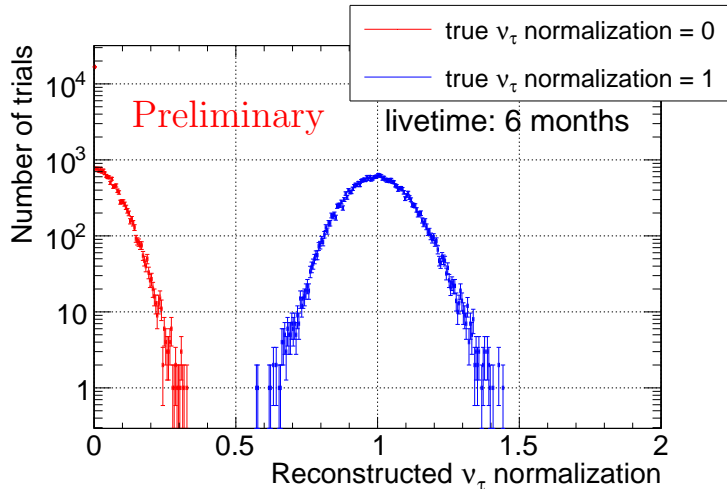


Figure 29: Resulting distribution of reconstructed  $\nu_\tau$  normalization obtained using the procedure described in the text. An  $x$ -axis value of 0 means no  $\nu_\tau$  appearance while a value of 1 corresponds to  $\nu_\tau$  appearance, as expected in the standard oscillation scenario. Under the assumptions of Gaussian distributions and standard oscillations, the median significance to exclude no  $\nu_\tau$  appearance is roughly  $13\sigma$  after six months of livetime.

### 3.5.3. Systematic uncertainties

We consider systematic uncertainties due to the overall normalization of the neutrino flux, the  $\nu_e$  flux in relation to the  $\nu_\mu$  flux, the  $\bar{\nu}$  rate in relation to the  $\nu$  rate, the atmospheric oscillation parameters ( $\Delta m_{31}^2$  and  $\theta_{23}$ ), and the spectral index and energy scale. All considered systematics are listed in Table 7 along with the priors used for either generating trials or for both the trial generation and the fitting.

These priors differ slightly from those used in other analyses described in this letter because of either a different implementation of degenerate parameters (as is the case for the spectral index of the  $\nu_\mu$  flux and effective area energy dependence). One particular instance where the prior is changed is the  $\nu_e/\nu_\mu$  flux normalization, where we assume a tighter prior based on [33]. The sampling distribution of the oscillation parameters was centered around maximal mixing for simplicity, and for both parameters used larger Gaussian errors than the current best fit values. We have also tested the impact of using either the DOM efficiency parametrization as done in Sec. 3.2 or the energy scale systematic, and found both yield very similar results, so we have decided to only use the energy scale systematic in this analysis with a 10% prior, as is done in Sec. 3.4.

Systematics	Gaussian prior
$\Delta m_{31}^2$ <sup>†</sup>	$(2.42 \pm 0.10) \times 10^{-3} \text{ eV}^2$
$\sin^2(\theta_{23})$ <sup>†</sup>	$0.500 \pm 0.055$
Normalization <sup>†</sup>	$\pm 15\%$
$\nu_e/\nu_\mu$ flux normalization	$\pm 2\%$
$\bar{\nu}/\nu$ normalization	$\pm 15\%$
Spectral index of $\nu_\mu$ flux	$\pm 0.05$
Energy scale	$\pm 10\%$

Table 7: List of systematics and priors used for this analysis. For systematics marked with a <sup>†</sup> the priors listed are only used in the generation of trials.

Additional systematic effects considered in other PINGU neutrino oscillation analyses but not in this one, such as the uncertainty related to the atmospheric neutrino flux model investigated in Sec. 3.4, are not expected to significantly impact the result.

#### 3.5.4. Results

Performing this analysis for several different detector livetimes, we expect to reach  $5\sigma$  exclusion of the no- $\nu_\tau$ -appearance hypothesis with one month of data, as shown in Fig. 30. The effect of statistical fluctuations in the measurement are shown by the colored bands.

With one year of data taking, and assuming the expected rate of  $\nu_\tau$  appearance from standard three-flavor oscillations, the precision of the  $\nu_\tau$  normalization measurement should be better than 10%, as shown in Fig. 31. The current analysis has a  $\mathcal{O}(1\%)$  bias in the determination of the true  $\nu_\tau$  normalization that shrinks with time and is much smaller than the uncertainty in the parameter determination.

Alternatively, instead of assuming the  $\nu_\tau$  normalization is the one given by three-flavor oscillations, we can estimate the level at which we can distinguish different true values of the  $\nu_\tau$  normalization from the three-flavor oscillation prediction. As shown in Fig. 30, excluding standard  $\nu_\tau$  appearance in the case where there is none can be reached with a little bit more than one month of livetime. With a year of data the true  $\nu_\tau$  normalizations can be distinguished at the  $5\sigma$  level for a true  $\nu_\tau$  normalization of 0.6, and at the  $3\sigma$  level for a true  $\nu_\tau$  normalization of 0.8, as shown in Fig. 32.

The expected median significances from Figs. 30 and 32 for distinguishing the case where

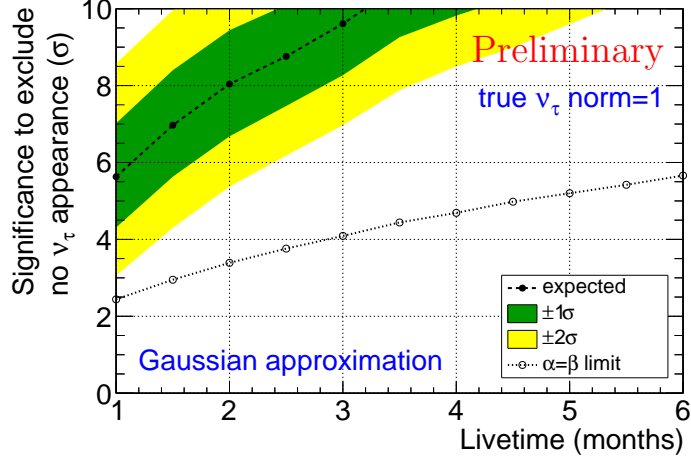


Figure 30: Significance to exclude no  $\nu_\tau$  appearance assuming the expected  $\nu_\tau$  appearance from the standard three-flavor  $\nu$  oscillation. The expected result along with the  $\pm 1\sigma$  and  $\pm 2\sigma$  regions are shown, as well as the significance at which the type-I error ( $\alpha$ ), that is incorrectly rejecting a true hypothesis, has the same probability as the type-II error ( $\beta$ ), that is incorrectly accepting a false hypothesis.

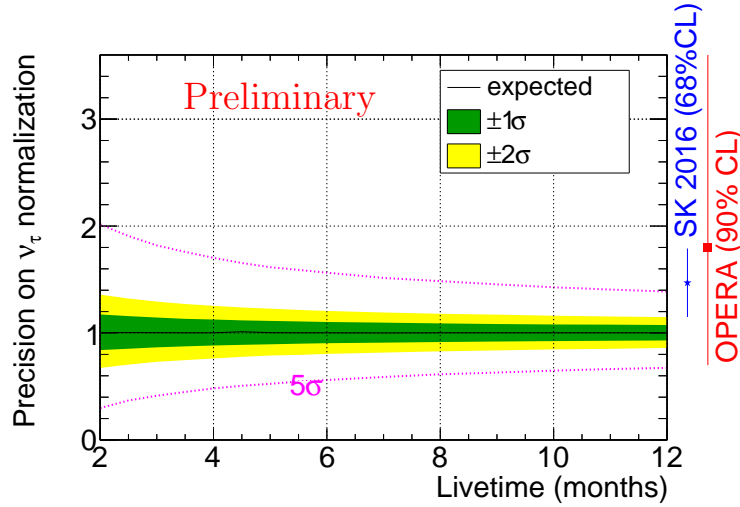


Figure 31: Precision with which the rate of  $\nu_\tau$  appearance can be measured, in terms of the PMNS expected rate, as a function of exposure (in months). The true value is assumed to be 1.0 (the standard expectation) for illustration. The expected  $\pm 1\sigma$  and  $\pm 2\sigma$  regions and  $\pm 5\sigma$  limits are shown, as well as measurements by Super-Kamiokande [64, 65] and OPERA [66].

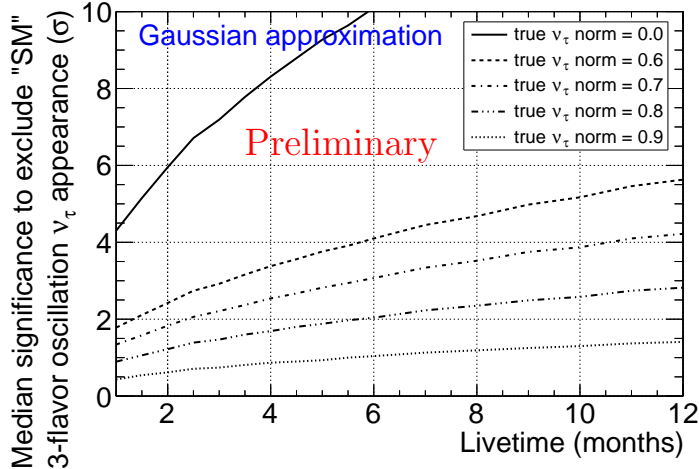


Figure 32: Significance to exclude the usual three-flavor  $\nu$  oscillation for different true  $\nu_\tau$  normalizations for the median case. For estimations above  $3\sigma$  a Gaussian approximation is used.

there is no  $\nu_\tau$  appearance are different because in each figure a different assumption is made. Each case is therefore defined by a different expected rate of events that will produce slightly different required livetimes to exclude the other case at the same significance.

### 3.5.5. Comparison to other measurements

Recently OPERA reported finding a 5<sup>th</sup>  $\nu_\tau$  candidate event [66] from a  $\nu_\mu$  beam produced at CERN, increasing their significance for having observed  $\nu_\tau$  appearance to  $5.1\sigma$ . Super-Kamiokande has also published evidence of  $\nu_\tau$  appearance at  $3.8\sigma$  [64] and, more recently, announced evidence at the  $4.6\sigma$  level [65], using atmospheric neutrinos. With these measurements it is clear that there is  $\nu_\tau$  appearance occurring in conjunction with  $\nu_\mu$  disappearance.

It is important to increase the precision on the determination of the rate of  $\nu_\tau$  production in order to verify the unitarity of the neutrino mixing matrix and to test for NSI. While OPERA may find additional events in the remaining portion of their data and Super-Kamiokande may update their results using additional years of data, the current precision will not increase significantly; OPERA has stopped taking data and Super-Kamiokande's newly announced result was based on data from 1996 until 2016 with an exposure of 22.5 kton over roughly 5 000 days while their published result was based on data from

1996 until 2008 with a 12-yr exposure of 22.5 kton over 2 806 days. Therefore by the time PINGU is expected to start taking data Super-Kamiokande is expected to have increased their sample size by about 50%.

### *3.5.6. Conclusion*

PINGU's dense instrumentation and the resulting improvement of the reconstruction quality for low-energy events will allow PINGU to measure  $\nu_\tau$  appearance with improved accuracy. We expect to be able to exclude the “no  $\nu_\tau$  appearance” scenario at  $5\sigma$  significance with 1 month of data, and have a better than 10% precision on the  $\nu_\tau$  appearance normalization after the first year of data. Also with the first year of data we would be able to distinguish a true  $\nu_\tau$  normalization below 0.6 at a level of  $5\sigma$ .

## 4. Other Neutrino–Based Analyses

In addition to neutrino oscillation measurements using atmospheric neutrinos, PINGU has the ability to make several other scientifically compelling measurements. These measurements may use other neutrino sources in addition to the atmosphere and are detailed below.

### *4.1. Neutrino Tomography*

#### *4.1.1. Motivation*

Seismological data based on primary (compressional) p-waves and secondary (shear) s-waves have been used in the construction of the preliminary reference Earth model (PREM) [43] that describes the Earth matter density profile. While the matter density is well known through these measurements, the chemical composition of the interior of the Earth has not yet been measured. Neutrino tomography provides the first, and possibly the only, way to directly probe the Earth’s composition. By exploiting the dependence of neutrino oscillation probabilities on the electron density, PINGU, with its large atmospheric neutrino sample, could be the first experiment to be able to use neutrino tomography to begin distinguishing between proposed Earth-core composition models. Systematic uncertainties associated with the unknown true values of oscillation parameters are reduced by the observation of neutrinos that do not pass through the Earth’s core.

#### *4.1.2. Introduction and Earth Composition Models*

The Earth’s geomagnetic field was discovered at the end of 16th century [67]. Since then many models have been proposed to explain its origin. The dynamo model is the leading explanation of the field. It implies that the Earth contains a conducting fluid that is convecting [68]. A measurement of the composition of the Earth’s interior may help resolve the longstanding mystery of the origin of the geomagnetic field and further advance our understanding of the Earth.

Direct sampling of the interior of the Earth is limited by the reach of drills, which have only penetrated down to a depth of about 12 km [69]. Coarse information about deeper regions of the Earth can be obtained by eruption entrainment sampling [70], and the interior of the Earth has mainly been studied using seismic waves.

The inner Earth consists of two distinct parts: “silicate Earth”, and the core (see Fig. 13 for a schematic view). The silicate Earth consists of the crust and lower and upper mantles while the core is divided into the outer and inner regions. Boundaries between these layers are known with uncertainties on their positions smaller than 10 km [71]. The outer core was determined to be liquid from the absence of detected s-waves [72]. The PREM matter density structure was developed by combining astronomic-geodetic parameters, free oscillation frequencies, and seismic wave velocity [43]. The uncertainty on the average density of the lower mantle is estimated to be less than 0.7% [73], and that of the inner core as less than 0.5% [74]. Interestingly, mantle densities could also be measured with PINGU itself with a few percent precision [75].

It is believed that the bulk chemical composition of the Earth is the same as the composition of the “Ivuna” type carbonaceous chondritic meteorites (CI) [76]. The crust and upper mantle contain less iron, nickel, and sulfur than CI chondrites, implying the core region should contain more iron and nickel. By comparing high pressure experimental data and seismological velocity profiles, the inner and outer core are presumed to be mostly made of iron with some additional light elements [77].

The outer core is assumed to have a combination of thermal and compositional convection. Without the compositional convection, it is difficult to maintain the geo-dynamo [78]. Measuring the composition of the Earth’s core is therefore expected to lead to understanding the geo-dynamo model. In addition, scenarios of the Earth’s formation depend on the core composition models [79]. There is little doubt in the interpretation that the outer core is composed of liquid iron alloyed with nickel and some light elements, but the content and type of the light elements are still uncertain because of the limitations of the observational data. From high-pressure experimental constraints, possible candidates for the light elements are hydrogen, carbon, oxygen, silicon, and sulfur [80]. While, among these, hydrogen is the least understood in the context of Earth’s chemical composition, liquid iron alloyed with 1% hydrogen by weight could also explain the outer core density [81]. A variety of other outer core compositions have been proposed [71, 82, 83].

#### 4.1.3. Methodology

The Earth composition study with PINGU is made feasible by the fact that neutrino oscillations depend on the electron density,  $N_e$  [84]. The electron density is related to the mass density via the factor  $Y = Z/A$  (the proton to nucleon ratio), weighted by the relative elemental abundances. As an example iron has a value of  $Y = 0.466$ , while lighter elements have values closer to  $Y = 0.5$ , and hydrogen has a very distinctive value

of  $Y = 1.0$ .

The effect of a different core composition (or electron density) on the survival probability for muon-type neutrinos is illustrated in Fig. 33, with the “distinguishability metric” plot included for these cases. Modifications are visible for the up-going neutrino events that cross the inner or outer core, corresponding to zenith angles greater than  $\theta_\nu = 168^\circ$  ( $\cos \theta_\nu = -0.98$ ) for the inner core while the outer core extends from the inner core to  $\theta_\nu = 147^\circ$  ( $\cos \theta_\nu = -0.84$ ). The most relevant energy range is between about 2 GeV and 6 GeV. Good neutrino energy and zenith angle resolutions in this energy range are essential for the success of a neutrino tomography measurement.

#### 4.1.4. Analysis Method

The tomography analysis presented here uses the same atmospheric neutrino sample discussed in Sec. 3, leading to approximately 30 000 upward-going  $\nu_\mu$  CC events per year. Roughly 50% of these will have energies between 2 and 6 GeV. The reconstruction and PID (see Sec. 2.4) proceed in the same manner as previously discussed.

For the sensitivity calculation, a likelihood ratio test as described in Sec. 3 is performed for different core composition models. For each bin, the likelihood for a given core composition is calculated. Systematic uncertainties are treated as nuisance parameters in the fitting procedure. These uncertainties include the atmospheric spectral index, the muon-to-electron neutrino flux ratio, the neutrino-to-antineutrino flux ratio, an overall rate normalization, the energy scale, and the neutrino oscillation parameters  $\Delta m_{31}^2$ ,  $\theta_{23}$ , and  $\theta_{13}$ . Priors are given in Table 3. The likelihood is computed for a given  $Z/A$  ratio with respect to the Asimov dataset obtained for a pure-iron outer core.

Scans over the electron density of the Earth’s outer core, i.e. the proton-to-nucleon ratio  $Z/A$  can be seen in Fig. 34. The top panel assumes normal ordering to be true and ten years of livetime with  $\theta_{23}$  in the first octant. The bottom panel shows how the sensitivity changes for  $\theta_{23}$  in the second octant and with more livetime and improved reconstruction. The significance of excluding a given  $Z/A$  is shown when the true value of  $Z/A=0.4656$  corresponds to that of pure iron. The top axis shows the equivalent hydrogen content by weight in an iron core. For each point, the nuisance parameters have been fit so that the likelihood is maximal. From a comparison of dashed and solid lines, one can see that the systematic uncertainties reduce the significances of the measurement by roughly 20%. For the baseline reconstruction, and if  $\theta_{23}$  lies in the second octant, a true electron density of  $Z/A=0.4656$  for the outer Earth core can be constrained with an accuracy of  $\pm 13\%$  ( $1\sigma$ )

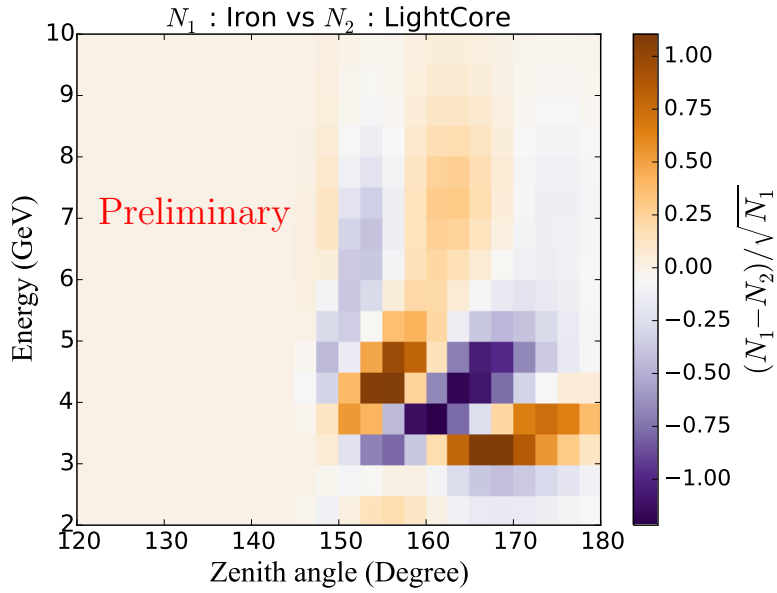
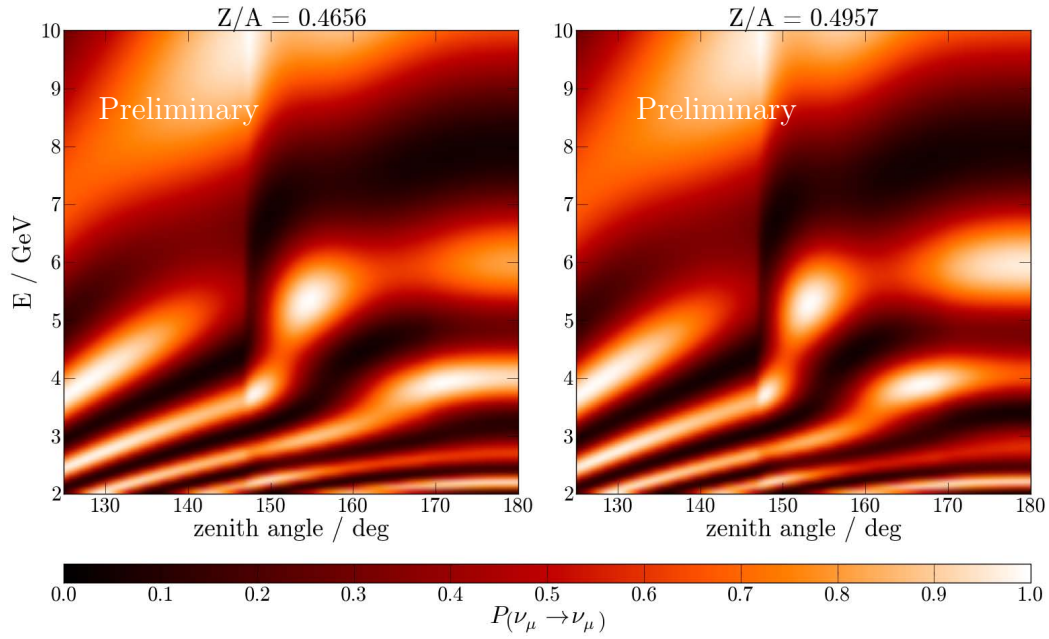


Figure 33: (Top) The impact of a changed core composition on the muon-neutrino survival probabilities is demonstrated by comparing the left figure (pure iron core,  $Z/A = 0.4656$ ) with the right (iron mixed with lighter elements,  $Z/A = 0.4957$ ). (Bottom) “Distinguishability metric” plot showing the ratio between the expected difference in number of events and their statistical uncertainty assuming one year of data with 40% electron neutrino contamination. Events are binned by their true neutrino energy and direction.

after ten years of livetime, assuming statistical uncertainties only.

The systematic uncertainties dominating this measurement are those on the neutrino-to-antineutrino ratio, the overall rate normalization, and the energy scale. In the studies presented in sections 3.2 and 3.3, the energy scale uncertainty was reduced from 10% to 0.5% and a new systematic covering the direct optical efficiency was added with a 10% uncertainty. In both cases the new systematics improved the precision of the measurements. While this verification has not yet been studied in the context of the presented measurement, it is expected the effect of changing these systematics to either have no impact on the result or increase the significance to distinguish between models. No significant dependence on the inner core composition is observed.

Improvements in the event reconstruction performance are expected over the lifetime of the detector. Figure 34 shows the impact of further improved reconstructions, simultaneously improving the energy and angular resolution by 10% and 20%, respectively.

Figure 35 shows the exclusion level vs. time for a pure iron core ( $Z/A = 0.4656$ ) relative to other compositions (the top panel of Fig. 34 corresponds to a vertical slice of Fig. 35 at ten years). A mantle-like pyrolite core ( $Z/A = 0.4957$ ) can be distinguished with more than 68% confidence with systematic uncertainties in 10 years or 40 megaton-years (as the average effective mass of PINGU is  $\sim 4$  megaton in the energy range 2 GeV to 6 GeV) assuming normal neutrino mass ordering and  $\theta_{23}$  in the first octant. Lead could be excluded at 80% confidence after 8 years. The right axis of Fig. 35 shows that the hydrogen content in the outer core could be constrained with 68% confidence to less than 5% by weight after 10 years.

The tomography measurement strongly depends on the neutrino mass ordering. If the ordering is inverted, the possibility to exclude one model with respect to another drops by 50%. Under the normal ordering, resonant matter oscillations [10, 11, 12, 13] occur only for neutrinos; under the inverted ordering, they occur only for antineutrinos. In the energy range of interest, the cross section for the interaction of neutrinos with matter is roughly twice that of antineutrinos [85]. This decreases the relative number of signal events in the inverted ordering case, leading to a drop in significance. The octant of  $\theta_{23}$  also has a significant impact on the measurement where assuming  $\theta_{23}$  is in the second octant improves sensitivities by about 25%.

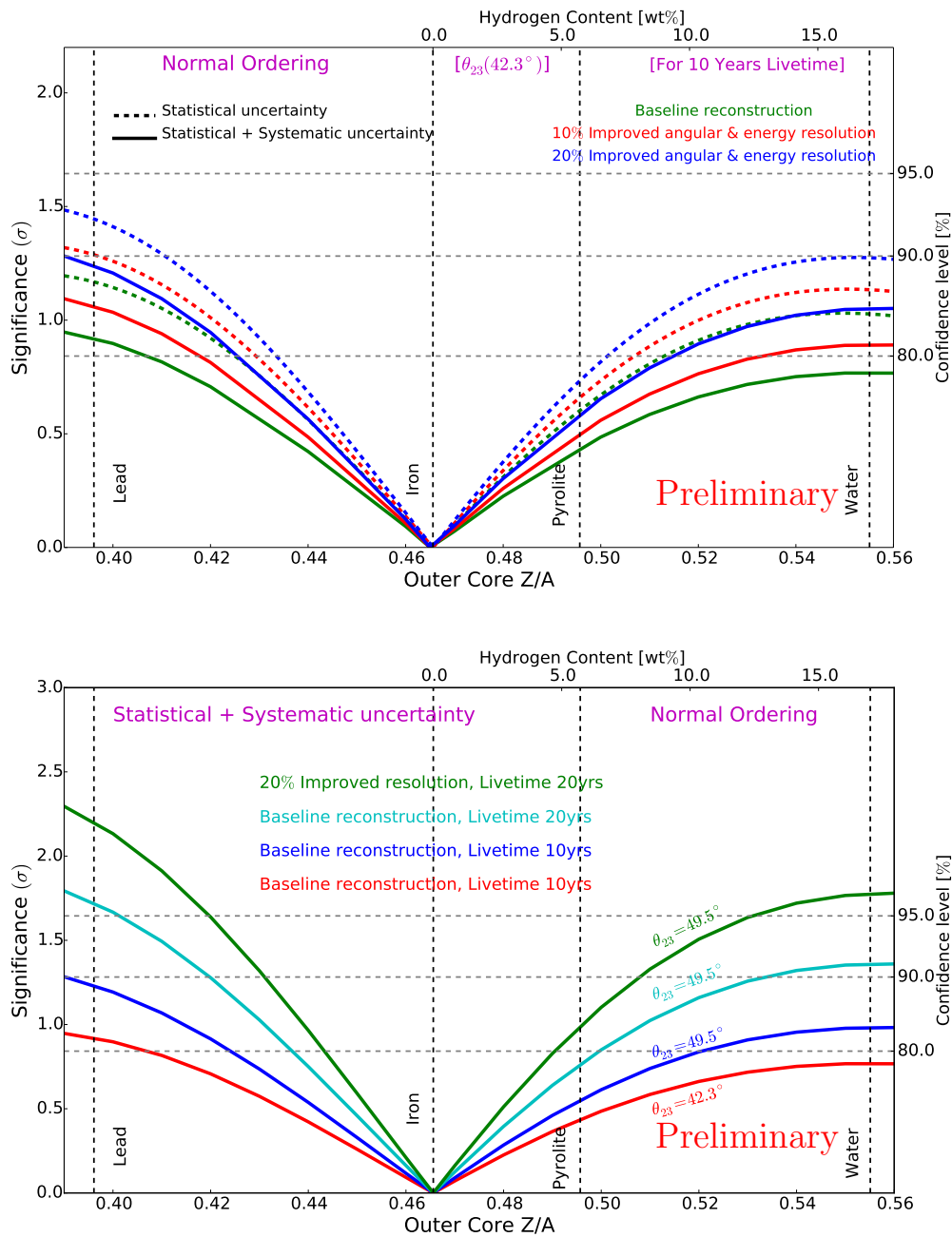


Figure 34: Significances obtained from the mean of  $10^5$  likelihood scans over proton to nucleon ratio  $Z/A$  of the inner and outer Earth core with 10 years of PINGU data. The input value assuming a pure iron Earth core is reproduced correctly. The bottom plot shows how sensitivity improves for  $\theta_{23}$  in the second octant, with more livetime, and with improved reconstructions.

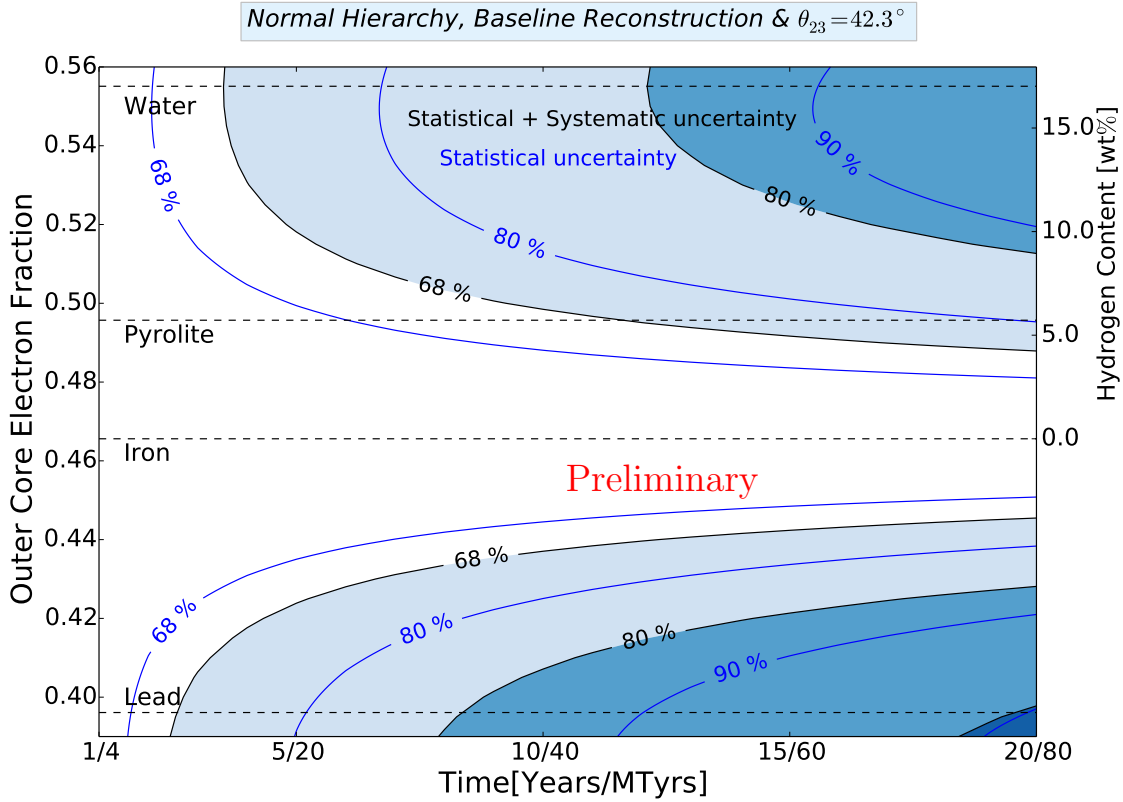


Figure 35: Contour plot of exclusion levels with respect to a pure iron core as function of livetime using the LLR method.

#### 4.1.5. Conclusions

Resonant neutrino oscillations inside the Earth (driven by the relatively large magnitude of the  $\theta_{13}$  mixing angle) can be used to probe the composition of the Earth's core. Since these oscillations are sensitive to the electron density, with good knowledge of the mass density from seismic measurements one can derive the proton-to-nucleon ratio  $Z/A$  inside the Earth. In particular, the composition of the liquid outer core can be tested. PINGU could be the first experiment able to verify the Earth has an iron-like core. In this measurement, knowledge of the neutrino mass ordering is critical for understanding the composition of the core. However, measurement of the mass ordering is not strongly dependent on the core composition since the ordering measurement also uses neutrinos that cross only the mantle. These neutrinos can be used to fix the oscillation parameters

and minimize the induced systematics. The uncertainty on  $\theta_{13}$  is small enough to have negligible impact on the Earth model determination. PINGU thus offers the best and possibly only way to test geophysical models of the composition of the Earth's core by measuring the matter-induced neutrino oscillations of atmospheric neutrinos.

Further improvements to the Earth tomography analysis are possible with an improved event selection, potentially based on high-level reconstructions described in Sec. 2.4. These improvements would yield higher statistics in the region of interest, and allow a better identification of matter-induced oscillation effects by adding inelasticity measurements to the likelihood fit.

## 4.2. *Supernova Neutrinos*

As some stars approach the end of their life, they collapse to a neutron star. The majority of the energy radiated away during this collapse is in the form of neutrinos of all flavors, emitted in a span of tens of seconds. These neutrinos have energies much lower than those discussed in the previous sections; between 10 MeV and 30 MeV instead of  $\mathcal{O}(1 \text{ GeV})$ .

Due to the significantly lower energy of the neutrinos from supernovae, the detection method is different from those detailed previously. Whereas the atmospheric neutrino analyses use the light produced by hadrons and leptons following charged or neutral current interactions, supernova neutrinos are detected after an inverse beta decay interaction. The positron produced in this interaction carries away the majority of the energy from the neutrino, and it produces Cherenkov light along a short track (roughly 0.6 cm/MeV and 325 photons/cm [86]).

The lower energy of the neutrinos arriving in the detector from a supernova collapse also rules out reconstructing the initial neutrino direction in IceCube. As such, studies of supernova neutrinos search for a short-term, coherent increase in the rate of signals in all the DOMs in the detector. The noise rates of individual DOMs are roughly 500 Hz, which can be cut approximately in half by applying an artificial deadtime, eliminating most of the correlated noise observed at low temperatures.

### 4.2.1. *IceCube Sensitivity to Supernova Neutrino Bursts*

If a core-collapse supernova explosion were to happen in our galaxy, IceCube would provide the world's most precise neutrino rate determination, with a significance larger than 20 standard deviations for distances up to 30 kpc [86]. The supernova detection significance deteriorates significantly at the positions of the Magellanic Clouds and beyond because the intrinsic DOM noise becomes dominant while the supernova neutrino fluence drops with the inverse distance squared. Furthermore, individual neutrino interactions are not detected, meaning that the energy and type cannot be determined for each neutrino. However, it has been shown [87] that the average neutrino energy can in principle be determined to better than 30% accuracy for distances less than 10 kpc. Recently, the IceCube data acquisition system has been upgraded to store the timestamps of all hits. With this information at hand, one can deduce the neutrino energy from a comparison of the rate at which a single neutrino interaction deposits light in just one module vs. two (or more) neighboring modules. In IceCube, however, the coincidence rates (with a suitably tight time window) are only on the order of a few per thousand.

Due to the increased sensor density both vertically and horizontally, the coincidence rates in PINGU will be much higher, of order 1%. This will lead to a much improved determination of the average neutrino energies, particularly at larger distances, and will allow the extraction of information concerning the neutrino energy spectral shape. In addition, some improvement in the detection significance for supernova explosions in dwarf galaxies orbiting our Milky Way may be achieved by employing coincidences in a short interval,  $\Delta t$ . Note that the significance for a supernova detection with  $n_k$  signal events and optical module noise  $r$  roughly scales like  $n_k \cdot (\Delta t \cdot r)^{-k/2}$  for a  $k$ -fold coincidence.

#### *4.2.2. Monte Carlo Simulation*

Two simulations were conducted to independently characterize the sensitivity of the PINGU detector. In the first simulation, the effective volume is evaluated for various coincidence conditions for each detector configuration, namely IceCube, DeepCore, and PINGU with an older, truncated geometry of 20 strings of 60 standard IceCube DOMs operating with  $4\pi$  sensitivity, leading to a conservative result. In the second simulation, the significance of the collective rate deviation is determined with respect to supernova distance for the IceCube detector in comparison to its subsequent generation extensions, DeepCore and PINGU. This simulation considers the  $40 \times 96$  and  $20 \times 192$  PINGU geometries. For supernova neutrinos, we expect that a  $26 \times 192$  PINGU geometry will provide minor improvements over the  $40 \times 96$  geometry.

The first simulation was conducted and cross checked with two independent GEANT4-based [19] codes for various detector configurations (IceCube and DeepCore, plus the PINGU  $20 \times 192$  geometry). The light yield is found to roughly scale with the absorption length in the ice. Uncertainties connected to varying the optical properties of the ice as a function of depth were assessed.

Since it is important to reject atmospheric muons when applying tight coincidence criteria, atmospheric muon simulations were also produced. These simulations were generated following the Gaisser flux model [88], to which a simple and efficient muon rejection algorithm was applied. A second atmospheric muon background set was simulated as a cross check, using standard IceCube simulation tools and the CORSIKA air shower generator [89]. These studies demonstrated that the distance reach and average energy determination are not strongly affected by the presence of the remaining atmospheric muon background. Some improvements to these results should be possible by using the realistic description of the detector, particularly by including the outer detector layers that act as a veto.

The detector sensitivity can be characterized by the effective volume for positrons per optical module  $V_{\text{eff}}(e^+) = N_{\text{detected}}/n(e^+)$ , where  $N_{\text{detected}}$  is the number of detected hits in each optical module for a given coincidence condition. The energy-dependent density of positrons from neutrino interactions in the ice is denoted by  $n(e^+)$ . Table 8 summarizes these effective volumes, assuming an average neutrino energy  $\langle E_{\bar{\nu}_e} \rangle = 12.6$  MeV. The numbers are provided for IceCube, DeepCore and the truncated  $20 \times 60$  PINGU geometry, imposing various coincidence criteria. Clearly, PINGU provides substantially larger coincidence probabilities than IceCube.

Detector	single hit	nearest neighbor	triple coincidence
IceCube	583 m <sup>3</sup>	0.6 m <sup>3</sup>	0.0002 m <sup>3</sup>
DeepCore	767 m <sup>3</sup>	2.7 m <sup>3</sup>	0.03 m <sup>3</sup>
PINGU ( $20 \times 60$ )	912 m <sup>3</sup>	4.4 m <sup>3</sup>	0.11 m <sup>3</sup>

Table 8: Effective volumes for positrons  $V_{\text{eff}}(e^+)$  per optical module for various coincidence conditions in IceCube, DeepCore and the truncated PINGU  $20 \times 60$  geometry, assuming  $\langle E_{\bar{\nu}_e} \rangle = 12.6$  MeV.

In the second study, low energy supernova neutrinos were injected in each detector geometry (IceCube, DeepCore, and the  $40 \times 96$  PINGU geometry) with levels responding to an O-Ne-Mg,  $8.8M_{\odot}$  supernova [90] at 10 kpc. The collective hit rate throughout the entire detector is compared to the expected non-Poissonian noise levels, generated with the detector noise model. The significance, calculated as the collective rate excess per DOM,  $\Delta\mu$ , divided by its measured uncertainty  $\sigma_{\Delta\mu}$ , is approximately proportional to the square root of the total number of optical modules within the detector (see Fig. 36). For statistically independent DOM rates, it should be distributed according to a Gaussian with unit width<sup>4</sup>, such that its value corresponds to the number of standard deviations from the null hypothesis of no signal.

#### 4.2.3. Determination of the average neutrino energy

The methods described above search for supernovae by examining the collective hit rate within the detector. This method provides a large target but very little information is obtained from the events. A second method considers coincident hits from events occurring very close to the strings [91]. This method reduces the effective volume of the

---

<sup>4</sup>In practice, statistically correlated hits introduced by atmospheric muons cannot be fully removed, leading to a widening of the distribution.

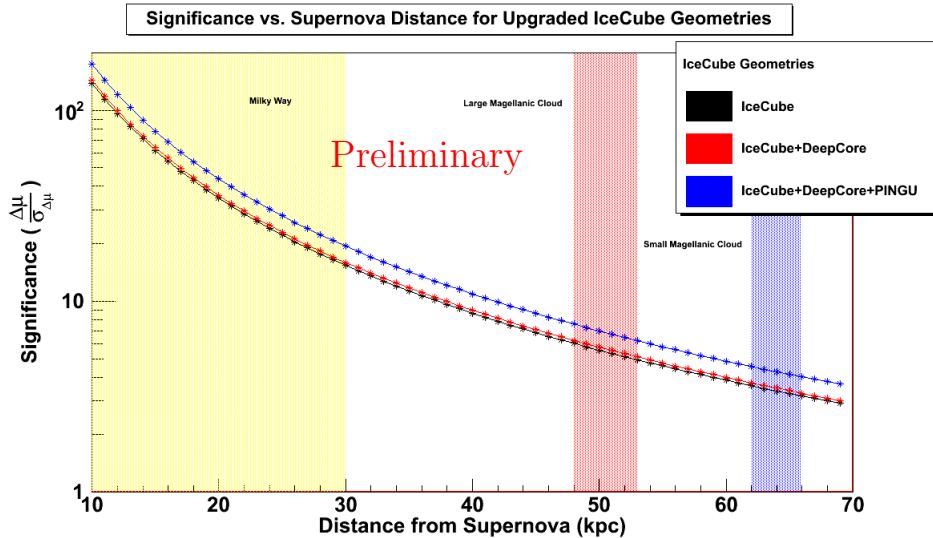


Figure 36: Significance as a function of distance for an O-Ne-Mg,  $8.8M_{\odot}$  supernova [90]. The sensitivity of the  $40 \times 96$  PINGU geometry is compared to the standard IceCube geometries. For reference, the positions of the Milky Way and the Magellanic Clouds are indicated. Note that a trial factor is not included.

detector, but may provide more information about the events themselves, and the average neutrino energy could be determined in IceCube with MeV resolution for a supernova at 10 kpc. The energy dependence becomes stronger when the optical modules are closer together yielding a higher rate of coincidences. It has previously been demonstrated that sub-MeV resolutions for dense core detectors [87, 92] can be achieved.

The relative precision of the energy determination is depicted in Fig. 37 as a function of distance and average energy. To be most conservative, flux, energy, and spectral shape were taken from the collapse of an O-Ne-Mg  $8.8M_{\odot}$  progenitor star, the lowest mass progenitor known to undergo a core collapse. We also assume the conservative case of the truncated ( $20 \times 60$ ) PINGU geometry.

#### 4.2.4. Providing a measure of the spectral shape

Different coincident hit modes (e.g. multiple hits on single DOMs or between neighbors) show distinct differences in the neutrino energy dependence [93]. These can be used to characterize the spectral shape of the neutrino emission, in addition to the determination

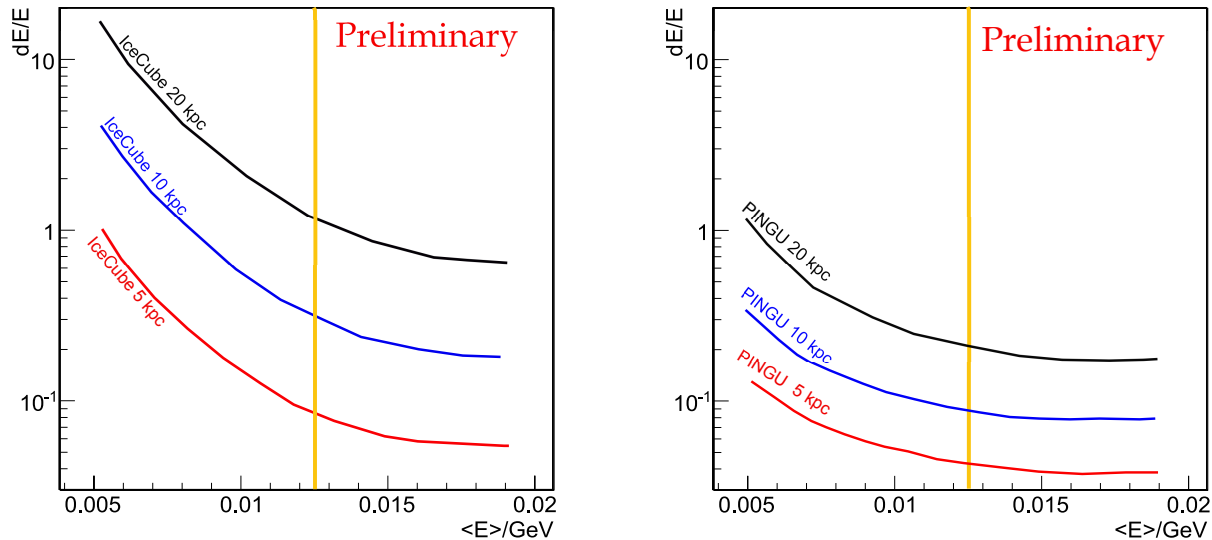


Figure 37: Comparison of the precision on the determination of the average neutrino energy in (left) IceCube and (right) the truncated PINGU  $20 \times 60$  geometry for a supernova at 20 (black), 10 (blue) and 5 (red) kpc distance.

of the average energy. Assuming a neutrino spectral shape parametrized with three parameters (the luminosity  $L_\nu$ , the average neutrino energy  $\langle E_{\bar{\nu}_e} \rangle$  and a shape parameter  $\alpha$  [94]) and using single, double and triple coincident hit modes in a  $\chi^2$  fit,  $\langle E_{\bar{\nu}_e} \rangle$  and  $\alpha$  can be extracted simultaneously.

A scan of the parameter space for a simulated supernova at 10 kpc distance is shown in Fig. 38 as function of average energy and  $\alpha$  for IceCube and PINGU. The color scale indicates the  $\log_{10}(\chi^2)$  value for the parameter values tested. Note that  $\alpha$  and  $\langle E_{\bar{\nu}_e} \rangle$  are almost degenerate. The increased rates at higher hit modes in PINGU lead to a substantially smaller uncertainty on the parameters.

#### 4.2.5. Conclusions and outlook

PINGU will enhance IceCube's ability to detect and interpret very low energy ( $E_\nu \sim 15$  MeV) neutrino bursts from supernova explosions. Taking IceCube and DeepCore together with the  $40 \times 96$  PINGU geometry, the galactic supernova sensitivity will increase by approximately  $\sqrt{2}$  when compared to IceCube alone. The greatest benefit comes from the improved determination of the average supernova neutrino energy provided by

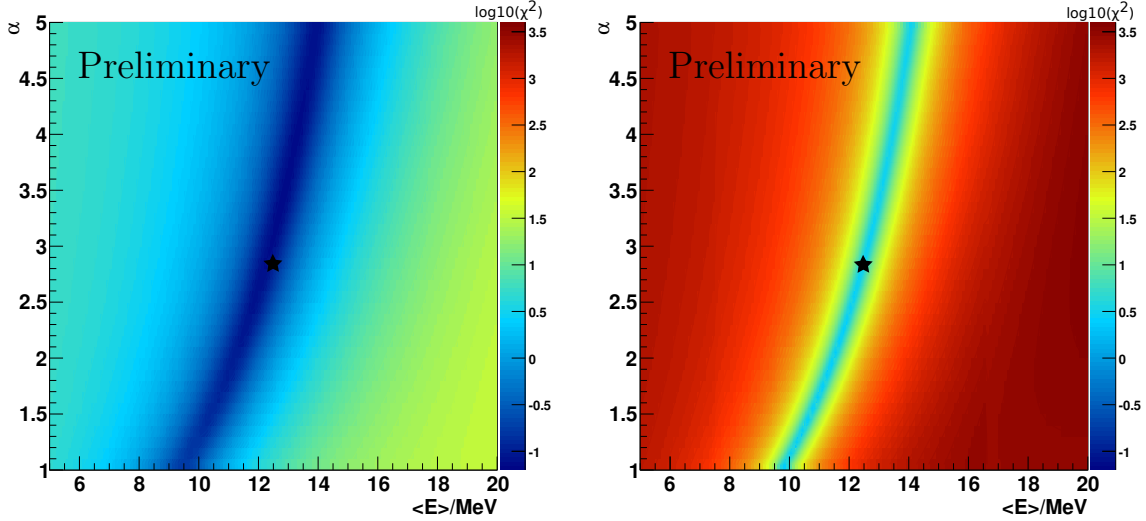


Figure 38: Combined determination of the average neutrino energy and the spectral shape parameter  $\alpha$  for IceCube (left) and PINGU (right) using a  $\chi^2$  method. The input value ( $\langle E_{\bar{\nu}_e} \rangle = 12.6 \text{ MeV}$ ,  $\alpha = 2.84$ ) is denoted by a star.

PINGU’s closer module spacing. The average energy will also be measured roughly a factor of five better than with IceCube. As shown with the truncated  $20 \times 60$  geometry, PINGU would also allow us to determine the spectral shape, once the average neutrino energy is known. A PINGU geometry with significant increase in the module density will improve this result.

Lowering the PMT noise rates will be an important ingredient for the detection of supernovae in neighboring galaxies in an envisaged low energy, multi-megaton future detector succeeding PINGU. Very low noise rates could be achieved by collecting light with wavelength shifters read out with highly sensitive PMTs with a small cathode area. Extending the accepted wavelength range down to 200 nm by using fused quartz windows would increase the detection efficiency by a factor of approximately 2.7 (weighted for the optical module sensitivity and the  $1/\lambda^2$  dependence of the Cherenkov photon flux). The PINGU deployment may allow us to test these technical improvements by deploying prototype modules as discussed in Sec. 5.4.3.

### 4.3. Dark Matter

#### 4.3.1. Motivation

Observational evidence indicating the existence of dark matter can be obtained at a wide variety of scales, from the motion of stars to imprints on the cosmic microwave background (CMB) [95, 96, 97]. Many dark matter candidates could be indirectly detected through the observation of particles created in dark matter self-annihilations. The search for neutrinos created as part of these annihilations is of particular interest, since neutrinos can be used to probe the properties of the dark matter, including its self-annihilation and nucleon scattering cross-sections. One of the attractive candidates for this dark matter is the Weakly Interacting Massive Particle (WIMP, denoted by  $\chi$ ). This candidate arises naturally in many theories beyond the Standard Model of Particle Physics developed to explain the origin of electroweak symmetry breaking and solve the gauge hierarchy problem [97]. Although we will use the terms “WIMP” and “dark matter candidate” interchangeably in the rest of the section, the reader should note that there are other scenarios that provide viable non-WIMP dark matter candidates [98, 99] with similar signatures in neutrino telescopes.

Given that they interact gravitationally, WIMPs could be captured in the Sun (after scattering off nuclei), accumulate, and self-annihilate producing a flux of neutrinos. Under the assumption of equilibrium between WIMP capture rate ( $\Gamma_C$ ) and annihilation rate ( $\Gamma_A$ ) in the Sun,  $\Gamma_A$  depends only on the total scattering cross-section. Since the Sun is primarily a proton target, strong constraints can be derived on the spin-dependent WIMP-proton scattering cross-section ( $\sigma_{p,SD}$ ) by measuring a neutrino flux from the Sun. IceCube has set the world’s best limits on this process for WIMP masses above 50 GeV [100].

Searches for dark matter annihilation signals in the Milky Way can be used to test the thermal average of the WIMP annihilation rate, which is the product of the annihilation cross-section and the relative velocity of WIMPs averaged over the velocity distribution,  $\langle\sigma_{Av}\rangle$ . IceCube has set tight constraints on  $\langle\sigma_{Av}\rangle$  with searches for signals from the Galactic halo [101], Galactic Center [102], and dwarf spheroidal galaxies and clusters of galaxies [103, 104]. These results improved upon theoretical predictions [105, 106].

The lowered energy threshold of PINGU will allow the enhancement of current searches to test WIMP masses that are below the IceCube detection threshold. WIMP scenarios motivated by DAMA’s annual modulation signal [107] and isospin-violating scenarios [108] would also be testable.

### 4.3.2. Limit Calculation

The primary WIMP annihilation spectrum is model-dependent, hence we consider two extreme benchmark scenarios, where WIMPs annihilate exclusively to  $\tau^+\tau^-$  and  $b\bar{b}$ . The first case results in a “hard” neutrino spectrum, while the second case leads to a “soft” spectrum with lower average neutrino energy. One can expect that a general model with a mix of various annihilation channels will be bracketed by these two extrema.

### 4.3.3. Experience from DeepCore

The most recent IceCube Solar WIMP analysis [100] searched for signal neutrinos originating from potential WIMP masses ranging from 20 GeV to 5 TeV. Within this mass-range, signal events can have very different event topologies in the detector. To accommodate all expected event topologies within one single analysis, the full dataset is split into three independent, non-overlapping event selections that were later combined. The first division is into two seasonal data streams, “summer” and “winter”, when the Sun is above and below the horizon at the South Pole, respectively. The winter dataset is then further divided into a low-energy and high-energy sample. During the summer period, downward-going events are selected that interact inside DeepCore to reduce the atmospheric muon background. The winter high-energy event selection has no particular track-containment requirement, selecting upward-going muon tracks. The low-energy counterpart is focused on upward-going starting or fully-contained neutrino-induced muon tracks inside DeepCore.

The inclusion of DeepCore thus allowed the search to be extended to the austral summer when the Sun is above the horizon and expanded the WIMP mass reach from 50 GeV to 20 GeV, which was not accessible to previous IceCube searches [100]. With its lower energy threshold, PINGU will allow further extension to even lower WIMP masses.

### 4.3.4. Solar WIMPs

Building on the experience gained with DeepCore analyses, we utilize the lowered energy detection threshold of PINGU to significantly improve the sensitivity for WIMP masses in the range between 5 and 50 GeV. We perform a straightforward event-based Monte Carlo (MC) study, using the  $26 \times 192$  PINGU geometry (see Table 1). The datasets are identical to those used in the atmospheric neutrino studies, described in Sec. 3.1.1. In contrast to previous IceCube WIMP searches where we relied solely on the track channel produced by

muon-type neutrino CC interactions, here we include all neutrino flavor channels taking advantage of PINGU’s directional reconstruction capability for cascades. PINGU will also offer the potential to use energy spectral information [109], however to be conservative it is not used for the calculation of the sensitivity. This study focuses on the low-mass WIMP range and considers only events that interact inside the PINGU volume.

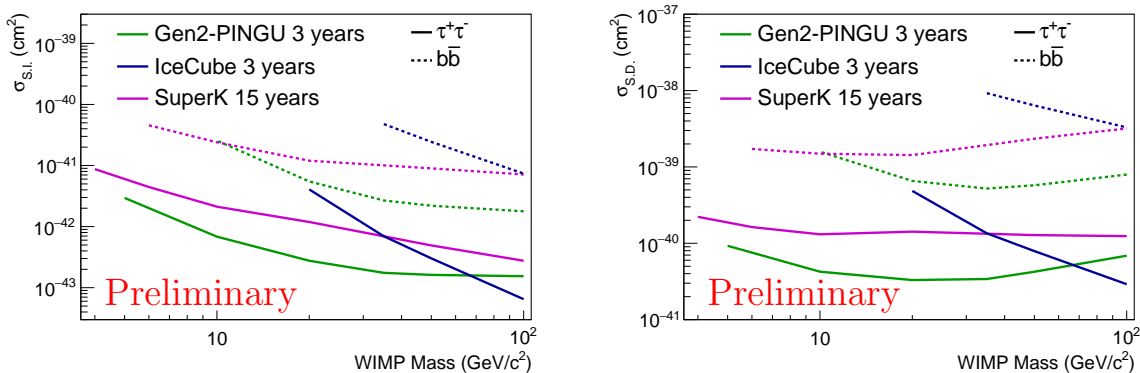


Figure 39: Sensitivity of the  $26 \times 192$  PINGU geometry to  $\sigma_{p,SI}$  (left figure) and  $\sigma_{p,SD}$  (right figure) for hard (solid lines) and soft (dashed lines) annihilation channels over a range of WIMP masses for a livetime of three years. The sensitivities are compared to the present IceCube limits [100] and limits from Super-K [110].

In accordance with the assumptions in Sec. 3.1.1, the down-going atmospheric muon background is assumed to be reduced to a negligibly small level, so that the background consists only of atmospheric muon neutrinos, which are generated following the flux model in [44]. The background at final analysis level from solar atmospheric neutrinos (those neutrinos generated in the atmosphere of the Sun) has previously been calculated to be of order one event in 317 days of data [100], and is consequently not included.

All signal simulations are made with DarkSUSY [111] and WimpSim [112], which describe the capture and annihilation of WIMPs inside the Sun and the consequent production and propagation of neutrinos from the core of the Sun to the detector, including three-flavor oscillations and matter effects. The expected neutrino signal flux from WIMP annihilations in the Sun is calculated by weighting the simulated neutrino events with the WIMP channel dependent neutrino spectra obtained from DarkSUSY. The zenith-dependent Sun position throughout the year is taken into account.

In the absence of signal, we estimate the 90% C.L. median upper limit  $\mu_s^{90}$  on the number

of signal events, given  $n_{\text{bg}}$ , following [113]. The limit on  $\mu_s^{90}$  is compared to  $n_s$ , which was calculated for  $\Gamma_A = 1 \text{ s}^{-1}$ , to derive the 90% C.L. limit on  $\Gamma_A$  for each WIMP model. Limits on  $\Gamma_A$  are then converted into limits on the spin-dependent ( $\sigma_{p,SD}$ ) and spin-independent ( $\sigma_{p,SI}$ ) WIMP-proton scattering cross-sections using the method from [112]. Figure 39 shows the calculated sensitivities as a function of WIMP mass for the soft (dashed) and hard (solid) annihilation channels obtained in this study. Additional ideas to further advance this search are discussed below.

#### 4.3.5. Galactic Center WIMPs

The expected differential neutrino flux from dark matter annihilations at the Galactic Center (GC) is proportional to the differential neutrino multiplicity per annihilation,  $\frac{dN_\nu}{dE}$ , and the line of sight integral over the square of the dark matter density at an angle of  $\psi$  from the GC,  $J(\psi)$  [105].

Searches for dark matter self-annihilations in the GC have been performed by IceCube using the NFW dark matter density profile [114] as a benchmark. The first GC analysis used the partially instrumented 40-string IceCube detector, probing  $\langle\sigma_A v\rangle$  for WIMP masses down to 100 GeV for several annihilation channels [102]. The two most recent GC analyses use the almost-completed IceCube detector (comprised of 79 strings), including DeepCore [115]. The sensitivity to  $\langle\sigma_A v\rangle$  in the GC was improved by up to four orders of magnitude for WIMP masses of 100 GeV ( $\tau^+\tau^-$ ) compared to the previous IceCube 40-string analysis. For PINGU an even lower energy threshold in the sub-10 GeV region is expected.

The GC, in the southern hemisphere at  $-29^\circ$  declination, is a challenging target for IceCube due to the high rate of down-going atmospheric muon background events. Veto methods against atmospheric muons [115], developed for the most recent IceCube 79-string GC analysis, significantly improved the sensitivities of analyses focused on low-energy events in the southern hemisphere. This turns IceCube into an efficient  $4\pi$  detector for indirect dark matter searches. These methods reject muon background while retaining low energy starting events inside a fiducial region, and make it feasible to achieve an event selection with an adequate neutrino purity for PINGU.

The sensitivity to  $\langle\sigma_A v\rangle$  for a GC analysis for WIMP masses between 5 and 30 GeV with PINGU is derived in a straightforward event-based MC analysis. This analysis is very similar to the study described in Sec. 4.3.4. In contrast to the solar WIMP analysis, where a perfectly efficient atmospheric muon veto was assumed, we use the

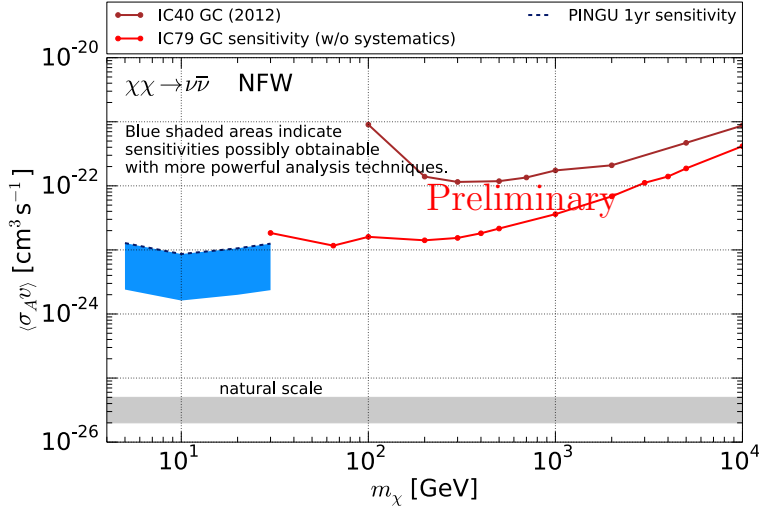


Figure 40: Sensitivity of the  $40 \times 96$  PINGU geometry to  $\langle\sigma_{Av}\rangle$  for direct annihilations into neutrinos over a range of WIMP masses for a live-time of one year. In light of the results presented in Sec. 3, for this signature we expect the  $40 \times 96$  and  $26 \times 192$  geometries to perform comparably well. The sensitivities are compared to limits from the IceCube 40-string analysis [102] and the sensitivities of the most recent IceCube 79-string GC analyses [115].

level of atmospheric muon background in the IceCube 79-string GC analysis (neutrino purity of 10% at final analysis level). This provides a conservative sensitivity estimate for PINGU. As for the solar WIMPs, we assume a live-time of one year, the  $40 \times 96$  PINGU detector geometry, and WIMP annihilations into neutrinos for this study. The resulting neutrino line spectrum yields approximately equal numbers of neutrinos and anti-neutrinos of all flavors after annihilation and neutrino oscillations. We consider muons produced through CC interactions as the only signal-detection channel for this conservative study (all-flavor prospects are discussed below). The number of signal and background events are calculated in a cone around the GC with a half-opening angle of  $10^\circ$  by weighting the simulated neutrino events according to the expected signal and atmospheric neutrino background flux respectively. The number of expected atmospheric muon background events ( $n_{\text{bg},\mu}$ ) are added to the atmospheric neutrino background ( $n_{\text{bg},\nu}$ ) with expected purity to determine the total background ( $n_{\text{bg}}$ ).

Using the statistical method as described in Sec. 4.3.4, we derive the 90% C.L. limit on  $\langle\sigma_{Av}\rangle$  for each WIMP model. Figure 40 shows the calculated sensitivities as a function of WIMP mass for the direct neutrino annihilation channel obtained in this study. The blue shaded areas indicate the expected range of sensitivity which could be obtained with

improved analysis techniques. Here, the expected range of sensitivities is driven by the remaining contribution of atmospheric muons to  $n_{\text{bg}}$ . Consequently, the most optimistic range of the blue shaded area assumes a more efficient atmospheric muon veto (perfect muon veto in the limit).

#### *4.3.6. Outlook and conclusions*

With one year of data, PINGU will be able to test direct detection claims of signals in the spin-independent region using dark matter annihilations in the Sun with hard neutrino spectra. The search for neutrinos from dark matter annihilations in the Sun will provide an independent method to test the longstanding anomalous annual modulation signal from DAMA/LIBRA [116, 107]. PINGU will also probe a region of parameter space that is intrinsically difficult to access in direct detection and has often resulted in excess events in searches, such as CoGeNT [117, 118], and the silicon data from CDMS-II [119] (CDMS-Si), as well as being able to test for dark matter annihilations near the Galactic Center.

The PINGU sensitivities discussed here are based on standard analysis methods utilized in IceCube, which have been kept intentionally simple. The results presented are therefore conservative, since PINGU offers the possibility of applying analysis methodologies that go beyond what we have used thus far in IceCube and DeepCore. These include a more precise definition of contained and partially-contained events, a better energy estimation from the measured track length allowing us to use spectral information, and particle identification, each of which can potentially confer greater sensitivity to dark matter.

## 5. Instrumentation

### 5.1. Introduction

In this section we present initial design considerations for PINGU sensors, down-hole cables and the drill. Experience gained with IceCube is leveraged in many instances to reduce design effort and mitigate risk. At this stage in the design process, several possible sensor ideas are being pursued. While simulations based on IceCube DOMs enable us to perform detector studies using existing IceCube Software infrastructure, improved sensor designs are expected to provide better performance at lower cost. We note the cable and drill designs are not strongly dependent on the sensor design.

### 5.2. Sensor Configuration

As described in Sec. 2.2, an initial detector design consists of 26 strings with 4992 sensors (PINGU Digital Optical Modules, or PDOMs) deployed within the DeepCore section of the IceCube volume (Fig. 4), at depths of 2150-2450 m. Following the design of the IceCube/DeepCore DOM [120], each module houses a 10-inch diameter high-quantum-efficiency PMT along with electronics to operate the PMT, send digitized signals to the surface, and perform calibration tasks.

### 5.3. Optical Sensor Design

Figure 41 shows a sketch of the PDOM, whose external components (glass sphere, cable penetrator, connector, etc.) are essentially identical to that of the IceCube DOM. Internal components (PMT, optical gel, etc.) would also be similar. IceCube experience demonstrates the robustness of the DOM design: of the 5160 IceCube DOMs deployed at depth, 98.4% were operable after this critical phase, with only 0.4% failing in subsequent long-term operation.

As shown in Fig. 42, the PDOM has a single “Main Board” containing electronics responsible for waveform digitization, control, and communication with the surface. Modules on this board reproduce most of the functionality of the original DOM Main Board, which cannot be identically recreated because several of the key parts are obsolete and unavailable. The new design is simplified and uses modern electronic technology to reduce cost,

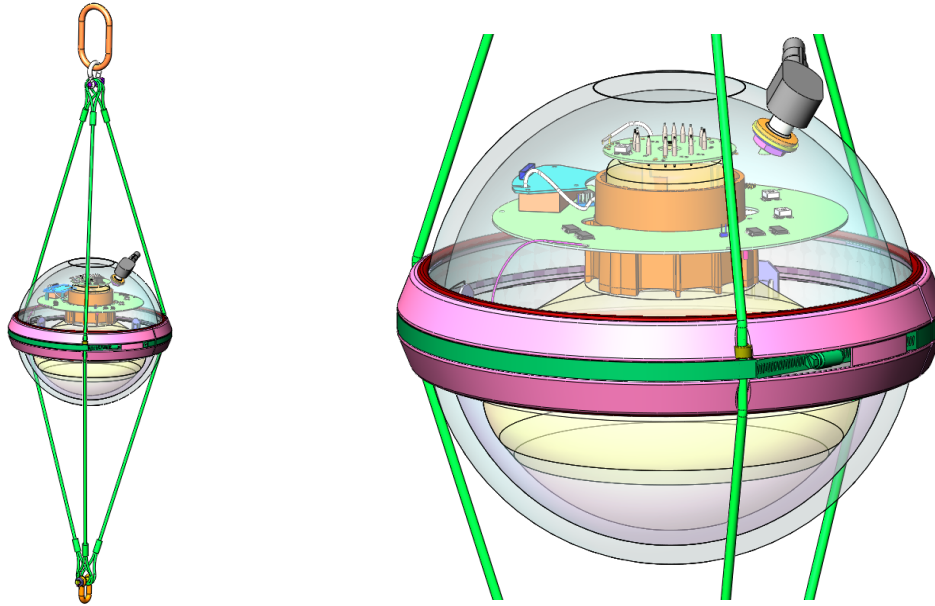


Figure 41: PINGU Digital Optical Module (PDOM).

power and board space. The previous multi-channel analog circuitry and custom digitizers are replaced by a single commercial ADC chip, with triggering and data processing handled by a more capable FPGA-based processor. All triggered waveforms are sent to the surface after suitable compression, allowing the new design to omit complex circuitry and *in situ* interconnections previously used to detect local coincidences between modules. As now found in IceCube modules, PMT waveforms will be digitized and deconvolved into individual photoelectron signals as needed; the new design will allow the deconvolution to be done before transmission of data to the surface.

Simplification of the Main Board's design will reduce component count, complexity, and overall cost. The previous design also included an analog delay board to allow for triggering the custom waveform digitizers after detection of a PMT pulse. This is not needed in the new design because the continuously-digitized PMT output is buffered in the FPGA while threshold crossings are detected digitally.

New PDOM firmware is being written as part of the Main Board redesign. The code preserves the original structure and communications protocols as much as possible, en-

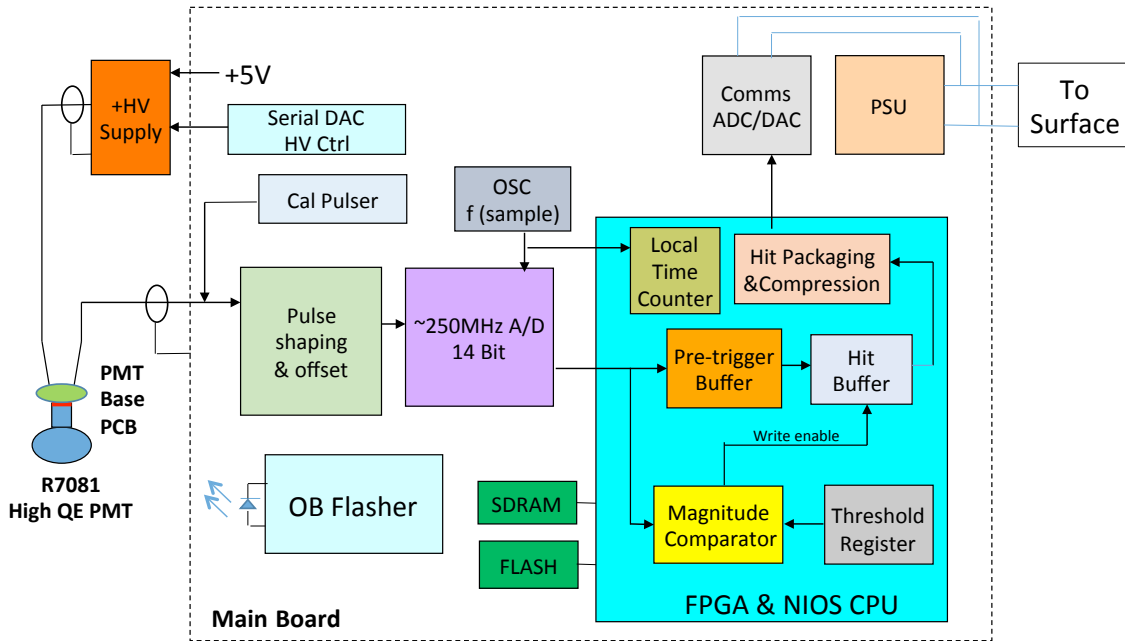


Figure 42: Functional block diagram for data acquisition in the PDOM, focusing on the Main Board.

ensuring a high level of compatibility with existing modules in the IceCube data acquisition system.

Figure 43 shows first-revision hardware for the PDOM high voltage system. The High Voltage Divider (HVD) board provides the high-voltage resistive bias and output signal coupling networks for the PMT, while the High Voltage Supply (HVS) board provides a simple analog interface for controlling and monitoring the system’s high voltage setting. The design utilizes a miniaturized high voltage DC-DC converter module, which is capable of supplying a maximum 2 kV output voltage while consuming only 125 mW under the HVD’s nominal 130 M $\Omega$  load. The total ripple injected into the PMT’s output signal by the high-voltage system has been measured as  $<10 \mu\text{V}$ . These new designs hew closely to the proven high-voltage design strategies of operating IceCube DOMs, while also employing recent advances in passive component technology to increase voltage de-ratings and improve manufacturability.

A prototype design for the PDOM’s on-board digitizer, called the Digitizing Daughter Card (DDC), is shown in Fig. 44. At the heart of the DDC is the Texas Instru-

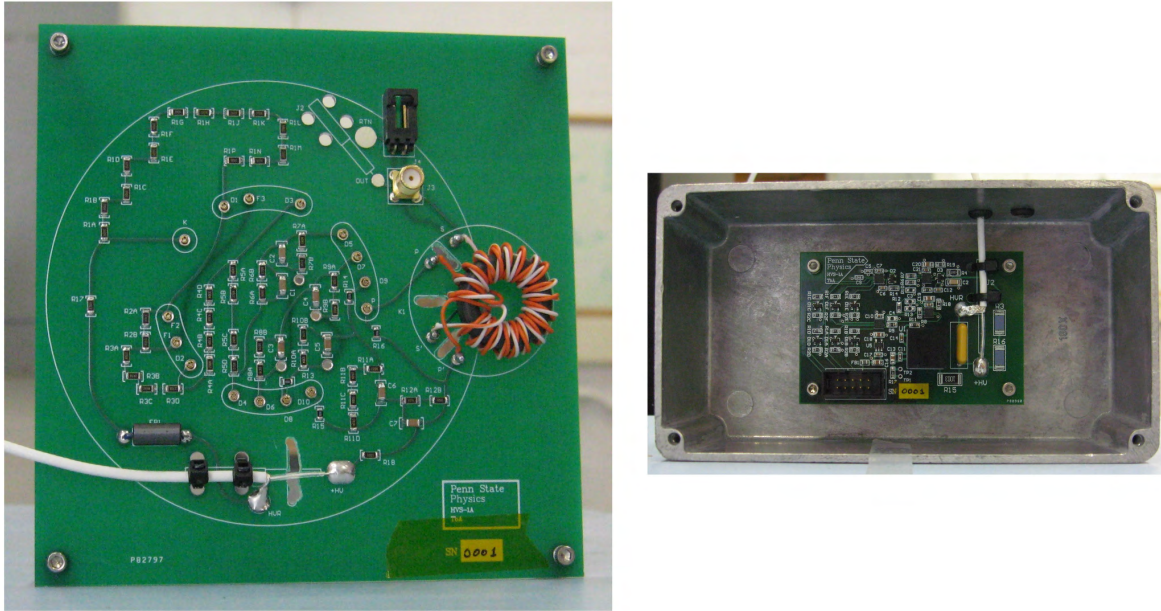


Figure 43: The prototype Gen2-DOM HVD (left) and HVS (right) boards.

ments ADS4149, a 14-bit, differential ADC, configured to sample at its maximum rate of 250 Msps. The DDC also employs an Analog Devices ADA4930 fully differential amplifier for the dual purposes of single-ended to differential signal conversion, and signal shaping for optimal identification of single photoelectron pulses. Various other bits of circuitry (*e.g.*, an anti-aliasing filter, a baseline offset adjustment circuit, an external trigger circuit, and digital expansion headers) are also included on the DDC. Figure 44 also shows a measurement of the DDC's baseline distribution with its input terminated to 100  $\Omega$ . The measured  $\sim 1.4$  RMS error in ADC counts is very close to the manufacturer's  $\sim 1$  RMS error specification for typical ADS4149 transition noise.

The DDC is controlled and read out by the Terasic Inc. System-on-a-Chip Development Kit (SoCKit). The SoCKit utilizes Altera's Cyclone V SX-series FPGA, a 110K logic element FPGA which includes a built-in ARM Cortex-A9 hard processor. The DDC connects to the SoCKit via Samtec's High Speed Mezzanine Connector (HSMC). Figure 45 shows a block diagram representation of the firmware which was developed to read out the DDC. The ADC-FPGA Interface module divides the incoming Double Data Rate (DDR) 250 Msps ADC data stream into four parallel Single Data Rate (SDR) streams, each running at 62.5 Msps. Dividing the data stream in this way allows the design to easily



Figure 44: The DDC and SoCKit (left) and a measured baseline distribution (right).

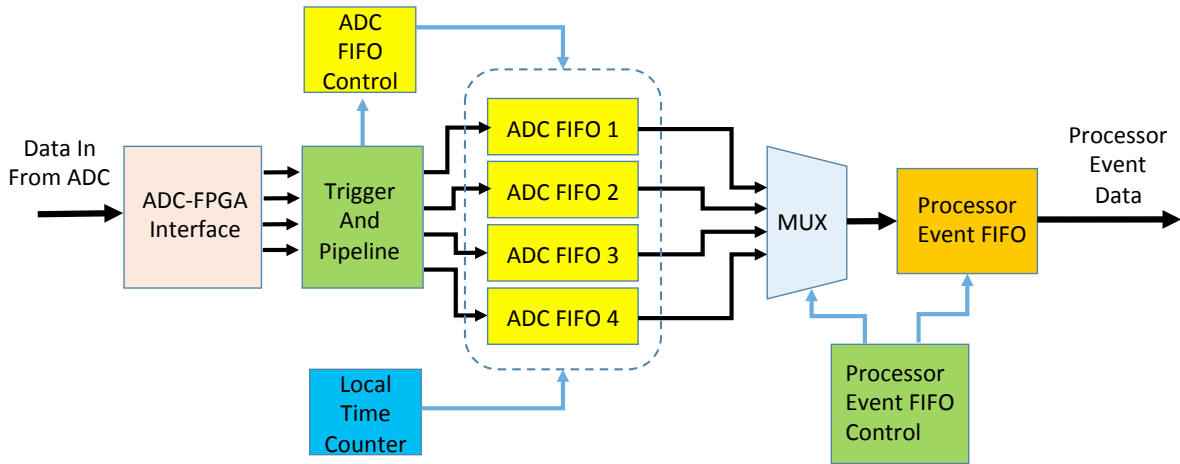


Figure 45: The prototype firmware block diagram.

meet all synchronous timing requirements, while making only modest tradeoffs in resource utilization and design complexity. The Trigger and Pipeline module examines the data stream for the occurrence of any of a number of user-programmable trigger conditions, signalling the ADC FIFO Control module to begin filling the ADC FIFOs with event data when the active trigger condition is satisfied. A 48-bit timestamp generated by the Local Time Counter module is also stored with each event. Data on the output side of the ADC FIFOs are sequentially re-ordered by the Processor Event FIFO Control module and presented to the FPGA's processor for formatting and transmission to the user.

The prototype hardware described above was combined to make an early test setup, as shown in the block diagram of Fig. 46. This test setup was used in order to exercise all prototype electronics elements according to their expected end use, and also to begin to characterize overall system performance. An IceCube R7081-02 Hamamatsu 10-inch PMT was mounted on the HVD, and the resulting assembly was placed in a dark box. The PMT's anode signal was read out by the DDC. High voltage was supplied to the PMT assembly from the HVS, which was controlled by the SoCKit with all control signals routed through a DDC expansion header. The high voltage setting was tuned for a PMT gain of  $\sim 10^7$ . Single photoelectron pulses were stimulated in the PMT by driving an LED with a pulse generator whose amplitude and width settings were adjusted such that only  $\sim 1/50$  pulse generator triggers resulted in a signal at the PMT's output. A second channel of the pulse generator was connected to the DDC's external trigger input in order to force coincidental triggering and readout.

Figure 47 shows a typical single photoelectron waveform and the resulting charge distribution of all events for which a 0.25 PE amplitude threshold was surpassed. The typical SPE is seen to be easily distinguishable from the baseline noise, and the measured charge distribution exhibits a relative width and peak-to-valley ratio similar to the characteristics of typical DOMs being used by IceCube.

#### *5.4. New Photon Detection Technologies*

In parallel to the PDOM design described in Sec. 5.3, alternative optical modules are also under active development. The focus of this development is to increase the photon collection area, minimize the noise, and improve the time and directional resolution of the optical module. Full detector simulations for PINGU and other detectors using the new types of optical modules are currently being developed, focusing on the following two key areas:

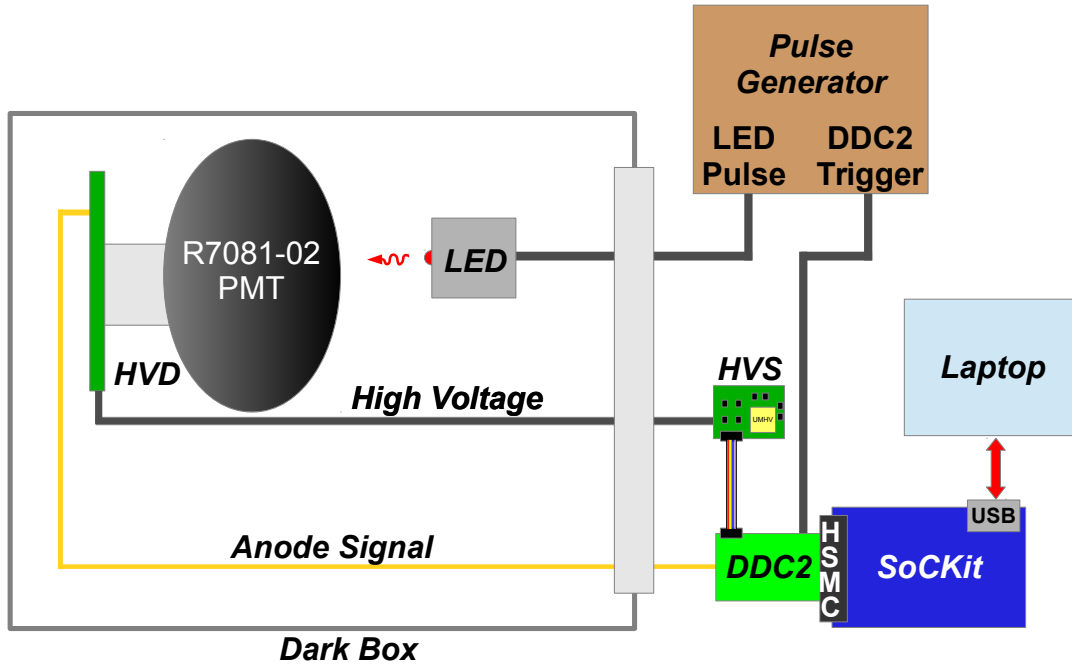


Figure 46: Block diagram of the test setup for the prototype Gen2-DOM hardware.

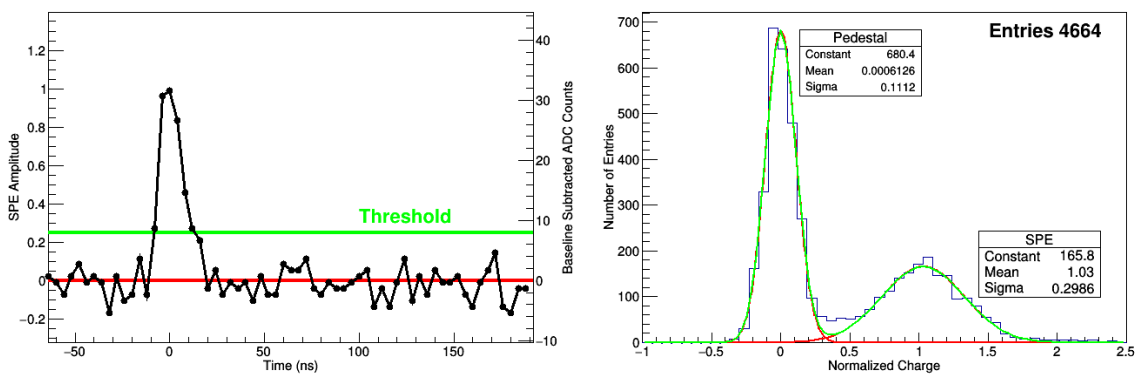


Figure 47: A typical single photoelectron waveform (left) and the resulting charge distribution for the run (right).

**Photon Collection Area:** The energy and zenith resolutions of the detector will improve with the count statistics of measured photons. To a good approximation, the total number of emitted photons scales linearly with the neutrino energy.

**Directional Sensitivity:** Even though scattering dominates over absorption in the Antarctic ice, the average scattering angle is small. The distribution of detected Cherenkov photons therefore partially maintains its directional characteristics present at emission, carrying important information about the direction of the emitting particle. This is especially true for distances that are comparable to the scattering length, as in PINGU. Figure 48 shows the number of photons as a function of the angle between the direct, unscattered Cherenkov path, and the impact direction on the optical module. For an emitter-receiver distance of 14 m, typical for these events, it has been seen that the signal is dominated by direct light. Thus optical modules with intrinsic directional resolution can deliver additional input for event reconstruction. Even at a distance of 125 m some of the directionality is preserved, in particular when considering the arrival time with respect to that of a unscattered photon.

The installation of PINGU may allow for deployment of new photon detection instruments that will improve the overall sensitivity to photons as well as potentially providing additional information about the events themselves. Taking advantage of the properties of Antarctic ice (low temperature, low radioactivity, and little absorption above UV wavelengths of 200 nm) the R&D efforts so far focus on two major directions:

- multi-PMT optical modules (*e.g.* mDOMs and D-Eggs, discussed below) with increased photodetection sensitivity and directional information and
- low noise, UV-sensitive, wavelength-shifting modules (*e.g.* WOMs, also discussed below) with large area but relaxed timing requirements.

While both approaches provide an enhanced photodetection sensitivity, the directional information and precise timing of the mDOM and D-Egg may prove particularly beneficial for accurate event reconstruction. The mDOM in particular may provide strong advantages in the PINGU energy regime. The low noise and UV-sensitivity of the WOM approach mostly promises a reduced energy threshold and improved energy resolution. Beyond PINGU, these technologies may eventually be combined to exploit their complementarity.

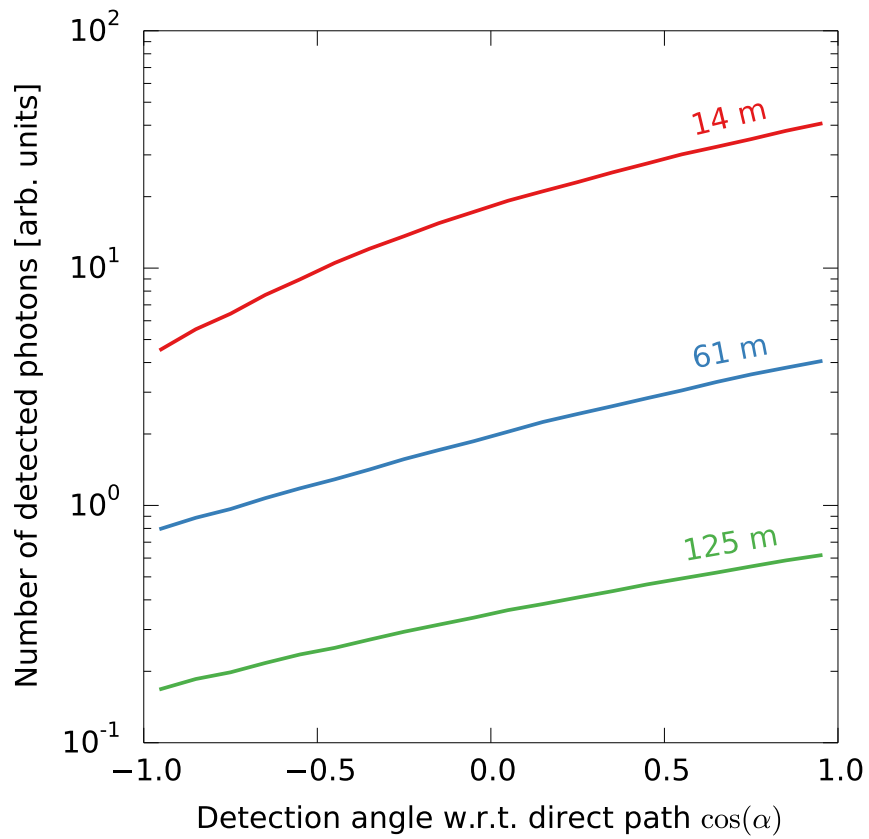


Figure 48: Number of Cherenkov photons from a bare muon track arriving at an optical module with a given angle with respect to the direct, unscattered light path for different distances between the emitter and optical module.

#### 5.4.1. Multi-PMT Optical Modules (*mDOMs*)

As discussed previously, the IceCube neutrino telescope uses optical modules consisting of a spherical glass pressure vessel containing a single large-diameter PMT, as well as front-end and digitization electronics. In contrast, multi-PMT optical modules [121], such as those developed for the KM3NeT neutrino telescope in the Mediterranean Sea, house arrays of many small PMTs and their read-out electronics. Such modules offer a number of attractive advantages compared to the PDOM:

- increased photocathode area with almost uniform  $4\pi$  acceptance,
- improved event reconstruction and background suppression due to directional sensitivity,
- improved photon counting due to segmentation of the photocathode area,
- local coincidence recognition for improved signal selection and background suppression, and
- superior timing without the need for magnetic shielding.

We adapted the KM3NeT multi-PMT concept by incorporating 24 three-inch PMTs in a 14-inch spherical glass housing with a short cylindrical extension suitable for deployment in holes achievable with the IceCube drill equipment (Fig. 49a,b). The goal is to achieve an overall price per cathode area at least as low as in conventional optical modules. The status of the R&D and prototyping efforts is discussed below.

**Housing:** Unlike full glass spheres, spherical pressure vessels with a cylindrical extension, required by the *mDOM* to accommodate the main electronics board, are not commercially available in the appropriate form factor and pressure rating. Cooperation with a glass vessel manufacturer (Nautilus GmbH) has resulted in a technical solution which, according to the manufacturer specifications, fulfills the requirements. The pressure vessel consists of two glass half-spheres which are extended at their equator with a cylinder of 27.5 mm height (see Fig. 49b). The two segments will be joined centrally using beveled glass surfaces and application of low pressure. Each hemisphere is able to house 12 three-inch PMTs providing an almost uniform  $4\pi$  sensitivity in the full module (see Fig. 49c).

**PMTs:** At the time of this writing, three companies (Hamamatsu, ET Enterprises, HZC) provide three-inch PMT prototypes that have been optimized for KM3NeT, including

length ( $< 12$  cm), and transit time spread (RMS  $< 2$  ns). Their mushroom-shaped entrance windows offer superior timing and 10 dynodes provide the required gain. For the first mDOM prototype, the Hamamatsu R12199-02 model has been selected due to its better form factor with respect to the dimensions of the pressure vessel.

**Internal PMT Support structure:** The PMTs (and possibly calibration devices) will be suspended using a support structure that will also accommodate reflector rings around each PMT. The reflector rings increase the sensitivity of the PMTs in the central  $\pm 50^\circ$  direction by about 30%, thereby enhancing the directional sensitivity of the module significantly. The support structure has to provide temperature resistance, limited shrinkage due to pressure and temperature, negligible chemical reactivity with PMT glass and optical silicon gel, low intrinsic radioactivity, and durability throughout the lifetime of the experiment. The first prototypes of such a holding structure (see Fig. 49b) have been produced by rapid prototyping (“three-dimensional printing”) by an external company. For mass production, alternative, more cost-effective production methods are being investigated.

**Readout electronics:** The front-end readout electronics will be based on an extended KM3NeT layout. The high voltage is generated on the PMT base with Cockcroft-Walton circuitry designed by Nikhef [122]. For the digitization of the analogue waveform produced by the PMT, two concepts are currently under investigation. In the baseline concept, the waveform is split after amplification and passed to four discriminators with different thresholds. The time-over-threshold signal from each discriminator is routed to an FPGA on the main board where the leading and trailing edge times for each channel are determined. In a more ambitious approach, the waveform is fed into a custom Application-Specific Integrated Circuit (ASIC) currently under development, which incorporates 63 thresholds. The ASIC contains a  $2^N - 1$  to  $N$  encoder which reduces the data to a 6-bit output word. Processing of the output corresponds to that of the baseline concept. In the ASIC scheme, the larger number of thresholds allows for a detailed sampling of even complex waveforms. The target for the total energy consumption of the mDOM is  $< 3$  W.

**Current project status:** The design of the pressure vessels has been finalized. First prototypes have been delivered and will undergo pressure tests. Three-inch PMT prototypes from Hamamatsu are on hand and will be incorporated in the first mDOM prototype. A climate chamber is available to measure properties crucial for the use in deep ice, such as the dark rate, under realistic conditions (down to  $-50^\circ\text{C}$ ). A first design of the PMT support structure has been developed and a prototype manufactured. Work on the design of the PMT base incorporating the pre-amplifier and time-over-threshold circuitry

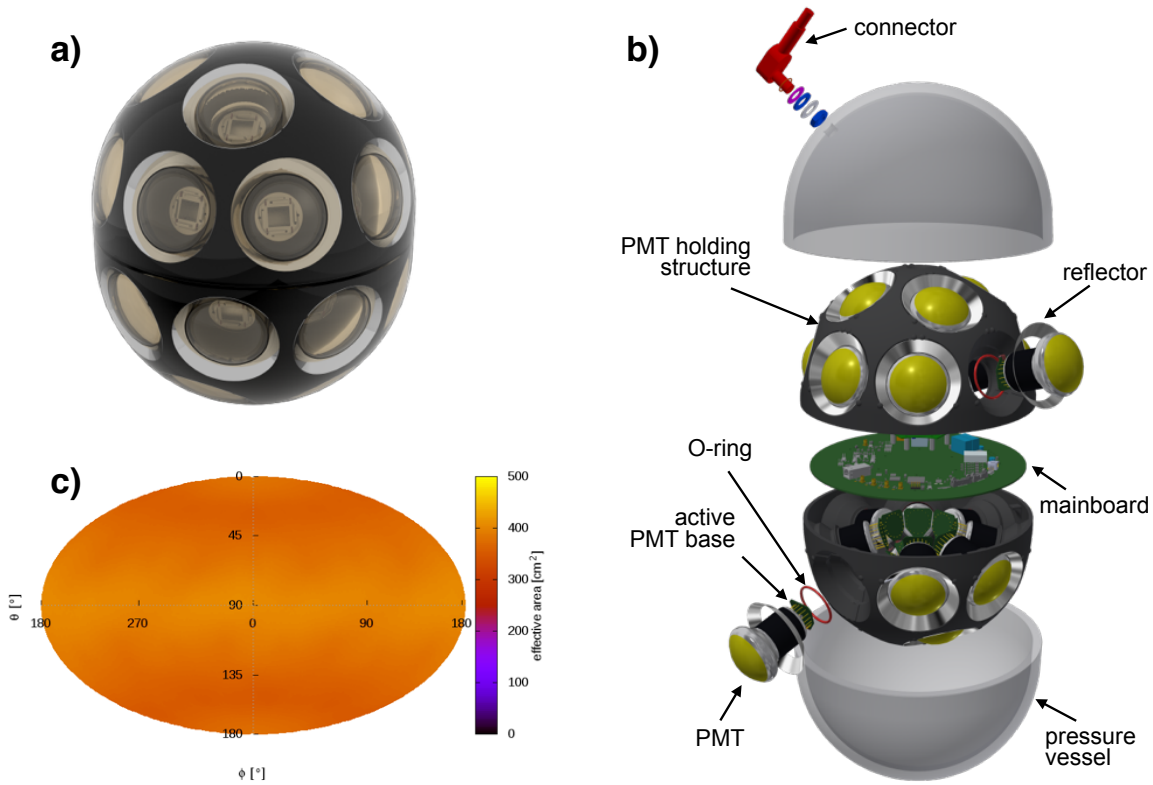


Figure 49: Rendering (a) and exploded view (b) of current mDOM design. (c) mDOM effective area for a plane wave front as a function of its zenith and azimuth angle simulated at 470 nm, quantum efficiency not included.

(both discrete and ASIC) are progressing. Simulations are currently underway to address the optical properties of the module including the signature of optical background from radioactive processes in the glass and the impact of the utilization of mDOMs on the physics performance of PINGU.

#### 5.4.2. Dual optical sensors in an Ellipsoid Glass (D-Egg)

The existing IceCube DOMs have a proven record of very high stability. Each DOM carries a 10-inch PMT (Hamamatsu R7081-2) which looks downwards into the ice. The D-Egg design is based on the successful technology of the current IceCube DOM but housing two 8-inch PMTs (Hamamatsu R5912-100) with one looking up and one looking down. The improved aspects of this setup will be detailed here.



Figure 50: The D-Egg schematic: the height of the glass vessel is 534 mm and its diameter at the equator is 300 mm.

**Housing:** The glass housing of the D-Egg has been optimized to ensure the best optical performance while preserving the mechanical strength necessary to withstand the pressure stresses to which it will be exposed. The mechanical strength of the glass housing has been tested up to 70 MPa, which is higher than the greatest pressure observed during the freeze-in process of the current IceCube strings.

The thickness of the glass varies with latitude, being thicker at the housing's equator and thinner at its poles. The diameter of the D-Egg at the equator is 300 mm, which is 30.2 mm less than the current IceCube DOM. This will reduce the drilling costs by allowing for holes with smaller diameter (and therefore less fuel). Figure 50 shows the existing components of the D-Egg. The electronics and digital outputs are under development and are based on modifications of the PDOM designs.

**Improved sensitivity to UV photons:** The transmittance of the glass for UV photons has been improved compared to the current IceCube glass. For instance 40% of 350 nm photons are absorbed by the current IceCube glass while over 95% of vertical photons pass through the D-Egg glass at the pole. A comparison of the transmittance of the glass and the gel is shown in Fig. 51.

The quantum efficiency (QE) of the PMT has also been improved and is shown together with the transmittance of the glass in Fig. 51. At  $\lambda = 380$  nm, the QE of the 8-inch D-Egg PMT is increased from 25% to  $\sim 33\%$  compared to a standard IceCube PMT. It can be inferred that the acceptance of UV photons at  $\lambda = 320$  nm is limited by the quantum efficiency of the PMTs. The photon detection probability of the D-Egg (with glass and gel) has been measured in a freezer with five LEDs of wavelengths 340, 365,

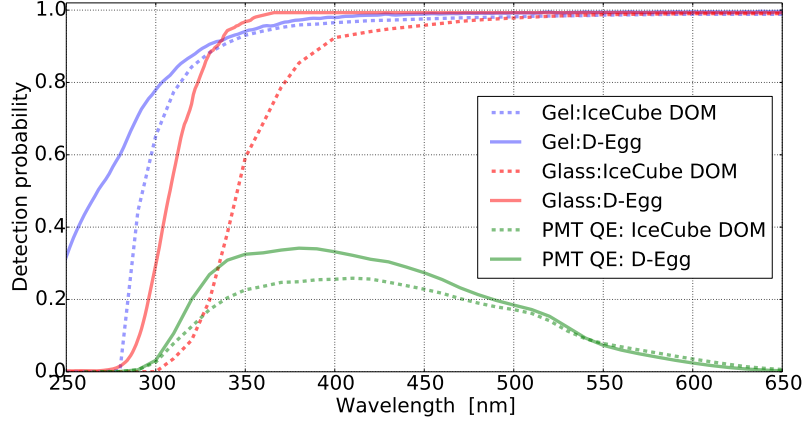


Figure 51: The photon detection efficiency is determined by the glass, gel, and PMT. The transmittance of the glass and gel and the QE of the PMTs for the D-Egg and IceCube DOMs are shown as a function of wavelength.

470, 520, and 572 nm. The result is compared to GEANT4 simulations which take into account the absorption of the glass and the gel, the geometry of D-Egg and the properties of the PMTs (Fig. 52).

The QE measured by Hamamatsu has been corrected by the charge response of  $\sim 90\%$  and compared to simulations of the bare PMT. More measurements are planned to verify the simulations, especially at UV wavelengths and at different photon-incident angles. Compared to the current IceCube DOM, the detection efficiency of photons at 350 nm has been increased by almost a factor of two.

**$4\pi$ -coverage of acceptance:** The D-Egg has two PMTs covering  $4\pi$  solid angle of the detection volume. This is important in the case of vetoing down-going muons. It also provides directional information of the incoming photons and potentially could help reconstructing events which are cascade-like. Detailed studies are in progress.

The geometric and optical properties of the D-Egg have been implemented in GEANT4 [19]. Photons of wavelengths 300 nm to 650 nm are simulated in circular beams with a diameter of 0.534 m, which is the height of the D-Egg. The quantum efficiency of the PMTs has also been included in the simulation. Photon beams are then injected and rotated from the bottom to the top of the optical module. The effective areas of the D-Egg and the IceCube DOM at different wavelengths and photon angles are shown in Fig. 53.

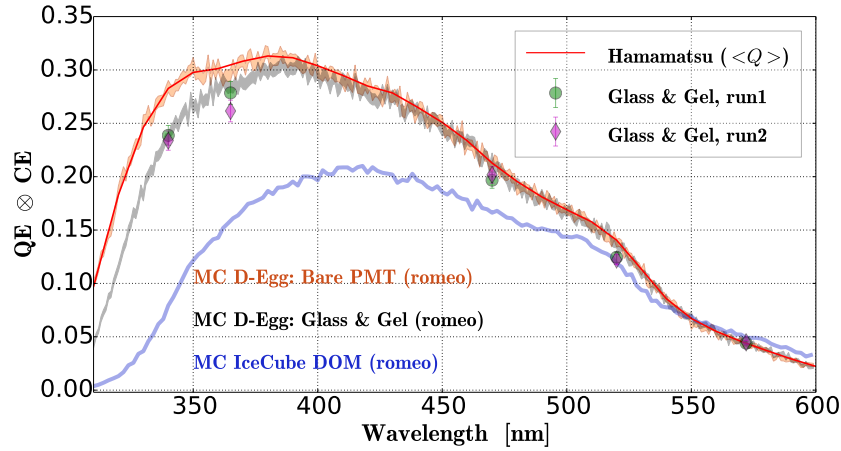


Figure 52: Comparison between the quantum efficiency measured in the lab and generated in the simulations, based on GEANT4 and Romeo. The bare-PMT simulation is compared to Hamamatsu measurements which have been corrected for the charge response. The blue curve shows the simulated efficiency when photons hit the centre of the photocathode of an IceCube DOM.

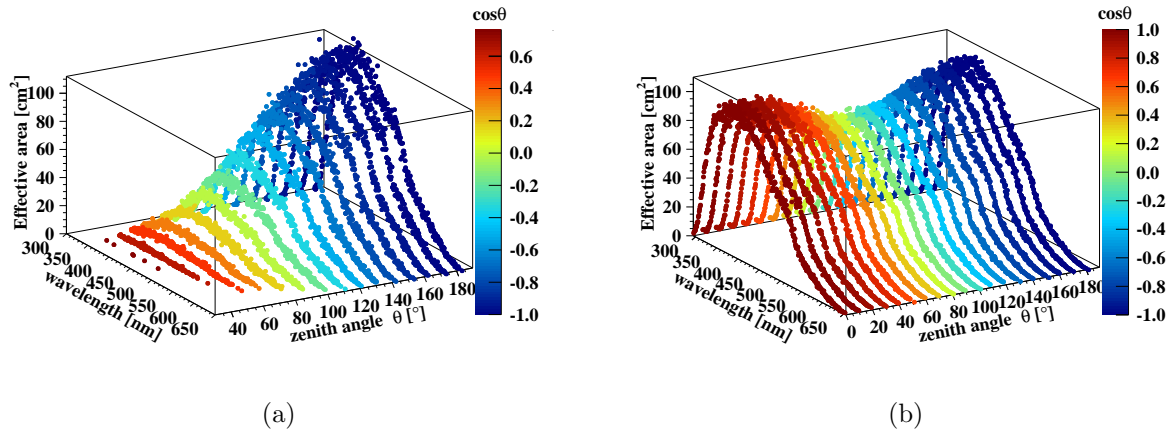


Figure 53: The effective area of the current IceCube DOM (a) and the D-Egg (b). The optical properties of the glass and gel have been implemented in GEANT4 simulations. The PMT simulations include the charge response correction and the quantum and collection efficiency. Each point scales with the probability of a photon of a certain wavelength and zenith angle being converted to a photoelectron.

The IceCube DOM has greater sensitivity to photons arriving from below while the D-Egg has nearly isotropic sensitivity to photons from all angles. At 340 nm, the effective area of the D-Egg integrated over all angles is  $\sim 4$  times the effective area of the IceCube DOM.

The assembly of a complete D-Egg is expected in 2017 including the final version of the HV divider board and signal readouts. The performance of 8-inch PMTs with transformer-based or capacitor-based HV boards is being tested in a freezer at  $-45^{\circ}\text{C}$ .

#### *5.4.3. Wavelength-Shifting Optical Modules (WOMs)*

One way to improve the photo-collection efficiency of the photodetectors is through the use of wavelength-shifting and light-guiding materials to concentrate the light from a large area onto one or a few PMTs with small photocathode area. The goal of this R&D project is to provide modules with the following properties:

- very low noise rates on the order of 10 Hz,
- high UV sensitivity,
- large geometric acceptance and module sensitivity,
- long term stability,
- no necessity for magnetic shielding, and
- adequate timing resolution.

The essential idea of the WOM is to increase the sensitive area of a PMT by using passive components that act as light collectors and concentrators, as illustrated in Fig. 54. The use of cigar-shaped modules maximizes the photon collection area that can be deployed, for modules produced at a price per photosensitive area that is lower than that of standard optical modules. The dimensions are mainly limited by the requirement to safely withstand high pressure and be handled easily. With a larger photo-detection efficiency, the resulting geometry can provide a more elongated module that has a significantly smaller diameter, allowing a decrease in the hole size and thus yielding another significant cost reduction. Except for the readout electronics, all components for a first prototype have been produced and are currently evaluated with the results discussed below.

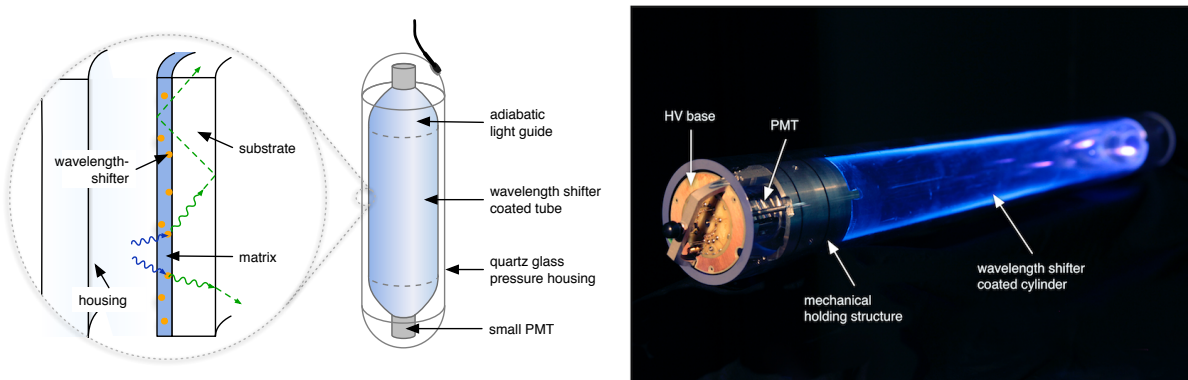


Figure 54: Schematic drawing of the Wavelength-shifting Optical Module (left) and a prototype illuminated under UV light (right). Converted light guided in the cylinder is focused onto the PMT by an adiabatic light guide (within the holding structure).

**Housing:** In order to provide sensitivity at wavelengths below 300 nm and suppress noise arising from radioactivity in the glass, quartz tubes of suitable dimensions have been investigated. An R&D project with the glass vessel manufacturer Nautilus GmbH resulted in a technical solution designed to withstand pressures of 68 MPa, significantly larger than what is expected during the freeze-in process. The final design specs of 9 mm thickness, 114 mm diameter, and 1200 mm length (with hemispherical borosilicate end caps) are a compromise with weight, achievable dimensional accuracy and cost taken into consideration.

In total six modules were fabricated. One module has been successfully pressure-cycled multiple times to a pressure above 34 MPa. The optical transparency was measured on smaller samples from the same production batch and shows excellent transmittivity for wavelengths larger than 290 nm, and  $\gtrsim 20\%$  transmittivity down to a wavelength of 215 nm.

**Wavelength-shifting cylinder:** A wavelength shifting and light-guiding cylindrical tube, with a diameter to allow for only a small air gap between the tube and the pressure vessel, provides the optimal geometry for light collection and concentration. In order to enhance the performance towards the UV, transparent tubes are coated with a thin film containing fluorescent dye. Cherenkov photons, peaking in the UV, are absorbed and re-emitted isotropically in the dye at a larger wavelength. Of these photons, a large fraction (up to 75%) are guided towards the ends via total internal reflection. The dye is applied as a thin (few  $\mu\text{m}$ ) film on cast PMMA tubes through a dip-coating technique, resulting

in high light yield, durability and long-term stability.

**PMT and readout:** On both ends of the tube, the light is guided to the spherical surface of a PMT through adiabatic light guides. In principle, the minimum diameter of the PMT is determined by the wall thickness of the light-guiding tube, however the selection is limited by the availability of small PMTs with sufficient gain to detect single photo-electrons. For the current prototype, we use the same 3 inch Hamamatsu PMT (R12199-02) with a peak quantum efficiency of 25% at 390 nm that is evaluated for the mDOM concept (c.f. §5.4.1). The dark-noise rate of this PMT has been measured to be  $\lesssim 30$  Hz over the full temperature range of interest from  $-50^\circ\text{C}$  to  $-10^\circ\text{C}$ . The readout electronics for the PMT will be based on those developed for the PDOM (c.f. §5.3), but altered to match the smaller dimensions of the housing.

**System performance:** Different wavelength-shifting materials have been tested in lab measurements as candidates for use in such a sensor, and their photon capture efficiency (including conversion and light-guiding) has been measured. Best results have been obtained with a dye that is made from a mixture of different wavelength shifters in the same polymer matrix. For the prototype, we use a PEMA-matrix (Paraloid B72) with an admixture of 0.6%<sub>w</sub> of 1,4-Bis(2-methylstyryl)benzol (Bis-MSB) and 1.2%<sub>w</sub> p-Terphenyl (pT) as active ingredients. Photon capture and transport efficiencies well above 20% and as high as 50% have been achieved in this configuration, depending on the dye concentration, surface quality of the coating and other factors. Figure 55 shows the Cherenkov spectrum-weighted effective photosensitive area of the prototype module, including the transparency of the pressure housing, the measured capture and transport efficiency and the quantum efficiency, of the currently used PMT. In particular for short wavelengths, the performance of the prototype built with readily available technology exceeds that of modules currently used in IceCube. Stronger absorption and scattering of the UV-light reduces the effect, resulting in the most notable gain for close-by horizontal events. For a geometry with a 24 m string spacing, the average distance to the closest sensor is 7.2 m.

With the current design already outperforming the existing modules, in particular for dense sensor geometries, future improvements are to be expected by increasing the light capture and transport efficiency and a more optimal choice of PMT.

### 5.5. Cable

Sets of PINGU sensors will be deployed along a single cable similar to those used for IceCube. These cables consist of multiple twisted wire quads, each of which serves power

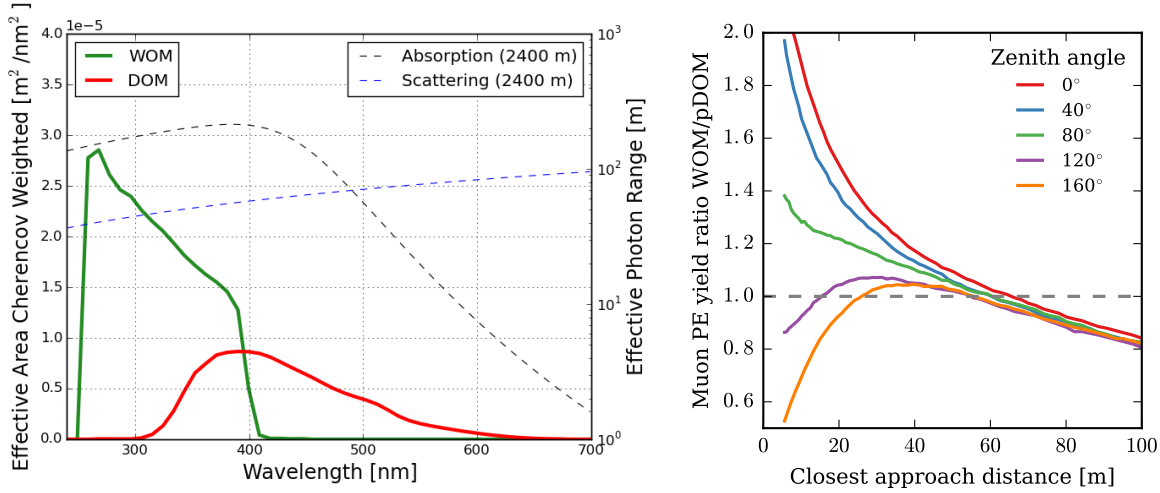


Figure 55: Left: Cherenkov spectrum weighted effective photo-detection area as a function of incident wavelength for the Wavelength-shifting Optical Module (WOM) and an IceCube high-QE module (DOM). Absorption and scattering length in the ice at a depth of 2400m are shown for reference. Right: Average relative photoelectron yield from minimum ionizing muons compared to the PDOM as a function of distance and zenith angle.

and communications for several sensors, a polymer core for structural support, and a robust outer sheath. The PINGU sensor spacing motivates some changes to the cable attachment configuration, but the electrical and mechanical specifications will be essentially the same as for previous IceCube cables. This allows reuse of a proven engineering solution, leveraging the IceCube project experience with procurement and verification of this critical component.

Figure 56 shows how PDOM sensors could be attached to the down-hole cable. The attachment of other sensor designs, such as the mDOM, would be similar. The cable itself carries the load from the top of the PDOM chain, 2150 m up to the surface of the ice. In the instrumented depth range, the load is carried alternately by short segments of steel wire rope and the PDOM harnesses, with electrical cables secured alongside. The main load is transferred from the down-hole cable to the steel rope by grips above the topmost PDOM and at the bottom of the chain. These cable grips are like those used in IceCube above and below every DOM, but the closer PINGU module spacing allows most of them to be replaced by the simpler and lower cost steel rope hardware. The strings are connected to the data acquisition computers via surface cables that run to the IceCube

laboratory building.

With a lower power design and improved data compression, more sensors can be serviced by each wire pair than in IceCube. As shown in Fig. 56, each group of four sensors is serviced by one wire pair broken out from the main cable. This is compared with only two DOMs per wire pair in IceCube. Another simplification of the cable design comes from the omission of extra wires previously dedicated to detecting local coincidences between modules hit, so that each breakout construction is much more straightforward. These changes allow considerably more sensors to be deployed on each cable, reducing cable and drilling costs and avoiding the need for redesign and attendant risk. The same advantages apply to other sensor designs, such as the mDOM, D-Egg, and WOM.

### *5.6. Drilling and Deployment*

PINGU strings will be deployed in holes drilled with an upgraded IceCube Enhanced Hot Water Drill. Each hole is approximately 55 cm diameter and 2500 m depth, the same as the original IceCube holes. The drill provides 5 MW of thermal power in the form of a high-pressure (1000 psi) and high flow (200 gallons/minute) 90°C water jet which will melt ice to a depth of 2500 m in 30 hours. After drilling each hole, a string of modules is deployed over a period of 10 hours and will be fully frozen-in after 3 weeks.

During the construction of IceCube, a highly trained crew of 30 drillers were able to drill up to 20 holes in each South Pole construction season (Table 9). Key personnel from the IceCube project and the South Pole support network remain active in hot water drilling and will still be available for PINGU, leveraging their extensive experience to optimize the required drilling time and effort. Existing equipment and procedures can be utilized, including necessary refurbishment and replacement of some components, to complete the construction of the 26-string PINGU within 1 + 2 seasons. As shown in Table 10, the first season will be used for reassembly, staging and testing of the drill equipment, followed by two for drilling and deployment.

The IceCube drill is a complex system with many components, with complete written and video documentation of its operation. Following the last deployments in 2010–2011, the system was winterized for storage and to facilitate reuse (Fig. 58). Major components remain in IceCube/NSF stewardship, such as the hose reel, drill towers, and associated structures. These represent significant engineering solutions and assembly efforts that can be reused by PINGU. Heating plants, high pressure pumps, and water tanks remain similarly available. Other components were allocated for use by other projects, of which

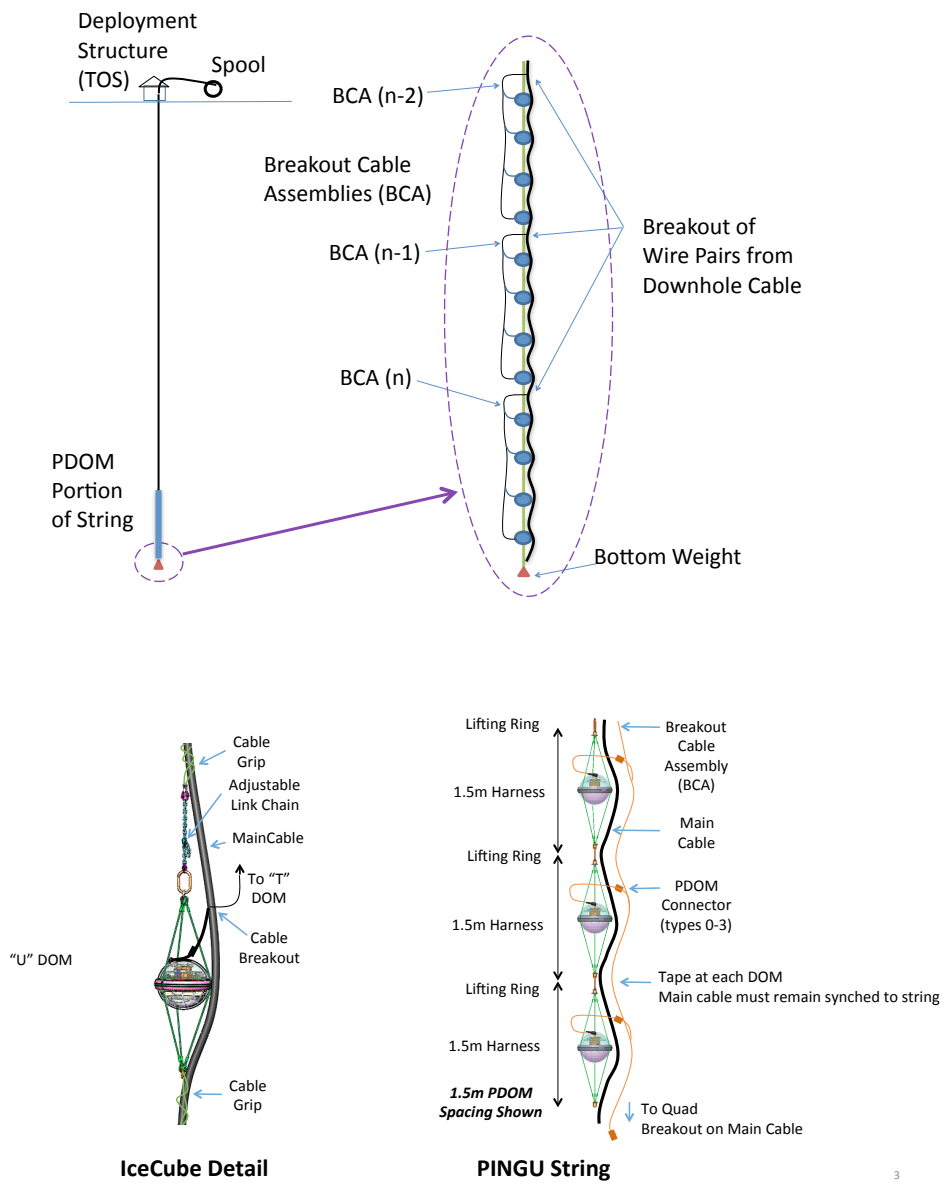


Figure 56: Attachment and support of PDOMs along a PINGU string. The Seacon XSJJ connectors are of the same type used in IceCube.

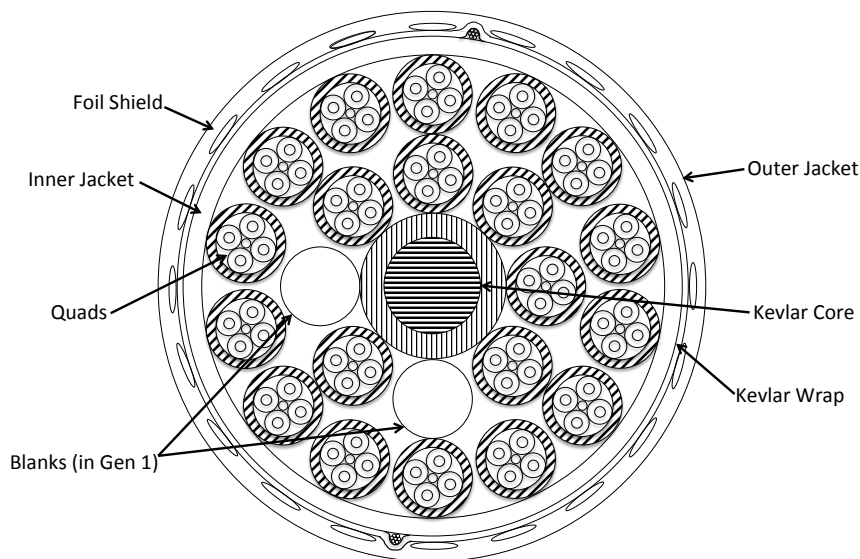


Figure 57: Cross section of an Ericsson cable designed for a PINGU string. The outer diameter is 36 mm.

only some are still at the South Pole. A preliminary inventory of drill-related equipment needing replacement has been made for PINGU cost estimation (see Sec. 9). To recommission the drill system, PINGU will likely need to replace the main drill hose, cable reels, electrical generators and distribution, the independent firm drill, and the Rodwell system that supplies make-up water from melted snow.

Certain aspects of the drilling system will be upgraded for PINGU. In particular, improvements are planned that will increase optical clarity of the refrozen ice near the deployed sensors. In AMANDA and IceCube, it was found that light scattering is enhanced in such refrozen ice [123] (or “hole ice”) modifying the DOMs’ angular response function and complicating calibration and systematic error studies. The effect is most apparent for near-vertical background muons, where downward traveling light can be scattered in the upward direction and more easily strike the PMT photocathode (Fig. 59). Study of the number and timing of photons in such events has resulted in a quantitative hole ice model that is routinely used for simulation and analysis of neutrino events in IceCube. Subse-

Season	Strings deployed
2004-2005	1
2005-2006	8
2006-2007	13
2007-2008	18
2008-2009	19
2009-2010	20
2010-2011	7

Table 9: IceCube yearly records for drilling and deployment.

Season	Special activities	Strings Deployed
1	Drill Rebuilding and Staging, Firm Pre-drilling	
2	Recommission Drill	6-10
3	Decommission Drill	10-16

Table 10: PINGU drilling and deployment schedule.

quently, a camera system was deployed in one IceCube hole and confirmed the scattering visually [124].

The hole ice scattering is believed to be caused by dissolved gas that is released from the solution as very small bubbles during the refreezing process. Glacial ice incorporates air entrained with the snow from which it was slowly formed over thousands of years, but in a clathrate solid form (the air is trapped within the crystal structure) that is optically clear. The hole-refreezing process takes place over a much shorter time scale, apparently causing the observed reduction in hole ice clarity. Supporting this view is the amount of air measured in the original ice, about 600 mg/kg, and the solubility of air in cold water, only 20 mg/kg at 1 bar. Drill circulation passes about two-thirds of the meltwater through equipment at the surface, where much of the gas can escape, but the remaining one-third still contributes 200 mg/kg to the final mix. During refreezing, the inward growing ice phase can exclude this dissolved gas into the remaining liquid phase along the axis, where the concentration thus increases until it reaches saturation even at the high pressures in the hole (200 bar). At this point bubbles can be expected to form a reduced-transparency core, consistent with the camera observations.



Figure 58: IceCube drill components stored at South Pole, 2011.

For the surface tanks of the IceCube array (IceTop), a special degassing system was used to ensure clear ice, but this degassing was not performed for water in the deep holes of AMANDA and IceCube. For PINGU, the drilling operation will be modified so that the instrumented region of the hole contains only water that has been brought to the surface and degassed. Standard membrane degassing equipment will remove 85% of air dissolved at atmospheric pressure, leaving only 3 mg/kg for return to the hole. By slowing the drilling in the bottom 350 m of depth and then raising the drill head slowly while injecting cold degassed water, gas-laden water will be displaced above the PINGU fiducial volume while adding only a few hours to the drilling time. Additional filtering will also prevent the introduction of mineral impurities from the heating equipment and their possible precipitation. Possible ways to reduce ice fracturing through pressure reduction during the refreeze are also under consideration. In this way the PINGU hole ice is expected to be made effectively clear. Remaining light scattering near PINGU modules, as well as in the bulk ice away from the holes, will be precisely calibrated by studies with LED beacons

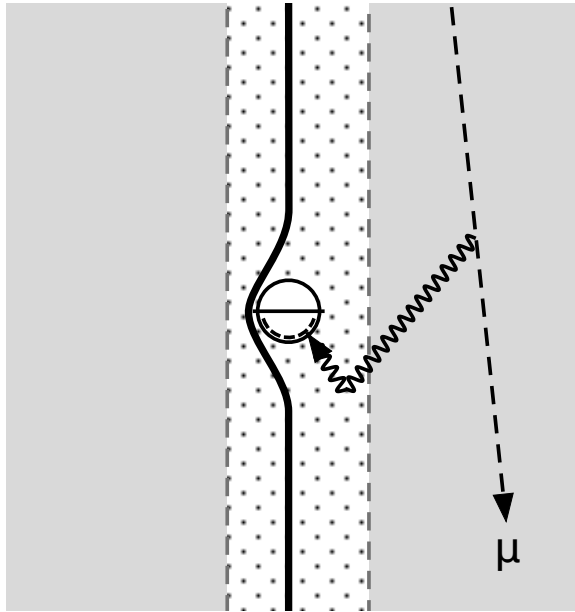


Figure 59: Scattering of light by bubbles in hole ice near DOMs in IceCube. The photocathode is on the bottom side of each DOM, indicated with a dashed curve.

and downgoing background muons (Sec. 7).

Deployment of sensors into PINGU holes will be similar to IceCube deployment, with some modification for the use of steel wire rope between modules (Fig. 56). One AMANDA string was successfully deployed with such steel rope, but the standard IceCube procedure involved attachment of harnessed DOMs directly to the main electrical cable, with installation of special grips for transferring the vertical load between harness and cable. In PINGU, the chain of modules will be assembled and lowered by repeatedly adding harnessed modules and steel rope links. This is done in an iterative process that supports the already deployed section on a tethered hook while the next module or rope segment is suspended above it from a chain hoist. After attachment of the new component, the whole load is hoisted up slightly to allow detachment of the tether and then lowered a few meters to allow attaching the new top to the tether. In synchrony, the main electrical/support cable is lowered and secured appropriately to the module chain, along with its breakout cable assemblies that connect to the modules. After the final module link is deployed, support is transferred to a grip on the main cable and the assembly is then lowered 2150 m into the hole. The equipment for handling the main cable, the enclosing

structure, and procedural safeguards can all be reused from IceCube, giving confidence in achieving a similarly successful operation.

## 6. The Data Acquisition System

The IceCube data acquisition system (DAQ) is now a mature and well-understood composition of firmware and software components maintained by a team of IceCube scientists and software professionals. In order to leverage the existing infrastructure, both the optical modules will be designed in such a way as to be fully compatible with the IceCube DAQ system.

### 6.1. Firmware and Software

As described in Sec. 5.3, PINGU modules, like their IceCube counterparts, trigger and digitize PMT pulses autonomously. The digitization process is foreseen to be continuous and the trigger formed digitally with logic in the FPGA. Triggered pulses will then be processed by a deconvolution algorithm existing in firmware, software, or some combination of the two running within the module. The algorithm will extract the underlying photon pulse charge and local time stamp from the sampled waveforms and output the resulting list of (charge, time) pairs to a memory buffer. The data volume of this representation of the pulses is approximately ten times more compact than the uncompressed waveforms, thereby dramatically increasing the effective buffer depth of the module and decreasing the bandwidth requirements on the module-to-surface communications channel. The information content of these data objects will be made compatible with the stream output by the IceCube DOM; the minimum needed to process the objects is an identifier of the originating channel and a timestamp. Further information, such as charge, is optional and may be used if available. To support these anticipated changes in the module hardware design, the following new features will be implemented:

- module-specific digitizer hardware, including firmware-based trigger,
- firmware and software to perform in-module pulse deconvolution (under development), and
- firmware to support the higher density of channels per wire pair relative to the IceCube DOM (under development).

### 6.2. Integration of PINGU Channels into IceCube Surface DAQ

PINGU channels will be integrated into the IceCube data acquisition system as shown in Fig. 60. The PINGU readout hub (StringHub) components are each connected to a string

of modules. They extract hit summaries (channel and time information, currently) from the stream of data buffers sent by the modules and send them to a trigger unit. Each trigger unit examines the stream of hits and identifies patterns of interest by sending a trigger to the Global Trigger unit. The Global Trigger unit merges triggers from the sub-detectors which overlap in time. A global trigger is then sent to an Event Builder processor which requests the full readout data, including waveform information buffered in the hubs, in time windows around the triggers, packaging this data into an event data structure on disk.

The individual components, and their changes relative to IceCube entities are discussed next.

### *6.2.1. Communications System and Readout Electronics*

It is expected that between 4 and 8 modules will share a common copper pair connection to the surface in order to reduce the cost and size of the surface-to-DOM cables relative to the IceCube in-ice cable system. This is a two- to four-fold increase in the channel aggregation and will require upgraded communications firmware. At the same time it will be necessary to increase the density of the readout electronics in order to accommodate additional PINGU channels in the rack space available in the IceCube Computing Laboratory. An improved readout system is currently being designed to meet these new requirements of PINGU. The communications must be made compatible with existing IceCube channels to allow for a uniform deployment of readout hardware across all channels. Despite this requirement, it will be possible, via advanced protocol-discovery during the link negotiation phase, to encompass the improved communications protocol of the PINGU channels using more robust phase-shift keying modulation techniques while still supporting the baseband signalling currently used in IceCube.

In addition to data communication, the IceCube and PINGU data transmission protocols are required to implement a mechanism for time translation between the local timestamps in the IceCube and PINGU modules and the globally referenced time system UTC. In IceCube this mechanism is known as RAPCal and is fully documented in [120]. The corresponding solution for PINGU DOMs is currently under design with requirements for the same or better time resolution with respect to RAPCal (less than 5 ns) which loosens the cable crosstalk specification. With the above-mentioned phase-shift keying modulation schemes, pseudo clock recovery can be implemented.

At the application level, the PINGU StringHubs should function nearly identically to

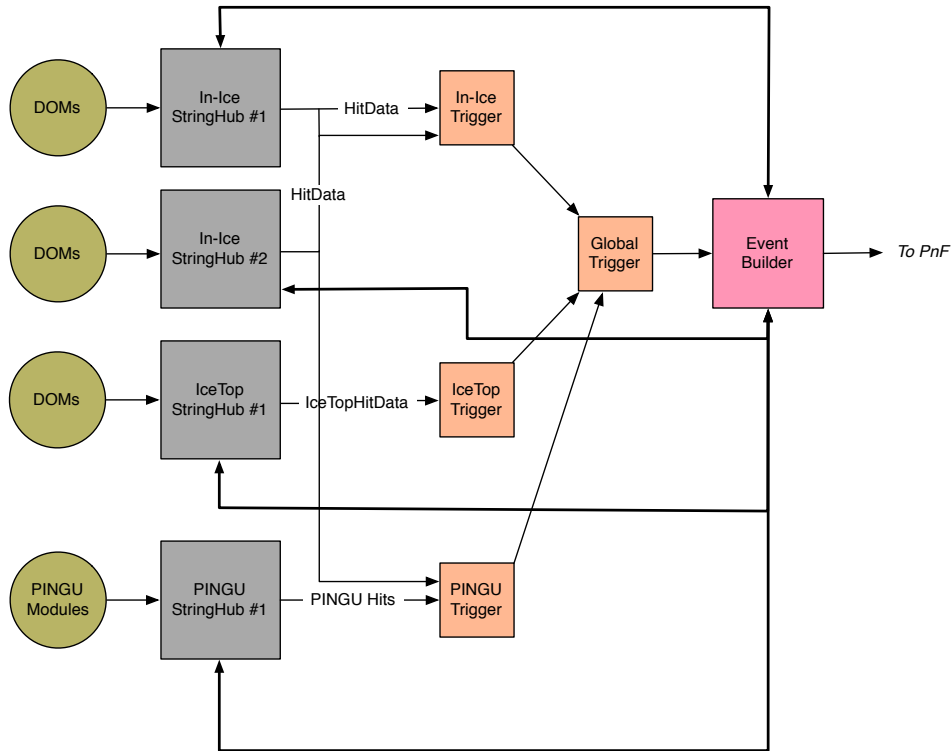


Figure 60: Schematic representation of the integration of the PINGU modules into the IceCube data acquisition system. At left are the modules (circles), an entire string of which are connected to data collection processes running on the readout computers (grey boxes). In IceCube there are 86 such entities corresponding to the deep ice modules and another 11 entities for the IceTop surface channels. From software there is no limitation to the number of readout hosts in the system. The StringHub readout processors forward module hit summaries to the trigger processors which may, upon detection of an interesting hit pattern, request a readout of all hits in the detector in a given time window around the trigger time. Trigger processors can operate on hits from both PINGU and the existing IceCube and DeepCore DOMs in combination. Each global trigger results in an event being built by the Event Builder. These events are then sent to the Processing and Filtering (PnF) farm at the South Pole for initial reconstruction and data reduction.

those of IceCube: each hub collects and buffers data, sending pulse hit summaries to the trigger processors. The notable extension to the functionality concerns the tagging of hits that are sent to the triggers. Due to past computing limitations in sending the full 2.5 MHz rate of hits to the triggers, only hits tagged with “local coincidence” in the ice are forwarded. This reduces the rate of hits resulting in triggers to approximately 50 kHz. Recent improvements in both the computing hardware and the IceCube DAQ will support hit sorting and triggering at the expected aggregate PINGU hit rate, also roughly 2.5 MHz.

### *6.2.2. Triggers*

The DAQ layout depicted in Fig. 60 explicitly separates the PINGU trigger processor from the IceCube trigger processor, providing a degree of isolation between the two. Development of another trigger processor specific to PINGU is the only infrastructure development foreseen at the DAQ level. These modifications are minimal and only involve adding additional bookkeeping data structures to the trigger code. While existing DAQ trigger algorithms can be re-parameterized and used in PINGU, new trigger algorithms will also likely be developed to fully exploit the capabilities of the new subdetector. It is also possible that the PINGU trigger could operate as one or more algorithms within the In-Ice Trigger unit. This latter configuration has the advantage that a single trigger can be formed from the combination of information from IceCube and PINGU channels.

### *6.3. Event Builder*

The Event Builder interacts with the readout computers through a rather simple network interface. The PINGU StringHub will implement this interface and thereby participate directly in the event assembly process. As such, there are no customizations needed in the Event Builder for PINGU deployment.

## 7. Calibration

### 7.1. Overview

PINGU event reconstruction uses the timing, location, and amount of deposited light to reconstruct the properties of the incident particle: position, time, direction and energy. Accurate reconstruction relies on calibration of the timing (arrival time of photons at the modules), geometry (module positions), photon detection efficiency (photosensor sensitivity), and a model for the optical properties of the ice. The latter determines how Cherenkov photons propagate through the ice from their creation until they are absorbed or reach a module. Uncertainties in any of these measurements constitute the detector-based systematic uncertainties in PINGU physics measurements. Other systematic errors come from uncertainties in the atmospheric neutrino flux, including the energy spectrum and zenith angle distribution, the atmospheric oscillation parameters  $\Delta m_{\text{atm}}^2$ ,  $\theta_{23}$  and  $\theta_{13}$ , the neutrino cross-section and branching ratios to specific final states, and the light output from a given neutrino interaction final state. As shown in Sec. 3.4.1, the largest impact in the neutrino mass ordering measurement is from uncertainty in the atmospheric oscillation parameters.

Here we review the impact of detector-based uncertainties on PINGU physics measurements. We then discuss the methods for detector calibration in IceCube and PINGU, and planned calibration devices for PINGU. In this section, the NMO analysis is used as a proxy for all PINGU analyses, as it is one of the most sensitive analyses and is susceptible to the impact of most of systematic uncertainties discussed in Sec. 3.

Note that these calibration devices could equally well be deployed and used in the proposed Phase 1 detector ([Appendix D](#)), with the same benefits to low energy oscillation analyses. In [Appendix D](#) we also describe the advantages that would accrue to high energy IceCube neutrino analyses as well.

### 7.2. Impact of Detector Systematics in PINGU

A complete study of the impact of detector-based uncertainties on PINGU's sensitivity to the NMO requires more simulation statistics than are currently available. At present, the only detector-based systematics incorporated in the NMO study are the optical properties of the ice and module efficiency. Conservatively, the uncertainties on these quantities are

taken to be the current IceCube values, and these values are sufficient to measure the NMO.

The default model of the optical properties of the ice is the SPICE Mie model, based on LED flasher data from IceCube [1]. This model is compared to the more recent SPICE Lea model [23], which has a similar basis but includes an observed azimuthal anisotropy in the scattering length. The effect of unsimulated anisotropy in SPICE Mie appeared as a spread in the difference between the predicted and observed charge deposited in IceCube DOMs by the LED flashers. The difference between SPICE Mie and SPICE Lea is used therefore as a proxy for unsimulated, as yet unknown, effects in the ice model. The DOM efficiency is known to within 10% in IceCube; a conservative estimate of the uncertainty in PINGU uses this number. In order to evaluate the impact of these parameters in the existing simulations, the mean PINGU module efficiency has been shifted by 10%, and the individual module efficiency has been smeared by sampling from a Gaussian distribution with a width of 10%. This method of including the efficiency shift is applicable to all modules used in PINGU, and the results are not expected to change with the module type.

Of all detector systematics evaluated thus far in the simulation, the overall shift in the mean value of the module efficiency has the largest impact on the energy scale in PINGU, as shown in Fig. 61. The shift in the energy scale corresponds to a shift in the mean value of the module efficiency. Therefore, the uncertainty in the energy scale is taken to be 10% in the NMO systematics study in Sec. 3.4.1, corresponding to the current uncertainty in the IceCube DOM efficiency.

### 7.3. Detector Calibration

IceCube *in-situ* detector calibration employs reference electronics onboard the DOMs, LED flashers co-located with each DOM, in-ice calibration lasers and low energy muons in the ice. Most of these methods will be used again in PINGU.

#### 7.3.1. Geometry

The positions of IceCube DOMs have been measured to within 1 m with several methods, which we will also use in PINGU. During module deployment, the position of strings will be surveyed and the absolute depth of the modules will be estimated using data from the drilling process and pressure sensors attached to the bottom of each string. The

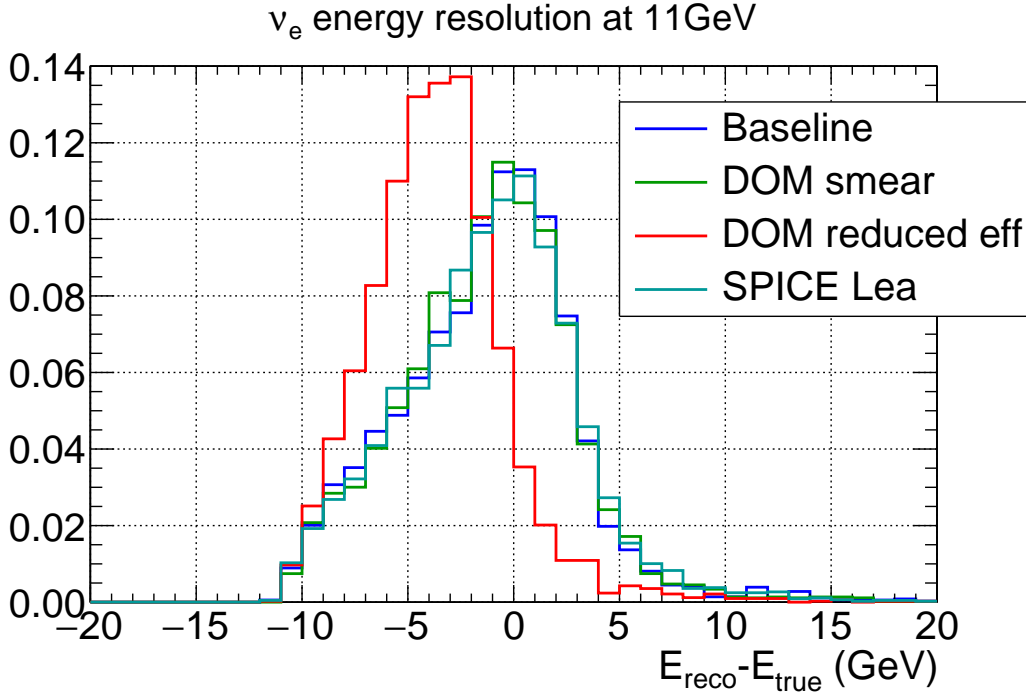


Figure 61: Energy resolution for 11 GeV electron neutrinos in PINGU (charged current only). Blue: baseline geometry and SPICE Mie ice model. Red: Mean module efficiency reduced to 70% of nominal; this is larger than our 10% uncertainty in order to see the impact more clearly. Green: Individual module efficiency smeared by 10%. Blue-green: SPICE Lea ice model. The largest shift is seen for the change in the mean module efficiency; the peak of the reconstructed energy distribution is reduced by the same amount as the efficiency.

vertical distance between modules will be measured with a laser ranger or similar device during deployment, and will be corrected for possible cable stretching. Corrections to these measurements will be determined using *in situ* light sources to triangulate the final position of modules in the ice. Given the PINGU interstring spacing of about 20 m, an uncertainty of 1 m in the interstring spacing corresponds to a less than  $3^\circ$  error in direction resolution. Studies are underway to determine how much the geometry measurement may be improved in PINGU.

IceCube also includes several DOMs with onboard inclinometers to measure a possible differential ice flow that would cause time-dependent changes in the detector geometry. Significant changes have not yet been observed, but similar devices may be installed in PINGU.

In addition to the position of the modules, the azimuthal orientation of the modules after freeze-in will be measured by LED flashers and/or onboard compasses. In IceCube, the azimuthal orientations of the DOMs are measured with LED flashers to within  $10^\circ$  [1].

### *7.3.2. Timing*

The IceCube time calibration system uses reciprocal pulses sent between the free-running clock in each DOM and the master clock on the surface, resulting in a time synchronization across the detector of 3 ns or better [15]. PINGU will use a similar method, but with a continuous clock signal that is integrated into the communications system as opposed to isolated discrete pulses. Small transit time offsets in each PMT will be measured using pulses from integrated LEDs. Calibration light sources with independent timing will be used during commissioning to verify that overall time offsets among modules are accurately tracked throughout the hardware and data processing chain.

### *7.3.3. Module Gain and Sensitivity*

Similar to IceCube, PINGU reconstruction will make use of PMT output waveforms based on the time and number of photons arriving at each module. From observed single photon responses, PMT high voltage settings will be chosen for gain close to  $10^7$ . In order to control for small offsets or drifts from the nominal single photoelectron (SPE) response of 1.6 pC, PINGU will continuously monitor the waveforms for SPEs in triggered events. The result is a measured SPE charge for each module, including any effects due to PMT or electronic gains. This will then serve as the fundamental calibration quantity when making precise correspondences between PMT waveforms and photon counts. In IceCube, such an SPE calibration has been shown to be stable at the level of 1% or better.

Linear response of the module to pulses with multiple photons will be verified by in-ice LED flashers capable of operating at different brightnesses. As previously done in IceCube [22], ratios between pulse brightness can be gauged by counting single photon responses in sufficiently distant modules, and then used to map any nonlinearities in near modules.

Independent measurements of module optical sensitivity will be performed in the lab before shipping and deployment in the ice. In particular, the sensitivity of a selected subset of modules will be thoroughly characterized as a function of wavelength and angle. To transfer this detailed characterization to the full population, all modules will undergo

a time-efficient testing process similar to that used in IceCube [15], but with increased emphasis on angular and wavelength dependences. Similar measurements of IceCube DOMs [125] suggest that a systematic error of 2% can be achieved in the laboratory.

The efficiency in ice includes the effect of the local ice properties, and is measured in IceCube using low energy muons [22], with an uncertainty of 10%. This measurement may be improved by better reconstruction of the position and direction of low energy muons.

#### 7.3.4. Ice Properties

The ice into which the modules are deployed consists of two components: the undisturbed bulk ice between strings, and the melted and refrozen hole ice in which strings are deployed. The optical properties of the bulk ice depend on local dust concentrations, which were measured in IceCube with dust-logging devices during deployment and with LED flashers after deployment [1]. IceCube measurements have shown that the scattering and absorption properties of the bulk ice between the holes are highly location-dependent. Concentrations of dust in the ice vary with depth, creating approximately horizontal layers. These dust layers are not perfectly horizontal, and the concentration of dust at a given depth for one string can therefore differ from the concentration of dust at the same depth for another string. Both the absorption and scattering lengths of the ice track the dust concentrations. Additionally, the strength of scattering in the ice appears to be anisotropic with respect to the azimuthal angle of the photon direction [23].

At the depth where PINGU will be deployed (between 2150 and 2450 m below the surface of the ice), typical scattering and absorption lengths are greater than 25 m and greater than 100 m, respectively [1]. The scattering length is therefore comparable to or longer than the PINGU inter-string spacing of about 20 m. Currently the scattering and absorption lengths in IceCube are measured to within 10% using LED flashers co-located with IceCube DOMs [1]. In addition to the 10% uncertainty on the optical properties of the ice, there is additional uncertainty due to unsimulated effects, which appears as a difference in the simulated and actual charge deposited by LED flashers. For example, if the anisotropy is not simulated, this introduces a 30% spread in the difference between the simulated and actual charge [1]. Improvements to the LED flashers in PINGU are under study (see Sec. 7.4) in order to better measure the bulk ice properties.

The hole ice includes bubbles from the refreezing process in the columns surrounding the sensors, as discussed in Sec. 5.6. These bubbles modify the angular sensitivity of the

Table 11: Summary of proposed PINGU calibration devices and their purposes.

	LED flashers	POCAM	Cameras	MTOMs	Compass	Inclinometer
Energy scale	✓	✓				
Bulk ice	✓	✓				
Hole ice	✓	✓	✓			
Sensitivity	✓	✓		✓		
Geometry	✓		✓		✓	✓
Timing	✓					
Azimuth	✓		✓		✓	✓
Ice motion	✓					✓
Cable shadow			✓			

module in ice, especially in the forward direction, as measured by flashers and muons in ice [1]. The degassing process planned for PINGU deployments (see Sec. 5) is intended to reduce or eliminate the formation of bubbles in the hole ice. Instruments discussed in Sec. 7.4 will investigate any residual effects of the hole ice.

#### 7.4. Calibration Devices

As the studies of calibration requirements progress, we are looking at cost-effective improvements to the calibration devices used in IceCube. In this section, we will discuss several new or improved calibration devices designed to significantly improve our understanding of the detector. A summary of calibration devices and their purposes is shown in Table 11.

##### 7.4.1. LED Flashers

LED flashers are installed with IceCube/DeepCore DOMs [126] and will be co-located in all PINGU modules. Flashers are versatile devices with a range of settings which have been used in IceCube to measure ice properties, module sensitivity, timing, orientation and the coordinates of deployed modules. Measuring the highly location-dependent variation in the optical properties of the ice requires calibration sources at multiple locations within the PINGU instrumented volume. Several improvements are planned for both the design and characterization of PINGU light sources in order to achieve the desired calibration goals. A conceptual sketch of a PDOM with upgraded PINGU flashers is shown in Fig. 62. An

extensive simulation effort is currently underway to optimize the properties of the flashers.

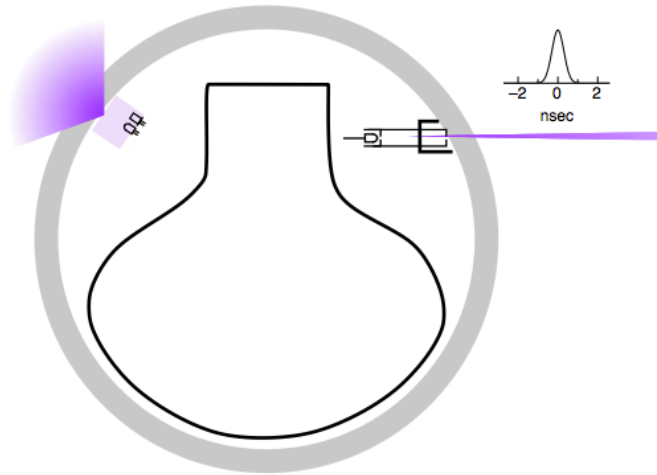


Figure 62: An upgraded PINGU module with flashers.

- **LED light output:** Photodiode monitoring of the LEDs on the control board will increase confidence in the laboratory characterization and will allow for better control of the brightness settings, especially at low light levels, which will be necessary in order to measure the ice properties across the short distances between PINGU modules.
- **LED pulse timing profile:** In IceCube, the minimum LED pulse width is 7 ns. In order to measure the scattering function more precisely over short distances, the LED pulse width should be reduced below 2 ns so that the time behavior of the received light is almost entirely due to scattering rather than the source pulse shape. R&D efforts are underway to determine the feasibility of producing a 1 ns pulse in the ice. Pulse widths of 3 ns have been produced in the lab using IceCube LEDs, and it is expected that widths of 1-2 ns can be achieved with an updated driver circuit. A very simple fast driver, proposed by Kapustinsky *et al.* [127], has been successfully used by a variety of experiments for calibration.
- **LED orientation:** IceCube LEDs are positioned at one of two zenith angle orientations: pointing horizontally outward (perpendicular to the cable) and pointing

upwards at an angle of  $45^\circ$  above horizontal. Other angles are being investigated for PINGU flashers, such as flashers pointed straight upward in order to be maximally sensitive to the optical properties of the hole ice. The mDOM sensor design allows the most flexibility in placement of LEDs.

- **LED direction:** The orientation of the IceCube LEDs within a DOM is only known to within  $\pm 5^\circ$ . A housing for the LED in the PINGU module would control the direction to within  $1^\circ$ , which is better than needed given the spacing in PINGU. The azimuthal LED orientations will be determined *in situ* using the observed light pattern in surrounding modules.
- **LED angular emission profile:** IceCube LEDs have a beam width of  $10^\circ$  in ice. Both wider and narrower beam widths are under investigation; a wide beam can be achieved by coupling the LED to a diffuser, and a narrow beam can be achieved by using a collimator. The LED emission pattern will be measured in the lab.
- **LED wavelength:** Most IceCube LEDs have a wavelength of 405 nm, with a few modules containing LEDs with wavelengths of 505, 450, 370 and 340 nm. These LEDs have been used to validate the wavelength dependence of the scattering and absorption lengths in the ice. PINGU modules may contain different wavelength LEDs in order to further study the wavelength dependence of the ice properties and the module response in ice.

#### 7.4.2. POCAM

A diffuse light source called the Precision Optical CALibration Module (POCAM) is under development to complement the LED flashers [128]. The POCAM is a light source that will not be located inside a module, but rather on the cable alongside the modules. The main goal of the POCAM is isotropic illumination of a large part of the PINGU volume by building a light source that is not shadowed by a PMT. Similar to the LED flashers, we plan to use monochromatic LEDs with several different wavelengths as a primary light source. A single LED per wavelength is used to achieve isotropic illumination. The POCAM will be self-calibrating and the light output will be continuously monitored.

The PINGU baseline geometry shows an overall symmetry in the azimuthal direction. However, for the PDOM has an up-down asymmetry due to the module's asymmetric construction (see Fig. 41). In addition, the orientation of any module (sensor or POCAM) will be random in azimuth along the string axis during deployment and will be fixed after

hole ice refreezing. Given that, we aim to reach an ice illumination in the azimuthal direction with a homogeneity on the order of 1 % and relax the requirement on homogeneity in the zenith direction to  $< 10\%$ . Overall, we aim to measure the POCAM’s emission profile with a precision better than 1 %.

Initial POCAM studies used the well-tested IceCube pressure sphere as the housing, and we identified three major components that challenged the isotropic-emission requirement. These included (a) the cable penetrator, (b) the main cable itself and (c) the waistband and harness, which causes a certain amount of shadowing, interrupting the homogeneity of the illumination.

We developed a dedicated Geant4 [19] simulation to study and optimize the light emission of the POCAM [129]. We investigated the POCAM’s performance for two configurations: (a) a multi-port (see Fig. 63, left) and (b) a diffusing semi-transparent layer setup (shown in Fig. 63, middle). In the first configuration we investigated the light homogeneity and timing depending on the integrating sphere diameter, the number of ports, the position and the radius. To investigate the properties of the second configuration we modified only the radius of the semi-transparent sphere and its thickness and thus the probability of photons being reflected, transmitted or absorbed through the sphere’s wall. Investigation of shadowing, and inhomogeneities which limited light emission in the spherical design, led to an updated pill-shaped design (see Figure 63, right). This design allows light emission over  $4\pi$  from two separated hemispheres. The simulation results shown below are for the spherical POCAM but have informed the development of the pill-shaped POCAM.

The performance of both configurations was studied for two diameters, 24 cm and 6 cm. The larger diameter is limited by the size of the IceCube pressure sphere leaving some space for electronics and cables. The smaller diameter was chosen empirically considering handling during construction. The settings of those four configurations are summarized in Table 12.

The resulting inhomogeneities for three zenith angle bands, together with the decay constants of the time response of the integrating spheres, are also listed in the Table 12. In Fig. 64 we show the average photon emission direction in azimuth for  $1^\circ$  zenith angle bands (left) and the emission time profile (right) of the studied integrating spheres.

Generally, the smaller spheres for both versions of the setup show better homogeneity, reaching  $\sim 2\%$  inhomogeneity in azimuth direction inside narrow zenith bands in the regions not affected by shadowing. On the other hand the diffuse semi-transparent

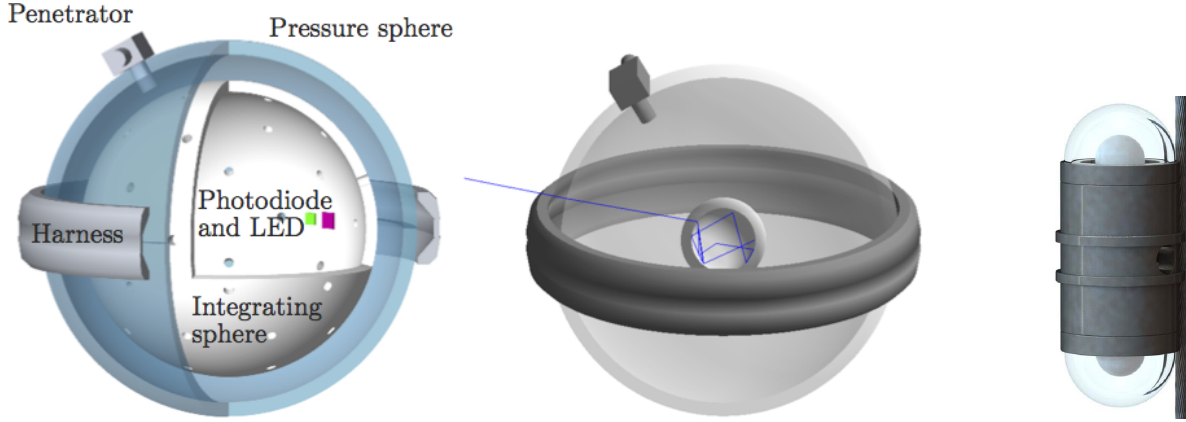


Figure 63: Left: A multi-port POCAM placed in the IceCube pressure sphere. Middle: A diffusing semi-transparent setup of the POCAM. The blue line shows a sample simulation of a photon emitted from a LED and undergoing several reflections before leaving POCAM. Right: cylindrical POCAM design.

Table 12: POCAM configurations: integrating sphere diameter  $D$ , number of ports  $n$ , port opening angle  $\alpha$ , effective photon transparency  $T$ , photon absorption  $A$ , and inhomogeneity for three different zenith angle zones  $\theta$ .

Config.	$D/\text{cm}$	$n$	$\alpha/^\circ$	$T/\%$	$A/\%$	Inhomogeneity/%			$\tau/ns$
						$\theta < 60^\circ$	$60^\circ \leq \theta \leq 120^\circ$	$\theta > 120^\circ$	
$C1$	24	768	1	1.5	61.0	11.9	18.5	11.6	35.1
$C2$	6	768	1	1.5	74.4	14.7	56.4	10.3	11.7
$C3$	24	-	-	2.5	50.3	12.4	14.5	12.4	13.1
$C4$	6	-	-	2.5	50.7	14.3	61.3	10.3	3.1

configurations show significantly shorter response compared to the multi-port version of the same diameter. Overall we can conclude that a POCAM consisting of a diffuse semi-transparent integrating sphere with a diameter of 6cm shows the smallest inhomogeneities while giving the shortest response time. The pill-shaped POCAM design uses glass hemispheres with an external diameter of 4.5 inches, with the diffuse semi-transparent layer made of polytetrafluoroethylene (PTFE).

We also plan to investigate the feasibility of using a completely different approach for a diffusing light source based on the concept of a diffusing ball described in [130]. This concept provides a simple and inexpensive solution for the POCAM.

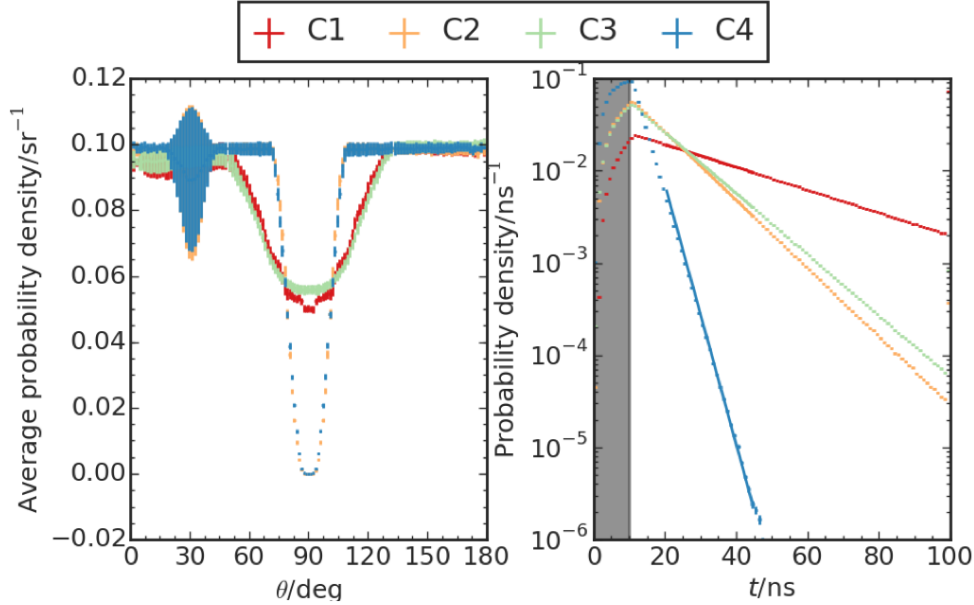


Figure 64: Left: Average photon emission direction in azimuth direction for different zenith angle bands. The error bars show the standard deviation. Right: Emission time profile. The shaded area refers to the rectangular LED time profile with a width of 10 ns. An exponential distribution is fitted to each time profile for  $t > 20$  ns and shown as a solid line. The decay times are listed in Table 12.

For the POCAM’s light source we are investigating individual monochromatic fast-switched (few nanosecond) LEDs and a fast LED driver circuit. The Kapustinsky driver is able to drive LEDs with pulses of  $\Delta t = 1 - 2$  ns (FWHM), and the LED provides light pulses with up to  $10^9$  photons per pulse. This photon yield corresponds to an electromagnetic shower with an energy of  $\sim 6$  TeV. Light intensity can be controlled directly by the applied supply voltage ( $V_{CC} < 24$  V). Assuming the dynamic range of the modules is large enough, and that they do not saturate, the energy resolution can reach 1% in the case of an ideal detector.

An important feature of the POCAM is the continuous pulse-by-pulse monitoring of the light emission with a precision of  $\sim 1\%$ . Here we are considering fast solid-state detectors such as photodiodes or silicon photomultipliers. In the recent years the technology of the latter sensors shows a continuous improvement in performance, which makes it an interesting alternative to photodiodes.

### 7.4.3. Cameras

A high-resolution camera similar to the one already deployed in IceCube [124] will be deployed with at least one string to photograph the hole ice during and after refreezing. Comparison of PINGU hole ice photographs with photographs taken by IceCube will provide early data on the efficiency of the degassing and filtering program.

We are also planning a more comprehensive set of visual hole ice data via deployment of low cost cameras [131]. These on-board cameras, located on all or a large fraction of PINGU modules, could provide quantitative data and qualitative information about the local environment of each module, valuable to the interpretation of other calibration measurements. Together with the cameras, one or more bright LEDs are required as light sources for the system. The goals of the camera measurements can be categorised into five groups: (1) Hole-ice measurements, (2) Bulk-ice measurements, (3) Geometry calibration, (4) Freeze-in observations, (5) General survey of the module environment. Figure 65 illustrates the potential camera measurements.

The main goal of the camera system is to better understand the hole ice. It could be utilised to observe where individual modules are located with respect to the interface between the bulk ice and the hole ice. The camera would detect bubbles in the refrozen hole, dust or large contaminants. The camera system could also determine the module position with respect to the cable and thereby reliably measure the effect of cable shadowing on the module sensitivity.

Measurements of bulk ice properties are possible by observing the scattered light from LEDs on adjacent strings to the observing camera. A variety of geometry measurements that compliment the standard IceCube-like geometry calibration are also possible. These measurements could range from measuring the module  $\phi$ -orientation to measuring inter-string distances. Observations during and after freeze-in allow for a better understanding of the fundamental hole-ice properties and ice formation process. Another virtue of the camera system is the ability to survey changes in the module environment.

The camera system would use small inexpensive fixed focus CMOS or CCD cameras mounted on the main board or attached to penetrator of the pressure sphere. For increased light sensitivity and reduced data volume, black and white cameras would be used. Colored images could still be obtained by illuminating with RGB-LEDs. CMOS cameras combine low power usage ( $\sim 0.3$  W), wide field of view, high resolutions, and good light sensitivity. CCD cameras have a significantly higher light sensitivity compared

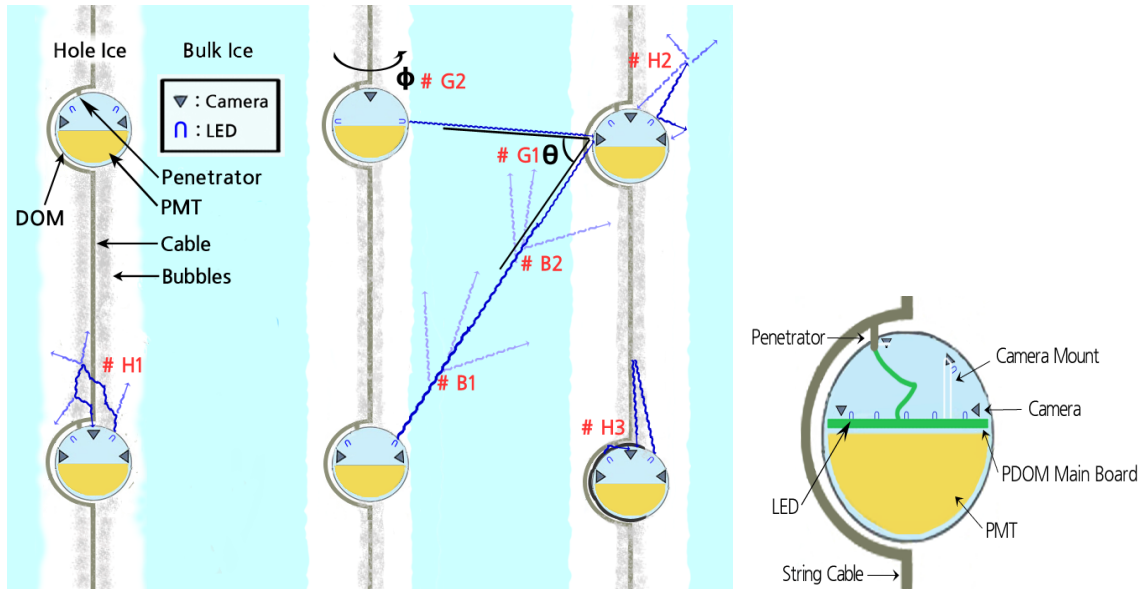


Figure 65: Left: Schematic drawing to illustrate potential camera measurements: (H1) Hole ice survey; (H2) Mapping of hole shape; (H3) Cable position and orientation; (B1) Light transmission and scattering at hole ice - bulk ice interface; (B2) Light attenuation and scattering in the bulk ice; (G1) Orientation of the camera in the module; (G2) module geometry. Right: Potential camera positions in the PDOM.

to CMOS cameras, but consume more power ( $\sim 1\text{W}$ ) and have lower resolutions. Figure 66 compares light sensitivities in the PINGU geometry. Long-exposure still images would be taken that are only limited by the intrinsic camera noise.

As an example, to see a typically bright LED ( $\sim 2\text{--}3$  candela) located in a neighboring module in the adjacent string at 20 m distance, the camera should have sensitivity  $\sim 0.001$  lux (typical sensitivity of a CMOS camera). A fish-eye lens might be used to increase the field of view of the camera. Precise knowledge of the camera and LED position and orientation on each module is required to use the system for geometry calibration.

IceCube data transfer rates even allow for large raw images to be transferred on time scales of several minutes, keeping calibration measurements short. Images would be analysed offline, corrected for image distortions from the pressure sphere, and used to study ice properties and hole ice conditions.

The camera system would be mounted separately on a small camera board, and communicate with the module mainboard via an SPI (Serial Peripheral Interface) or similar interface. The camera board (approximately  $35\text{ mm} \times 35\text{ mm}$ ) would contain a MCU

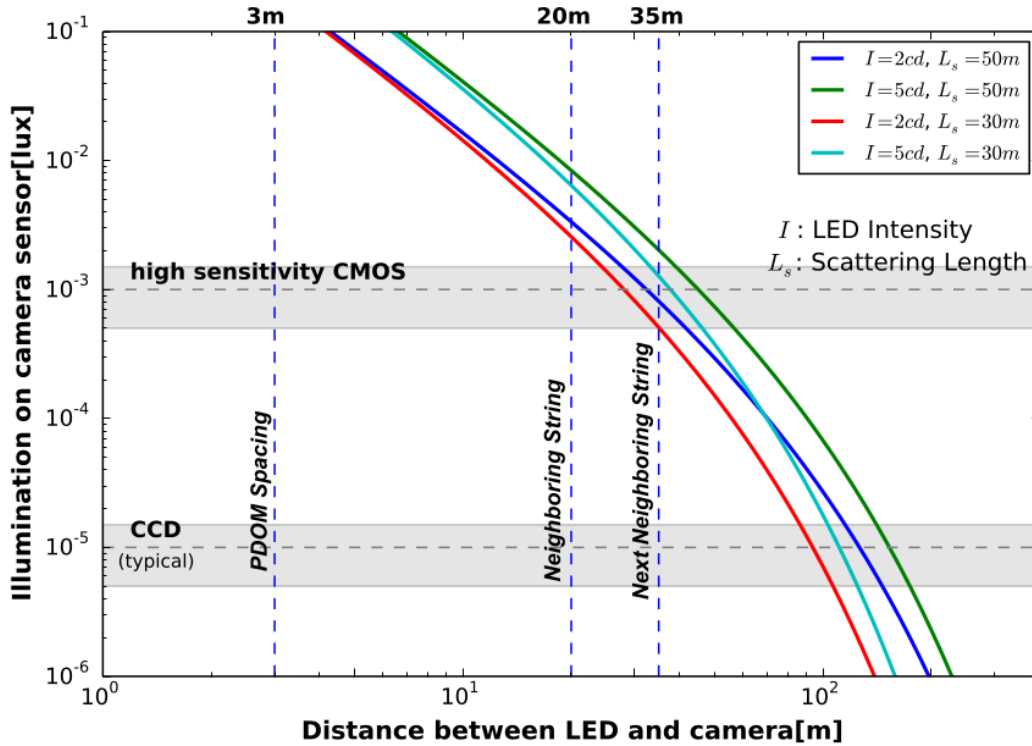


Figure 66: The minimum illuminance required for a camera to see an LED located in the neighboring module on the same string, and on an adjacent string, are shown. An exposure time of 1s is assumed. The gray area at the top is that of a typical CMOS camera sensitivity. The gray area at the bottom represents the typical sensitivity of a CCD camera.

(Micro Controller Unit) next to the camera for image processing. Most of the time this system operates in power-saving mode.

#### 7.4.4. Muon Tagging Optical Module (mTOM)

We are investigating the possibility of deploying scintillator detectors called Muon Tagging Optical Modules (mTOMs) in PINGU to tag the position of muons with high precision (to within a few cm). This approach is inspired by a recent study using the DM-Ice17 dark matter detector, that consists of two 5-inch NaI crystals deployed in the IceCube volume [132]. While the primary purpose of the DM-Ice17 detector is the direct detection of dark matter, the crystals detect 1-2 muons per day that also trigger the IceCube array.

A study of the impact in energy, direction, and position uncertainty of muons using the DM-Ice17 detector in conjunction with IceCube has been performed [133]. This has shown a reduction in mis-reconstructed events, when tagging the muon using the NaI crystals, as well as an improvement in the track reconstructed position. Given that the mTOM's size is 10 times smaller than the DM-Ice17 crystal, the track can be better localized.

The mTOMs in PINGU would be constructed of solid,  $5\text{ cm} \times 5\text{ cm} \times 1\text{ cm}$  plastic scintillator block placed within a light-tight reflective aluminium casing. A prototype of this design has been developed in the context of a stand alone desktop muon counter [134]. The optical read-out is provided via a silicon photomultiplier (SiPM). These Modules have a thin profile, so that they require very little space within the module, making it possible to have four modules per PDOM. The detector would be hardwired into the standard PINGU DAQ.

If four mTOMs were deployed in each PINGU DOM, we expect to detect approximately  $10^6$  downgoing cosmic ray muon interactions per year. These identified muons could then be used for detailed calibration of PINGU.

## 8. Monte Carlo Simulation Software

Simulations of the PINGU detector have been carried out using the Monte Carlo tools developed for the IceCube experiment. The strong similarities between the IceCube and PINGU hardware permit capitalizing on the extensive efforts that have gone into refining the IceCube simulation model of both the Antarctic ice and also the hardware response. However, some modifications to the standard IceCube tools were necessary to produce reliable simulations of neutrino interactions in the range of 1–20 GeV, and there have been modifications to the IceCube simulation tools in order to more correctly simulate the detector. All of these elements are detailed in this section.

### *8.1. Neutrino Event Generator*

Although most high-energy IceCube neutrino simulations rely on the NuGen event generator (based on ANIS [135]), simulations of neutrinos interacting in the PINGU detector are based on the GENIE Neutrino Monte Carlo generator [18] version 2.8.6, that is used extensively in the accelerator-based neutrino physics community. GENIE conducts a full simulation of the neutrino-nucleon interaction, and produces a list of secondary particles exiting from the interaction vertex, modeling intranuclear interactions where necessary. All neutrino interaction channels are modeled by GENIE, although the bulk of the events detected by PINGU arise from deep inelastic scattering (DIS).

A wrapper was created to embed GENIE within the IceCube software framework. Events are generated isotropically from a user-defined power law distribution (normally  $E^{-1}$ ) and need to be reweighted to reproduce the atmospheric neutrino spectrum [33]. A newer atmospheric model was specifically developed for use at the South Pole [136] in order to accurately incorporate the Earth’s geomagnetic effects on the arrival directions of cosmic rays. The asymmetry in the resultant neutrino flux as a function of azimuth and zenith starts at  $\sim 10$  GeV and becomes more pronounced at lower energies. While a rewrite of the weighting software to incorporate the asymmetry is underway, an average flux over the full azimuth range was used to produce an atmospheric neutrino flux value. The spectrum currently used for generation ( $E^{-1}$ ) is very different from the expected spectrum so that the higher energy events can be sampled more efficiently. This is necessary for parameterizing the response at all energies as explained in Secs. 2.4 and [Appendix A](#).

In addition to considering the atmospheric weighting, this reweighting procedure permits rapid assessment of the impact of uncertainties in the true flux and spectrum of

the atmospheric neutrinos. GENIE enables extensive modeling of the uncertainties for neutrino interaction physics [18] be taken into account in the simulation. Specifically, the uncertainties that are studied address the neutrino interactions for the major types of events that are simulated for use in the analyses: deep inelastic scattering (DIS), resonance production (RES) and quasi-elastic (QEL) interactions. These interactions are each addressed separately.

Deep inelastic scattering events will be the most prevalent type in the PINGU low-energy dataset. In the GENIE simulation code employed for PINGU simulations, the model used is that provided by Bodek and Yang [137] which accounts for higher twist and corrections to the target mass. The parameters specifically used in the PINGU analysis for the DIS events deal with the twist parameterization (AhtBY and BhtBY) and the correction to the  $u$  valence quark in the GRV98 PDF (CV1uBY and CV2uBY).

The resonance production events are generated based on the Rein-Sehgal model [138] and have the associated uncertainties included in the production calculations for the axial mass parameter for charged current (MaCCRES) and neutral current (MaNCRES) interactions. Finally, the QE events are also considered and the axial mass is also taken into account for charged current interactions (MaCCQE). In all these cases, the effects of variations of these parameters up to  $\pm 2\sigma$  are computed and parameterized for use in the analysis.

To improve performance, neutrino interactions were simulated inside a cylinder of 200 m radius and 500 m height centered on PINGU. Because the atmospheric muon veto is extremely effective at rejecting particles originating outside of the PINGU fiducial volume, the reduction in neutrino rate at the analysis level introduced by this approximation should be negligible.

## *8.2. Atmospheric Muon Event Generators*

Computational resource limitations do not permit generation of event samples comparable to the expected atmospheric muon rates, so we rely primarily on the demonstrated muon rejection performance of the IceCube DeepCore detector to support our estimates of muon background rates. Since the extra instrumentation available in PINGU will improve the currently available reconstructions in the DeepCore volume, the existing algorithms that reject atmospheric muons will be further improved and, therefore, this estimate should be strongly conservative. Accordingly, our neutrino efficiencies are calculated by applying slightly modified DeepCore event selection routines to our simulated neutrino events, and

the atmospheric muon samples produced for PINGU are primarily intended to confirm that these event selections behave as expected.

Two methods were used to produce samples of the atmospheric muon background. The first utilized full Corsika [89] simulation of air showers produced by cosmic rays incident on the upper atmosphere, tracking the muons produced in such air showers to the PINGU detector. The second, known as the “muon gun,” parametrizes the angular and energy distributions of the muons produced in the Corsika simulations and injected muons from a hemisphere extending just outside the IceCube detector volume.

### *8.3. Particle Propagation*

The relativistic particles produced at a GENIE neutrino interaction vertex were tracked by GEANT4 [19] until they, and any daughter particles produced, fell below the Cherenkov threshold. All of the Cherenkov photons produced were stored for propagation through the ice by a separate program (see below). This provided a more detailed model of the light emission from the neutrino interaction vertex than the standard IceCube tools, which relies instead on parametrized descriptions of prototypical hadronic and electromagnetic showers. Atmospheric muons traveling through the detector were modeled using the standard IceCube particle propagator PROPOSAL [139], instead of GEANT4.

### *8.4. Light Propagation*

Once the relativistic particles were propagated through the detector volume by GEANT4 or PROPOSAL, the Cherenkov photons produced were tracked by the IceCube software tool “clsim.” This is a parallelized, GPU-based software package that permits full treatment of photon propagation throughout the extremely large volume occupied by IceCube. The depth-dependent optical properties of the Antarctic ice have been extensively studied by the IceCube Collaboration, and the full details of this optical model [1] were included. At each propagation step, photon scattering is modeled by numerical approximations to the Mie scattering function, as developed and tuned by IceCube.

### *8.5. Detector Response*

The main optical elements of the planned PINGU DOMs are identical to those used in DeepCore, so the detector response modeling of the DOMs was used without modification

(except that an average calibration function was used for each DOM, rather than the individualized DOM models used in IceCube simulations). Recent studies of dark noise in IceCube have shown that there is a significant non-Poissonian component to the DOM noise, possibly arising from scintillation in the pressure housing glass or the PMT glass at very low temperatures; this effect was included in the detector simulation. Improvements to this noise model [21] were some of the main updates included in the simulation since the first version of this letter.

Although the digitization electronics used in PINGU will differ from the IceCube and DeepCore design, no modifications were made to this aspect of the simulation software. The dynamic range of PINGU may be slightly narrower, but given the much lower energy range of the neutrinos of interest, saturation of the PINGU electronics should be rare for events in the desired energy range. The timing resolution of the PINGU electronics will be similar to that of IceCube, so the photon timing and pulse resolution should be similar. The PINGU electronics will provide this timing resolution over the full event time range, whereas the IceCube electronics occasionally need to fall back on a slower FADC with coarser timing resolution.

In IceCube and DeepCore, data rates from individual DOMs are reduced by imposition of a local coincidence in hardware. If neighboring DOMs also detect light, a full data record is transmitted to the surface; otherwise, only a brief summary record is sent. No dedicated local coincidence circuitry is planned for PINGU, but we anticipate that onboard photoelectron pulse extraction in FPGAs, and string-level software coincidence logic at the surface, will allow us to fit PINGU data comfortably within the available cable bandwidth. Again, to the extent that the PINGU hardware differs from the model used in simulation, the additional flexibility in software-based coincidence logic will only improve PINGU performance over the model used in simulation. We therefore have a high degree of confidence in our simulation of PINGU.

The trigger rate in DeepCore is quite low, demanding only three close-neighbor DOMs with locally-coincident hits within a time window of a 2.5 microseconds. Although this threshold may not be feasible given the much higher number of DOMs in PINGU, very few simulated neutrino events near the trigger threshold survive the relatively strict event selection applied to neutrino events used in the performance studies presented in this document. We anticipate that the inclusion of spatial, as well as temporal, information into the PINGU trigger will permit use of trigger algorithms which would record all of the events used in these studies.

Project Year	Activities
1	Drill engineering and refurbishment, Optical module production
2	Drill engineering and refurbishment, Firn drill transport, Optical Module production and transport
3	Drill transport, Site preparation, Optical module production and transport
4	Deployment, optical module transport
5	Deployment

Table 13: Summary schedule for construction of PINGU.

## 9. Schedule and Cost

The proposed schedule and cost for PINGU is largely based on the successful construction of IceCube. IceCube was completed on time and on budget over a 10 year period that included eight seasons of construction and installation at the South Pole starting in the austral summer of 2003/2004. IceCube construction was completed in January 2011. The plan for the construction schedule of PINGU incorporates knowledge obtained from IceCube along with considerations related to the length of time between IceCube completion and the start of PINGU. The schedule is driven primarily by funding availability and is not technically limited.

We anticipate that two years will be required for refurbishment and improvement of the IceCube hot water drill. Optical module assembly and transportation to the South Pole would occur in parallel with this effort. Once the drill and optical modules are available at the South Pole, the full PINGU array can be deployed in two seasons. Some preparatory activity (snow compacting, firn drilling) would be required in the prior South Pole season to enable a prompt start to deployment once the drill arrives. A summary of the envisaged schedule is shown in Table 13.

In summary, PINGU will take approximately five Project Years to build and will require two austral summer deployment seasons at the South Pole. The schedule does not currently take into account possible funding constraints related to federal budget years that begin each October. If a Phase 1 proposal is approved, all of the work related to the drill and module development will be completed in advance of a full PINGU deployment, cor-

responding to approximately the first three years of a full PINGU construction timeline. There would also be a commensurate reduction in the cost for completion of PINGU, since development, transportation and testing of the drill, as well as module development, will have already been completed. Similarly, Phase 1 will retire virtually all of the associated risk for PINGU.

The start of module production is planned for PY1 with an expected integration and test rate of 24 modules per week at each production site. One such site will be the Physical Sciences Laboratory (PSL) in Stoughton, Wisconsin. PSL successfully integrated and tested approximately 3500 Digital Optical Modules for IceCube from 2004 to 2009. Physical infrastructure including important Dark Freezer Labs, along with key personnel, remain at PSL making this a natural choice for one of the several production facilities.

The first scheduled module deployment season for PINGU will be in PY4. It is planned that 6–8 holes would be drilled in this initial season. To accommodate a potentially faster drilling schedule, 10 complete strings of instrumentation will ship from production sites and the associated cable system production site to meet Polar Program logistics requirements. Instrumentation production would take place continuously to accommodate the deployment of the remaining additional strings of detectors in PY5. Final string commissioning and IceCube integration would occur late in PY5 when PINGU would be complete.

As with the schedule estimates described above, the cost estimates for PINGU are largely based on extensive experience obtained from IceCube construction. We have created a detailed Work Breakdown Structure (WBS) with the following top level task areas:

1. Project Office
2. Drilling
3. Detector Modules
4. Cable System
5. Power, Communications, and Timing System
6. Calibration System
7. IceCube Integration
8. Polar Operations (except drilling)
9. Antarctic Support Contractor

A detailed bottom-up estimate that extends three levels into the WBS, including inflation but not contingency, has been performed for the 40-string, 96 module/string PINGU

	Cost (20 Strings)	Cost (26 Strings)
Drill refurbishment	\$5M	\$5M
Deployment (labor)	\$5M	\$5M
Instrumentation	\$24M	\$32M
Management & other costs	\$5M	\$5M
Total	\$39M	\$47M
Fuel	146 000 gal	190 000 gal

Table 14: Summary costs for construction of PINGU in U.S. dollars. Deployment labor includes the scientists and engineers associated with the hot water drill and string installation effort. Fuel requirements for the hot water drill are provided as volumes due to uncertainties in the price of oil and the impact of the overland traverse on transport costs; recent costs are approximately \$20/gal.

geometry [14]. This earlier estimate leveraged some cost savings with PINGU being a part of a large-scale IceCube high energy extension of order 100 strings. However, with PINGU built in two seasons with many fewer strings, its overall cost decreases even when budgeted as a standalone project. With fewer holes drilled in fewer seasons, but more modules per string, project costs are driven less by drilling, cable and deployment expenses, and more by module procurement and production expenses. Experience gained from the IceCube deployment indicates that installing up to 20 strings in a single season is feasible. The anticipated schedule involves the installation of 8 strings in the first season (allowing time for restarting the procedure) and 18 in the second for a total of 26. A pessimistic scenario is also presented in which 6 strings are installed in the first season and 14 in the second for a total of 20. In each of these scenarios, the number of modules per string has been increased to 192. The rough costs of these two scenarios are given in Table 14.

The potential for the use of a new optical module has also been considered with minimal impact on the total budget. The cost for an IceCube-like PDOM is \$5.2k while the cost for the mDOM-like module (see Sec. 5.4.1) has been estimated to be \$8k. (An mDOM has more than double the photocathode area of a PDOM.) The use of 125 mDOMs per string would then result in a net savings while increasing the overall number of photons collected.



Figure 67: The Amundsen-Scott South Pole Station.

## 10. Antarctic South Pole Facility and Logistics

At the Amundsen-Scott South Pole Station, operated as a scientific facility on behalf of the National Science Foundation (NSF), astrophysical observations have been underway for several decades, and to date represent the majority of ground-based astrophysical work in Antarctica. Relatively recent overviews of neutrino, cosmic ray and astronomy programs at the South Pole have been presented at a workshop in 2011 in Washington [140] and at the Symposium 288, *Astrophysics from Antarctica*, at the International Astronomical Union General Assembly [141].

The Amundsen-Scott station provides excellent infrastructure for scientific activities at the South Pole, including the IceCube Laboratory (see Fig. 1) building that houses power, communications, and data acquisition systems for IceCube. The South Pole Station facility, shown in Fig. 67, was completed in 2008, prior to the completion of IceCube. The realization of IceCube established the South Pole ice cap as an underground laboratory that is available as a resource for scientific endeavors beyond IceCube.

The station is accessible by aircraft from approximately November through mid-February, supporting a summer population of approximately 150, including both scientists and support personnel. During the remainder of the year, the station is occupied by approximately 40 winter-over personnel. Scientists typically make up around 25–30% of the personnel on station.

Whereas during the construction of IceCube all Antarctic intercontinental passenger and cargo transport was via ski-equipped LC-130 aircraft operated by the New York Air National Guard, the US Antarctic Program has been transitioning fuel and cargo transport to tractor traverses between the McMurdo and Amundsen-Scott stations (see Fig. 68). The cargo capacity of a single traverse, 350 metric tons, is thirty fold that of an LC-130 mission. A number of forty-five day round trip traverses have been achieved in recent austral seasons. This has dramatically reduced the program’s dependency on the limited LC-130 fleet, and cargo and fuel costs per unit of load delivered to South Pole are more cost efficient by \$11.50 per kg compared to an LC-130 airlift.

The PINGU effort is expected to rely heavily on the overland traverse to deliver many of its large-scale components, including elements of the drill, fuel, down-hole cables and modules. This will dramatically reduce the logistical footprint of PINGU construction at the South Pole, as will the significantly shorter active drilling and deployment duration of two seasons.

IceCube uses 60 kW of power and has access to a bandwidth of more than 100 GB/day for data transmission and detector control. Although PINGU and IceCube will have a comparable number of deployed sensors, PINGU is being designed to require roughly 1/5 the power and 1/10 the bandwidth of IceCube. PINGU is also being designed to integrate seamlessly with the IceCube data acquisition cyberinfrastructure at the South Pole, leading to economies of scale that reduce the additional computational power needed on the surface. Electrical power is provided by the station generators and is highly reliable with the IceCube detector operating with an uptime of approximately 99%. The primary means of data transmission from the South Pole is via a TDRS satellite link maintained by the NSF.

## 11. Acknowledgements

IceCube acknowledges the support from the following agencies: U.S. National Science Foundation-Office of Polar Programs, U.S. National Science Foundation-Physics Division,



Figure 68: From *Economic Analysis of the South Pole Traverse* [142]: “Three SPoT sled trains heading up the Leverett Glacier en route to the South Pole during the 2008–09 season. The front-most train includes the living and generator modules (red). Next in line is an MT865 towing a steel fuel sled (grey) and eight 3000 gal. bladders on flexible sleds (tan). The red Quadtrac is towing two coupled sets of bladder sleds, initially consisting of twelve 3000 gal. bladders but subsequently reduced by fleet consumption.”

University of Wisconsin Alumni Research Foundation, the Grid Laboratory Of Wisconsin (GLOW) grid infrastructure at the University of Wisconsin - Madison, the Open Science Grid (OSG) grid infrastructure; U.S. Department of Energy, and National Energy Research Scientific Computing Center, the Louisiana Optical Network Initiative (LONI) grid computing resources; Natural Sciences and Engineering Research Council of Canada, WestGrid and Compute/Calcul Canada; Swedish Research Council, Swedish Polar Research Secretariat, Swedish National Infrastructure for Computing (SNIC), and Knut and Alice Wallenberg Foundation, Sweden; German Ministry for Education and Research (BMBF), Deutsche Forschungsgemeinschaft (DFG), Helmholtz Alliance for Astroparticle Physics (HAP), Research Department of Plasmas with Complex Interactions (Bochum), Germany; Fund for Scientific Research (FNRS-FWO), FWO Odysseus programme, Flanders Institute to encourage scientific and technological research in industry (IWT), Belgian Federal Science Policy Office (Belspo); Science and Technology Facilities Council (STFC) and University of Oxford, United Kingdom; Marsden Fund, New Zealand; Australian Re-

search Council; Japan Society for Promotion of Science (JSPS); the Swiss National Science Foundation (SNSF), Switzerland; National Research Foundation of Korea (NRF); Villum Fonden, Danish National Research Foundation (DNRF), Denmark

## Appendix A. Mass Ordering Analysis Techniques

### Appendix A.1. Simulation of experimental Outcome

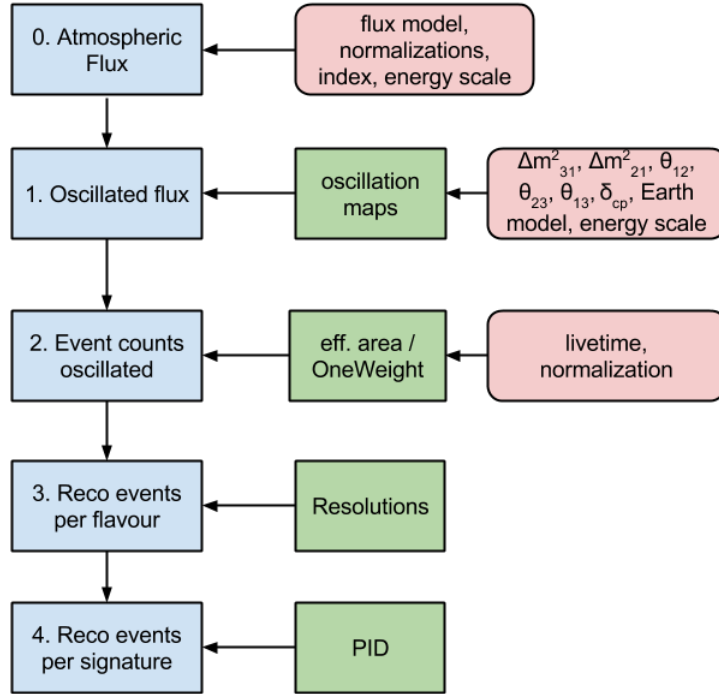


Figure A.69: Template simulation scheme. See text for details.

All statistical analysis methods presented here require an experimental expectation for the number of neutrinos, which is created in the simulation step (see Sec. 8). The same code is used to obtain this distribution of events in the  $(E_\nu, \cos\theta_\nu)$  or “template” for any given set of physical and systematic parameter values. Within the template the event information is binned in 20 equally spaced linear bins in the cosine of the zenith angle for the range  $-1 < \cos\theta_\nu < 0$  and 39 logarithmically spaced bins in energy for the range  $1 \text{ GeV} < E_\nu < 80 \text{ GeV}$ . The bins are chosen to be small enough to not artificially degrade the resolution, yet large enough to keep the computational effort affordable and retain sufficient statistics in each bin. To generate the template, we employ a staged approach, in which we assume that the effect modeled by each step is independent of any of the other steps. Figure A.69 shows the generation scheme that yields the final level templates. The individual detector response functions are generated using a set of simulated events,

thus fully taking into account both the physics modelled by GENIE, GEANT4, and the propagation of Cherenkov photons within a realistic ice model (see Sec. 8), as well as the effects of the detector resolution predicted by the full reconstruction and event selection pipeline (Sec. 2.4).

The simulation starts off at the flux stage, where two-dimensional maps of the expected primary atmospheric neutrino flux as a function of  $(E_\nu, \cos \theta_\nu)$  are produced for  $\nu_e$ ,  $\nu_\mu$  and the corresponding anti-particles. Here, we allow for uncertainties in the neutrino-to-antineutrino ratio, the muon-to-electron flavor ratio and the spectral index.

In the second step, the oscillation probabilities are computed on a fine grid for a given set of 3-flavor mixing parameters, taking into account the varying electron densities from Ref. [43] as the neutrinos traverse the Earth’s mantle or core. Since this is a task that is highly parallelizable for different trajectories through the Earth, we have adapted the existing GPU version of the `Prob3++` neutrino oscillation library [45] from Ref. [143] to be able to take into account layers of alternating matter density. Calculating the probabilities on a GPU instead of a CPU reduces the template generation time by up to a factor of 30, from around 3 s down to around 0.1 s. The four histograms containing the electron and muon (anti)neutrino fluxes are then each weighted with the appropriate survival and appearance probabilities of the various oscillation channels (averaged over the bin) to get the corresponding histograms for the oscillated flux, of which there are twelve in total.

Oscillated fluxes are converted into event counts by multiplying with the desired detector livetime, and folding in the detector’s effective areas for the various interaction channels. The effective areas follow from the event selection procedure laid out in Sec. 3.1.1. This is the stage at which the simulated detector response is included into this process.

Both the energy and angular resolutions of the detector are accounted for by multiplying the 2D histogram of detected events in the true parameters  $(E_\nu^{\text{true}}, \cos \theta_\nu^{\text{true}})$  with the 3D detector response matrix  $\mathcal{R} : E_\nu^{\text{true}} \rightarrow (E_\nu^{\text{reco}}, \cos \theta_\nu^{\text{reco}})$ . The matrix maps the true parameters on the reconstructed parameters  $(E_\nu^{\text{reco}}, \cos \theta_\nu^{\text{reco}})$  as a function of energy, thereby properly accounting for events that are lost due to being mis-reconstructed outside of the considered energy or zenith ranges.

In order to model the reconstruction resolutions as accurately as possible in each bin of  $(E_\nu^{\text{true}}, \cos \theta_\nu^{\text{true}})$ , we employ a variable-bandwidth kernel density estimation (VBW KDE) algorithm, that smoothes the reconstructed neutrino energy and direction histograms obtained directly from MC simulations. This is necessary in order to mitigate the effect

of the limited amount of MC statistics available, which would otherwise artificially bias the analysis results. As mentioned in Sec. 2.4, our algorithm is the fusion of two previously-published methods: first, a fixed-bandwidth KDE is made [26], with a modified version of the Sheather-Jones bandwidth selection criteria [28] that does not assume that the underlying distribution is normal. The individual kernels’ bandwidths for the full VBW KDE are then derived from the pilot density estimate [27]. A Gaussian kernel shape is used for both the fixed- and variable-bandwidth parts of the algorithm. At this step, a distinction is not currently being made between interactions of neutrinos and antineutrinos of the same flavor, nor do we assume different resolutions for NC interactions of different-flavor neutrinos.

Application of the event classification probabilities (as depicted in Fig. 11 and described in Sec. 2.6), but as a function of reconstructed neutrino energy, leads to the two final level templates, with event counts classified as either track-like or cascade-like using the particle identification.

### Appendix A.2. Log-Likelihood Ratio Analysis

The most statistically detailed analysis we employ—the log-likelihood ratio (LLR) analysis—entails two concepts: that of a *template* (introduced previously) and that of a *pseudo-experiment*, which is generated by calculating a bin-wise Poisson variation of the template.

The log-likelihood of observing the pseudo-data given a certain realization of physical and systematic parameters (the hypothesis used to generate the template)

$$\mathcal{L} \equiv \ln L = \sum_{i,j} n_{ij} \ln \mu_{ij} - \mu_{ij} - \ln n_{ij}! , \quad (\text{A.1})$$

where  $n_{ij}$  is the content of the  $(i, j)$ -th bin in the pseudo-data and  $\mu_{ij}$  is the expectation for that bin, taken from the template corresponding to the hypothesis. Gaussian priors are included via an additional sum of the form  $\mathcal{L}_{\text{prior}} = -\sum_k (\Delta p_k)^2 / (2\sigma_k^2)$ , where  $\Delta p_k$  is the deviation of the  $k$ -th systematic parameter from its central value, and  $\sigma_k$  is the width of its prior distribution.

Compared to the original version of this document [14], we are now able to include a larger number of systematics through the use of a numerical minimizer that maximizes the log-likelihood  $\mathcal{L}$  over all parameters, instead of performing a scan of the multi-dimensional space. The CPU time required to perform a single fit to a given pseudo-experiment

depends on the dimension of the parameter space and on the rigorousness of the minimizer, but is of the order of one to two minutes for our default settings in the eight dimensional space.<sup>5</sup>

The LLR test statistic is used in the NMO analysis to determine how much more one ordering (either the Inverted Ordering (IO) or the Normal Ordering (NO)) is favored by the pseudo-experiment. For any given pseudo-experiment, the two log-likelihoods  $\mathcal{L}(\text{pseudo-experiment} | \text{IO})$  and  $\mathcal{L}(\text{pseudo-experiment} | \text{NO})$  are calculated by finding the respective maxima of  $\mathcal{L}$ . Since the pseudo-experiment can be generated assuming either the IO or the NO is correct, this leads to the four possible combinations

$$\mathcal{L}(\text{IO}|\text{IO}) \quad \text{and} \quad \mathcal{L}(\text{IO}|\text{NO}), \quad \text{or} \quad \mathcal{L}(\text{NO}|\text{IO}) \quad \text{and} \quad \mathcal{L}(\text{NO}|\text{NO}). \quad (\text{A.2})$$

These, in turn, are used to create the LLRs<sup>6</sup>

$$\mathcal{L}(\text{IO}|\text{IO}) - \mathcal{L}(\text{IO}|\text{NO}) \quad \text{and} \quad \mathcal{L}(\text{NO}|\text{IO}) - \mathcal{L}(\text{NO}|\text{NO}), \quad (\text{A.3})$$

respectively. By choice of this convention higher values of this test statistic imply that the data is more consistent with the IO, while lower values suggest better agreement with the NO. By producing a large number of pseudo-experiments for each ordering, in which the individual outcomes each are subject to random fluctuations, one can build up the two LLR distributions, and quantify the agreement and disagreement between the underlying hypothesis and both hierarchies on a statistical basis. An exemplary case of the LLR distribution is shown in Fig. A.70.

### *Appendix A.2.1. Median Sensitivity*

Due to its use throughout the literature, we haven chosen to adopt the median sensitivity  $\alpha(\beta = 0.5)$ , which yields the confidence level  $1 - \alpha$  at which an experiment will reject the wrong ordering hypothesis with  $\beta = 50\%$  probability [32]. Figure A.70 demonstrates how the median sensitivity is obtained from two LLR distributions (A.3): we employ a one-sided test, i.e.  $\alpha$  is given by the fraction of cases in which the log-likelihood ratio of a wrong ordering experiment exceeds (true IO) or falls below (true NO) the median

---

<sup>5</sup>Note that whenever the mixing angle  $\theta_{23}$  is a free parameter the same pseudo-experiment is fit twice under the same hypothesis, with the minimizer being started in a different octant each time. This ensures that the global minimum is found, even when the likelihood landscape exhibits a strong octant degeneracy.

<sup>6</sup>Logarithm of the likelihood ratios, equivalent to the difference between the log-likelihoods.

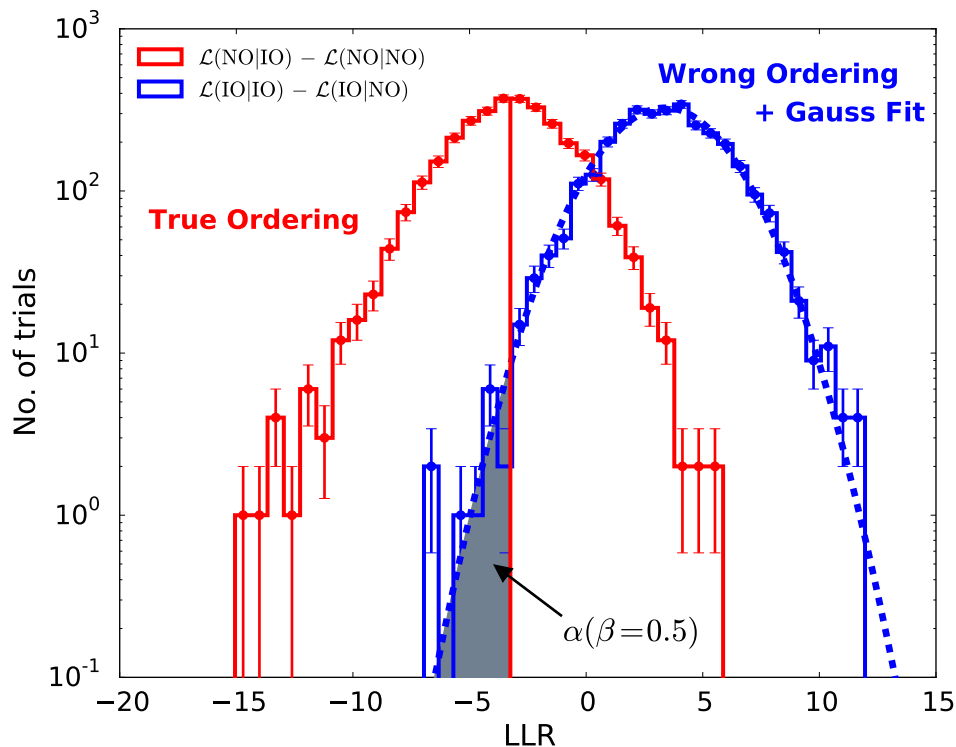


Figure A.70: Calculation of the median NMO sensitivity using the log-likelihood ratio (LLR) method. Shown are the LLR distributions based on a particular set of pseudo-experiments for true NO. The vertical red line indicates the median LLR for the underlying NO fiducial model. From a Gaussian fit to the wrong ordering distribution (here: IO), we determine the probability  $\alpha(\beta = 0.5)$  to misidentify the ordering in the “average” experiment. See text for details.

log-likelihood ratio of a true ordering experiment. The double-sided convention is applied to convert it into a corresponding number of Gaussian standard deviations,

$$n_\sigma = \sqrt{2} \operatorname{erfc}^{-1}(\alpha) . \quad (\text{A.4})$$

To mitigate statistical fluctuations on the determination of  $\alpha$ , we fit a Gaussian model to the test statistic distribution for the wrong/opposite hypothesis with a large number of trials (see [Appendix A.2.2](#)). Now the question arises of how to calculate the median sensitivity; every ensemble of pseudo-experiments we generate is based on one well-defined, fixed hypothesis, i.e. a certain combination of the ordering and oscillation parameter values, as well as the detector exposure time. Ideally in the next step, one would select one pseudo-experiment within the ensemble at hand, compute the best fitting solution

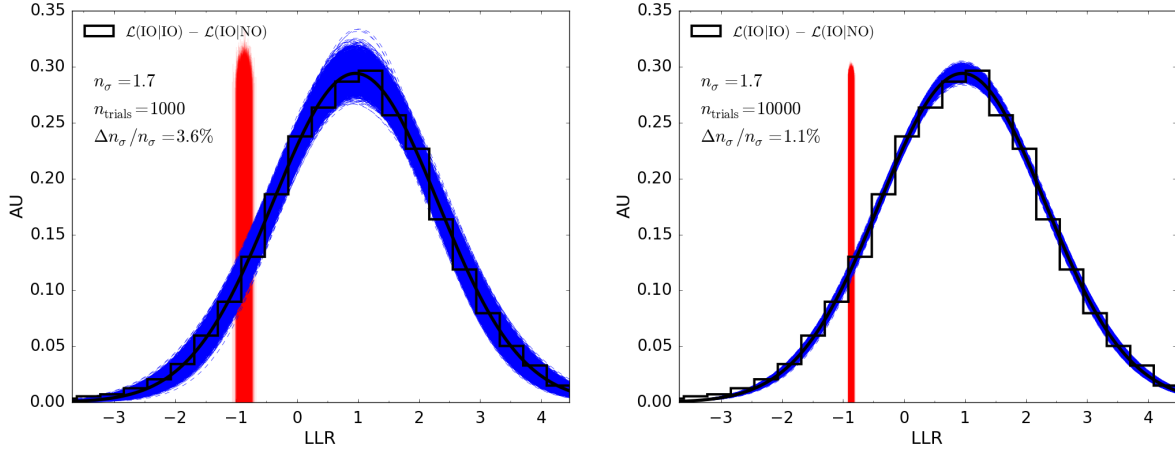


Figure A.71: 10 000 Gaussian fits (dashed blue) and TO-LLR means (red) from randomly sampling the underlying (Gaussian) LLR distributions. The left panel shows the case of 1000 pseudo-experiments, while in the right panel 10 000 pseudo-experiments were generated. See text for details.

within each ordering and produce one ensemble of pseudo-experiments for each hypothesis, in order to build up the LLR distributions (A.3) and calculate  $\alpha(\beta = 0.5)$ . Repeating this for each pseudo-experiment in the original ensemble would yield a distribution of sensitivities, the median of which would constitute the confidence level at which the average experiment would be able to exclude the wrong ordering, valid for the hypothesis assumed to be true in the first place. The problem with this approach is the number of pseudo-experiments that would be needed to be fit in order to adequately sample median sensitivities and LLR distributions. It would be of the order of  $(10^4)^2 = 10^8$ , for only one possible realization of the NMO, each requiring roughly two minutes to fit the systematic parameters to the pseudo-experiment.

Instead, we take an approach that is still highly computationally demanding, but much more feasible. Here, we also generate pseudo-experiments for a certain fixed hypothesis, but adjust the procedure laid out above in two aspects. First, only a single true ordering (TO) LLR distribution is created by directly fitting to these pseudo-experiments, from which the median LLR for the underlying hypothesis is determined. Second, the combination of the atmospheric parameters ( $\theta_{23}$  and  $\Delta m_{31}^2$ ) are adjusted to determine the realization of the wrong ordering (WO) most resembling the true one on average. The test statistic is then built based on those true ordering and wrong ordering hypotheses only, reducing the number of pseudo-experiments that are fitted to roughly  $10^4$ .

*Appendix A.2.2. Estimate of Statistical Uncertainty of Median Sensitivity*

The fact that the number of available pseudo-experiments is not infinite means that the quoted median sensitivity is subject to statistical fluctuations. In general, the statistical uncertainty will depend mainly on the number of trials  $n_{\text{trials}}$ , but also on the value of the sensitivity itself. In order to ensure that the relative statistical error is on the order of a few percent or less, we have repeatedly simulated each LLR procedure 10 000 times by randomly drawing  $n_{\text{trials}}$  samples from the Gaussian fit to the LLR distribution, refitting those samples, and calculating the deviations of the obtained sensitivities from the original one. This allows us to give an estimate of the standard error on the (two-sided) median sensitivity, given  $n_{\text{trials}}$ . Here, we make the assumption that we can determine the mean of the true-ordering LLR distribution with an accuracy of  $\sigma_{\text{mean}} = \sigma_{\text{TO}}/\sqrt{n_{\text{trials}}}$ , where  $\sigma_{\text{TO}}$  is the standard deviation of its Gaussian fit. Two examples depicting this procedure can be seen in Fig. A.71, where we compare the spreads in the TO-LLR mean and the variations of the WO-LLR Gaussian fits for the 1-year NO dataset for the (hypothetical) cases of 1 000 and 10 000 pseudo-experiments. The black histogram corresponds to the original LLR distribution, while the Gaussian fit, assumed to represent the true shape of the distribution, is also shown in black. Here, the ten-fold increase in the number of pseudo-experiments would reduce the relative statistical uncertainty of the median sensitivity from 3.5% to 1.1%, i.e. by roughly a factor of  $\sqrt{10}$  in accordance with the analytical calculation of that uncertainty.

Tables A.15 and A.16 give an overview of the number of pseudo-experiments we have processed for different detector livetimes and true values of  $\theta_{23}$ , and also show the obtained median sensitivities including their relative statistical uncertainties estimated via simulation.

livetime (years)	# Trials	$n_{\sigma}$ (NO/IO)	$\Delta n_{\sigma}/n_{\sigma}$ (NO/IO) (%)
1	16220	1.7/1.5	0.9/0.9
4	11120	2.9/2.6	1.1/1.1
5	3240	3.1/2.8	1.9/1.9
10	16000	4.2/3.8	0.9/0.9

Table A.15: Number of pseudo-experiments generated and fitted for different PINGU livetimes at the two NMO fiducial models, together with the obtained median NMO sensitivities and their relative statistical uncertainties based on the finite number of trials. No prior is applied for  $\theta_{13}$  or  $\Delta m_{31}^2$ .

$\theta_{23}$ ( $^\circ$ )	# Trials	$n_\sigma$ (NO/IO)	$\Delta n_\sigma/n_\sigma$ (NO/IO) (%)
39	2000	2.6/2.8	2.4/2.4
42	1930	3.2 (IO)	2.5 (IO)
42.3	11120	2.9 (NO)	1.1 (NO)
45	1500	4.4/3.3	2.8/2.8
47	2000	5.5/2.9	2.5/2.4
49	2000	6.7 (NO)	2.4 (NO)
49.5	11120	2.6 (IO)	1.1 (IO)
52	2000	7.2/3.0	2.5/2.4

Table A.16: Same as Tab. A.15, but here for a fixed livetime of four years and different true values of  $\theta_{23}$  in both NMOs (unless given otherwise).

### Appendix A.3. Asimov Analysis

Our second analysis method makes use of the  $\Delta\chi^2$  metric also used extensively in the literature. It is based on the usual definition of  $\chi^2$  as the weighted sum of squared differences between  $n$  measurements (bins)  $x_i$  drawn from the normal distributions with standard deviation  $\sigma_i$  and corresponding median outcomes  $\mu_i$ ,

$$\chi^2 = \sum_{i=1}^n \frac{(x_i - \mu_i)^2}{\sigma_i^2}. \quad (\text{A.5})$$

When the model predictions  $\mu_i$  are dependent on a set of  $P$  parameters  $\{p_i\}$ , one usually considers the minimum

$$\chi_{\min}^2 \equiv \min_{\{p_i\}} \chi^2 \quad (\text{A.6})$$

with respect to  $p_i$ . The quantity  $\chi^2$  can be minimized with respect to the (nuisance) parameters either using the NO or the IO hypothesis, leading to the two minima

$$\chi_{\text{NO(IO)}}^2 \equiv \min_{\{p_i\} \in \text{NO(IO)}} \chi^2. \quad (\text{A.7})$$

The test statistic

$$\Delta\chi^2 \equiv \chi_{\text{NO}}^2 - \chi_{\text{IO}}^2 \quad (\text{A.8})$$

is then employed to determine which one of the two ordering hypotheses constitutes the better fit to the data, with  $\Delta\chi^2 < 0$  ( $\Delta\chi^2 > 0$ ) favouring the NO (IO) hypothesis, in close analogy to the LLR method detailed in the previous section.

In the so-called ‘‘Asimov’’<sup>7</sup> approach, the randomly sampled pseudo-data  $x_i$  are replaced by the exact model predictions  $\mu_i$  at the nominal parameter values  $p_0$  within the corresponding true ordering:

$$\overline{\Delta\chi_{\text{TO}}^2}(p_0) \equiv \min_{p \in \text{WO}} \sum_{i=1}^n \frac{(\mu_i^{\text{TO}}(p_0) - \mu_i^{\text{WO}}(p))^2}{\sigma_i^2}, \quad (\text{A.9})$$

where the minimization is performed over the parameters  $p$  within the wrong ordering. Since by construction  $\chi_{\text{TO}}^2 = 0$  when using the Asimov data set,  $\overline{\Delta\chi_{\text{IO}}^2}$  is the equivalent of the test statistic defined in Eq. (A.8), while  $\overline{\Delta\chi_{\text{NO}}^2}$  only differs by the sign.<sup>8</sup> The Gaussian prior penalty term added to  $\overline{\Delta\chi_{\text{TO}}^2}$  is  $-2\mathcal{L}_{\text{prior}}$ .

Essentially, this technique assumes that statistical fluctuations in the experimental data are as likely to reinforce as to obscure the signature of the correct ordering, so that only the single data set most likely to be observed for any given set of oscillation parameters needs to be analysed.

Usually,  $\overline{\Delta\chi^2}$  is transformed into an actual sensitivity by evaluating it under the assumption that it is  $\chi^2$ -distributed with 1 degree of freedom, so that the number of Gaussian standard deviations at which a given ordering can be identified is simply  $n_\sigma = \sqrt{\overline{\Delta\chi^2}}$ . As detailed in Ref. [144], this approach is not well justified due to the discrete nature of the neutrino mass ordering, but it turns out that a precise frequentist definition of the sensitivity for any desired rejection power is possible under the Gaussian approximation for the distribution of the test statistic  $\Delta\chi^2$  [57]. In these references it is shown that  $\chi_{\text{TO}}^2$  is  $\chi^2$  distributed with  $n - P$  ( $P$  being the number of parameters) d.o.f., while  $\chi_{\text{WO}}^2$  follows a non-central  $\chi^2$  distribution, and as a result

$$\Delta\chi^2 = \mathcal{N}\left(\pm\overline{\Delta\chi^2}, 2\sqrt{\overline{\Delta\chi^2}}\right), \text{ with } + (-) \text{ for IO (NO)} \quad (\text{A.10})$$

is Gaussian distributed, with mean  $\overline{\Delta\chi^2}$  and standard deviation  $2\sqrt{\overline{\Delta\chi^2}}$  [57].  $\overline{\Delta\chi^2}$  depends on the true parameter values within the given mass ordering, especially the mixing

---

<sup>7</sup>This is a reference to the Isaac Asimov short story *Franchise*, in which the single most typical voter replaces the full electorate.

<sup>8</sup>This is the reason for denoting this quantity by ‘‘ $\overline{\Delta\chi^2}$ ’’, and not by ‘‘ $\Delta\chi^2$ ’’. Also, be aware that the subscript denotes the assumed true ordering and not the one that is minimized over, as in Eq. (A.7), since minimization over the parameters within the WO will always be implied.

angle  $\theta_{23}$ , which determines the amplitude of the matter effect and thus significantly alters the event rates.

Following Ref. [57], in order to obtain an estimate of the median sensitivity under the Gaussian assumption that is consistent with our Monte Carlo based approach of generating pseudo-experiments laid out in Appendix A.2.1, one has to start off with the critical value  $\Delta\chi_\alpha^2$ , such that a certain ordering hypothesis can be rejected at the Confidence Level  $\text{CL}(1 - \alpha)$ . From the definition (A.8) it is clear that in the case of true NO, we would decide to reject the IO hypothesis at  $\text{CL}(1 - \alpha)$  if  $\Delta\chi^2 < \Delta\chi_\alpha^2$ , i.e.  $\alpha = P(\Delta\chi^2 < \Delta\chi_\alpha^2)$ . Using Eq. (A.10) one finds

$$\alpha = \frac{1}{2} \operatorname{erfc} \left( \frac{\overline{\Delta\chi_{\text{IO}}^2} - \Delta\chi_\alpha^2}{\sqrt{8\overline{\Delta\chi_{\text{IO}}^2}}} \right), \quad (\text{A.11})$$

$$\beta = \frac{1}{2} \operatorname{erfc} \left( \frac{\overline{\Delta\chi_{\text{NO}}^2} + \Delta\chi_\alpha^2}{\sqrt{8\overline{\Delta\chi_{\text{NO}}^2}}} \right), \quad (\text{A.12})$$

so that requiring  $\beta = 0.5$  implies  $\Delta\chi_\alpha^2 = -\overline{\Delta\chi_{\text{NO}}^2}$ . Applying the two-sided convention to convert  $\alpha$  into a number of Gaussian standard deviations, the median sensitivity is

$$n_\sigma = \sqrt{2} \operatorname{erfc}^{-1} \left[ \frac{1}{2} \operatorname{erfc} \left( \frac{\overline{\Delta\chi_{\text{IO}}^2} + \overline{\Delta\chi_{\text{NO}}^2}}{\sqrt{8\overline{\Delta\chi_{\text{IO}}^2}}} \right) \right] \quad (\text{A.13})$$

for true normal ordering. The true inverted ordering case is calculated analogously.

Both  $\overline{\Delta\chi_{\text{IO}}^2}$  as well as  $\overline{\Delta\chi_{\text{NO}}^2}$  above will depend on the true parameter values  $p_0$  within the respective hypotheses. This means that we actually need to perform two fits for any given true hypothesis TO, with injected values  $p_0^{\text{TO}}$ . Again sticking to true NO for illustration purposes, first we determine  $\overline{\Delta\chi_{\text{NO}}^2}(p_0^{\text{NO}})$  (Eq. (A.9)). The resulting best fitting parameters under the IO hypothesis then serve as the IO fiducial model  $p_0^{\text{IO}}$  for which the expected experimental outcome under the IO is computed, from which in turn  $\overline{\Delta\chi_{\text{IO}}^2}(p_0^{\text{IO}})$  is obtained. The median sensitivity then follows directly from Eq. (A.13).

The usual  $\sqrt{\Delta\chi^2}$  prescription frequently encountered in the literature is recovered if the one-sided convention is employed to convert from  $\alpha$  to  $n_\sigma$ , and if the moduli of the means of the two test statistic distributions are approximately the same, i.e.  $\overline{\Delta\chi_{\text{IO}}^2} \approx \overline{\Delta\chi_{\text{NO}}^2}$ . We

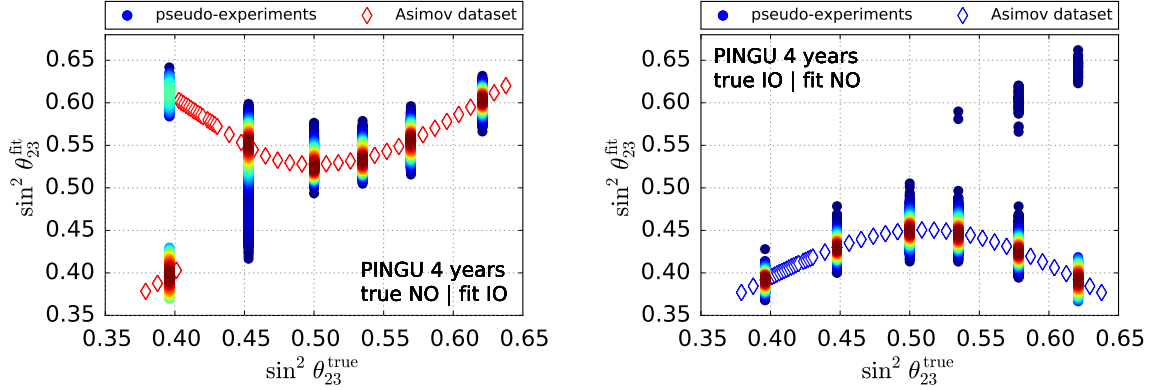


Figure A.72: Distribution of best fit values  $\sin^2 \theta_{23}^{\text{fit}}$  as a function of the true value  $\sin^2 \theta_{23}^{\text{true}}$ , when the NMO is misidentified. Both the outcomes of individual pseudo-experiments (point density color-coded) as well as fits to the corresponding Asimov datasets are shown, for true normal ordering in the left panel, and for true inverted ordering on the right.

find that this approximation does not hold for  $\sin^2 \theta_{23} \gtrsim 0.5$  and the case in which NO is true, where it actually leads to an underestimation of the sensitivity. The reason is that while  $\overline{\Delta\chi_{\text{NO}}^2}$  continues growing in this region of parameter space,  $\overline{\Delta\chi_{\text{IO}}^2}$  stays small due to the ordering-octant degeneracy: the best fit  $\theta_{23,\text{IO}}$  lies in the second octant, which means that the expected experimental outcome under the wrong (inverted) ordering hypothesis is reasonably well fit with  $\theta_{23,\text{NO}}$  in the first octant. This behavior is depicted in Fig. A.72: here we compare the fit results for  $\sin^2(\theta_{23})$  based on the Asimov dataset to the outcomes of the individual pseudo-experiments in the LLR method.

In Fig. A.73 we provide an example of how the distribution of the LLR test statistic obtained from performing several thousands of pseudo-experiments compares to the Gaussian approximation (A.10) of  $\Delta\chi^2$ . Here, we show two representative datasets; the left panel corresponds to the true NO case and maximal mixing, for four years of detector livetime, while the right panel displays the distributions obtained for true IO, with  $\theta_{23} = 49.5^\circ$ . Only the atmospheric oscillation parameters are included as systematics (cf. Tab. 5). The vertical line in each panel is drawn at the position of the mean of the  $\Delta\chi_{\text{TO}}^2$  distribution; its absolute value corresponds to the “Asimov- $\Delta\chi^2$ ”, i.e.  $\overline{\Delta\chi_{\text{TO}}^2}$  defined in Eq. (A.9).

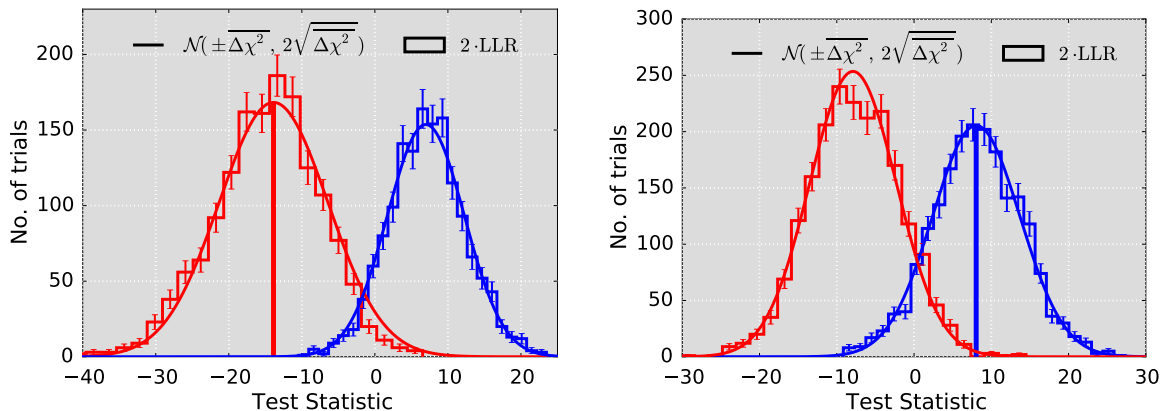


Figure A.73: Gaussian approximations for the distribution of  $\Delta\chi^2$ , together with the corresponding LLR distributions (scaled by a factor of two) obtained from pseudo-experiments. The left panel shows a representative dataset assuming the NO, while the right panel shows a case where the IO is true. Only two systematic parameters are included, see text for details.

### Appendix A.3.1. Notes on the Validity of the Gaussian Approximation (A.10)

In the scheme we describe above it is not guaranteed that all the assumptions upon which Eq. (A.10) rests indeed hold. This applies especially to the case in which there is a tight prior penalty term on one or more parameters, when the WO fiducial model is tested, with corresponding “true” fiducial values  $p_0^{\text{TO}}$ . Illustratively, the reason is that the injected value of the  $i$ -th parameter  $p_{0,i}^{\text{TO}}$  does not necessarily correspond to the central value of its prior (since it is obtained from a fit to the alternative ordering), so that the minimum within the same ordering will be pulled away from  $p_{0,i}^{\text{TO}}$ , and be systematically biased. As a result,  $\chi_{\text{TO}}^2(p_0^{\text{TO}})$  will follow a non-central  $\chi^2$  distribution also, and the expression (A.10) is no longer valid. The modification of  $\Delta\chi^2$  is not as trivial as just a shift of its mean by  $\chi_{\text{TO}}^2(p_0^{\text{TO}})$  however, as it also affects the higher percentiles. As a consequence, for studies using the current NuFit prior on  $\Delta m_{31}^2$  we only rely on pseudo-experiments as in the LLR methodology to determine the significance.

Fig. A.74 shows the expected evolution of the NMO sensitivity as a function of full detector livetime both without and with including current knowledge of the oscillation parameters  $\theta_{23}$  and  $\Delta m_{31}^2$ . In the former case we compare the significances yielded by the Gaussian approximation of the  $\Delta\chi^2$  test statistic to those obtained from fitting Poisson-fluctuated pseudo-experiments in the LLR approach (cf. Tab. A.15). In the latter, however, only results from the LLR method are shown due to the limitations of the Gaussian approx-

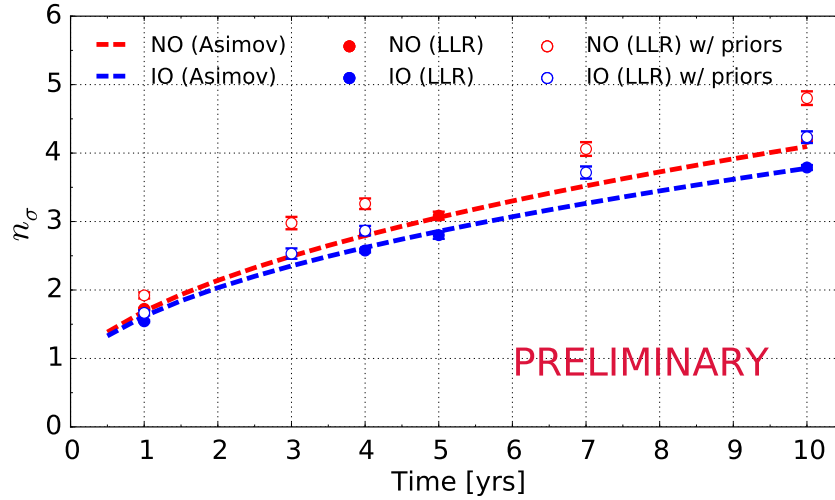


Figure A.74: Projected evolution of median NMO sensitivity as a function of full detector livetime, in number of Gaussian standard deviations as defined in Eq. (A.4), for both true normal (red) and true inverted (blue) ordering. For the case of no external constraints on  $\theta_{23}$  and  $\Delta m_{31}^2$ , results from the Asimov method are shown as dashed lines, while LLR results are shown as filled points. Circles represent the sensitivities obtained in the LLR method with NuFit 2.0 [47] constraints applied to the two oscillation parameters in addition. See text for details.

imation (A.10) pointed out above. The prior on  $\Delta m_{31}^2$  is assumed to be Gaussian, with central value and standard deviation taken from [47], and chosen according to the NMO assumption of the fit. The (non-Gaussian) constraints placed on  $\theta_{23}$  are shown in the lower panel of Fig. 23. We apply the according prior to  $\theta_{23}$  whenever it is fit within a given NMO, but remove the overall penalty of about one unit in  $\Delta\chi^2$  when NO is assumed in the fit. Even though one would not expect different shapes for NO and IO if current oscillation data were not sensitive to the ordering, this procedure allows us to capture the impact of the current constraints on  $\theta_{23}$  while retaining the two global best fits as central values and without introducing an external preference for the IO in the NMO determination.

Both priors are implemented as penalty terms added to Eq. A.1, and are applied when fitting both NMO assumptions to pseudo-experiments, and when searching for the wrong-ordering hypothesis that mimics the average true ordering experiment the most. The observed increase in NMO sensitivity with respect to the case of no external constraints on  $\Delta m_{31}^2$  and  $\theta_{23}$  is on the order of 10 – 20%.

#### *Appendix A.4. Atmospheric Oscillation Parameter Sensitivity*

In Sec. 3.2 we determine regions of various two-dimensional confidence levels for the atmospheric oscillation parameters  $(\Delta m_{31}^2, \sin^2 \theta_{23})$  by generating the mean experimental outcome under the “true” model and evaluating  $\chi_{\text{TO}}^2$  defined in Eq. (A.7) on a fine grid in the plane of the two parameters, assuming the correct NMO in the fit. Under the assumption that  $\chi_{\text{TO}}^2$  follows a  $\chi^2$  distribution with 2 d.o.f., each iso-contour is easily converted into a corresponding C.L. at which an experiment will yield a combination of  $(\Delta m_{31}^2, \sin^2 \theta_{23})$  contained within.

Since it is not guaranteed that the distribution follows that of a  $\chi^2$  with a given number of d.o.f., we have compared the C.L. associated with different iso-contours to their true coverage. This can be done by determining the outcomes of a large number of pseudo-experiments, as mentioned in Sec. 3.2.3 and depicted in Fig. 16, and then finding the fraction of outcomes a given contour of constant  $\chi_{\text{TO}}^2$  actually contains.

The result of this study is shown in Fig. A.75, for the same three injected values of  $\sin^2 \theta_{23}$  used in Sec. 3.2, and true NO. As one can see from the plot, the fractions of pseudo-experimental outcomes found inside the iso-contours exceed the expectations based on assuming a  $\chi^2$  distribution with 2 d.o.f. up to about 95% (expected) C.L., implying that the extents of the respective contours are conservative. For true IO, we do not anticipate a qualitatively different picture.

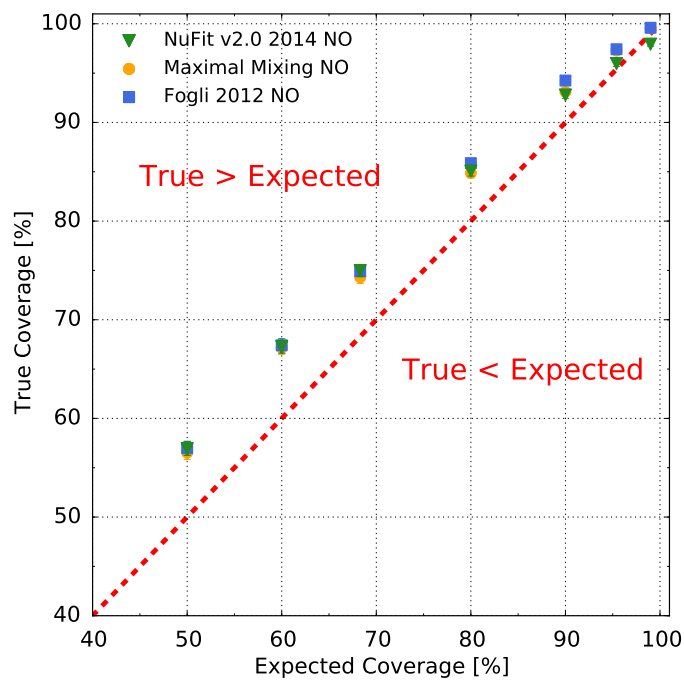


Figure A.75: True coverage of various joint confidence regions for the atmospheric oscillation parameters  $(\Delta m_{31}^2, \sin^2 \theta_{23})$  from the Asimov approach, as a function of the expected confidence level obtained according to a  $\chi^2$  distribution with 2 d.o.f. See text for details.

## Appendix B. Neutrino Cross-section and Model Uncertainties

Neutrino interaction models play an important role in oscillation analyses; the oscillation probability is inferred from the event rate, which is a convolution of the flux, cross section, efficiency and oscillation probability. In the PINGU mass ordering analysis, as an example, the relative difference in  $\cos(\text{zenith})$  vs. E space for neutrinos and antineutrinos is used to infer the mass ordering. Flavor separation of charged current (CC)  $\nu_\mu$  interactions and  $\nu_e, \nu_\tau$  into track and cascade samples also introduces dependence on the relative population of these interactions, as predicted by the interaction model and efficiency. In addition, neutral current (NC) interactions contribute to the backgrounds in cascade samples. The uncertainties on these models therefore play an important role in the determination of the physics results obtained from the neutrino analyses.

### *Appendix B.1. Neutrino interaction processes from 1-100 GeV*

PINGU is sensitive to neutrino and antineutrino interactions above a few GeV, as shown by Fig. 5 which shows the effective areas divided into neutrinos and antineutrinos. Both of these interactions are then important to consider in the final analysis of the event rates.

Figure B.76, copied from Ref [85], shows the neutrino and antineutrino cross section processes as a function of neutrino (or antineutrino) energy. The dominant processes in the PINGU event sample, as shown later, are CC and NC deep inelastic scattering (DIS) interactions, in which a neutrino ( $\nu_\ell$ ) strikes a quark in a nucleon ( $N$ ), which produces a hadronic shower,  $X$ , and the corresponding flavor lepton partner ( $\ell = e, \mu, \tau$ ) in the final state:

$$\nu_\ell + N \rightarrow \ell^- + X \tag{B.1}$$

In the case of antineutrino interactions  $\bar{\nu}$ , the final state lepton will be positively charged ( $\ell^+$ ); we note PINGU is insensitive to the charge of the final state lepton and separates antineutrino from neutrino interactions through the neutrino and antineutrino cross sections and relative initial flux.

At energies of a few GeV the most significant contribution to the total cross-section is from CC resonant (RES) interactions, in which the neutrino interacts with a nucleon, exciting a resonance, which decays to a meson, and predominantly to a pion:

$$\nu_\ell + N \rightarrow \ell + N' + \pi, \tag{B.2}$$

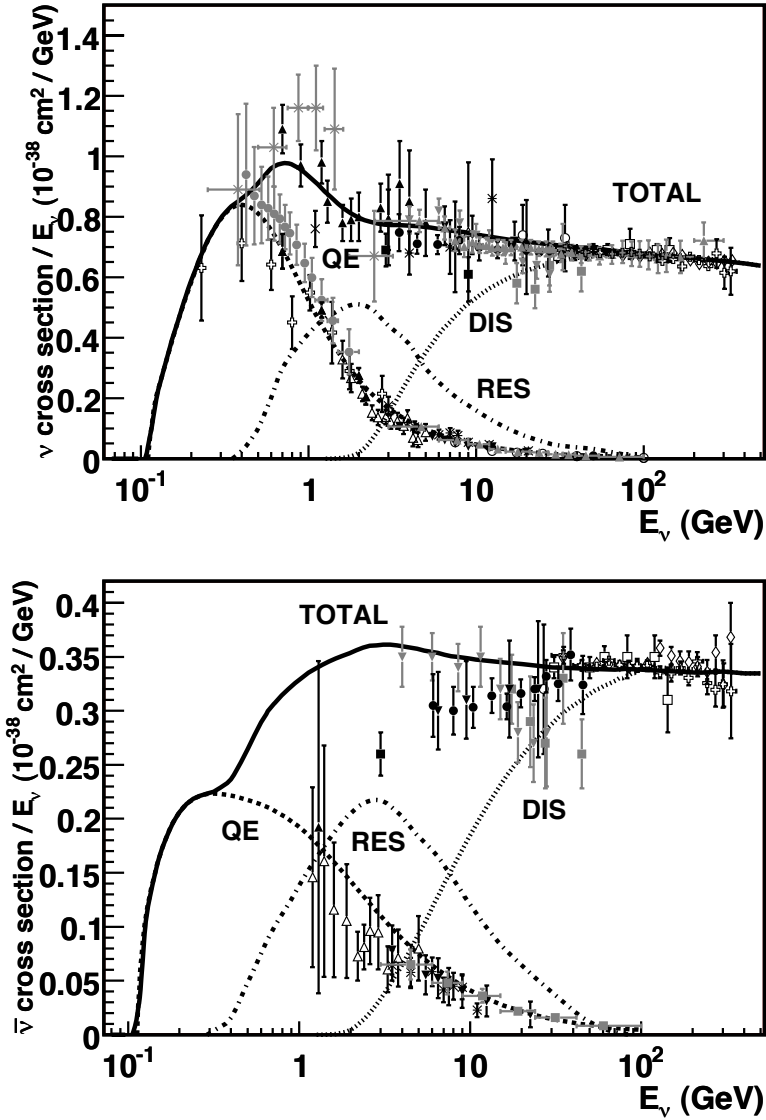


Figure B.76: Total neutrino and antineutrino per nucleon CC cross sections (for an isoscalar target) divided by neutrino energy and plotted as a function of energy. Contributions include quasi-elastic scattering (dashed), resonance production (dot-dash), and deep inelastic scattering (dotted). Example predictions for each are provided by the NUANCE generator [145]. Note that the quasi-elastic scattering data and predictions have been averaged over neutron and proton targets and hence have been divided by a factor of two for the purposes of this plot.

where  $N'$  represents the final state nucleon.

Below 1 GeV, the dominant process is CC quasi-elastic scattering (CCQE):

$$\nu_\ell + N \rightarrow \ell + N', \quad (\text{B.3})$$

There are also NC analogs of each of these processes, which result in a neutrino in the final state instead of the charged lepton. Table B.17 lists the contributions to the total event rate for the default simulation, separated by flavor and assuming the Honda flux model.

### *Appendix B.2. The GENIE event generator*

GENIE is a software package [18] which simulates neutrino interaction; GENIE stands for Generates Events for Neutrino Interaction Experiments. For the PINGU analysis studies discussed here, the version of GENIE used was 2.8.6. That this version of GENIE includes a bug fix to the GRV98 PDF, having  $\approx 1\%$  effect on the total cross-section.

Table B.18 summarizes the errors on the parameters in GENIE believed to be the most significant for PINGU. These are taken directly from the GENIE Users Manual [146]). No justification is provided in the GENIE documentation, however in the following sections we provide additional information to explain why these parameters are the most significant and why others may be disregarded at this time.

### *Appendix B.3. Uncertainties not considered*

Table B.17 shows that several of the potential process do not contribute significantly to the overall event rate and therefore need not be considered in the analysis. These include the coherent production channel for both CC and NC events (contributing 0.7 and 0.2% respectively) and elastic scattering for NC events (totalling  $4 \times 10^{-3}\%$ ). Grouped into the “Other” category are single kaon,  $\eta$ , and  $\Lambda$  production as well as inverse muon decay. These events may be considered for a future analysis and can be either neglected or included with a large uncertainty.

The total DIS cross-section is known at approximately the 3-5% level. We do not consider this as a source of systematic uncertainty because a floating normalization on the dominant channel would be degenerate with the neutrino or antineutrino normalization. Therefore,

Interaction	$\nu_\mu&\bar{\nu}_\mu$	$\nu_e&\bar{\nu}_e$	$\nu_\tau&\bar{\nu}_\tau$
CC	83.8	84.9	61.9
QE	9.8	9.7	6.5
RES	13.7	13.3	9.8
COH	0.7	0.8	0.03
DIS	59.5	61.1	45.6
Other	0.0	0.0	0.0
NC	16.2	15.1	38.1
QE	0.004	0.007	0.04
RES	0.3	0.3	1.0
COH	0.2	0.2	0.5
DIS	15.8	14.6	36.6
Other	0.02	0.0	0.0

Table B.17: The breakdown of the event rate, in percentage, using the default GENIE simulation for each neutrino flavor. This table was made using the Honda flux model.

Name	nominal value	uncertainty (%)
$M_A^{CCQE}$	0.99	-15, +25
$M_A^{RES}$	1.120	$\pm 20$
$A_{HT}^{BY}$	0.538	$\pm 25$
$B_{HT}^{BY}$	0.305	$\pm 25$
$C_{V1u}^{BY}$	0.291	$\pm 30$
$C_{V2u}^{BY}$	0.189	$\pm 30$

Table B.18: List of parameters and their associated uncertainties based on GENIE. Nominal values of parameters from Appendix B of the GENIE User Manual, Section 8.1.

for this analysis we focus on aspects which may affect the relative difference between neutrino or antineutrino event rates, including:

- Possible variations in the cross section model which may affect the shape of the predicted event spectrum with energy
- Differences between channels (CC vs. NC)
- Differences between flavors

Due to the technical implementation of the cross section systematics into the analysis (via effective area) it is not possible to study the effect of uncertainties on the hadronic final state. However, systematic errors from the hadronic system are rather minor in this analysis [147].

While we recognize the importance of CC vs. NC uncertainties, we do not consider any additional uncertainties on this ratio for DIS, RES or QE. According to Table B.17, the only significant contribution to the analysis comes from NC DIS interactions and the Bodek-Yang model parameters, discussed in later sections, affect both CC and NC cross sections as implemented in GENIE.

This analysis is also constrained by the error propagation method used in GENIE, a technique often called “re-weighting”. This technique is applied in GENIE for a set of physics parameters  $p$ . For each  $p$  that can be reweighted, there is a corresponding systematic parameter  $x_p$ . Tweaking this systematic parameter modifies the physics parameter  $p$  as:

$$p \rightarrow p(x_p) = p \cdot \left(1 + x_p \frac{\delta p}{p}\right) \quad (\text{B.4})$$

where  $\delta p$  is the estimated standard deviation of  $p$ . After tweaking  $p$  by some value, a new cross section is calculated. This allows one to see the effect on the cross section as compared to the nominal cross section [18]. Because the new cross-sections are weighted to the nominal cross-section with different weights, there are no effects on the reconstructed variables such as energy.

The only uncertainties considered on the neutrino cross-section models are those on the QE, RES, and DIS models, which will be addressed in the following sections.

#### *Appendix B.4. Uncertainties on QE and RES model*

For the greater neutrino community, most experiments are at lower energies than the region of interest for PINGU (less than a few GeV) where cross section uncertainties are very important. In those experiments QE and resonant events dominate the sample and the uncertainties on these types of interactions are relatively high. Although PINGU will be dominated by DIS events, we have addressed the uncertainties associated with the QE interactions.

The largest effect on the overall shape of CCQE events is driven by uncertainties on the axial mass in the axial form factor,  $M_A^{CCQE}$ . It is suspected that  $M_A^{CCQE}$  is merely an effective parameter; it reproduces the right differential cross section at low energy but is masking nuclear physics processes which are not included in the current GENIE model. The two extreme effects on the analysis are either a raw increase to the CCQE cross section, achieved by  $M_A^{CCQE}$ , or the presence of “multi-nucleon effects”<sup>9</sup> where the neutrino interacts on a correlated pair of nucleons. Multi-nucleon interactions, as a high momentum transfer process which mimics CCQE, can create a bias in the neutrino energy reconstruction for low energy experiments, however generous uncertainties on the RES channel, which produce a similar feed down, can mitigate the effect.

#### *Appendix B.5. Uncertainties on the DIS model*

The dominant contribution to the total cross-section at the energy ranges of interest with PINGU comes from DIS interactions. In GENIE, the DIS model uses the Bodek-Yang correction (BY) [137]; the uncertainties in this model are encapsulated in the parameters,  $A_{HT}^{BY}$ ,  $B_{HT}^{BY}$ ,  $C_{V1u}^{BY}$ ,  $C_{V2u}^{BY}$ . The parameter  $A$  is used to account for the higher order QCD terms and dynamic higher twist in the form of an enhanced target mass while the parameter  $B$  is used to account for the initial state quark transverse momentum. The  $C_{V1u}$  and  $C_{V2u}$  parameters are used by vector  $K$  factors so the GRV98 PDFs have the correct form in the low  $Q^2$  photo-production limit. There is an additional  $K$  factor that is used for sea quarks but at neutrino energies less than 50 GeV, the charm sea contribution is very small and can be neglected [148].

At sufficiently high energies, the masses of the leptons can be neglected in the cross-section

---

<sup>9</sup>These are sometimes referred to two particle, two hole (2p2h) effects or meson exchange current (MEC).

calculations. However, at energies near the production threshold, one must consider differences between the  $\nu_e, \nu_\mu$  and  $\nu_\tau$  cross-sections. This effect is assumed to be negligible at PINGU's energies.

### *Appendix B.6. Implementation*

The effects of the neutrino cross section systematics on the neutrino mass ordering study were studied using the  $\overline{\Delta\chi^2}$  method. Apart from the addition of the GENIE systematics, the same systematics were used in the other  $\overline{\Delta\chi^2}$  results as described in Table 3.

The neutrino cross section systematics were included with the assumption that they would only change the effective areas and not the reconstructed variables. Indeed this is true when GENIE is only used to propagate cross-section systematics to the effective area where the error is propagated as a weight on an event. Because of this, we are currently not able to investigate the effects of these systematics on the energy or zenith reconstruction and this will be investigated in the future. In practice, the GENIE systematic weights are multiplied with the standard weights and the new effective area is calculated. This is done at the  $-2\sigma$ ,  $-1\sigma$ ,  $1\sigma$ , and  $2\sigma$  values for each of the six parameters. These files are then used in a line fit to obtain slopes  $\Delta A_i$ . The modified effective area is calculated as

$$A'_{\text{eff}}(E) = A_{\text{eff}} \left( 1 + \sum_i p_i \Delta A_i \right). \quad (\text{B.5})$$

### *Appendix B.7. Results*

By allowing each of the six GENIE systematics errors to be fitted individually, the total effect of each parameter can be determined.

The total impact on the NMO significance over time can be seen in Fig. B.77. This graph shows that the significance when including the six extra systematics is consistent to within 1% of the standard systematics case for livetimes below 5 years and still give small to negligible impacts at livetimes up to 10 years.

We suspect that the  $A_{HT}^{BY}$  and  $B_{HT}^{BY}$  along with the  $C_{V1u}^{BY}$  and  $C_{V2u}^{BY}$  may be correlated with each other. We have looked into this by fully correlating the higher twist parameters and the valence quark parameters and by having each parameter independent. It was found that when a prior is included, all results are compatible with each other.

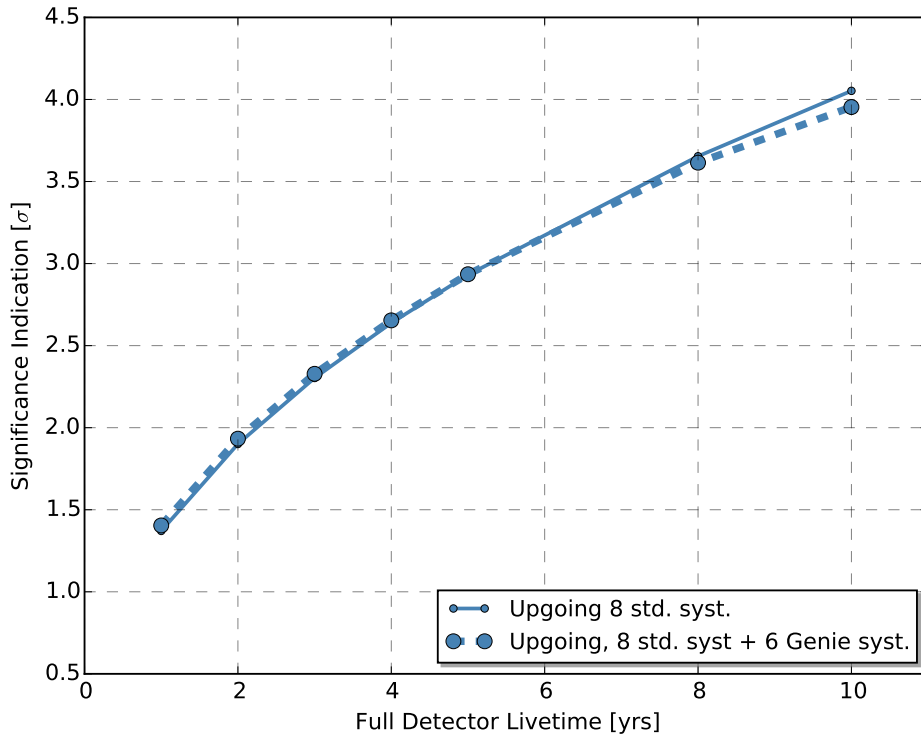


Figure B.77: The NMO significance shown with (dashed line) and without (solid line) the GENIE systematics added.

## Appendix C. Neutrino flux uncertainties

Atmospheric neutrinos are generated in hadronic showers induced by the interactions of primary cosmic rays in the Earth’s atmosphere. Their flux therefore depends on the properties of the primary flux (spectrum and composition) and of the atmosphere (in particular its density profile) as well as the hadron shower physics. At cosmic ray energies  $E_{\text{CR}} \lesssim 20\text{GeV}$ , the Earth’s magnetic field additionally affects the primary cosmic ray flux, effectively shielding against low-energy charged particles and thus providing a *geomagnetic cutoff*. Detailed Monte-Carlo simulations are employed to predict the resulting neutrino flux at various places on Earth [44, 149], which on the one hand enhances the precision of the calculation, but simultaneously limits the exploration of systematic effects to a few selected scenarios [44, 136]. While faster calculation methods based on one-dimensional cascade equations are available [150], the collinear approximation in the shower development limits their application to  $E_\nu > 100\text{GeV}$ .

In the following we will briefly discuss the various sources of uncertainty in the calculations of the atmospheric neutrino flux and their effects on the determination of the neutrino mass ordering with PINGU.

### *Appendix C.1. Primary flux uncertainties*

To study modifications of the flux by the geomagnetic cutoff effect, the primary cosmic ray spectrum is measured in balloon-borne, satellite or space-station experiments [151, 152, 153, 154, 155, 156]. While most magnetic spectrometers provide high statistics measurements of the flux in the range of 1 – 200GeV per nucleon, calorimetric approaches typically have a larger energy threshold of  $\sim 1\text{TeV/n}$ . This leaves a gap, particularly in the intermediate energy range, that has only recently been populated by data from the AMS-02 [154], PAMELA [155] spectrometer and CREAM [156] calorimeter experiments.

In the absence of this data, the so called GSHL power-law approximation [157]

$$\Phi(E_p) = a \left[ E_p + b \exp \left( c\sqrt{E_p} \right) \right]^{-d} \quad (\text{C.1})$$

has been adopted in earlier calculations which introduces four parameters  $a$ ,  $b$ ,  $c$ , and  $d$  that are obtained from fits to the data. In a study by Barr et al. [53], the impact of varying these parameters within their model [149] is performed, assuming the uncertainties listed in Tab. C.19.

Parameter	Proton fluxes	Nuclear fluxes
$a$ (normalization)	$1.49 \pm 0.10$	$0.060 \pm 0.004$
$b$ (shape)	$2.15 \pm 0.025$	$1.25 \pm 0.03$
$c$ (shape)	$2.21 \pm 0.02$	$0.14 \pm 0.02$
$d$ (index) $> 200\text{GeV}/n$	$2.74 \pm 0.01$	$2.64 \pm 0.02$
$d$ (index) $< 200\text{GeV}/n$	$2.74 \pm 0.03$	$2.64 \pm 0.04$

Table C.19: Parameter values and uncertainties for the GSHL parameterization of the primary cosmic ray flux, taken from [53]

The red curves in Figure C.78 shows the ensuing uncertainty on the atmospheric neutrino flux as a function of neutrino energy, from each parameter respectively. The spectral index uncertainty clearly dominates and ranges from 10 – 20% in the neutrino energy range of interest. The uncertainty in normalization is independent of energy in the resulting neutrino flux at a value of  $\sim 5\%$ , while the *shape* parameters  $a$  and  $b$  provide a negligible impact at low energies. This is consistent with a more recent investigation [158] using newly available data to find a deviation from the power-law approach of  $< 8\%$  over the whole energy range.

To incorporate these uncertainties in our calculation, the spectral index of the atmospheric neutrino flux is allowed to vary in a range of  $\pm 0.05$ , while the overall normalization is a free parameter (c.f. Table 3). It should be noted that this is a very conservative approach, as the newly available data on the primary cosmic ray flux is incorporated. While it reveals additional features in the spectrum [154, 155, 156] that can not be modelled with the simple GSHL parameterization given in Eq. C.1, the significantly improved event statistics constrain the primary flux much more tightly. Detailed Monte Carlo studies will be necessary to assess the remaining uncertainty.

### Appendix C.2. Magnetic fields

Today, not only the spatial but also the the temporal evolution of the Earth’s magnetic field are known with high precision [159]. The geomagnetic cutoff, which effectively shields the Earth from cosmic rays at energies below  $E_{\text{CR}} \lesssim 20\text{GeV}$  and affects the neutrino flux at energies below  $E_\nu \lesssim 5\text{GeV}$  can therefore be calculated with sufficient accuracy [42].

However, another complication which is dealt with in modern Monte Carlo calculations is the lateral spreading of the cosmic ray showers both from transverse momentum acquired

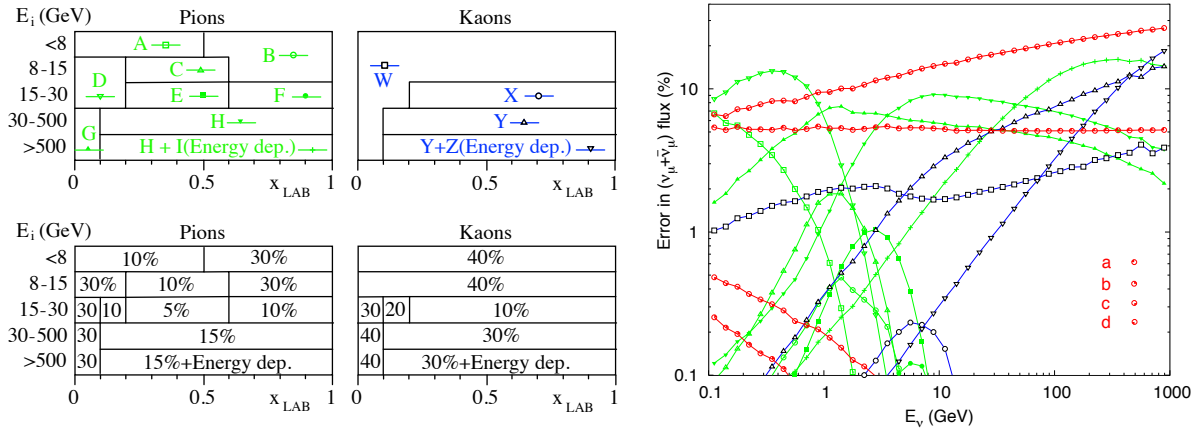


Figure C.78: Uncertainties of the atmospheric neutrino flux from variations of the primary flux parameterization (a-d, red) as well as from uncertainties in various kinematic ranges of the hadronic interactions of pions (A-I, green) and kaons (W-Z, blue). Figure adapted from [53]

in the interactions and decay of mesons and from bending of muons in the Earth's magnetic field. The field is not symmetric enough to allow for a simplification of the problem. This makes the computation challenging as it requires the generation of particles in all directions at all points on the Earth.

As a consequence, the neutrino flux has to be calculated individually for each detector location. A commonly used speed-up trick is to extend the size of the detector to cover a large area surrounding it [149, 136]. Through the geomagnetic effects described above, this generates a systematic bias in the calculated flux that is corrected for by studying how the flux changes as a function of the detection radius [42, 44]. The resulting uncertainty on the atmospheric flux depends on the Monte Carlo statistics employed in the calculation, but is typically  $\lesssim 1\%$  [42].

We therefore do not include any systematic effects related to the geometry or magnitude of the magnetic field.

### Appendix C.3. Seasonal variation

The atmosphere of the Earth has been studied in great detail and a plethora of atmospheric data has been available for a long time. For simplicity, most atmospheric neutrino flux

calculations [160, 149, 42] employ the time-averaged atmosphere model *US-standard '76* presented in [161]. In a recent calculation [44], the newer *NRMLSISE-00* model [162] has been adopted since it provides a temporally and spatially changing atmospheric model.

Comparing the flux calculated with the *US-standard '76* and the time-averaged flux calculated with the *NRMLSISE-00* model results in differences of  $\lesssim 2\%$ , significantly smaller than the variability introduced by seasonal effects. The most important parameter in these calculations is the atmospheric density, where the primary effect on the neutrino flux is the concurrency of interaction and decay of the generating mesons in the atmosphere. The resulting variation over the course of the year – shown in Figure C.79 – is well below 1% at a neutrino energy of  $E_\nu \simeq 1\text{GeV}$ , but increases to  $\pm 5\%$  at  $E_\nu \simeq 1\text{TeV}$ , where the pions and kaons experience stronger time-dilatation effects that suppress their decay. While this effect works the same on all neutrino flavors, the muons originating in the mesons decay lose more energy in a denser atmosphere before they decay. Therefore the variability of  $\nu_e$  which are predominantly generated from the decay of these muons is enhanced at  $E_\nu \simeq 10 - 100\text{GeV}$  with respect to the variability of the  $\nu_\mu$  flux.

Despite the large effective volume of the PINGU detector, event statistics comprising several years of data will have to be collected in order to determine the neutrino mass ordering (c.f. Sec. 3.4 and Appendix A). It is therefore expected that atmospheric variations largely cancel out in the resulting dataset. We do not incorporate any systematic effect to account for this uncertainty. Detailed atmospheric data is available [163] that allows to correct for temporal variations should it become necessary.

We note however, that the matter effects giving rise to the mass ordering sensitivity arises from the asymmetry in the  $\nu/\bar{\nu}$  flux and interaction ratios. The sensitivity is therefore affected less by uncertainties in the absolute flux, and more by uncertainties in the ratios of  $\nu_\mu/\bar{\nu}_\mu$  and  $\nu_e/\bar{\nu}_e$ . Low energy muons leave short tracks in the detector, leading to poor flavour identification at those energies, as the muon neutrinos cannot be disentangled from the rest of the sample with high purity. Thus the ratio of  $(\nu_\mu + \bar{\nu}_\mu)/(\nu_e + \bar{\nu}_e)$  is of interest for the neutrino mass ordering determination. Figure C.79 shows the variation of these ratios with the seasonal changes in the atmosphere. Both the  $\nu_\mu/\bar{\nu}_\mu$  and  $\nu_e/\bar{\nu}_e$  ratios stay constant throughout the year, while the electron neutrino fluxes are suppressed in summer as a result of the decreased cosmic ray interaction height causing more muons to hit the ground before they decay. An uncertainty of  $\pm 3\%$  on the ratio of  $(\nu_\mu + \bar{\nu}_\mu)/(\nu_e + \bar{\nu}_e)$  is adopted in our calculation, and of  $\pm 10\%$  on the ratios of  $\nu_\mu/\bar{\nu}_\mu$  and  $\nu_e/\bar{\nu}_e$ . Both are chosen significantly larger than the atmospheric variability would suggest, as they additionally incorporate uncertainties in the hadronic interaction models (see Appendix C.4) and

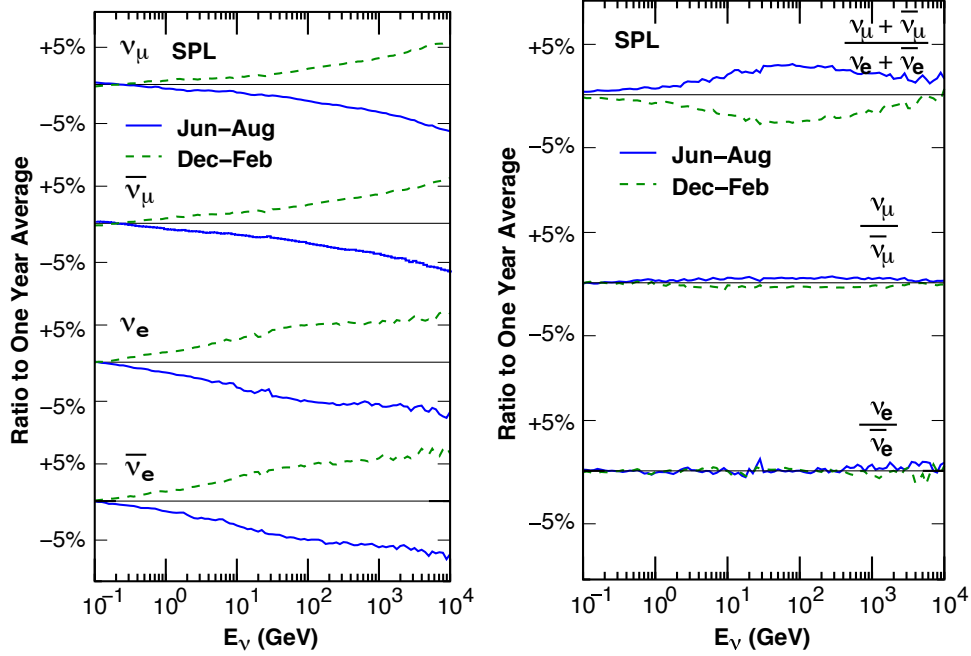


Figure C.79: Temporal variation of atmospheric neutrino fluxes at the South Pole for different flavors (left) and of flavor ratios(right). Figure taken from [44]

neutrino cross-sections.

#### Appendix C.4. Hadronic interaction uncertainties

A dominant source of uncertainty in the atmospheric neutrino flux stems from the not well determined hadronic production rates for mesons generated in  $pN \rightarrow \pi^\pm X$  and  $pN \rightarrow K^\pm X$  reactions, where  $p$  denotes an incoming cosmic ray nucleus,  $N$  is a target nucleus in the atmosphere and  $X$  represents the rest of the interaction products. In the absence of comprehensive experimental results and with the computational challenge involved in a detailed exploration of the allowed ranges in the underlying nuclear physics models, early analyses have constrained themselves to a comparison of a number of selected hadronic interaction models [160].

In contrast, Barr et al. [53] have made an assessment of the uncertainties based on a collection of available experimental data. The parameter space is defined in the kinematic variables  $E_i$  and  $x_{\text{lab}}$ , where  $E_i$  is the energy of the incident projectile,  $E_s$  is the energy

of the secondary meson and  $x_{\text{lab}} = E_s/E_i$ . Figure C.78 shows the uncertainty in the hadronic meson production assigned in [53] to each region in the  $(E_i, x_{\text{lab}})$ -space. To proceed with the calculation of the resulting uncertainties in the atmospheric neutrino flux, a number of zones (denoted A-I for pions and W-Z for kaons) is defined. Within each zone, the meson production rates are varied in the calculation assuming  $\pm 1\sigma$  ranges as given by the hadronic meson production uncertainties, with the assumption that these uncertainties are 100% correlated within each zone, and fully uncorrelated between zones. From these variations, uncertainties on the atmospheric neutrino flux are determined as shown in figure C.78.

While (through the higher kaon mass) kaon production uncertainties only become relevant at higher energies, uncertainties in the pion production (regions D,C,H) dominate the overall flux uncertainties below  $E_\nu < 1\text{GeV}$ , and are second largest (after the spectral index) in the remaining energy range. Yet, in contrast to the spectral index variations which provide a smooth power-law modification of flux as a function of energy, uncertainties in the hadronic production may be confined to a narrow range in energy. As the neutrino mass ordering effect also reveals itself in atmospheric neutrino data through enhancements or suppressions of the flux in well defined energy ranges, hadronic production uncertainties will provide a larger impact on the NMO sensitivity.

In order to determine this impact we continue the strategy described in [53], assuming that each of the zones described above provides the source of a systematic uncertainties with the resulting flux variation being 100% correlated within the zone and fully uncorrelated between zones. In analogy to the approach in Appendix B.6, we then treat the flux variations  $\Delta\Phi(E)$  shown in Fig. C.78 as  $\pm 1\sigma$  variation of these uncertainties, to calculate the modified flux  $\Phi(E)'$  from the original flux  $\Phi(E)$  as

$$\Phi(E)' = \Phi(E) \left( 1 + \sum_j p_j \Delta\Phi_j(E) \right) \quad (\text{C.2})$$

with the uncertainties parameters  $p_j$  in units of  $\sigma$  of the associated hadronic production zone and Gaussian priors of width  $\sigma(p_j) = 1$ . Figure C.80 shows the resulting loss in significance, which amounts to about 10% in the neutrino mass ordering estimator (red line). However, this result is overly conservative as we are treating the zones as fully uncorrelated, while in reality a smooth transition is expected between them. This conservative approach allows the parameters  $p_j$  to take e.g. extreme positive and negative value in adjacent zones, therefore providing stronger shape modifications than expected.

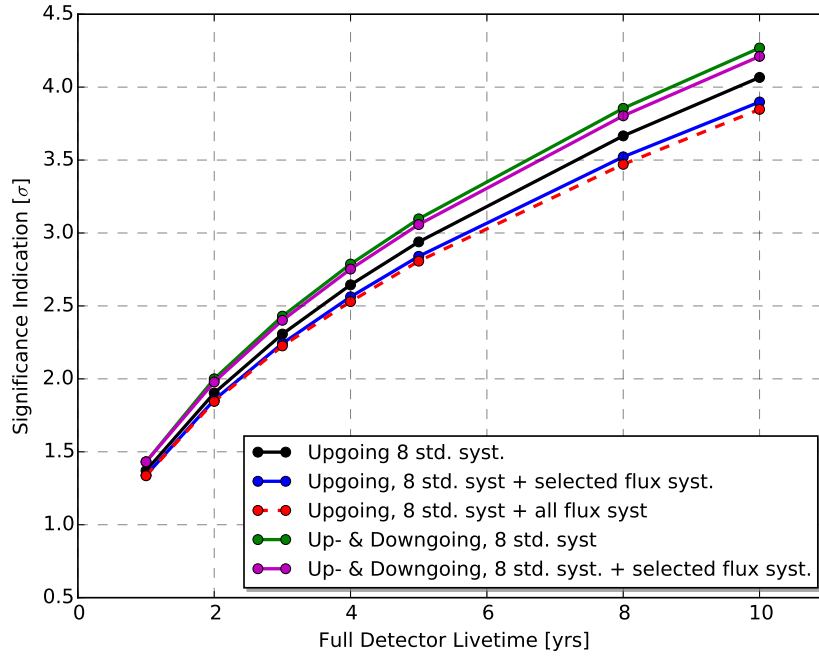


Figure C.80: Neutrino mass ordering significance estimator vs. detector lifetime using up-going events and the standard set of systematic uncertainties listed in Tab. 3 (black) as well as including 13 additional flux systematic uncertainties described in the text (red dashed) or just the 4 most relevant of those (blue). Extending the analysis to the down-going region (green) enhances the sensitivity due to earth-penetrating neutrinos that are mis-reconstructed above the horizon. Together with better constraints on the uncertainties from measuring the down-going flux, this over-compensates some of the sensitivity loss induced by the hadronic production uncertainties (purple).

Consistent with this expectation, we find that variations in zones  $H, Y, E$  and  $I$  which generate shape modifications in the same energy range as the neutrino mass ordering effect provide the largest impact on the significance, while variations in all other zones can be neglected (compare blue and red dashed line in figure C.80). Furthermore, there is more experimental data available now (and more will be available in the future), which will more tightly constrain the hadron production rates and therefore decrease the uncertainties. Finally, we note that our calculation only uses neutrino events reconstructed as up-going, while the PINGU detector will at the same time measure the down-going neutrino flux, allowing the constraint on uncertainties in the atmospheric neutrino flux.

In a first exploration of this option we extend our calculation to incorporate the full zenith range of  $-1 < \cos(\theta_z) < 1$ , optimistically assuming the same effective area for the up- and down-going flux. Even without taking into account the additional constraints on the hadron production uncertainties  $p_j$ , this results in a significant boost in sensitivity to the neutrino mass ordering (c.f. green line in Figure C.80) due to events that have penetrated the Earth and therefore are affected by matter effects, but are mis-reconstructed as down-going events in PINGU. Adding back the relevant hadronic production uncertainties (purple line in Figure C.80), there is still a net gain in the sensitivity to the neutrino mass ordering provided by the additional constraints on the atmospheric neutrino flux uncertainties. A more detailed study also taking into account potentially larger remaining atmospheric muon background in the down-going region will be required to fully assess the benefit of a  $2\pi$  measurement.

## Appendix D. IceCube–Gen2 Phase 1

As a first step toward a future IceCube–Gen2 detector, the IceCube–Gen2 Collaboration has proposed to install a Phase 1 upgrade of the IceCube detector. The Phase 1 upgrade will consist of seven new strings of photosensors and optical calibration devices, installed in the center of the existing detector within the volume proposed for PINGU.

The full scientific program of the Phase 1 upgrade, including the impact on high energy neutrino astrophysics, will be described in detail elsewhere. In this Appendix we discuss the reach of Phase 1 with regard to the PINGU science program. Phase 1 will enable a world-leading measurement of tau neutrino appearance and provide the most stringent test of unitarity in the tau sector of the PMNS matrix (detailed in Sec. 3). Phase 1 will also enable a world-class measurement of atmospheric  $\nu_\mu$  disappearance and extend IceCube’s indirect search for dark matter [100] down to WIMP masses of a few GeV.

The calibration devices will greatly improve our understanding of the complex optics of the glacial ice, not only in the central region but throughout the IceCube volume. This will permit the retroactive reanalysis of over a decade of archived IceCube data, providing substantial improvements in IceCube’s measurements of high energy astrophysical neutrinos, including angular resolution (especially for high energy cascades), energy resolution, and tau neutrino identification. The new photosensors will fill part of the proposed PINGU volume, and would greatly enhance IceCube’s performance in the 10 GeV energy regime. The Phase 1 design is such that more strings can be added in a later deployment, to attain a complete PINGU detector.

The new strings are envisioned to have roughly 125 multi-PMT Digital Optical Modules (mDOMs), as described in detail in Sec. 5.4.1. The mDOM will provide more photocathode area per module, at a lower cost per unit photocathode area and with improved determination of photon directionality, than the traditional IceCube DOM. The layout of these strings in the IceCube detector is shown in Fig. D.81.

### *Appendix D.1. Science Objectives*

#### *$\nu_\tau$ Appearance and the Unitarity of the PMNS Matrix*

The chief physics goal of the Phase 1 detector is to make a world-leading measurement of  $\nu_\tau$  appearance and exploit the resulting sensitivity to potential deviations from PMNS

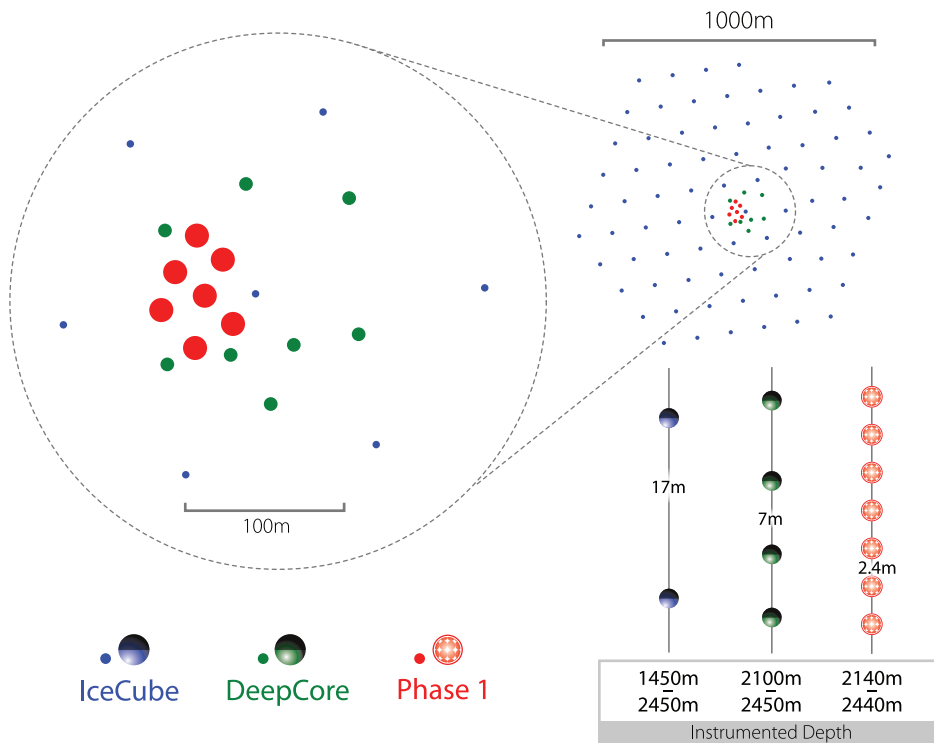


Figure D.81: The layout of the IceCube–Gen2 Phase 1 strings, shown in red. The locations of the existing IceCube and DeepCore strings are also shown in blue and green respectively. The areas of the circles in the zoomed-in top-view are proportional to the relative photocathode density on each string. This is illustrated further in the lower right corner showing the spacings on each of the strings progressing from IceCube (17 m) to DeepCore (7 m) to Phase 1 (2.4 m).

matrix unitarity. This topic has been discussed in detail in Sec. 3.5 for the full PINGU detector. The projected results for Phase 1 are shown in Fig. D.82.

The relatively high mass of the tau lepton suppresses  $\nu_\tau$  interactions in accelerator-based experiments, but at the higher atmospheric neutrino energies available to the Phase 1 detector, the event rate from  $\nu_\tau$  appearance is high. IceCube’s existing DeepCore extension already detects about 800  $\nu_\tau$  CC+NC interactions per year; the addition of Phase 1 strings would increase that to 2500. (For comparison, the Super-K experiment accumulated an estimated 180 atmospheric  $\nu_\tau$  events with a livetime of 2806 days [64].) Since insignificant numbers of  $\nu_\tau$  are produced directly in cosmic ray air showers, the  $\nu_\tau$  observed in DeepCore and Phase 1 arise from  $\nu_\mu \rightarrow \nu_\tau$  oscillations at specific  $L/E$  (the ratio of the neutrino’s path length through the Earth to its energy). For these path lengths, the oscillation maximum is at roughly  $E_\nu = 10\text{--}30$  GeV, comfortably above the DeepCore and Phase 1 detector thresholds.

These  $\nu_\tau$  events can be distinguished on a statistical basis from the background of  $\nu_e$  and  $\nu_\mu$  CC and NC events by their characteristic angular distribution and energy spectrum. This allows Phase 1 to measure the rate of  $\nu_\tau$  appearance with a precision of better than 10% with about 5 yrs of data, as shown in Fig. D.82, providing a significantly deeper probe of PMNS matrix elements dependent on the  $\nu_\mu$  and  $\nu_\tau$  flavors than current state-of-the-art experiments [64, 66]. The measurement will either strengthen the 3-flavor model and the underlying unitarity of its corresponding mixing, or point us in the direction of new physics due to sterile neutrinos, non-standard interactions, or other effects.

#### *$\nu_\mu$ Disappearance; Sterile Neutrino Searches; Dark Matter*

The Phase 1 detector will have improved sensitivity to additional key atmospheric neutrino oscillation parameters, as well as to sterile neutrinos and to neutrinos from dark matter annihilations, supplementing its highly important  $\nu_\tau$  appearance measurement. Figure D.83 shows the reach of Phase 1 for the atmospheric neutrino oscillation parameters. The two graphs in the figure show the predicted Phase 1 result with 3 yrs of livetime, assuming maximal and non-maximal true values of  $\theta_{23}$ . The Phase 1 measurement of the atmospheric mixing parameters will reach a precision competitive with that predicted from leading accelerator-based experiments such as NOvA [164] and T2K [165], but with very different energies and systematics, strengthening aggregate understanding of neutrino oscillations. In addition, Phase 1 will have sensitivity to the  $\theta_{23}$  octant and maximal mixing, of particular current interest due to the mild tension in recent measurements, with T2K [165] consistent with maximal mixing and NOvA [164] excluding it at  $2.5\sigma$ .

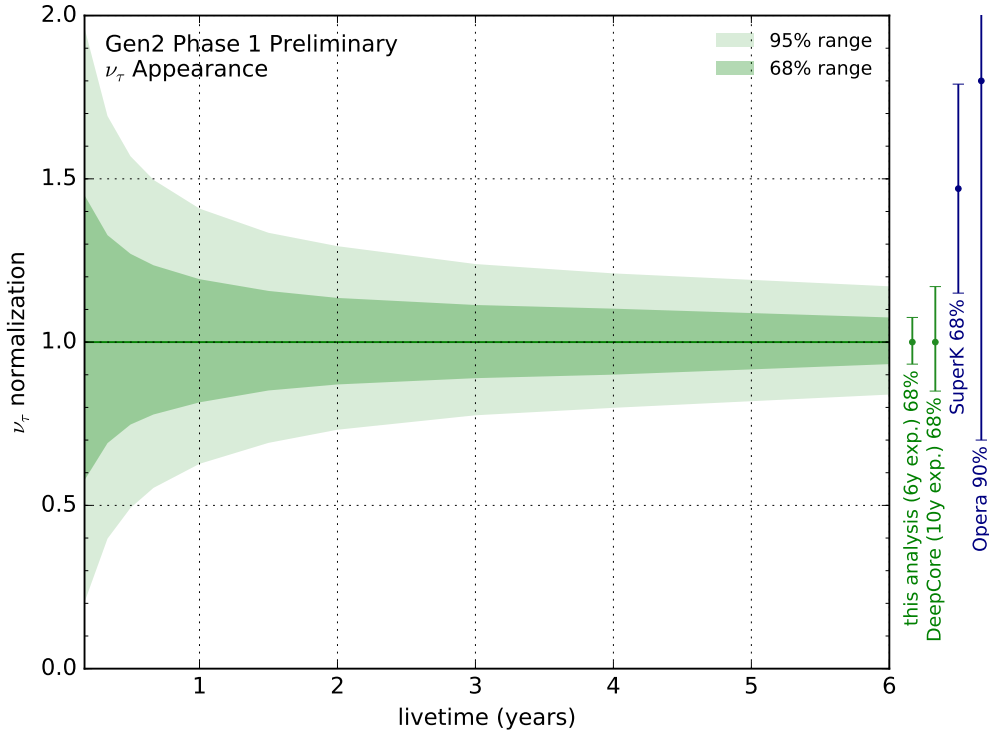


Figure D.82: Predicted measurement of the tau neutrino normalization vs. time for Phase 1, with results from Super-K [64] and OPERA [66], and predicted results from 10 yrs of DeepCore, shown for comparison. The Phase 1 prediction uses fully reconstructed simulated data (but without taking advantage of better reconstruction predicted with mDOMs) and has a full suite of systematic errors applied. With the Phase 1 strings we improve the worldwide precision by a factor of two with less than 2 yrs of livetime, and reach roughly 10% precision on this key measurement with about 5 yrs of livetime. The combined DeepCore+Phase 1 is much more sensitive than DeepCore alone, which plateaus at roughly 15% precision. Including 10 yrs of DeepCore data, the livetime that will have been accumulated when Phase 1 starts taking data, will slightly improve the overall precision beyond what is shown here. (Note: The OPERA 90% range is only shown to the top of the plot scale but in fact extends to 3.6.)

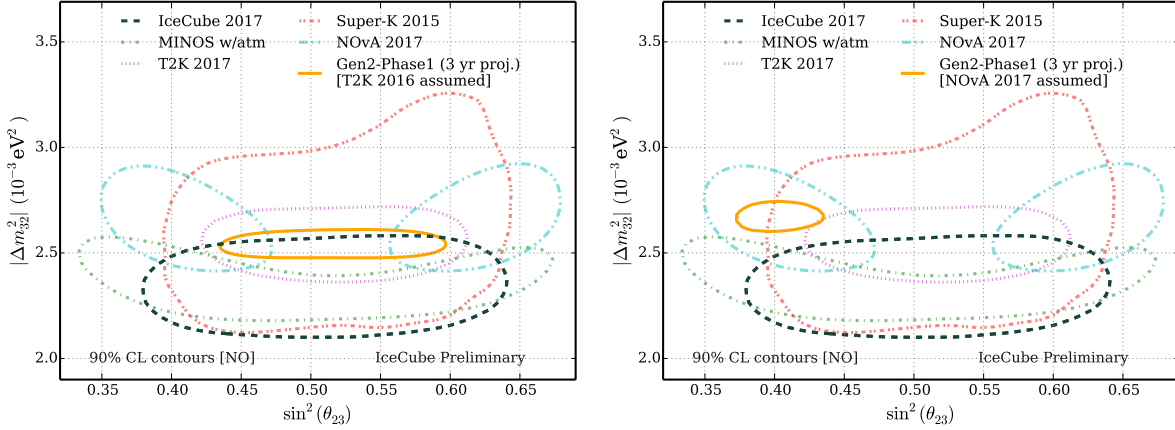


Figure D.83: The orange lines show the sensitivity of the IceCube–Gen2 Phase 1 detector to atmospheric  $\nu_\mu$  disappearance parameters after 3 yrs of livetime. The sensitivity in the left-hand graph assumes the true values of the parameters to be  $\Delta m_{32}^2 = 2.51 \times 10^{-3} \text{ eV}^2$  and  $\theta_{23} = 45^\circ$ , which are the T2K best-fit point from reference [166]. The sensitivity in the right-hand graph assumes the true values of the parameters to be  $\Delta m_{32}^2 = 2.67 \times 10^{-3} \text{ eV}^2$  and  $\sin^2 \theta_{23} = 0.404$ , which are the lower-octant NOvA best-fit point (statistically degenerate with their upper-octant best-fit point) from reference [164]. The graphs also show the most recent measurements from IceCube–DeepCore [167], MINOS [168], T2K [165], Super-Kamiokande [169] and NOvA [164].

Phase 1 will be able to exclude maximal mixing at  $3\sigma$  in roughly 3 yrs if the true value of  $\theta_{23}$  is at the current NOvA best-fit value. Under conservative assumptions, Phase 1 will also be able to exclude the wrong neutrino mass ordering (NMO) at  $1.5\text{--}2\sigma$  with 3 yrs of data (with favorable  $\theta_{23}$  and normal ordering, it could reach  $3\sigma$  in the same time frame).

The greater event rate at low neutrino energies will also enable Phase 1 to improve IceCube’s world-leading sensitivity to sterile neutrinos [170, 171]. Phase 1 can improve on the currently limits on  $|U_{\tau 4}|^2$  from DeepCore and Super-K by about a factor of three. This greater event rate will enable Phase 1 to test for non-standard neutrino physics directly, complementing its ability to do so indirectly via  $\nu_\tau$  appearance.

Finally, with Phase 1 we will be able to extend our search for neutrinos from solar WIMP annihilations down to WIMP masses as low as 5 GeV (see Fig. D.84), building on IceCube’s highly competitive results on indirect dark matter detection [100].

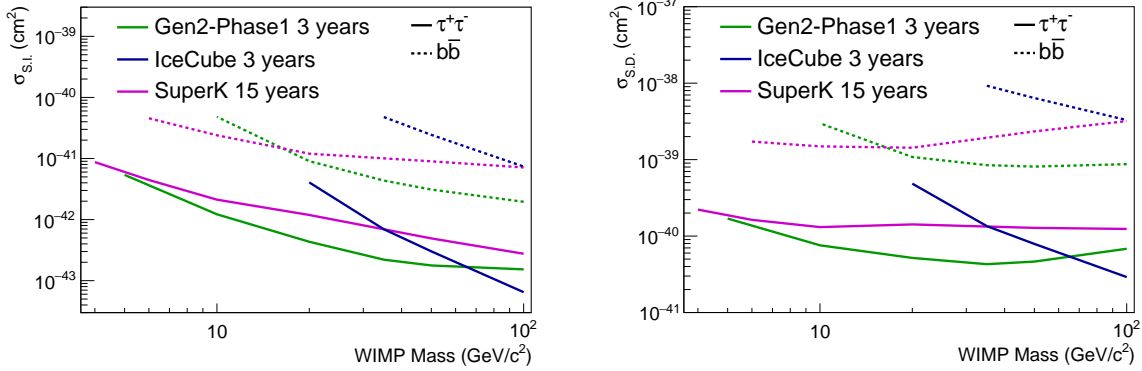


Figure D.84: The IceCube–Gen2 Phase 1 sensitivity to neutrinos from solar WIMP annihilations for spin-independent (left) and spin-dependent (right) models. This sensitivity is compared to existing limits from Super-Kamiokande [110] and IceCube [172].

### Calibration

Phase 1 provides an opportunity to deploy new calibration sources, which are intended to build on the lessons learned from IceCube and to improve our knowledge of the ice, leading to corresponding improvements in many IceCube analyses, including those at energies relevant for neutrino oscillation analyses. The majority of the calibrations in IceCube are performed using LED flashers, co-located with the IceCube DOMs. These have been used to measure the detector geometry, validate time calibration and, most importantly, to measure the optical properties of the ice (the unaltered “bulk ice” between the strings, and the refrozen “hole ice” in which the strings are deployed).

The IceCube LED brightness levels and directions are known to only 20% and 10 degrees, respectively [3]. There are also no vertically oriented LEDs that can directly probe the hole ice. The proposed Phase 1 devices are listed below.

- The Precision Optical CALibration Module (POCAM) [128, 129]: An isotropic light source with a well understood light output to measure *in situ* the optical efficiency of the DOMs to within 3% (see Sec. 7.4.2).
- LED flashers in the mDOMs: Housed in the internal support structure for the PMTs for precisely measured custom placement and orientation. With horizontal distances as low as 20 m between Phase 1 mDOMs, multiple flashers can be coordinated to

probe “double bang” signatures at the 20 m baseline at which IceCube is most sensitive to high energy  $\nu_\tau$  observation (see Sec. 7.4.1).

- Video cameras: Deployed with the mDOMs or in dedicated camera modules in order to monitor the hole ice, determine if the degassing process is successful and measure light from LEDs in order to further probe the absorption and scattering properties of the bulk ice (see Sec. 7.4.3).

#### *Appendix D.2. Additional Science Benefits*

Beyond exploiting the distinct capabilities of an enhanced IceCube in-fill array to achieve the core science mission of Phase 1, neutrino oscillation measurements by a combined DeepCore and Phase 1 will complement accelerator and reactor neutrino experiments, as the different set of systematic uncertainties confronting it and the weak impact of  $\delta_{\text{CP}}$  on its measurements will increase the robustness of global neutrino oscillation fits. Comparison of DeepCore+Phase 1 observations to those made by both currently running experiments such as T2K [173] and NOvA [174] and planned experiments such as DUNE [175], Hyper-Kamiokande [176], and JUNO [177] will therefore also provide broad and model-independent potential for discovery of new physics.

Moreover, a restart of deep ice drilling at the South Pole enables future particle astrophysics at this unique site. The deep ice at the South Pole is an optimal location for deployment of a direct dark matter detector with scintillator crystals (DM-Ice [2]) to confirm or reject the annual modulation of WIMP dark matter claimed by DAMA [116]. With surrounding IceCube strings used as a veto shield, the South Pole site offers a highly stable, nearly background-free environment. Deep ice drilling also allows for the possibility of deploying next-generation optical sensor technology prototypes for ultimate use in a fully-realized IceCube-Gen2 Neutrino Observatory. The opportunity to retire risk at an early stage of development would shorten the design phase of this formidable endeavor and provide a pathway for utilization of novel and potentially game-changing photodetection technology.

## References

- [1] **IceCube** Collaboration, M. Aartsen *et al.*, “Measurement of South Pole ice transparency with the IceCube LED calibration system,” *Nucl. Instrum. Meth.* **A711** (2013) 73–89, [arXiv:1301.5361](#).
- [2] J. Cherwinka, R. Co, D. Cowen, D. Grant, F. Halzen, *et al.*, “A Search for the Dark Matter Annual Modulation in South Pole Ice,” *Astropart. Phys.* **35** (2012) 749–754, [arXiv:1106.1156](#).
- [3] **IceCube** Collaboration, M. G. Aartsen *et al.*, “The IceCube Neutrino Observatory: Instrumentation and Online Systems,” *JINST* **12** (2017), no. 03 P03012, [1612.05093](#).
- [4] D. Mei and A. Hime, “Muon-induced background study for underground laboratories,” *Phys. Rev.* **D73** (2006) 053004, [astro-ph/0512125](#).
- [5] **IceCube** Collaboration, M. G. Aartsen *et al.*, “Evidence for High-Energy Extraterrestrial Neutrinos at the IceCube Detector,” *Science* **342** (2013) 1242856, [arXiv:1311.5238](#).
- [6] **IceCube** Collaboration, M. Aartsen *et al.*, “Measurement of Atmospheric Neutrino Oscillations with IceCube,” *Phys. Rev. Lett.* **111** (2013) 081801, [arXiv:1305.3909](#).
- [7] **IceCube** Collaboration, S. Euler, L. Gladstone, C. Wiebusch, *et al.*, “Measurement of atmospheric neutrino oscillations with IceCube/DeepCore in its 79-string configuration,” in *Proceedings of the 33rd International Cosmic Ray Conference (ICRC2013)*, 2013. [arXiv:1304.0735](#).
- [8] **IceCube** Collaboration, M. Aartsen *et al.*, “Determining neutrino oscillation parameters from atmospheric muon neutrino disappearance with three years of IceCube DeepCore data,” *Phys. Rev.* **D91** (2015) 072004, [arXiv:1410.7227](#).
- [9] **IceCube** Collaboration, M. G. Aartsen *et al.*, “IceCube-Gen2: A Vision for the Future of Neutrino Astronomy in Antarctica,” [arXiv:1412.5106](#).
- [10] L. Wolfenstein, “Neutrino oscillations in matter,” *Phys. Rev.* **D17** (1978) 2369–2374.
- [11] S. Mikheyev and A. Y. Smirnov, “Resonant neutrino oscillations in matter,” *Prog. Part. Nucl. Phys.* **23** (1989) 41–136.

- [12] E. K. Akhmedov, A. Dighe, P. Lipari, and A. Y. Smirnov, “Atmospheric neutrinos at super-kamiokande and parametric resonance in neutrino oscillations,” *Nucl. Phys.* **B542** (1999) 3–30, [arXiv:hep-ph/9808270](#).
- [13] S. T. Petcov, “Diffractive - like (or parametric resonance - like?) enhancement of the earth (day - night) effect for solar neutrinos crossing the earth core,” *Phys. Lett.* **B434** (1998) 321–332, [hep-ph/9805262](#). See also [hep-ph/9811205](#).
- [14] **IceCube PINGU** Collaboration, M. G. Aartsen *et al.*, “Letter of Intent: The Precision IceCube Next Generation Upgrade (PINGU),” [arXiv:1401.2046](#).
- [15] **IceCube** Collaboration, A. Achterberg *et al.*, “First Year Performance of The IceCube Neutrino Telescope,” *Astropart. Phys.* **26** (2006) 155–173, [arXiv:astro-ph/0604450](#).
- [16] **IceCube** Collaboration, R. Abbasi *et al.*, “The Design and Performance of IceCube DeepCore,” *Astropart. Phys.* **35** (2012) 615–624, [arXiv:1109.6096](#).
- [17] T. Benson *et al.*, “IceCube Enhanced Hot Water Drill functional description,” *Ann. Glaciol.* **55** (2014), no. 68 105–114.
- [18] C. Andreopoulos *et al.*, “The GENIE Neutrino Monte Carlo Generator,” *Nucl. Instrum. Meth.* **A614** (2010) 87–104, [arXiv:0905.2517](#).
- [19] **GEANT4** Collaboration, S. Agostinelli *et al.*, “GEANT4: A Simulation toolkit,” *Nucl. Instrum. Meth.* **A506** (2003) 250–303.
- [20] **IceCube** Collaboration, D. Chirkin, “Photon tracking with GPUs in IceCube,” *Nucl. Instrum. Meth.* **A725** (2013) 141–143.
- [21] M. Larson, “Simulation and Identification of Non-Poissonian Noise Triggers in the IceCube Neutrino Detector,” Master’s Thesis, University of Alabama, 2013.
- [22] **IceCube** Collaboration, M. G. Aartsen *et al.*, “Energy Reconstruction Methods in the IceCube Neutrino Telescope,” *JINST* **9** (2014) P03009, [arXiv:1311.4767](#).
- [23] **IceCube** Collaboration, D. Chirkin, “Evidence of optical anisotropy of the South Pole ice,” in *Proceedings of 33rd International Cosmic Ray Conference (ICRC2013)*, 2013. [arXiv:1309.7010](#).

- [24] M. Ribordy and A. Y. Smirnov, “Improving the neutrino mass hierarchy identification with inelasticity measurement in PINGU and ORCA,” *Phys. Rev.* **D87** (2013) 113007, [arXiv:1303.0758](#).
- [25] F. Feroz, M. P. Hobson, and M. Bridges, “Multinest: an efficient and robust bayesian inference tool for cosmology and particle physics,” *Mon. Not. Roy. Astron. Soc.* **398** (Oct., 2009) 1601–1614, [arXiv:0809.3437](#).
- [26] Z. I. Botev, J. F. Grotowski, and D. P. Kroese, “Kernel density estimation via diffusion,” *Ann. Statist.* **38** (10, 2010) 2916–2957.
- [27] I. S. Abramson, “On bandwidth variation in kernel estimates—a square root law,” *Ann. Statist.* **10** (12, 1982) 1217–1223.
- [28] M. C. J. S. J. Sheather, “A reliable data-based bandwidth selection method for kernel density estimation,” *Journal of the Royal Statistical Society. Series B (Methodological)* **53** (1991), no. 3 683–690.
- [29] **IceCube** Collaboration, M. Aartsen *et al.*, “Measurement of the Atmospheric  $\nu_e$  flux in IceCube,” *Phys. Rev. Lett.* **110** (2013) 151105, [arXiv:1212.4760](#).
- [30] J. Koskinen, “Atmospheric neutrino results from IceCube/DeepCore and plans for PINGU,” in *Proceedings of the XXVII international conference on neutrino physics and astrophysics (Neutrino 2016)*, 2016.
- [31] A. Hoecker, P. Speckmayer, J. Stelzer, J. Therhaag, E. von Toerne, and H. Voss, “TMVA: Toolkit for Multivariate Data Analysis,” *PoS ACAT* (2007) 040, [arXiv:physics/0703039](#).
- [32] **Particle Data Group** Collaboration, J. Beringer *et al.*, “Review of particle physics,” *Phys. Rev.* **D86** (Jul, 2012) 010001.
- [33] M. Honda, T. Kajita, K. Kasahara, S. Midorikawa, and T. Sanuki, “Calculation of atmospheric neutrino flux using the interaction model calibrated with atmospheric muon data,” *Phys. Rev.* **D75** (2007) 043006, [astro-ph/0611418](#).
- [34] **Super-Kamiokande** Collaboration, E. Richard *et al.*, “Measurements of the atmospheric neutrino flux by Super-Kamiokande: energy spectra, geomagnetic effects, and solar modulation,” [1510.08127](#).
- [35] **Frejus** Collaboration, K. Daum *et al.*, “Determination of the atmospheric neutrino spectra with the Frejus detector,” *Z. Phys.* **C66** (1995) 417–428.

- [36] **IceCube** Collaboration, R. Abbasi *et al.*, “Search for Point Sources of High Energy Neutrinos with Final Data from AMANDA-II,” *Phys. Rev.* **D79** (2009) 062001, [0809.1646](#).
- [37] **IceCube** Collaboration, R. Abbasi *et al.*, “The Energy Spectrum of Atmospheric Neutrinos between 2 and 200 TeV with the AMANDA-II Detector,” *Astropart. Phys.* **34** (2010) 48–58, [1004.2357](#).
- [38] **ANTARES** Collaboration, S. Adrian-Martinez *et al.*, “Measurement of the atmospheric  $\nu_\mu$  energy spectrum from 100 GeV to 200 TeV with the ANTARES telescope,” *Eur. Phys. J.* **C73** (2013), no. 10 2606, [1308.1599](#). [Eur. Phys. J.C73,2606(2013)].
- [39] **IceCube** Collaboration, M. G. Aartsen *et al.*, “Atmospheric and astrophysical neutrinos above 1 TeV interacting in IceCube,” *Phys. Rev.* **D91** (2015), no. 2 022001, [1410.1749](#).
- [40] **IceCube** Collaboration, R. Abbasi *et al.*, “Measurement of the atmospheric neutrino energy spectrum from 100 GeV to 400 TeV with IceCube,” *Phys. Rev.* **D83** (2011) 012001, [1010.3980](#).
- [41] **IceCube** Collaboration, R. Abbasi *et al.*, “First search for atmospheric and extraterrestrial neutrino-induced cascades with the IceCube detector,” *Phys. Rev.* **D84** (2011) 072001, [1101.1692](#).
- [42] M. Honda, T. Kajita, K. Kasahara, and S. Midorikawa, “Improvement of low energy atmospheric neutrino flux calculation using the JAM nuclear interaction model,” *Phys. Rev.* **D83** (2011) 123001, [arXiv:1102.2688](#).
- [43] A. Dziewonski and D. Anderson, “Preliminary reference earth model,” *Phys. Earth Planet. In.* **25** (1981) 297–356.
- [44] M. Honda, M. S. Athar, T. Kajita, K. Kasahara, and S. Midorikawa, “Atmospheric neutrino flux calculation using the NRLMSISE-00 atmospheric model,” *Phys. Rev.* **D92** (2015), no. 2 023004, [arXiv:1502.03916](#).
- [45] R. Wendell, “prob3++ software for computing three flavor neutrino oscillation probabilities.” <http://www.phy.duke.edu/~raw22/public/Prob3++/>, 2012.
- [46] S. S. Wilks, “The large-sample distribution of the likelihood ratio for testing composite hypotheses,” *Ann. Math. Statist.* **9** (03, 1938) 60–62.

- [47] M. C. Gonzalez-Garcia, M. Maltoni, and T. Schwetz, “Updated fit to three neutrino mixing: status of leptonic CP violation,” *JHEP* **11** (2014) 052, [arXiv:1409.5439](#).
- [48] G. L. Fogli, E. Lisi, A. Marrone, D. Montanino, A. Palazzo, and A. M. Rotunno, “Global analysis of neutrino masses, mixings, and phases: Entering the era of leptonic CP violation searchers,” *Phys. Rev.* **D86** (Jul, 2012) 013012.
- [49] “Nova plots and figures.” [http://www-nova.fnal.gov/plots\\_and\\_figures/plot\\_and\\_figures.html](http://www-nova.fnal.gov/plots_and_figures/plot_and_figures.html). Accessed: 2015.
- [50] **T2K** Collaboration, K. Abe *et al.*, “Neutrino oscillation physics potential of the T2K experiment,” *PTEP* **4** (2015) 043C01, [arXiv:1409.7469](#).
- [51] **SNO** Collaboration, B. Aharmim *et al.*, “Electron energy spectra, fluxes, and day-night asymmetries of B-8 solar neutrinos from measurements with NaCl dissolved in the heavy-water detector at the Sudbury Neutrino Observatory,” *Phys. Rev.* **C72** (2005) 055502, [arXiv:nucl-ex/0502021](#).
- [52] E. K. Akhmedov, S. Razzaque, and A. Y. Smirnov, “Mass hierarchy, 2-3 mixing and CP-phase with Huge Atmospheric Neutrino Detectors,” *J. High Energy Phys.* **1302** (2013) 082, [arXiv:1205.7071](#).
- [53] G. D. Barr, S. Robbins, T. K. Gaisser, and T. Stanev, “Uncertainties in atmospheric neutrino fluxes,” *Phys. Rev. D* **74** (Nov, 2006) 094009.
- [54] F. Capozzi, E. Lisi, and A. Marrone, “PINGU and the neutrino mass hierarchy: Statistical and systematic aspects,” *Phys.Rev.* **D91** (2015) 073011, [arXiv:1503.01999](#).
- [55] M. C. Gonzalez-Garcia, M. Maltoni, and T. Schwetz, “Global Analyses of Neutrino Oscillation Experiments,” *Nucl. Phys.* **B908** (2016) 199–217, [1512.06856](#).
- [56] A. Marrone, E. Lisi, A. Palazzo, D. Montanino, and F. Capozzi, “Global fits to neutrino oscillations: status and prospects,” *PoS* **EPS-HEP2015** (2015) 093.
- [57] M. Blennow, P. Coloma, P. Huber, and T. Schwetz, “Quantifying the sensitivity of oscillation experiments to the neutrino mass ordering,” *JHEP* **03** (2014) 028, [arXiv:1311.1822](#).

- [58] W. Winter, “Neutrino mass hierarchy determination with IceCube-PINGU,” *Phys. Rev.* **D88** (2013) 013013, [arXiv:1305.5539](#).
- [59] S.-F. Ge, K. Hagiwara, and C. Rott, “A Novel Approach to Study Atmospheric Neutrino Oscillation,” *JHEP* **06** (2014) 150, [1309.3176](#).
- [60] S.-F. Ge and K. Hagiwara, “Physics Reach of Atmospheric Neutrino Measurements at PINGU,” *JHEP* **09** (2014) 024, [1312.0457](#).
- [61] S. Antusch, C. Biggio, E. Fernandez-Martinez, M. Gavela, and J. Lopez-Pavon, “Unitarity of the Leptonic Mixing Matrix,” *JHEP* **0610** (2006) 084, [hep-ph/0607020](#).
- [62] S. Antusch, J. P. Baumann, and E. Fernandez-Martinez, “Non-Standard Neutrino Interactions with Matter from Physics Beyond the Standard Model,” *Nucl.Phys.* **B810** (2009) 369–388, [0807.1003](#).
- [63] D. Meloni, T. Ohlsson, W. Winter, and H. Zhang, “Non-standard interactions versus non-unitary lepton flavor mixing at a neutrino factory,” *JHEP* **04** (2010) 041, [0912.2735](#).
- [64] **Super-Kamiokande Collaboration** Collaboration, K. Abe *et al.*, “Evidence for the Appearance of Atmospheric Tau Neutrinos in Super-Kamiokande,” *Phys.Rev.Lett.* **110** (2013), no. 18 181802, [arXiv:1206.0328](#).
- [65] S. Moriyama, “New atmospheric and solar results from super-kamiokande.” Presented at the XXVII International Conference on Neutrino Physics and Astrophysics (Neutrino2016), 2016. [http://neutrino2016.iopconfs.org/IOP/media/uploaded/EVIOP/event\\_948/neutrino2016-moriyama-pub-2.pdf](http://neutrino2016.iopconfs.org/IOP/media/uploaded/EVIOP/event_948/neutrino2016-moriyama-pub-2.pdf).
- [66] **OPERA** Collaboration, N. Agafonova *et al.*, “Discovery of  $\tau$  Neutrino Appearance in the CNGS Neutrino Beam with the OPERA Experiment,” *Phys. Rev. Lett.* **115** (2015), no. 12 121802, [arXiv:1507.01417](#).
- [67] W. Gilbert, *De magnete*. 1600.
- [68] B. A. Buffett, “Earth’s core and the geodynamo,” *Science* **288** (2000), no. 5473 2007–2012, <http://www.sciencemag.org/content/288/5473/2007.full.pdf>.
- [69] Y. A. Popov, S. L. Pevzner, V. P. Pimenov, and R. A. Romushkevich, “New geothermal data from the Kola superdeep well SG-3,” *Tectonophysics* **306** (1999), no. 3–4 345 – 366.

- [70] A. W. Hofmann, “Mantle geochemistry: the message from oceanic volcanism,” *Nature* **385** (Jan., 1997) 219–229.
- [71] W. F. McDonough, “Compositional Model for the Earth’s Core,” *Treatise on Geochemistry* **2** (Dec., 2003) 547–568.
- [72] R. D. Oldham, “The constitution of the interior of the earth, as revealed by earthquakes,” *Q. J. Geol. Soc.* **62** (1906), no. 1-4 456–475, <http://jgslegacy.lyellcollection.org/content/62/1-4/456.full.pdf+html>.
- [73] J. S. Resovsky and J. Trampert, “Reliable mantle density error bars: an application of the neighbourhood algorithm to normal-mode and surface wave data,” *Geophys. J. Int.* **150** (Sept., 2002) 665–672.
- [74] D. E. Smylie, “The Inner Core Translational Triplet and the Density Near Earth’s Center,” *Science* **255** (Mar., 1992) 1678–82.
- [75] W. Winter, “Atmospheric Neutrino Oscillations for Earth Tomography,” *Nucl. Phys.* **B908** (2016) 250–267, [arXiv:1511.05154](https://arxiv.org/abs/1511.05154).
- [76] W. McDonough and S. Sun, “The composition of the Earth,” *Chem. Geol.* **120** (Mar., 1995) 223–253.
- [77] F. Birch, “Elasticity and constitution of the Earth’s interior,” *J. Geophys. Res.* **57** (June, 1952) 227–286.
- [78] D. R. Fearn and D. E. Loper, “Compositional convection and stratification of Earth’s core,” *Nature* **289** (Jan., 1981) 393–394.
- [79] C. J. Allègre, J.-P. Poirier, E. Humler, and A. W. Hofmann, “The chemical composition of the Earth,” *Earth Planet. Sc. Lett.* **134** (Sept., 1995) 515–526.
- [80] J. Li and Y. Fei, “Experimental Constraints on Core Composition,” in *Treatise on geochemistry, Vol. 2: The Mantle and core* (R. W. Carlson, ed.), vol. 2, ch. 2.14, pp. 1–31. Elsevier, Amsterdam, 2007.
- [81] O. Narygina, L. S. Dubrovinsky, C. a. McCammon, A. Kurnosov, I. Y. Kantor, V. B. Prakapenka, and N. a. Dubrovinskaia, “X-ray diffraction and Mössbauer spectroscopy study of fcc iron hydride FeH at high pressures and implications for the composition of the Earth’s core,” *Earth Planet. Sc. Lett.* **307** (July, 2011) 409–414.

- [82] C. Allègre, G. Manhès, and É. Lewin, “Chemical composition of the earth and the volatility control on planetary genetics,” *Earth and Planetary Science Letters* **185** (2001), no. 1–2 49 – 69.
- [83] H. Huang, Y. Fei, L. Cai, F. Jing, X. Hu, H. Xie, L. Zhang, and Z. Gong, “Evidence for an oxygen-depleted liquid outer core of the earth,” *Nature* **479** (11, 2011) 513–516.
- [84] C. Rott, A. Taketa, and D. Bose, “Spectrometry of the Earth using Neutrino Oscillations,” *Scientific Reports* *5*, 15225 (2015) [arXiv:1502.04930](#).
- [85] J. A. Formaggio and G. P. Zeller, “From eV to EeV: Neutrino cross sections across energy scales,” *Rev. Mod. Phys.* **84** (Sep, 2012) 1307–1341.
- [86] L. Köpke and IceCube Collaboration, “Supernova Neutrino Detection with IceCube,” *Journal of Physics Conference Series* **309** (Aug., 2011) 012029, [arXiv:1106.6225](#).
- [87] **IceCube** Collaboration, V. Baum, L. Demirörs, L. Köpke, and M. Ribordy, “Supernova detection with IceCube and beyond,” in *Proceedings of the 32nd International Cosmic Ray Conference (ICRC2011)*, 2011.
- [88] T. Gaisser, *Cosmic Rays and Particle Physics*. Cambridge University Press, 1991.
- [89] D. Heck, G. Schatz, T. Thouw, J. Knapp, and J. Capdevielle, “CORSIKA: A Monte Carlo code to simulate extensive air showers,” *Forschungszentrum Karlsruhe Report FZKA 6019* (1998).
- [90] L. Hüdepohl, B. Müller, H.-T. Janka, A. Marek, and G. G. Raffelt, “Neutrino Signal of Electron-Capture Supernovae from Core Collapse to Cooling,” *Physical Review Letters* **104** (June, 2010) 251101, [0912.0260](#).
- [91] M. Salathe, M. Ribordy, and L. Demirörs, “Novel technique for supernova detection with IceCube,” *Astropart. Phys.* **35** (2012) 485–494, [arXiv:1106.1937](#).
- [92] M. Ribordy, “Methods and problems in neutrino observatories,” *Proc. Int. Sch. Phys. Fermi* **182** (2012) 207–255, [1205.4965](#).
- [93] **IceCube** Collaboration, R. Bruijn, “Supernova Detection in IceCube: Status and Future,” in *Proceedings of the Neutrino Oscillation Workshop (NOW 2012)*, 2013. [arXiv:1302.2040](#).

- [94] M. T. Keil, G. G. Raffelt, and H.-T. Janka, “Monte carlo study of supernova neutrino spectra formation,” *The Astrophysical Journal* **590** (2003), no. 2 971.
- [95] F. Zwicky, “Die Rotverschiebung von extragalaktischen Nebeln,” *Helv. Phys. Acta* **6** (1933) 110–127.
- [96] **WMAP** Collaboration, E. Komatsu *et al.*, “Seven-Year Wilkinson Microwave Anisotropy Probe (WMAP) Observations: Cosmological Interpretation,” *Astrophys. J. Suppl.* **192** (2011) 18, [arXiv:1001.4538](#).
- [97] G. Bertone, D. Hooper, and J. Silk, “Particle dark matter: Evidence, candidates and constraints,” *Phys. Rep.* **405** (2005) 279–390, [arXiv:hep-ph/0404175](#).
- [98] G. Bertone, ed., *Non-WIMP Candidates*. Particle Dark Matter: Observations, Models and Searches. 2010.
- [99] I. F. M. Albuquerque, L. Hui, and E. W. Kolb, “High energy neutrinos from superheavy dark matter annihilation,” *Phys. Rev. D* **64** (2001) 083504.
- [100] **IceCube** Collaboration, M. Aartsen *et al.*, “Search for dark matter annihilations in the Sun with the 79-string IceCube detector,” *Phys. Rev. Lett.* **110** (2013) 131302, [arXiv:1212.4097](#).
- [101] **IceCube** Collaboration, R. Abbasi *et al.*, “Search for Dark Matter from the Galactic Halo with the IceCube Neutrino Observatory,” *Phys. Rev.* **D84** (2011) 022004, [arXiv:1101.3349](#).
- [102] **IceCube** Collaboration, M. Aartsen *et al.*, “Search for Neutrinos from Dark Matter Self-Annihilations in the centre of the Milky Way with 3 years of IceCube/DeepCore,” [arXiv:1705.08103](#).
- [103] **IceCube** Collaboration, M. G. Aartsen *et al.*, “IceCube Search for Dark Matter Annihilation in nearby Galaxies and Galaxy Clusters,” *Phys. Rev.* **D88** (2013) 122001, [arXiv:1307.3473](#).
- [104] **IceCube** Collaboration, R. Abbasi *et al.*, “The IceCube Neutrino Observatory IV: Searches for Dark Matter and Exotic Particles,” [arXiv:1111.2738](#).
- [105] H. Yuksel, S. Horiuchi, J. F. Beacom, and S. Ando, “Neutrino Constraints on the Dark Matter Total Annihilation Cross Section,” *Phys. Rev.* **D76** (2007) 123506, [arXiv:0707.0196](#).

- [106] B. Dasgupta and R. Laha, “Neutrinos in IceCube/KM3NeT as probes of Dark Matter Substructures in Galaxy Clusters,” *Phys. Rev.* **D86** (2012) 093001, [arXiv:1206.1322](#).
- [107] C. Savage, G. Gelmini, P. Gondolo, and K. Freese, “Compatibility of DAMA/LIBRA dark matter detection with other searches,” *J. Cosmol. Astropart. P.* **0904** (2009) 010, [arXiv:0808.3607](#).
- [108] J. L. Feng, J. Kumar, D. Marfatia, and D. Sanford, “Isospin-Violating Dark Matter,” *Phys. Lett.* **B703** (2011) 124–127, [arXiv:1102.4331](#).
- [109] C. Rott, T. Tanaka, and Y. Itow, “Enhanced Sensitivity to Dark Matter Self-annihilations in the Sun using Neutrino Spectral Information,” *J. Cosmol. Astropart. P.* **1109** (2011) 029, [arXiv:1107.3182](#).
- [110] **Super-Kamiokande** Collaboration, K. Choi *et al.*, “Search for neutrinos from annihilation of captured low-mass dark matter particles in the Sun by Super-Kamiokande,” *Phys.Rev.Lett.* **114** (2015), no. 14 141301, [arXiv:1503.04858](#).
- [111] P. Gondolo *et al.*, “DarkSUSY: Computing supersymmetric dark matter properties numerically,” *J. Cosmol. Astropart. P.* **0407** (2004) 008, [arXiv:astro-ph/0406204](#).
- [112] J. Edsjö, “WimpSim Neutrino Monte Carlo.” <http://www.fysik.su.se/~edsjo/wimpsim/>, 2013.
- [113] W. Rolke, A. Lopez, J. Conrad, and F. James, “Limits and Confidence Intervals in presence of nuisance parameters,” *Nucl. Instrum. Meth.* **A551** (2005) 493–503, [arXiv:physics/0403059v5](#).
- [114] J. F. Navarro, C. S. Frenk, and S. D. M. White, “The Structure of Cold Dark Matter Halos,” *Astrophys. J.* **462** (1996) 563–575, [arXiv:astro-ph/9508025](#).
- [115] **IceCube** Collaboration, M. G. Aartsen *et al.*, “The IceCube Neutrino Observatory Part IV: Searches for Dark Matter and Exotic Particles,” in *Proceedings, 33rd International Cosmic Ray Conference (ICRC2013)*, 2013. [arXiv:1309.7007](#).
- [116] **DAMA/LIBRA** Collaboration, R. Bernabei *et al.*, “New results from DAMA/LIBRA,” *Eur. Phys. J.* **C67** (2010) 39–49, [arXiv:1002.1028](#).

- [117] **CoGeNT** Collaboration, C. Aalseth *et al.*, “Results from a Search for Light-Mass Dark Matter with a P-type Point Contact Germanium Detector,” *Phys. Rev. Lett.* **106** (2011) 131301, [arXiv:1002.4703](#).
- [118] C. Aalseth, P. Barbeau, J. Colaresi, J. Collar, J. Diaz Leon, *et al.*, “Search for an Annual Modulation in a P-type Point Contact Germanium Dark Matter Detector,” *Phys. Rev. Lett.* **107** (2011) 141301, [arXiv:1106.0650](#).
- [119] **CDMS** Collaboration, R. Agnese *et al.*, “Silicon Detector Dark Matter Results from the Final Exposure of CDMS II,” *Phys. Rev. Lett.* **111** (2013), no. 25 251301, [arXiv:1304.4279](#).
- [120] **IceCube** Collaboration, R. Abbasi *et al.*, “The IceCube data acquisition system: Signal capture, digitization, and timestamping,” *Nucl. Instrum. Meth.* **A601** (2009) 294–316.
- [121] **KM3NeT** Collaboration, S. Adrian-Martinez *et al.*, “Deep sea tests of a prototype of the KM3NeT digital optical module,” *Eur. Phys. J.* **C74** (2014) 3056.
- [122] P. Timmer, E. Heine, and H. Peek, “Very low power, high voltage base for a photo multiplier tube for the KM3NeT deep sea neutrino telescope,” *JINST* **5** (2010) C12049.
- [123] J. Lundberg, P. Miocinovic, T. Burgess, J. Adams, S. Hundertmark, P. Desiati, K. Woschnagg, and P. Niessen, “Light tracking for glaciers and oceans: Scattering and absorption in heterogeneous media with Photonics,” *Nucl. Instrum. Meth.* **A581** (2007) 619–631, [astro-ph/0702108](#).
- [124] **IceCube** Collaboration, M. Rongen, “Measuring the optical properties of IceCube drill holes,” in *Proceedings of the 7th Very Large Volume Neutrino Telescope Workshop (VLVnT 2015)*, 2016. [http://www.epj-conferences.org/articles/epjconf/pdf/2016/11/epjconf-VLVnT2015\\_06011.pdf](http://www.epj-conferences.org/articles/epjconf/pdf/2016/11/epjconf-VLVnT2015_06011.pdf).
- [125] **IceCube** Collaboration, D. Tosi and C. Wendt, “Calibrating photon detection efficiency in IceCube,” *PoS TIPP2014* (2014) 157, [arXiv:1502.03102](#).
- [126] **IceCube** Collaboration, “The IceCube Collaboration: Contributions to the 30th International Cosmic Ray Conference (ICRC 2007),” in *Proceedings of the 30th International Cosmic Ray Conference (ICRC 2007)*, 2007. [arXiv:0711.0353](#).

- [127] J. Kapustinsky *et al.*, “A fast timing light pulser for scintillation detectors,” *Nucl. Instrum. Meth.* **A241** (1985), no. 2–3 612 – 613.
- [128] **IceCube Gen2** Collaboration, M. Jurkovi, K. Abraham, K. Holzapfel, K. Krings, E. Resconi, and J. Veenkamp, “A Precision Optical Calibration Module (POCAM) for IceCube-Gen2,” *EPJ Web Conf.* **116** (2016) 06001.
- [129] **IceCube** Collaboration, K. Krings, “A Precision Optical Calibration Module for IceCube-Gen2,” in *Proceedings of 34rd International Cosmic Ray Conference (ICRC2015)*, 2015. [arXiv:1510.05228](#).
- [130] B. Moffat *et al.*, “Optical calibration hardware for the sudbury neutrino observatory,” *Nucl. Instrum. Meth.* **A554** (2005), no. 1–3 255 – 265.
- [131] **IceCube** Collaboration, D. Bose, “PINGU Camera System to Study Properties of the Antarctic Ice,” *Proceedings of 34rd International Cosmic Ray Conference (ICRC2015)* (2015) [arXiv:1510.05228](#).
- [132] **DM-Ice17** Collaboration, J. Cherwinka *et al.*, “First data from DM-Ice17,” *Phys.Rev.* **D90** (2014), no. 9 092005, [arXiv:1401.4804](#).
- [133] A. Hubbard, *Muon-Induced Backgrounds in the DM-Ice17 NaI (Tl) Dark Matter Detector*. PhD Dissertation, University of Wisconsin – Madison, 2015.
- [134] S. N. Axani, J. M. Conrad, and C. Kirby, “The Desktop Muon Detector: A simple, physics-motivated machine- and electronics-shop project for university students,” *ArXiv e-prints* (June, 2016) [1606.01196](#).
- [135] A. Gazizov and M. P. Kowalski, “ANIS: High energy neutrino generator for neutrino telescopes,” *Comput. Phys. Commun.* **172** (2005) 203–213, [arXiv:astro-ph/0406439](#).
- [136] M. Sajjad Athar, M. Honda, T. Kajita, K. Kasahara, and S. Midorikawa, “Atmospheric neutrino flux at INO, South Pole and Pyhäsalmi,” *Phys. Lett.* **B718** (2013) 1375–1380, [arXiv:1210.5154](#).
- [137] A. Bodek and U. Yang, “Higher twist,  $\xi_W$  scaling, and effective LO PDFs for lepton scattering in the few GeV region,” *Journal of Physics G: Nuclear and Particle Physics* **29** (2003) 1899–1905, [arXiv:hep-ex/0210024v2](#).
- [138] D. Rein and L. M. Sehgal, “Neutrino Excitation of Baryon Resonances and Single Pion Production,” *Annals Phys.* **133** (1981) 79–153.

- [139] J.-H. Koehne, K. Frantzen, M. Schmitz, T. Fuchs, W. Rhode, D. Chirkin, and J. B. Tjus, “Proposal: A tool for propagation of charged leptons,” *Computer Physics Communications* **184** (2013), no. 9 2070 – 2090.
- [140] C. Pryke, A. Karle, and C. Kulesa, eds., *Report from the Workshop “Astrophysics from the South Pole: Status and Future Prospects”*. 2011.  
[http://find.spa.umn.edu/~pryke/southpolemeeting/sp\\_ws\\_wp.pdf](http://find.spa.umn.edu/~pryke/southpolemeeting/sp_ws_wp.pdf).
- [141] M. G. Burton, X. Cui, and N. F. H. Tothill, eds., *Symposium S288 (Astrophysics from Antarctica)*, vol. 8 of *Proceedings of the International Astronomical Union*. 2012. <http://www.phys.unsw.edu.au/IAUS288>.
- [142] J. H. Lever and P. Thur, “Economic Analysis of the South Pole Traverse, ERDC/CRREL TR-14-7.”  
<http://acwc.sdp.sirsi.net/client/search/asset/1035041>.
- [143] R. G. Calland, A. C. Kaboth, and D. Payne, “Accelerated Event-by-Event Neutrino Oscillation Reweighting with Matter Effects on a GPU,” *JINST* **9** (2014) P04016, [arXiv:1311.7579](https://arxiv.org/abs/1311.7579).
- [144] E. Ciuffoli, J. Evslin, and X. Zhang, “Confidence in a neutrino mass hierarchy determination,” *JHEP* **01** (2014) 095, [arXiv:1305.5150](https://arxiv.org/abs/1305.5150).
- [145] D. Casper, “The Nuance neutrino physics simulation, and the future,” in *Proceedings of the 1st International Workshop on Neutrino-nucleus interactions in the few GeV region (NuInt 01)*, 2002. [hep-ph/0208030](https://arxiv.org/abs/hep-ph/0208030).
- [146] C. Andreopoulos, C. Barry, S. Dytman, H. Gallagher, T. Golan, R. Hatcher, G. Perdue, and J. Yarba, “The GENIE Neutrino Monte Carlo Generator: Physics and User Manual,” [arXiv:1510.05494](https://arxiv.org/abs/1510.05494).
- [147] T. Katori and S. Mandalia, “PYTHIA hadronization process tuning in the GENIE neutrino interaction generator,” *J. Phys.* **G42** (2015) 115004, [arXiv:1412.4301](https://arxiv.org/abs/1412.4301).
- [148] A. Bodek and U.-k. Yang, “Axial and Vector Structure Functions for Electron- and Neutrino- Nucleon Scattering Cross Sections at all  $Q^2$  using Effective Leading order Parton Distribution Functions,” [arXiv:1011.6592](https://arxiv.org/abs/1011.6592).
- [149] G. D. Barr, T. K. Gaisser, P. Lipari, S. Robbins, and T. Stanev, “A Three - dimensional calculation of atmospheric neutrinos,” *Phys. Rev.* **D70** (2004) 023006, [astro-ph/0403630](https://arxiv.org/abs/astro-ph/0403630).

- [150] A. Fedynitch, R. Engel, T. K. Gaisser, F. Riehn, and S. Todor, “MCEQ - numerical code for inclusive lepton flux calculations,” in *Proceedings of the 34th International Cosmic Ray Conference (ICRC 2015)*, 2015. [arXiv:1503.00544](#).
- [151] K. Abe *et al.*, “Measurements of cosmic-ray proton and helium spectra from the BESS-Polar long-duration balloon flights over Antarctica,” *Astrophys. J.* **822** (2016), no. 2 65, [arXiv:1506.01267](#).
- [152] V. Kopenkin and T. Sinzi, “Cosmic ray primary composition in the energy range 10-1000 TeV obtained by passive balloonborne detector: Reanalysis of the RUNJOB experiment,” *Phys. Rev.* **D79** (2009) 072011.
- [153] M. J. Christ *et al.*, “Cosmic-ray proton and helium spectra: Results from the JACEE Experiment,” *Astrophys. J.* **502** (1998) 278–283.
- [154] **AMS** Collaboration, M. Aguilar *et al.*, “Precision Measurement of the Proton Flux in Primary Cosmic Rays from Rigidity 1 GV to 1.8 TV with the Alpha Magnetic Spectrometer on the International Space Station,” *Phys. Rev. Lett.* **114** (2015) 171103.
- [155] **PAMELA** Collaboration, O. Adriani *et al.*, “Measurements of Cosmic-Ray Hydrogen and Helium Isotopes with the PAMELA experiment,” *Astrophys. J.* **818** (2016), no. 1 68, [arXiv:1512.06535](#).
- [156] Y. S. Yoon *et al.*, “Cosmic-Ray Proton and Helium Spectra from the First CREAM Flight,” *Astrophys. J.* **728** (2011) 122, [arXiv:1102.2575](#).
- [157] T. K. Gaisser, T. Stanev, M. Honda, and P. Lipari, “Primary spectrum to 1-TeV and beyond,” in *Proceedings of the 27th International Cosmic Ray Conference (ICRC 2001)*, pp. 1643–1646, 2001. [http://www.copernicus.org/icrc/papers/ici6694\\_p.pdf](http://www.copernicus.org/icrc/papers/ici6694_p.pdf).
- [158] M. Honda, “HKKM atmospheric neutrino fluxes.” Presented at the 1st Atmospheric Neutrino Workshop, 2016. <http://indico.universe-cluster.de/indico/conferenceDisplay.py?confId=3533>.
- [159] E. Thébault *et al.*, “International Geomagnetic Reference Field: the 12th generation,” *Earth, Planets and Space* **67** (2015), no. 1 1–19.
- [160] G. Battistoni, A. Ferrari, T. Montaruli, and P. R. Sala, “The FLUKA atmospheric neutrino flux calculation,” *Astropart. Phys.* **19** (2003) 269–290, [hep-ph/0207035](#). [Erratum: *Astropart. Phys.*19,291(2003)].

- [161] “U.S. Standard Atmosphere, 1976.” U.S. Government Printing Office, 1976.
- [162] J. M. Picone, A. E. Hedin, D. P. Drob, and A. C. Aikin, “NRLMSISE-00 empirical model of the atmosphere: Statistical comparisons and scientific issues,” *Journal of Geophysical Research: Space Physics* **107** (2002), no. A12 SIA 15–1 to SIA 15–16. 1468.
- [163] “Airs – atmospheric infrared sounder.” <http://airs.jpl.nasa.gov/>.
- [164] **NOvA** Collaboration, P. Adamson *et al.*, “Measurement of the neutrino mixing angle  $\theta_{23}$  in NOvA,” *Phys. Rev. Lett.* **118** (2016) 151802, [arXiv:1701.05891](https://arxiv.org/abs/1701.05891).
- [165] **T2K** Collaboration, K. Abe *et al.*, “First combined analysis of neutrino and antineutrino oscillations at T2K,” *Phys. Rev. Lett.* **118** (2017) 151801.
- [166] **T2K** Collaboration, K. Abe *et al.*, “Measurement of muon antineutrino oscillations with an accelerator-produced off-axis beam,” *Phys. Rev. Lett.* **116** (2016) 181801.
- [167] **IceCube** Collaboration, M. G. Aartsen *et al.*, “Measurement of atmospheric neutrino oscillations at 6–56 GeV with IceCube DeepCore.” [arXiv:1707.07081](https://arxiv.org/abs/1707.07081), 2017.
- [168] **MINOS** Collaboration, P. Adamson *et al.*, “Measurement of Neutrino and Antineutrino Oscillations Using Beam and Atmospheric Data in MINOS,” *Phys. Rev. Lett.* **110** (2013) 251801, [arXiv:1304.6335](https://arxiv.org/abs/1304.6335).
- [169] R. Wendell, “Atmospheric neutrino oscillations at Super-Kamiokande,” *Proc. of Science ICRC 2015* (2015) 1062.
- [170] **IceCube** Collaboration, M. G. Aartsen *et al.*, “Searches for sterile neutrinos with the IceCube detector,” *Phys. Rev. Lett.* **117** (2016) 071801.
- [171] **IceCube** Collaboration, M. G. Aartsen *et al.*, “Search for sterile neutrino mixing using three years of IceCube DeepCore data,” *Phys. Rev.* **D95** (2017) 112002.
- [172] **IceCube** Collaboration, M. G. Aartsen *et al.*, “First search for dark matter annihilations in the Earth with the IceCube detector,” *Eur. Phys. J.* **C77** (2017) 82.
- [173] **T2K** Collaboration, K. Abe *et al.*, “Precise Measurement of the Neutrino Mixing Parameter  $\theta_{23}$  from Muon Neutrino Disappearance in an Off-axis Beam,” *Phys.Rev.Lett.* **112** (2014) 181801, [1403.1532](https://arxiv.org/abs/1403.1532).

- [174] **NOvA** Collaboration, P. Adamson *et al.*, “First measurement of electron neutrino appearance in NOvA,” *Phys. Rev. Lett.* **116** (2016), no. 15 151806, [1601.05022](#).
- [175] **DUNE** Collaboration, R. Acciarri *et al.*, “Long-Baseline Neutrino Facility (LBNF) and Deep Underground Neutrino Experiment (DUNE),” [1512.06148](#).
- [176] K. Abe, T. Abe, H. Aihara, Y. Fukuda, Y. Hayato, *et al.*, “Letter of Intent: The Hyper-Kamiokande Experiment — Detector Design and Physics Potential —,” [arXiv:1109.3262](#).
- [177] **JUNO** Collaboration, F. An *et al.*, “Neutrino Physics with JUNO,” *J. Phys.* **G43** (2016), no. 3 030401, [1507.05613](#).